DEUTSCHES ELEKTRONEN-SYNCHROTRON DESY

DESY 78/32
July 1978

Results from e^+e^- Interactions above 3 GeV

by

D. Cords

NOTKESTRASSE 85 · 2 HAMBURG 52

To be sure that your preprints are promptly included in the
HIGH ENERGY PHYSICS INDEX ,
send them to the following address (if possible by air mail) :

DESY
Bibliothek
Notkestrasse 85
2 Hamburg 52
Germany

RESULTS FROM e^+e^- INTERACTIONS ABOVE 3 GeV

by

D. Cords
Deutsches Elektronen-Synchrotron DESY, Hamburg

Lectures presented at the "International School of Elementary Particle Physics" at Kupari-Dubrovnik, Yugoslavia (18. Sept.-2. Oct. 1977)

1. Introduction

In this series of lectures I shall be concerned with e^+e^- interactions above 3 GeV. Merely six years ago, this energy region - well above the old vector mesons ρ, ω, and ϕ - was considered by many as asymptotically falling in cross section, having little or no structure. However, dramatic descoveries have emerged over the past four or five years and revealed a new type of spectroscopy in particle physics.

Before turning to the results I shall discuss some of the general characteristics of e^+e^- annihilations and point out the main differences to pp collisions at the ISR. e^+e^- colliding beams have proved to be powerful tools in high energy physics. When doing physics experiments at these complicated machines one has to be familiar with some of the storage ring properties like luminosity, beam-polarization, and energy spread. In order to assess the results one also has to know the main characteristics of the various detectors, some of which will be presented in Chapter 4. This report will not provide a complete survey of e^+e^- data above 3 GeV; for example the production of jets is omitted because it was presented in a parallel series of lectures[1] at the 1977 Kupari School. Other reports on this subject[2] emphasize or include other aspects. A review of recent results can be obtained from the Proceedings of the 1977 Symposium on Lepton and Photon Interactions.[3]

2. e^+e^- Annihilation Physics

To lowest order in electromagnetic coupling e^+e^- annihilation proceeds via one-photon exchange[4] and the matrix element can be written as a current-current interaction.

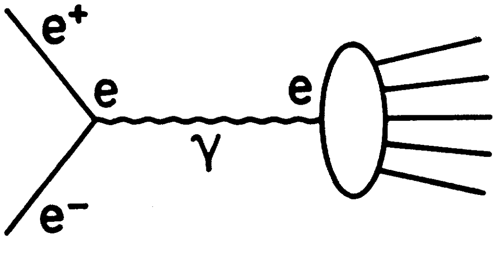

$$M = \frac{e^2}{s}\, j_\mu\, J_\mu \qquad (2.1)$$

j_μ = leptonic current

$$= \bar{\ell}\, \gamma_\mu\, \ell$$

J_μ = leptonic or $\underbrace{\text{hadronic current}}$

$$= \sum_i Q_i\, \bar{q}_i\, \gamma_\mu\, q_i$$

In the quark parton model⁵⁾ the hadronic vertex is considered as a sum of quark pair conversions and the coupling constant is modified by the fractional charges Q_i of the respective quarks q_i . For single quark pair creation the amplitude would read:

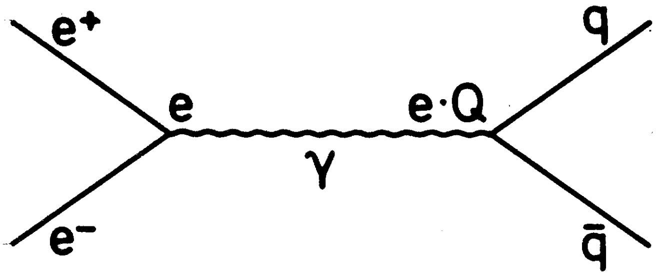

$$M_{q\bar{q}} = \frac{Qe^2}{s} \bar{\ell} \gamma_\mu \ell \cdot \bar{q} \gamma_\mu q$$

To make sure that no quarks escape and be observed it is assumed that the quarks convert to hadrons with unit probability.

In the following the discussion will be limited to these low-order electromagnetic processes, and higher-order contribution, like radiative corrections, will be mentioned only in passing.

2.1 Electromagnetic Processes

The cross sections for purely electromagnetic processes can be calculated from the well established theory⁴⁾ of quantum electrodynamics (QED). One example is the elastic electron position scattering or Bhabha scattering, in which case one has contributions from time-like and space-like diagrams (time propagation from left to right):

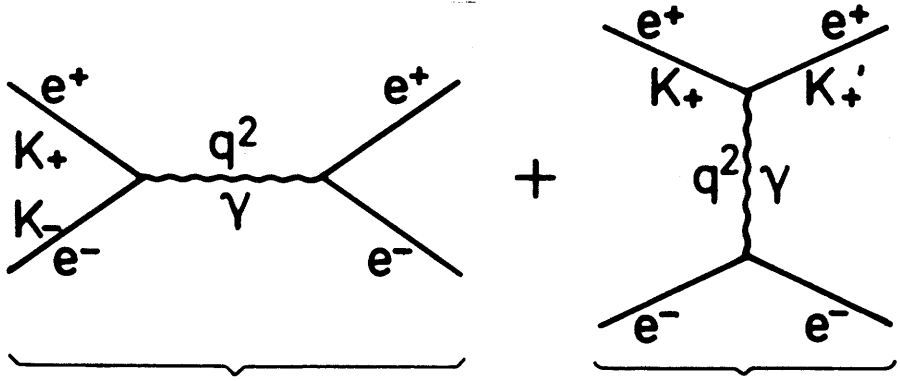

time-like diagram (annihilation)

space-like diagram
(t-channel exchange)

In e^+e^- head-on collisions the centre of mass system (cms) is identical with the laboratory system and in our kinematic considerations we shall neglect the difference due to small e^+e^- crossing angles provided at some storage rings. Therefore we have for the three-momenta $\vec{K}_+ = - \vec{K}_- = \vec{K}$, $|\vec{K}_+| = |\vec{K}'_+|$, and neglecting the electron mass we get the following simple relations for the momentum $\vec{K}$ and the total cms energy $\sqrt{s}$: $|\vec{K}| = E = E_{beam}$

$$\sqrt{s} = W = 2E$$

Using these relations the expressions for the momentum transfers squared q^2 of the time-like and space-like diagrams above can be easily evaluated:

$q^2 = (K_+ + K_-)$	$q^2 = (K_+ - K'_+)^2$	metric
$= - s < 0$	$= 4\|\vec{K}_+\| \cdot \|\vec{K}'_+\| \cdot \sin^2 \frac{\theta}{2}$ $= s \cdot \sin^2 \frac{\theta}{2} > 0$	$K = (\vec{K}, i E)$ $K^2 = \vec{K}^2 - E^2$
$= s > 0$	$= - s \cdot \sin^2 \frac{\theta}{2} < 0$	$K = (E, \vec{K})$ $K^2 = E^2 - \vec{K}^2$

The two metrices shown differ in the sign of the four-vector product definition. The first is used by Muirhead during his lectures$^{6)}$ at this school while the second metric is widely used by other authors. In terms of the second metric the time-like and space-like diagrams are characterized by positive and negative momentum transfers respectively. These diagrams are also sometimes referred to as annihilation graph and t-channel exchange contribution.

It was already implied by the matrix element (2.1) that the propagator is given by q^{-2} which is s^{-1} for the annihilation graph according to the time-like expression in the above table. However, for the space-like diagram the propagator is $s^{-1} \sin^{-2} \frac{\theta}{2}$, and therefore small angle Bhabha scattering is completely dominated by its space-like contribution.

Since the cross section is large for forward angles and QED is a save theory in this region, Bhabha scattering is taken for luminosity measurements, i.e. all measured e^+e^- event rates are normalized by the simultaneously measured

e^+e^- elastic cross section.

Another QED process of the same order of magnitude as Bhabha scattering is the annihilation into two photons:

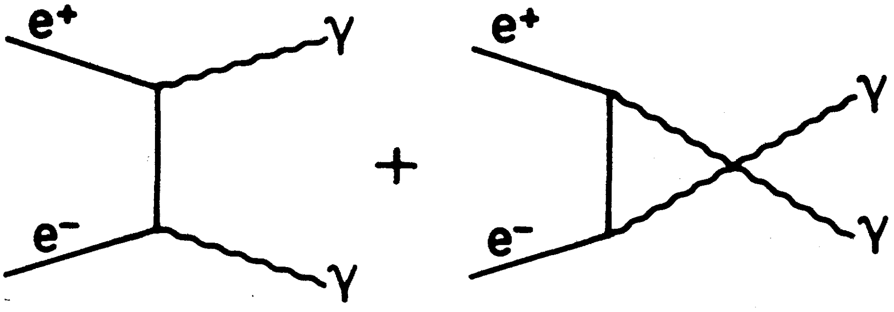

This process has only space-like diagrams, and therefore its angular distribution is strongly peaked towards the directions of the incident leptons.

When presenting the energy dependence of various e^+e^- cross sections, the data are very often referred to muon pair production which is the simplest e^+e^- process, since it has only a time-like contribution.

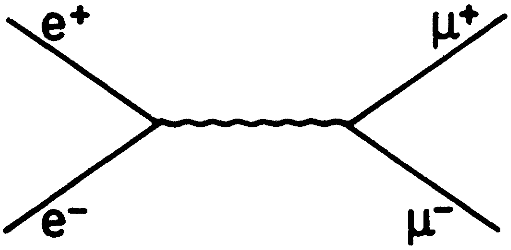

$$\sigma_{\mu\mu} = \frac{4\pi\alpha^2}{3s} = \frac{86.8\mu b}{s}\ , \text{ s in GeV}^2$$

$$= \frac{\pi\,\alpha^2}{3E^2} = \frac{21.7\mu b}{E^2}\ , \text{ E in GeV}$$

$$\alpha = \frac{e^2}{\hbar\,c} = \frac{1}{137}$$

The cross section scale and the angular dependence of the processes discussed in this section (and of $e^-e^- \rightarrow e^-e^-$) are shown in Fig.2.1 for beam energies of E = 1 GeV (1nb = 10^{-33} cm^2). These cross sections drop like $\frac{1}{E^2}$ with increasing energy whereas the cross sections for photoproduction or hadron collision approach a lower limit at high energies and in some cases rise afterwards. The size of the different types of cross sections differs by several orders of magnitude : Whereas for e^+e^- annihilation we have typically 20 to 100 nb at E = 1 GeV, the photoproduction and hadronic cross sections approach 100 to

200 μb and 20 to 40 mb, respectively at high energies.

2.2 Hadron Production

We shall consider here hadron production via one photo annihilation and neglect higher order terms.7)

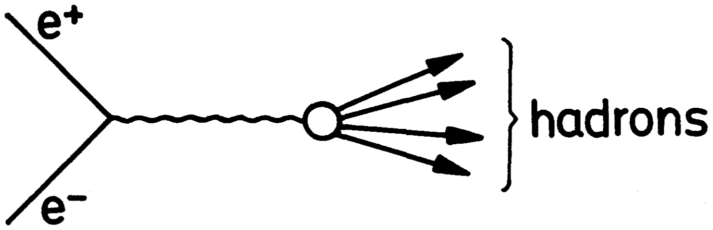

If conserved, the quantum numbers of the hadronic system should be those of the photon. Therefore spin, parity, and C-parity are given by $J^{PC} = 1^{--}$ and one can ask: Which consequences do arise for the cross section and the angular distribution?

Due to $J^P = 1^-$ the orbital angular momenta of the e^+e^- system are limited to $L = 0$ and 2. Using the classical definition $L = p \cdot r \simeq E \cdot r$, where $p \simeq E$ is the electron momentum (energy) and r the interaction radius, one obtains $r \sim \frac{1}{E}$ since L is limited. Inserting this and the electromagnetic coupling α into the geometrial cross section $\sigma = \pi r^2$ and remembering the above μ-pair cross section, one has for the total hadronic cross section

$$\sigma(e^+e^- \rightarrow \text{hadrons}) \sim \alpha^2 \pi r^2 = \frac{\alpha^2 \pi}{E^2}$$

$$= R \cdot \sigma_{\mu\mu}$$

Therefore it is expected that the hadronic cross section decreases as $1/E^2$. This is in strong contrast with purely hadronic interactions where the cross section becomes constant or even increases at high energies because higher and higher partial waves can contribute to hadron collisions.8)

Another characteristic of hadron scattering is the strongly forward peaked angular distribution of the final state particles. The hadrons from e^+e^- collisions, on the other hand, have a relatively flat angular distribution. Since the total angular momentum is limited to one, the most general angular distribution for the inclusive hadron production process $e^+e^- \to h + X$ is

$$\frac{d\sigma_h}{d\cos\theta} = a + b\cos^2\theta$$

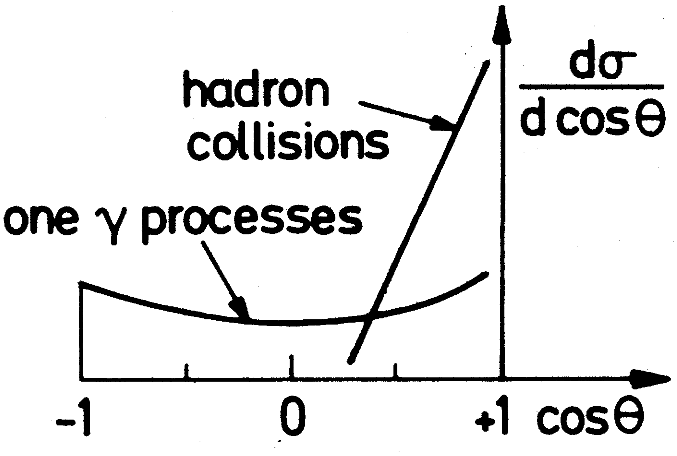

2.3 Quark Parton Model

The conventional spin $\frac{1}{2}$, fractional-charged quarks have the hadronic quantum numbers shown in the following table:

symbol	Q	I_3	S	C	Y
u	$\frac{2}{3}$	$\frac{1}{2}$	0	0	$\frac{1}{3}$
d	$-\frac{1}{3}$	$-\frac{1}{2}$	0	0	$\frac{1}{3}$
s	$-\frac{1}{3}$	0	-1	0	$-\frac{2}{3}$
c	$\frac{2}{3}$	0	0	1	$-\frac{2}{3}$

All quarks have baryon number $B = \frac{1}{3}$, and the hypercharge Y is connected with strangeness S and charm C by $Y = B + S - C$. The Gell-Mann Nishijima relation reads $Q = I_3 + \frac{1}{2}(B + S + C)$ where Q is the quark charge.

In the quark parton model[5,9] the total e^+e^- hadronic cross section at high energies is visualized as the production of quark pairs which in turn burst into hadrons.

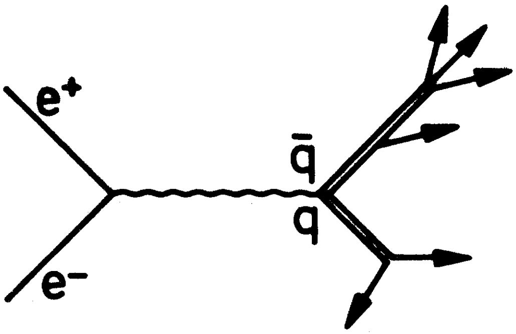

$$\sigma(e^+e^- \to q\bar{q}) = Q^2 \cdot \sigma_{\mu\mu}$$

Since the quarks are fermions the cross section is the same as for μ-pairs, only the quark charge Q modifies the $q\bar{q}$ coupling. To obtain the total cross section one has to sum over all quark pairs:

$$\sigma(e^+e^- \to \text{hadrons}) = \sum_i Q_i^2 \cdot \sigma_{\mu\mu} = R \cdot \sigma_{\mu\mu} .$$

Early experimental values[10,11] for R are shown in Fig. 2.2 with the dominant vector mesons indicated schematically. The remarkable rise at 4 GeV is attributed to the charm threshold. Inserting the charges for the up, down, and strange quarks below 4 GeV and including the charm quark above threshold yields $R = \frac{2}{3}$ and $\frac{10}{9}$ respectively which are by far too small. This was one of the reasons for introducing three quark colours and thereby increasing R by a factor of three. The new value R = 2 appears reasonable around 3 GeV and $R = \frac{10}{3}$ (including the charm quark) leaves some room for additional effects above 4 GeV which will be discussed later.

2.4 Vector Meson Production

Vector mesons carry the quantum numbers of the photon and therefore their resonance behaviour can be probed by e^+e^- annihilations:

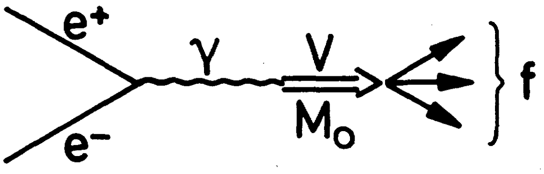

$$\sigma_f = \frac{3\pi}{s} \frac{\Gamma_{ee}\,\Gamma_f}{(M_0-\sqrt{s})^2 + \Gamma^2/4}$$

In the Breit-Wigner cross section formula Γ_{ee}, Γ_f, and Γ are the respective partial and total widths, M_0 is the mass of the vector meson V and $\sqrt{s} = 2E = M$ the e^+e^- energy. The electronic and hadronic widths - Γ_{ee} and Γ_h - can be obtained from the integrated cross sections:

$$\int \sigma_h \, dM = \frac{6\pi^2}{M_0^2} \frac{\Gamma_{ee}\,\Gamma_h}{\Gamma}$$

$$\int \sigma_{ee} \, dM = \frac{6\pi^2}{M_0^2} \frac{\Gamma_{ee}^2}{\Gamma}$$

with $\Gamma = \Gamma_h + \Gamma_{ee} + \Gamma_{\mu\mu}$.

Since the leptonic widths are usually much smaller than the hadronic width, we have $\Gamma \simeq \Gamma_h$ and obtain Γ_{ee} from the integrated hadronic cross section.

Knowing Γ_{ee} we get Γ from the integrated cross section of the leptonic decay mode. Some of the known vector mesons are given in the following table:$^{12)}$

V	M MeV	Γ MeV	Γ_{ee} keV
ρ	773 ± 3	152 ± 3	6.5 ± 0.8
ω	783 ± 1	10 ± 1	0.8 ± 0.2
ϕ	1020 ± 1	4 ± 1	1.3 ± 0.1
J/ψ	3098 ± 3	0.067 ± 0.012	4.7 ± 0.7

As one can see from colomns three and four, the electronic width has approximately the same value for all the vector mesons, whereas the total width of the J/ψ meson is several orders of magnitude smaller than for its low mass partners. This has been the first indication of a new quantum number, called charm, which will be discussed later.

Since in the framework of unitary symmetries mesons are composed of quark and anti-quark constituents, one can visualize the formation of vector mesons as quark pair production, the cross section of which is given by the muon pair production modified with the quark charges Q_i in an coherent sum:

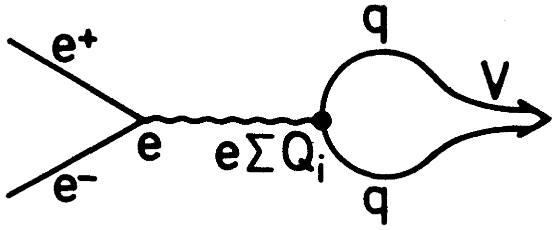

$$\sigma_{q\bar{q}} = \frac{4\pi\alpha^2}{3M^2}\left(\sum_i Q_i\right)^2$$

The total vector meson production can be obtained by integration:

$$\sigma_V^{peak} \cdot \Gamma \approx \int \sigma_V \, dM = \int \sigma_{q\bar{q}} \, dM = \frac{4\pi\alpha^2}{3}\left(\sum_i Q_i^2\right)\int \frac{dM}{M^2} \qquad (2.2)$$

Comparing this with the Breit-Wigner peak cross section

$$\sigma_V^{peak} = \frac{3\pi}{M_o^2} \cdot 4\,\frac{\Gamma_{ee}}{\Gamma}$$

one obtaines for the electronic width:

$$\Gamma_{ee} = \frac{\alpha^2}{9}\left(\sum_i Q_i\right)^2 M_o^2 \int \frac{dM}{M^2} \qquad (2.3)$$

From this expression we see that the leptonic width is a direct test of the coupling via the quark charges. Neglecting the mass dependence in (2.3) we can compare the expected and measured values in the following table where $u\bar{u}$, $d\bar{d}$, $s\bar{s}$, and $c\bar{c}$ denote the charges $\frac{2}{3}$, $-\frac{1}{3}$, $-\frac{1}{3}$, and $\frac{2}{3}$ respectively:

V	$\sum_i Q_i$	$(\sum_i Q_i)^2$	expected: $\frac{\Gamma_{V \to ee}}{\Gamma_{\omega \to ee}}$	: measured
ρ^o	$\frac{1}{\sqrt{2}}(u\bar{u} - d\bar{d})$	$\frac{1}{2}$	9	8.6 ± 2.2
ω	$\frac{1}{\sqrt{2}}(u\bar{u} + d\bar{d})$	$\frac{1}{13}$	1	1.0
ϕ	$s\bar{s}$	$\frac{1}{9}$	2	1.7 ± 0.4
J/ψ	$c\bar{c}$	$\frac{4}{9}$	8	6.2 ± 1.6

We observe an agreement within errors. By taking the mass dependence of the leptonic widths into account - for example within the framework of vector meson dominance[13] - one only spoils this agreement.

As a final example, we can estimate the peak cross section of the ρ by using formula (2.2):

$$\sigma_\rho^{peak} = \frac{4\pi\alpha^2}{3} \cdot \frac{1}{2} \cdot \frac{1}{\Gamma_\rho} \int_{2m_\pi}^{1.2\ \text{GeV}} \frac{dM}{M^2} = 1500\ \text{nb}$$

which is in rough agreement with the experimental value[14] of 1.6 μb. This shows that we can take these simple formulas to get correct orders of magnitude.

The energy dependence of the e^+e^- annihilation is shown in Fig. 2.3 with the vector mesons and SPEAR data indicated schematically. The data points between 1 and 3 GeV do not contain the new measurements[15] at ORSAY and FRASCATI which became available last year. The μ-pair cross section (dashed line) is given for comparison, and the generalized vector meson dominance model[13] (full line) accounts on the average for the low energy points by just allowing for the dominant ρ coupling. The energy dependence of the observed cross section above 3 GeV will be discussed in greater detail in Section 8.

3. e^+e^- Storage Rings

Why does one want to have such complicated machines like storage rings for physics experiments? Would it not be much simpler to use accelerators? Let us consider the kinematic range accessible to both types of machines:

accelerator

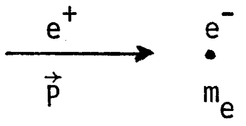

storage ring

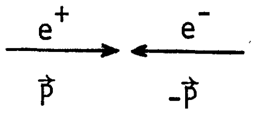

$$s = 2\ m_e + 2\ m_e E$$

$$\sqrt{s} \simeq \sqrt{2\ m_e E} \qquad\qquad \sqrt{s} = 2E$$

Here we see that the available cms energy $\sqrt{s}$ increases for accelerators as $\sqrt{E}$ and for storage rings linear in E. An additional handicap for an e^+ accelerator and an e^- target is that the target particle is so light. If we wanted to bombard protons with protons at a cms energy of 30 GeV we would either have to build a storage ring of 15 GeV beam energy each or an accelerator with 450 GeV. Both projects have been realized at CERN. However, in order to obtain e^+e^- collisions at 10 GeV one needs a storage ring of 5 GeV beam energy or an accelerator of 10^5 GeV. The latter project is financially completely out of range, and the reason is the small target mass.

Next we consider some of the important properties of e^+e^- storage rings like luminosity, energy spread, and beam polarisation.

3.1 Luminosity

Another consequence of the small electron mass is the fact that it easily emits a photon when forced into a curved orbit. This synchrotron radiation causes a strong energy loss which per electron and per turn is given by[17)]

$$W_{syn}(\mathrm{KeV}) = 88\ \frac{E^4\ (\mathrm{GeV})}{\rho\ (\mathrm{m})}$$

where E is the beam energy and ρ the bending radius. For SPEAR at SLAC and DORIS at DESY the bending radii are roughly 13 m. Therefore, taking a beam energy of 3.5 GeV, the synchrotron radiation per electron and turn amounts to 1 MeV. This energy loss has to be pumped back into the beam by radio frequency cavities which force the beam into a bunched structure, because an oscillating electric field has a maximum accelerating effect only at a certain phase with respect to the traversing beam. This bunched structure distinguishes e^+e^- machines from pp facilities with continuous beams like the ISR at CERN. It is evident that this feature adds an additional parameter in machine tuning and may affect the interaction rate. One may visualize the e^+ beam as carrying the flux and the e^- beam as the target:

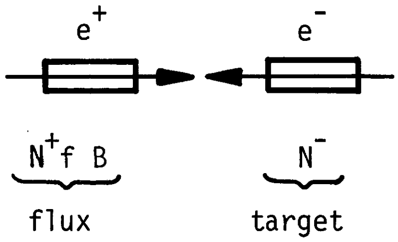

$N^\pm$: number of $e^\pm$/bunch

f : revolution frequency

B : number of bunches/ring

Then the interaction rate n for a given cross section σ is:

$$n = \left(\frac{\text{number of incident particles}}{\text{sec}}\right)\left(\frac{\text{number of target particles}}{\text{cm}^2}\right)\cdot\sigma$$

$$= \frac{N^+fBN^-}{F}\cdot\sigma$$

where F = overlap area of the two beams

$$= 4\pi\ \sigma_x\ \sigma_y,$$

assuming a Gaussian particle density distribution with rms radii σ_x and σ_y. The proportionality constant between interaction rate and cross section is called the luminosity and given by:

$$L = \frac{N^+N^-fB}{4\pi\sigma_x\sigma_y}$$

$$= \frac{1}{4\pi e^2}\ \frac{I^+\ I^-}{\sigma_x\sigma_y fB}$$

for $I^\pm = N^\pm efB$ being the beam currents.

From this formula we see that we get high luminosities for large beam currents and small beam cross sections. But what limits the luminosity to finite values? It is clear that, if we try to force an infinite current into a zero cross section, the system will escape towards greater thermodynamical equilibrium at the slightest distortion. Such distortions are inhomogeneities in the magnetic guide field and most important the beam interactions because one would like to force the beams through small cross sections at the interaction points. Everywhere else the beam cross section is unimportant. These distortions cause oscillations of the beams around their ideal orbits, the so-called betatron oscillations. Thus each beam produces for the other beam a shift ΔQ from its stable working point:

$$\Delta Q^{-}_{x,y} = \frac{r_e \, N^{+} \, \beta_{x,y}}{\gamma \cdot 2\pi\sigma_{x,y} \, (\sigma_x + \sigma_y)}$$

with r_e = classical electron radius = 2.82×10^{-13} cm

$\gamma = \frac{E}{m_e}$

$\beta_{x,y}$ = amplitude function at the interaction point.

Experience at the e^+e^- storage rings has shown that a stable operation is possible for values $\Delta Q_{x,y} < 0.06$. This limits the maximum number of particles per beam to:

$$N^{\pm}_{max} = \frac{\gamma \cdot 2\pi \, \sigma_{x,y} \, (\sigma_x + \sigma_y) \cdot 0.06}{r_e \cdot \beta_{x,y}}$$

Inserting typical values like $\beta \simeq 50$ cm, $\sigma_x = 0.1$ cm, and $\sigma_y = 0.01$ cm into this formula one obtains a maximum of 10^{11} particles per bunch at beam energies of 2 GeV. With a revolution frequency of 1 MHz for DORIS and SPEAR the maximum current could reach for one bunch:

$$I^{\pm}_{max} = N \cdot f \cdot e = 10^{17} \text{ e/sec} \simeq 10 \text{ mA}$$

Inserting the above values into the luminosity formula one obtains an upper limit for single bunch beams at 2 GeV:

$$L_{max} = \frac{N^+ N^- \; fB}{4\pi \; \sigma_x \sigma_y} = 10^{30} \text{ cm}^{-2} \text{ sec}^{-1}$$

This upper limit is not easily reached at e^+e^- storage rings. But with a higher bunch occupation number per beam - allowing an effective current of 100 to 200 mA - a luminosity of a few times 10^{30} cm^{-2} sec^{-1} has been obtained at DORIS.

For the design of an e^+e^- storage ring the variation of the luminosity with energy is an important quantity. The photon emission leads to an increase in the beam cross section:

$$\sigma_{x,y} \sim E$$

Using the above formulas for $N^{\pm}_{max}$ and L_{max}, we obtain the following variation with energy:

$$N \sim E^3 \quad \text{and} \quad L \sim E^4.$$

Therefore, the increasing luminosity more than compensates for the annihilation cross section falling like E^{-2}. But even faster than the luminosity the energy loss increases which has to be compensated by the r.f. power:

$$W_{r.f.} = W_{syn} \cdot (N^+ + N^-) \cdot f \cdot e \cdot B \sim E^7$$

Remember that the energy loss W_{syn} per electron per turn has already an E^4 dependence. When the limit of the r.f. power is reached, one can reduce the bunch number like $B \sim E^{-7}$ to keep $W_{r.f.}$ = const. This would imply a falling luminosity $L \sim E^{-3}$. However, when reaching the limit of a single bunch per beam one has to reduce the number of particles in the bunch like $N \sim E^{-4}$. This results in a dramatically decreasing luminosity:

$$L \sim E^{-10}$$

The results are summarized in the diagram to the left. A storage ring with many bunches can produce a higher luminosity at low energies than a single bunch machine. However, the multi-bunch operation requires a good separation of the two beams which is done at DORIS by stacking one ring on top of the other with crossings at the in-

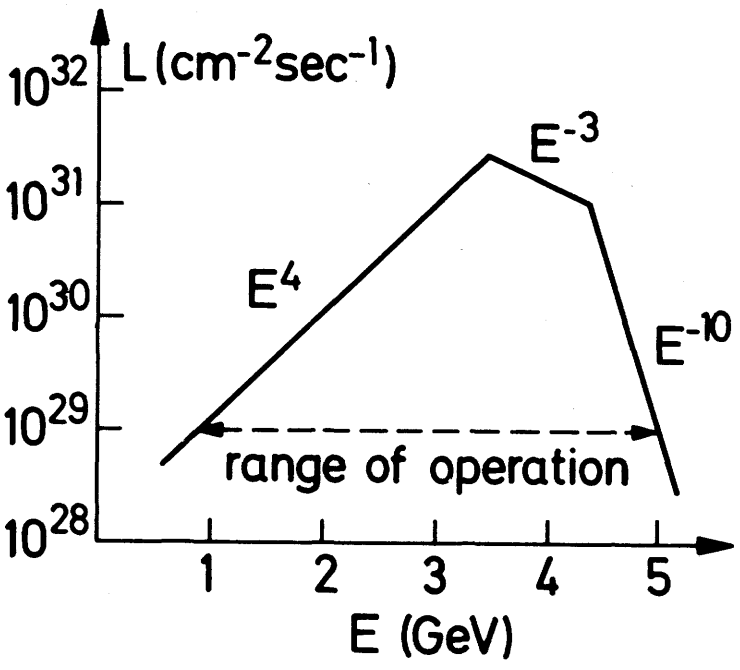

luminosity diagram

teraction regions. SPEAR on the other hand is a single bunch machine, and its range of operation does not extend to such low energies as indicated in the luminosity diagram above.

Before closing the remarks on luminosity, one should emphasize again, that the luminosity determination at e^+e^- storage rings does not depend on the methods described above, but is accomplished by measuring Bhabha scattering as a reference process.

3.2 Energy Spread

The electrons and positrons in a bunch have an energy spread due to synchrotron radiation. As a consequence the observed cms energy $W = \sqrt{s} = 2E$ has an rms width of:

$$\sigma_W \text{ (MeV)} = 1.3 \, \frac{E^2 \text{ (GeV)}}{\rho \text{ (m)}}$$

At SPEAR and DORIS this amounts to 0.1 MeV $(E/\text{GeV})^2$. Therefore, the narrow width of the J/ψ resonance cannot be observed directly but is folded with a Gaussian from the energy spread.

3.3 Beam Polarization

Let $\vec{S}$ denote the lepton spin and $\vec{B}$ the magnetic field vector. For the positron the transition from $\vec{S},\vec{B} = \downarrow\uparrow$ to $\vec{S},\vec{B} = \uparrow\uparrow$ is energetically favoured and accomplished by synchrotron radion. The opposite alignment is favoured for the electron. In this way a beam polarization P builds up naturally with a time delay described by [18]:

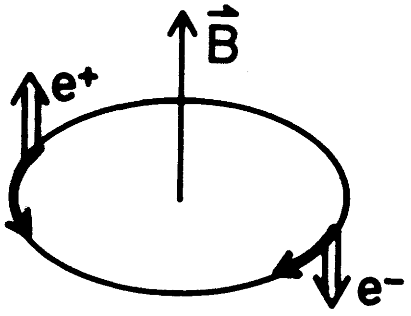

$$P(t) = P_o \quad 1 - \exp(-t/T)$$

where T = relaxation time

$$= 98 \text{ sec} \, \frac{\rho^2 \text{ (m)}}{E^5 \text{ (GeV)}} \, \rho_{av} \text{ (m)}$$

P_o = maximum attainable polarization
= 0.924

As mentioned before, the bending radius ρ for DORIS and SPEAR is 13 m and the average radius ρ_{av} is 30 m. Inserting these numbers we get

$$T = \frac{140 \text{ h}}{E^5 \text{ (GeV)}}$$

Therefore it takes 4.5 hours at E = 2 GeV and only 14 min at E = 4 GeV to obtain roughly 2/3 P_o, if no depolarizing effects are present.

3.4 Existing and Planned Storage Rings

As storage ring examples SPEAR and DORIS are shown in Figs. 3.1 and 3.2. Both have two interaction regions. Since SPEAR is a single ring machine it is operated in a single bunch mode. The various components are shown on the figure: the kickers and septums are needed for injection, the r.f. cavities balance the energy loss, and the quadrupoles focus the beams into small vertical dimensions at the interaction point. For DORIS the injection path is indicated: after leaving the linear accelerator, the leptons are carried in the synchrotron to their injection energy which is always close to the storage ring operation energy. SPEAR has been operated between 3 and 7.8 GeV cms energy. At DORIS most of the data have been taken between 3 and 5.2 GeV. However, at the time of writing the mode of operation is extended up to 10 GeV.

Fig. 3.3 gives a survey of the various e^+e^- storage rings (years of operation in brackets). From our previous discussion it is evident that the luminosity and energy range are two important parameters. The dash-dotted lines indicate machines which are no longer available for high energy physics: either phased out or dedicated to synchrotron radiation. The full rectangles are the presently operating e^+e^- facilities. The dashed lines, finally, show the storage rings scheduled for operation in the near future.

4. Storage Ring Detectors

From the discussion in the previous sections we know that the μ-pair cross section is 22 nb/E^2 (E in GeV) and that we can obtain a luminosity of $10^{30}\text{cm}^{-2}\text{sec}^{-1}$ at 1.5 to 2 GeV beam energy. Therefore we can expect the following event rates:

μ-pairs at E = 1.5 GeV	: 0.5 events/min
hadrons at E = 1.5 GeV	: 1 "
hadrons at J/ψ resonance (E = 1.55 GeV)	: 150 "

We see that the event rates are small outside the J/ψ resonance. Let us next consider what the main characteristics are when designing e^+e^- colliding beam experiments. Remember that many of the detectors - the results of which are discussed in this report - had to be outlined before the advent of the J/ψ.

It has already been known in 1972 from experiments at the Frascati National Laboratory[11)] that the hadron production was governed by many-body final states (average charged particle multiplicity of 3.5 at 3 GeV cms energy). In order to completely analyse high multiplicity hadronic events, the ideal detector should cover as much as possible of the full solid angle and identify the long-lived charged particles (e, μ, π, k, p) as well as photons. The detector has to determine the directions of the particles and, if possible, their momenta. Up to four unmeasured quantities can be obtained from energy and momentum conservation. The background from cosmic rays and beam gas interactions is reduced by requiring that some tracks of an event originate from the interaction region. Exclusive final states are best separated from the background if they are measured so well that they are kinematically overconstrained.

It is difficult and expensive to combine all the ideal requirements in a single detector. Therefore, different aspects have been emphasized by the various experimental teams. Those experiments, which reported results to the Symposium on Lepton and Photon Interactions in Hamburg, are listed in the following table:

detector name	institutions	detector type
-	DESY, Heidelberg	non-magnetic NaI or lead glass
MP^{2}SDS^2	Maryland, Pavia, Princeton, San Diego, SLAC, Stanford	
BONANZA	Bonn, DESY, Mainz	
DELCO	Irvine, Los Angeles, Stanford	Helmholtz coil and Č-counter
IRON BALL	Colorado, Pennsylvania, Wisconsin	azimuthal field in Fe
MARK I (SLAC-LBL)	Berkeley, Hawai, Northwestern, SLAC, Stanford	magnetic solenoid
PLUTO	Aachen, DESY, Hamburg, Siegen, Wuppertal	
MPP	Maryland, Pavia, Princeton	1 magn. spectrometer
DASP	Aachen, DESY, Hamburg, Munich, Tokyo	2 magn. spectrometers

The main characteristics of each detector are indicated in the table. All of the devices use wire chambers for track detection. In the following only some of the detectors can be presented in more detail and I shall select three different types for illustration.

4.1 A Non-Magnetic Detector (DESY - Heidelberg)

The DESY-Heidelberg detector (Fig. 4.1) consists of cylindrical drift chambers, surrounding the beam pipe, followed by NaI and lead glass counters, cosmic ray counters, an iron shield and the muon chambers. A mercury converter of two radiation lengths thickness in front of the last drift chamber can be filled or emptied between runs (see enlarged insert on top left of Fig. 4.1). The fraction of the full solid angle subtended for μ detection is 32%, for electron and photon detection 45% and for charged particles 95%. The energy resolution

$\Delta E/E$ is $\pm$ 2% x $E^{-1/4}$ for NaI and $\pm$ 6% x $E^{-1/2}$ for lead glass (E in GeV). An event trigger is defined by:

0 track in drift chamber and deposited energy ≥ 1.5 GeV or
1 track " " " " " " ≥ 0.9 GeV or
2 tracks " " " " " " ≥ 0.4 GeV etc.

With this type of detector one can measure the directions of charged particles and photons and distinguish leptons and photons from hadrons. Events with less than 5 tracks can be kinematically reconstructed from the particle directions.

4.2 Magnetic Solenoid Detector MARK I

The solenoidal magnet of the SLAC-LBL collaboration has a usable volume of 3 m in diameter by 3 m in length, filled with a uniform axial magnetic field of 4 KG. As shown in the cross section of Fig. 4.2, a particle leaving the beam pipe traverses a scintillation counter, four sets of cylindrical spark chambers with magnetostrictive readout, a time-of-flight counter, the coil of 1 radiation length thickness, a lead-scintillator shower counter for electron identification, and in the case of muons a 20cm thick iron yoke followed by a set of spark chambers. The magnetic volume allows a momentum resolution of $\Delta p/p$ = 1.5% x p (GeV/c). The event trigger requires two or more charged particles of at least 200 MeV/c momenta and covers 65% of the solid angle. Hadrons can be separated by time of flight: pions from kaons up to 600 MeV/c and kaons from protons up to 1.2 GeV/c.

This solenoid detector measures the momenta of charged particles in a large fraction of the solid angle and provides some information on showering electrons and converted photons. It is therefore well suited for few and multi-body analysis.

4.3 Double Arm spectrometer DASP

The experimental arrangement of a German Japanese collaboration consists of two detectors: The double arm spectrometer with limited acceptance (8% of 4π) and a nonmagnetic inner detector covering a large fraction of the solid angle (~70%). Each spectrometer arm (Fig. 4.3) has three wire chambers in front of the magnet and five chambers behind the magnet followed by a time of flight counter, a shower counter, and a range counter with a scintillator array after 70 cm of iron and additional slots to insert wire chambers. The maximum field length of each magnet is 18 kGm which corresponds to a momentum resolution of $\Delta p/p = \pm 0.7\% \times p$ (GeV/c). The time of flight counter separates pions from kaons up to 1.6 GeV/c and kaons from protons up to 3 GeV/c. The lead-scintillator shower counter for electrons and photons has an energy resolution of $\Delta E/E \simeq 30\% \times E^{-1/2}$(E in GeV). All counters are segmented in various ways to allow multiple hits.

The inner detector is located between the two magnets and a view along the beam pipe is shown in Fig. 4.4. In addition to the six wire chambers mentioned above there are four layers of sandwiches consisting of scintillator, lead and proportional tubes to measure the conversion points of photons. On the outside the inner detector is surrounded by lead-scintillator shower counters.

The double arm spectrometer is triggered purely inclusively on a single track traversing one of the beam pipe counters as well as the time of flight and shower counter. The inner detector is triggered on e^+e^- or $\gamma\gamma$ due to the energy deposited or on more than two tracks or photons.

This detector provides complete particle separation and momentum determination in a limited solid angle and measures the direction of charged particles and photons in the inner detector.

More details on these detectors and the names of the members of the respective groups are given in various publications quoted in the physics sections.

5. Quantum Numbers and Main Characteristics of J/ψ and ψ'

The J/ψ resonance was discovered independently by two experimental groups in 1974 and was worth a Noble price already two years later. The discovery was not the result of a systematic search but came unexpected. One of the experiments[19)] was performed at the Brookhaven National Laboratory investigating electron pairs from the reaction

$$\begin{array}{l} p + Be \rightarrow J + X \\ \qquad\qquad\ \ \hookrightarrow e^+e^- \end{array}$$

The other experiment[20)] was done with the above mentioned SLAC-LBL detector at SPEAR observing the direct formation and subsequent decays into various channels:

$$\begin{aligned} e^+e^- \to \psi &\to \text{hadrons} \\ &\to \mu^+\mu^- \\ &\to e^+e^- \end{aligned}$$

This is how the resonance got its double notation J/ψ. The data are shown in Figs. 5.1 and 5.2. Shortly after the discovery of the J/ψ another narrow state, named ψ', was found[21)] in e^+e^- annihilation by the SLAC-LBL group (Fig. 5.3). Both resonances were subsequently confirmed by experiments at the ADONE and DORIS storage rings[22)]. The various measurements of the resonance masses and decay widths are in reasonable agreement. The SLAC-LBL values are given in the following table:

	J/ψ	ψ'
mass (MeV)	3095 ± 4	3684 ± 5
Γ (KeV)	69 ± 15	228 ± 56
Γ_{ee} (KeV)	4.8 ± 0.6	2.3 ± 0.3
$\Gamma_{\mu\mu}$ (KeV)	4.8 ± 0.6	2.1 ± 0.3

The method for obtaining these values was already described in section 2.4. Because of the energy spread of the storage ring the observed width of the excitation curves (Figs. 5.2 and 5.3) is 1 to 2 MeV and therefore much larger than the decay widths given above. One can also see the effect of one of the electrons radiating off a photon in the initial state, which gives rise to the long tail on the high energy side of the curves in Figs. 5.2a and 5.3a. Due to this effect the peak cross section of these narrow resonances is lowered by 40%. However, I shall not enter here a detailed discussion of radiative effects[23)].

In this section we shall investigate the question of quantum numbers and finally ask the question:
Are the J/ψ and ψ' hadrons? From the wealth of experimental results the most instructive examples will be presented.

5.1 Spin, Parity, and C-Parity

Anticipating that the new particles are produced via one-photon annihilation, we expect the spin-parity quantum numbers to be $J^{PC} = 1^{--}$. This has been confirmed by investigating the interference pattern between the μ-pair decay of the J/ψ and the QED background$^{24)}$:

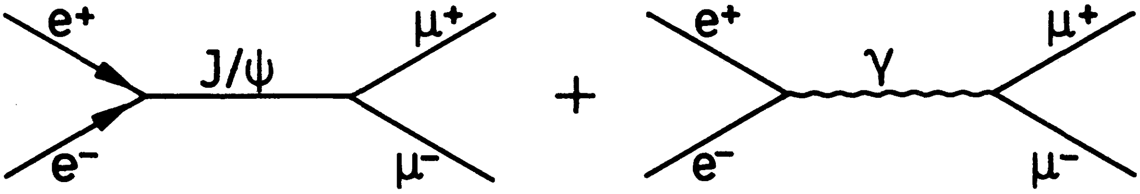

These two diagrams can interfere if the J/ψ has a spin different from zero and negative parity like the photon. The left diagram can be presented by a Breit-Wigner amplitude describing a circle in an Argand diagram whereas the QED contribution is real and negative. Assuming $J^P = 1^-$ the cross section can be written as:

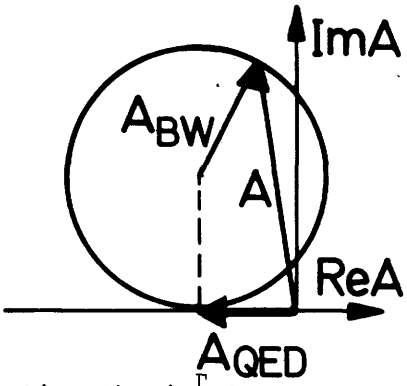

$$\sigma(e^+e^- \to \mu^+\mu^-) = |A_{J/\psi} + A_\gamma|^2$$

$$= \frac{3\pi}{s} \left| \frac{\Gamma_{\mu\mu}}{M_{J/\psi} - \sqrt{s} + i\,\frac{\Gamma}{2}} - \frac{2}{3}\,\alpha \right|^2$$

Neglecting the $i\,\frac{\Gamma}{2}$ term one sees immediately that the interference is destructive below and constructive above the resonance. This is observed for the data in Fig. 5.4 where $\sigma_{\mu\mu}/\sigma_{ee}$ is plotted for the J/ψ and ψ'. Therefore all the spin-parity assignments $0^\pm$, 1^+, 2^+,... resulting in no interference are excluded. Looking at the leptonic decay angular distributions of the J/ψ in Fig. 5.5 we observe a $1 + \cos^2\theta$ behaviour in agreement with $J^P = 1^-$. Notice that for the e-pair decay the QED background has to be subtracted. From the absence of higher powers of $\cos^2\theta$ in the angular distribution we conclude that 2^-, 3^-, ... are excluded as well and therefore $J^P = 1^-$ is our only choice for J/ψ. The same holds true for the ψ'.

The C-parity C = -1 follows from the parity, since CP invariance is expected to hold for the μ-pair final state:

$$\mu^+\mu^- = CP(\mu^+\mu^-) = -\,C(\mu^+\mu^-)$$

5.2 G-Parity and Isospin

The recipe for obtaining the G-parity is simply to count the number of pions in the decay. Take for example the decay

$$J/\psi \rightarrow \pi^+\pi^+\pi^-\pi^- X$$

and look at the effective mass spectrum of the recoiling system X. The data[25)] in Fig. 5.6b show an enhancement at $M^2_{\pi^0} = 0.02$ for the J/ψ whereas no such recoiling π^0 is observed outside the resonance (Fig. 5.6a). From the odd number of pions in the decay we infer a G-parity of -1 for the J/ψ.

However, the J/ψ resonance decays also into an even number of pions, although less abundantly. The branching ratio and width for the decay into two pions are[26)]:

$$\frac{\Gamma_{\pi^+\pi^-}}{\Gamma} = (1 \pm 0.7) \times 10^{-4} \text{ and } \Gamma_{\pi^+\pi^-} = 7 \pm 5 \text{ eV}$$

How can one explain this apparent discrepancy? Is the G-parity violated in the J/ψ decay? We have to keep in mind that the J/ψ couples to the photon not only in its production but also in its decay, and the photon in turn can couple to the old vector mesons like the ρ which should give a bigger contribution than ω and φ for $\pi^+\pi^-$ effective masses around 3 GeV.

In order to see whether this fraction of ππ final states can be explained by the ρ-tail, let us look at the following diagrams:

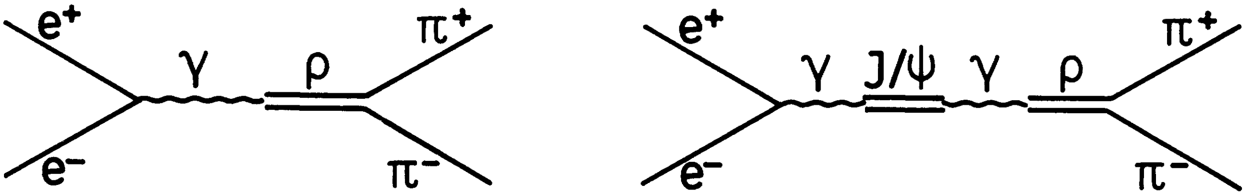

The contribution from the first graph at a center of mass energy of 3.1 GeV can be obtained from the Orsay measurement of 1.6 μb at the ρ-peak and the ρ-pole formula[14)]:

$$\sigma_{\pi^+\pi^-,\text{off}} = 1.6\ \mu\text{b}\ \frac{m_\rho^2}{s}\ \frac{m_\rho^2\,\Gamma_\rho^2}{(m_\rho^2 - s)^2 + m_\rho^2\,\Gamma_\rho^2} \approx 5\text{nb}$$

In this context "off" means off-resonance production. From this number we can get the contribution of the second graph. By using the μ-pair cross section from section 2.1 and the measured μ-pair decay width for J/ψ we obtain for its $\pi^+\pi^-$ decay width

$$\Gamma_{\pi^+\pi^-} = \left.\frac{\sigma_{\pi^+\pi^-}}{\sigma_{\mu^+\mu^-}}\right|_{\text{off}} \times \Gamma_{\mu^+\mu^-} \simeq 10 \text{ eV}$$

which agrees with the measured number. The ratio of multipion production on and off the J/ψ resonance (scaled with the μ-pair cross section) is plotted in Fig. 5.7 for multiplicities between 3 and 7. The fact that only the values for an odd number of pions are different from one shows that the direct decays of the J/ψ do not proceed via an even number of pions. Consequently G-parity is conserved in J/ψ decays and its value is $G = -1$. The same line of arguments holds for the ψ'.

From the proceeding discussion we have to remember that the width Γ_h for the direct hadronic decay of J/ψ or ψ' is obtained by subtracting the virtual photon width $\Gamma_{\gamma*}$ from the total width Γ where $\Gamma_{\gamma*}$ does not only include the leptonic widths but also the coupling of hadrons via the virtual photon:

$$\Gamma_h = \Gamma - \Gamma_{\gamma*} \text{ with } \Gamma_{\gamma*} = \Gamma_{ee} + \Gamma_{\mu\mu} + \Gamma_{\gamma* \to h}$$

The value for the last term is simply obtained by $\Gamma_{\gamma* \to h} = R_{\text{off}} \times \Gamma_{\mu\mu}$ where R is defined as in section 2.2. For the J/ψ with a total width of 69 KeV we get a hadronic width $\Gamma_h = 48 \pm 12$ KeV.

The last topic of this section is the isospin assignment. Inserting $G = -1$ and $C = -1$ into $G = C \times (-1)^I$, we see that only even values of isospin are possible. The observation of the direct decay into $p\bar{p}$ selects $I \leq 1$ and therefore the isospin for J/ψ is uniquely determined to be zero$^{26)}$:

$$\frac{\Gamma_{p\bar{p}}}{\Gamma} = (2.3 \pm 0.3) \times 10^{-3} \text{ or } \Gamma_{p\bar{p}} = 160 \pm 20 \text{ eV}$$

The $p\bar{p}$ width through an intermediate photon expected from generalized vector meson dominance calculations$^{27)}$ is less than 1 eV.

The ψ' being the heavier partner of the J/ψ, does it also have the same $I^G = 0^-$ assignment as the J/ψ? Let us look at the cascade decay $\psi' \rightarrow J/\psi + X$ in order to see which isospin and G-parity are carried away by X. With C = -1 as the only restriction the whole unnatural series 0^-, 1^+, 2^-, ... would be possible. What is the experimental situation? The data and the expected numbers are compared in the following table[28]:

X	$B_X = \frac{P(\psi' \rightarrow J/\psi + X)}{\Gamma\ \psi' \rightarrow J/\psi + \text{all})}$	relative B_X expected for $I^G = 0^-$	1^+	2^-
$\pi^+\pi^-$	0.63 ± 0.10	2	2	1
$\pi^o\pi^o$	0.32 ± 0.10	1	0	2
η	0.065± 0.026	allowed	0	0

These cascade decays account for roughly 60% of all the ψ' decays. From the ratio of $\pi^+\pi^-$ and $\pi^o\pi^o$ for X in the final state and from the occurence of η we conclude that $I^G = 0^-$ is the only choice for the ψ'.

5.3 SU(3) Assignment

It is well established that the pseudoscalar mesons can be grouped into a SU(3) monet in the following way:

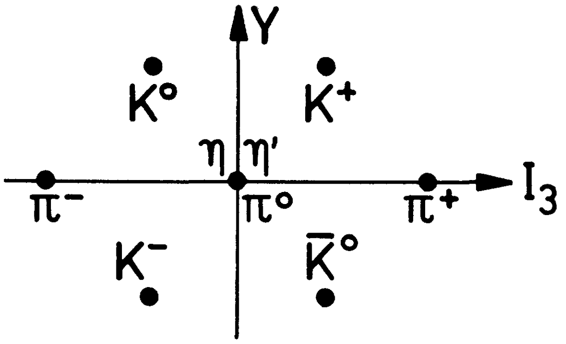

where the η' is predominantly a singlet state[8)] and the remaining particles form an octet. What may we infer from not observing a direct decay of J/ψ into $\pi^+\pi^-$, as discussed in the previous section? Is the J/ψ a SU(3) singlet state? This conclusion is correct if none of the decay final states form an octet state. Therefore, not only the decay into $\pi^+\pi^-$ but also the K^+K^- decay must be forbidden. The experimental branching ratios are given by[26]:

$$\begin{array}{lll}
J/\psi \rightarrow \pi^+\pi^- & \Gamma_f/\Gamma = & (1.0 \pm 0.7) \times 10^{-4} \\
 \rightarrow K^+K^- & = & (1.4 \pm 1.4) \times 10^{-4} \\
\psi' \rightarrow \pi^+\pi^- & & < 3.7 \times 10^{-4} \\
 \rightarrow K^+K^- & & < 1.4 \times 10^{-3}
\end{array}$$

These small values are consistent with decays via intermediate photons and rule out any direct $\pi^+\pi^-$ or K^+K^- decay. Therefore the singlet assignment for J/ψ and ψ' is definitely favoured. The two quantities for J/ψ are compared in the following section to form factor measurements at lower energies.

A mixture of singlet and octet amplitudes can contribute to the $\pi\rho$ and KK^* (890) decays of the J/ψ. These decays are identified by the ρ or K^* (890) recoil mass, observed in the double arm spectrometer (Fig. 5.8). The branching ratios are[26]:

$$\begin{array}{lll}
J/\psi \rightarrow \pi^\pm\rho^\mp & \Gamma_f/\Gamma = & (0.78 \pm 0.19) \times 10^{-2} \\
 \rightarrow K^\pm K^{*\mp} & = & (0.41 \pm 0.12) \times 10^{-2}
\end{array}$$

Inserting these experimental values into the corresponding SU(3) amplitudes

$$\begin{array}{ll}
A(\pi^\pm\rho^\mp) & = A_1 - 2A_8 \\
A(K^\pm K^{*\mp}(890) & = A_1 + A_8
\end{array}$$

and correcting for a phase space factor of 0.85 one gets for the ratio of octet to single amplitude

$$\frac{|A_8|}{|A_1|} \cos\delta = -0.7 \pm 0.06$$

where δ is the phase between the two amplitudes. This is, therefore, an independent check that J/ψ is predominantly a singlet state.

For completeness sake one should add, that the SLAC-LBL value[29] for the octet to singlet amplitude ratio above is slightly bigger, namely -0.12 ± 0.06. However, the results[30] for the $p\bar{p}$ and $\Lambda\bar{\Lambda}$ decay modes for this experiment are in perfect agreement with the singlet assignment, so that the overall picture of the J/ψ is that of an SU(3) singlet state.

5.4 Meson Form Factors

If we assume that the J/ψ does not decay directly into $\pi^+\pi^-$ or K^+K^-, the ratio of the following amplitudes

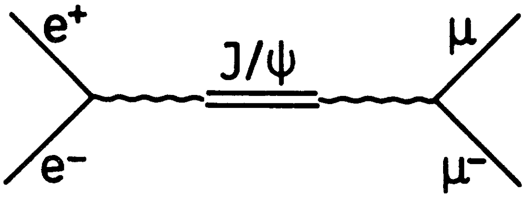

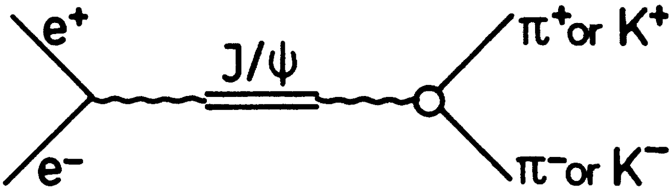

will measure the pion or kaon form factor:

$$|F_\pi|^2 = 4 \frac{\Gamma_{\pi^+\pi^-}}{\Gamma_{\mu^+\mu^-}} \, , \quad |F_K|^2 = 4 \frac{\Gamma_{K^+K^-}}{\Gamma_{\mu^+\mu^-}}$$

Inserting this into the cross section formula for pair production of pseudoscalar mesons one obtains[31)]

$$\sigma_{\pi,K} = \frac{\pi\alpha^2}{3s} |F_{\pi,K}(s)|^2 = \sigma_{\mu^+\mu^-} \frac{\Gamma_{\pi^+\pi^-,\, K^+K^-}}{\Gamma_{\mu^+\mu^-}}$$

The experimental values for J/ψ and ψ' are given in the following table where for comparison the ρ-pole form factor of the pion is shown as well:

$s\|GeV\|$	$\|F_\pi\|^2$	$\|F_\pi\|^2 = (1 - \frac{s}{m_\rho^2})^{-2}$	$\|F_K\|^2$
3.1	$(5.6\pm4.0)\times10^{-3}$	4.5×10^{-3}	$< 2 \times 10^{-2}$
3.7	< 0.15	2×10^{-3}	< 0.55

The form factor values at the J/ψ energy agree well with measurements at lower energies[32)] shown in Fig. 5.9.

5.5 Nucleon Form Factors

For purely electromagnetic $p\bar{p}$ production, the electric and magnetic nucleon form factors, G_E and G_M, would be obtained from the angular distribution[33)] of the reaction $e^+e^- \rightarrow p\bar{p}$:

$$\frac{d\sigma}{d\Omega} = \frac{\alpha^2 m^2}{s^2} \{|G_E|^2 \sin^2\theta + \frac{s}{4m^2} |G_M|^2 (1 + \cos^2\theta)\}$$

where m is the nucleon mass and θ the scattering angle. As mentioned before, however, the J/ψ decays directly into $p\bar{p}$ which then precludes any definite statement concerning the nucleon form factors at this energy. The $p\bar{p}$ pairs, identified by time of flight in the two opposite spectrometer arms of the DASP collaboration, are shown in Fig. 5.10 where the recoiling mass M_X is plotted[26)] versus the $p\bar{p}$ mass $M_{p\bar{p}}$. For the cluster of events at $M_{p\bar{p}}$ = 3.1 GeV all the energy is carried away by the nucleons. If we take these events and compare the ratio of $p\bar{p}$ to $\mu^+\mu^-$ production to corresponding measurements at lower energies[11,34)], we see from Fig. 5.11 that the DASP point lies well above the value expected from nucleon form factor contributions. The curve is an estimate by Renard[35)] and must be considered as an upper limit. More detailed calculations by Körner and Kuroda[27)] show a much faster fall-off of the $p\bar{p}$ cross section.

To interpret this direct decay of the J/ψ into $p\bar{p}$, the decay angular distribution is best written in terms of density matrix elements $\rho_{\lambda\bar{\lambda}}$ where $\lambda,\bar{\lambda}$ are the helicities of p and $\bar{p}$, respectively:

$$\frac{d\sigma}{d\Omega} \sim \rho_{\frac{1}{2}\frac{1}{2}} \sin^2\theta + \frac{1}{2}\rho_{\frac{1}{2}-\frac{1}{2}} (1 + \cos^2\theta).$$

These density matrix elements are connected with those for S- and D-waves via[36)]:

$$\rho_S = \rho_{\frac{1}{2}\frac{1}{2}} + 2\rho_{\frac{1}{2}-\frac{1}{2}}$$

$$\rho_D = -2\rho_{\frac{1}{2}\frac{1}{2}} + \rho_{\frac{1}{2}-\frac{1}{2}}$$

The angular distribution of the decay J/ψ → $p\bar{p}$ is shown in Fig. 5.12 together with a $\sin^2\theta(\rho_{\frac{1}{2}-\frac{1}{2}} = 0)$ and a $1 + \cos^2\theta(\rho_{\frac{1}{2}\frac{1}{2}} = 0)$ curve. For pure S-wave the angular distribution would be isotropic ($\rho_D = 0$). The $1 + \cos^2\theta$ curve seems to be compatible with the data. This means $\rho_{\frac{1}{2}\frac{1}{2}} = 0$ and we have a mixture of S- and D-waves with the major contribution coming from the S-wave.

5.6 Heavy Vector Meson Dominance

A direct way to determine how the photon couples to the new vector mesons consists in the measurement of their radiative decay widths. The expected decay widths would strongly depend on whether the photon couples only via the old vector mesons like the ρ or only via the new vector mesons like the J/ψ. For the J/ψ decay into $\eta'\gamma$ the following orders of magnitude are expected[37]:

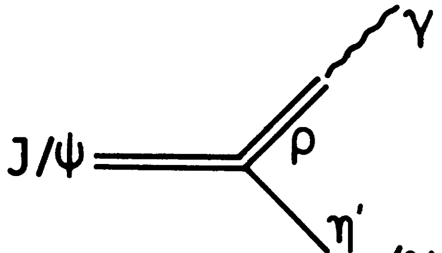

$\Gamma_{\eta'\gamma,\text{ theory}} \sim 1 \text{eV}$

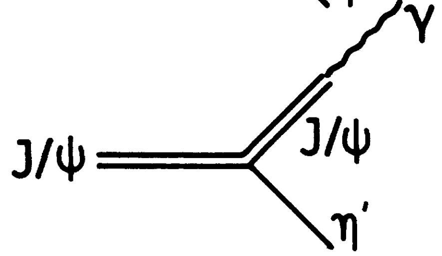

$\Gamma_{\eta'\gamma,\text{ theory}} \sim 1 \text{ keV}$

Do the experiments favour one of these values? In order to determine the $\eta'\gamma$ decay width one can utilize the fact that 30% of the η' decay proceeds via $\rho^0\gamma$. In Fig. 5.13 several invariant mass distributions[38] are shown for the $\pi^+\pi^-\gamma\gamma$ final state, where all charged tracks are assumed to be pions. The two photon spectrum in Fig. 5.13a shows a strong signal from π^0's some of which are produced in addition to the ρ^0 in Fig. 5.13b and some of which come from the decay of the $\rho^\pm$ in Fig. 5.13c. The η' signal is seen in Fig. 5.13d and the signal to background ratio is enhanced if π^0 events are excluded and $\pi^+\pi^-$ combinations from the ρ-region selected. All the relevant kinematic cuts are given on the figure. Form the observations we obtain the experimental value

$$\Gamma_{\eta'\gamma,\text{ exp}} = 160 \pm 50 \text{ eV}$$

and may conclude that the old vector meson dominance is not sufficient but that J/ψ and/or ψ' are required as new pieces of the electromagnetic current. The J/ψ decay into $\eta\gamma$ is smaller but of the same order of magnitude[39,64]:

$$\frac{\Gamma(J/\psi \to \eta'\gamma)}{\Gamma(J/\psi \to \eta\ \gamma)} = 2.4 \pm 1.0$$

5.7 Inclusive Spectra and Particle Ratios

In section 2.2 we have seen that the particles of hadron induced reactions have an angular distribution completely different from e^+e^- interactions. However, the large partial waves contribute mostly to forward hadron scattering and it might be interesting to compare the momenta of e^+e^- hadron production with the transverse momentum distribution of hadronic interactions. As already mentioned in the section on detectors, the double arm spectrometer allows π/k separation up to 1.6 GeV and k/p separation up to 3.0 GeV due to 0.6 nsec time resolution and a 5 m flight path. From Fig. 5.14a one can see the quality of the particle separation. Even for the momentum range between 1.2 and 1.5 GeV the relative amount of particles can be easily estimated. The excitation curve for the J/ψ resonance in Fig. 5.14b is obtained with the single particle inclusive trigger$^{40)}$.

Fig. 5.15 shows the differential cross sections $d\sigma/dp$ for the π, k, and $\bar{p}$ particles at the J/ψ and ψ' resonances. Because of background problems from beam gas interactions, the protons have been omitted from the analysis. Both resonances show roughly the same behaviour. The kinematic effect caused by different particle masses is taken into account by plotting the invariant cross sections $\frac{E}{4\pi p^2}\, d\sigma/dp$ in Fig. 5.16. The pion yield from the J/ψ can be described by a single exponential whereas for the ψ' one observes a break around $E_\pi = 400$ MeV due to the pions from the cascade decay $\psi' \rightarrow J/\psi + \pi^+\pi^-$. All particles at both resonances show a similar slope, compatible with kT = 170 MeV for the exponential$^{41)}$ $e^{-\frac{E}{kt}}$. Even more surprisingly, the same slope and also the same relative particle abundances are observed for particle production from pp collisions at the ISR$^{42)}$. The curves in Fig. 5.16a represent the ISR particle spectra ($\sqrt{s} = 53$ GeV and 89^0 scattering angle) scaled with a common factor to fit the π spectrum from e^+e^- collisions.

The particle ratios at the resonances are shown in Fig. 5.17 as a function of the momentum. The k and p ratios increase relative to the π yield with increasing momentum. Fitting the particle spectra with exponential functions one obtains the following particle yields for the entire momentum range$^{40)}$:

	$R_{\pi^\pm}$	$R_{k^\pm}$	$R_{p,\bar{p}}$
J/ψ	87.5 ± 1.5%	8.9 ± 1.0%	3.6 ± 0.9%
ψ'	90.8 ± 1.0%	6.9 ± 0.9%	2.3 ± 0.7%

5.8 Summary of J/ψ and ψ'Properties

We finally wanted to ask the question whether the J/ψ and ψ' are hadrons or not. The fact that they conserve all the standard quantum numbers of strong interactions tells us that they are hadrons.

Excect for its mass and width there is no outstanding property which distinguishes the ψ' from the J/ψ. They have identical quantum numbers $J^{PC} = 1^{--}$ and $I^{G} = 0^{-}$ and are compatible with being SU(3) singlets. Having the same quantum numbers as the photon they seem to add additional pieces to the electromagnetic current in the vector dominance model. The inclusive particle spectra are similar for the two resonances and agree with slopes and relative abundances of particles produced under 90^0 in the cms of the hadronic induced reaction.

The main decay widths and branching ratios are summarized in the following table:

decay into	J/ψ		ψ'	
	Γ(keV)	BR(%)	Γ(keV)	BR(%)
anything	69 ± 15		228 ± 56	
e^+e^- or $\mu^+\mu^-$ ($\Gamma_{ee} \simeq \Gamma_{\mu\mu}$)	2x(4.8±0.6)	14	2x(2.1±0.3)	2
$\gamma \rightarrow$ hadrons	12 ± 2	17	6.6 ± 0.9	3
J/ψ + ππ η			125 ± 32	55
γ + γ + J/ψ hadrons		<1	57 ± 18	25
'direct'hadrons:				
a) balance of previous numbers	48 ± 12	69	34 ± 16	15
b) actually seen	48 ± 12	69	23 ± 10	10

The radiative decays involving one or two photons will be discussed in the next paragraph and have been included here for completeness. The numbers for decays into 'direct' hadrons have been obtained firstly by taking the missing fraction in the upper part of the table and secondly by adding up all hadronic decay modes seen.

for the J/ψ the agreement is excellent and for the ψ' the deviation is within errors. The gap, reported in the early days for ψ', has been closed by thorough investigations. For a review of numerous hadronic decays of the new particles see for example Ref. 43.

6. Hidden and Open Charm

In the previous section we have discussed the properties of J/ψ and ψ' in the framework of the old quantum numbers. However, the extremely narrow decay widths of these new particles were the first indication of a new charm quantum number - in much the same way as the suppression of the ϕ-decay into pions can be taken as evidence for strangeness. As mentioned already in section 2.4 the ϕ is visualized as an $s\bar{s}$ state and therefore couples mainly to $K\bar{K}$ in its decay (Okubo-Zweig-Iizuka-rule[44]))

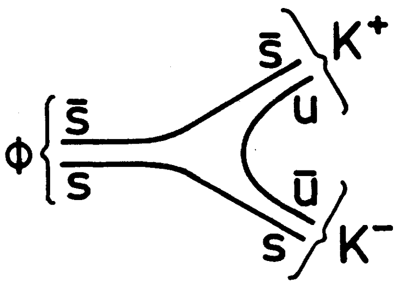

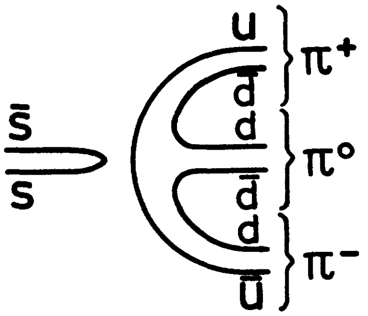

Since strange s quarks do not occur in the final state of the righthand diagram, this decay is forbidden and the experimentally observed suppression factor is 50. Introducing a fourth quark c, carrying the charm quantum number, one can apply this picture to the J/ψ and ψ' particles. The corresponding unconnected diagram represents the unfavoured hadronic J/ψ or ψ' decays and its experimental suppression factor is a few times 10^3 compared with normal hadronic resonances. The connected diagram - corresponding to a decay into particles with charm and anti-charm (like $K\bar{K}$) - is not seen in nature. Therefore, all the charmed particles must be heavier than half the ψ' mass, i.e. heavier than 1.84 GeV, and J/ψ as well as ψ' are considered as bound $c\bar{c}$ states. Before presenting the experimental results, we shall discuss some of the charm model features.

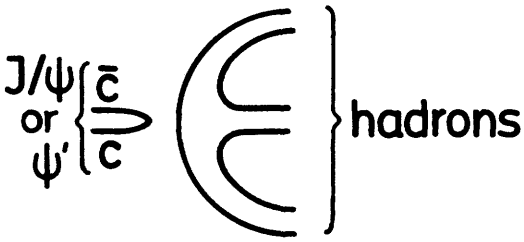

6.1 Some Implications of the Charm Picture

The concept of a charmed quark was introduced before the discovery of the new particles in order to achieve symmetry between leptons and quarks and to explain the absence of strangeness changing neutral currents[45]. Let us first consider mesons of hidden charm, which are built from a charm and an anti-charm quark[46,47], and therefore have charm quantum number zero. Such a system is called "charmonium"[48,49] in analogy to the electron positron bound state, "positronium"[50]. An essential point is that the mass of the charmed quark is roughly half of the ψ' mass and, therefore, a non-relativistic description may be used to compute the level scheme[51]. Using field theoretical arguments theorists have proposed a confining potential with an r-dependence somewhere between the Coulomb and the oscillator potential:

$$V(r) = -\frac{4}{3}\,\frac{\alpha_s}{r} + \lambda r + V_0 \tag{6.1}$$

Solving the Schrödinger equation with this potential, one can arrive at level schemes and transition rates. For a pure Coulomb potential (~ $\frac{1}{r}$) we get the familiar level sequence of the hydrogen atom (below left) and for the isotropic osciallator potential (~ r^2) the level spacing would be equidistant[52]:

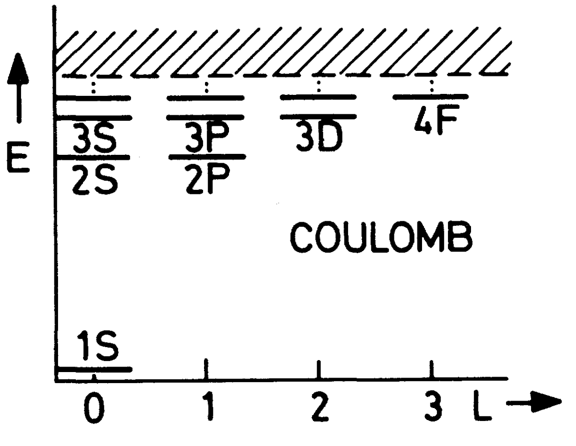

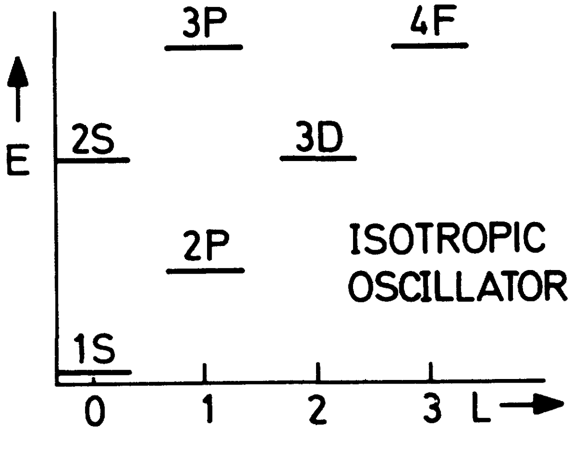

The effect of the λr term in the expression for the potential will be to lower the 2P state with respect to its Coulomb potential value. A level scheme of this type but with several of the mass values fixed by experimental numbers is shown in Fig. 6.1. Levels with the quantum numbers $J^{PC} = 1^{--}$, i.e. the states 1^3S_1, 2^3S_1, and 3^3D_1 can couple directly to the photon. The S-states correspond to J/ψ and ψ'. The evidence for the 3^3D_1 state will be discussed in the next section. The states which can be reached by radiative transitions from the J/ψ and ψ' are those with positive C-parity. As we shall see in the following, these radiative decays have been the object of extensive experimental investigations.

In order to illustrate the point of transition rates I shall repeat one argument from the excellent review by Jackson$^{49)}$. The J/ψ decay into lepton pairs can be thought of as $c\bar{c}$ annihilation

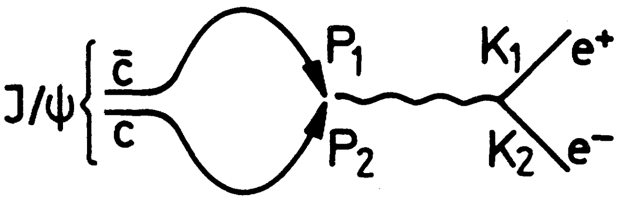

$$\left.\begin{array}{l} K = |\vec{K}_1| = |\vec{K}_2| \\ P = |\vec{P}_1| = |\vec{P}_2| \end{array}\right\} \text{in the CMS}$$

The QED cross section for this process is

$$\sigma_{QED} = \frac{\pi\,\alpha^2 Q_c}{s} \quad \frac{K}{P}\left(1 + \frac{\beta^2}{3} + \frac{4\,M_c^2}{s}\right)$$

where Q_c and M_c are the quark charge and mass. In the extreme relativistic limit ($\beta \to 1$, $M_c \ll \sqrt{s}$, $P \simeq K$) we get the familiar μ-pair cross section modified by the quark charge:

$$\sigma_{QED} = \frac{4\pi\,\alpha^2}{3s}\,Q_c^2 = \sigma_{\mu\mu} \cdot Q_c^{\,2} .$$

However, in the case considered the c quark has roughly half the J/ψ mass, and we therefore have to take the non-relativistic limit with $\beta \to 0$, $s \to 4M_c^2$, $K \simeq M_c$, and $P \to (M_c/2)\,v_{rel}$, where v_{rel} is the relative velocity of c and $\bar{c}$:

$$\sigma_{QED} \cdot v_{rel} = \frac{\pi\,\alpha^2\,Q_c^{\,2}}{M_c^2} .$$

This is the expression for a transition rate. In order to obtain the partial decay width $\Gamma(1^{--} \to e^+e^-)$, we have to multiply this expression by a factor of 3 due to colour, by a factor of $\frac{4}{3}$ to account for the fact that the spins are always in a triplet state for $J^P = 1^-$, and finally by the spatial wave function $|\,\phi\,(\vec{r})|^2 = |R\,(r)|^2\,/4\pi$ at the origin $r = |\vec{r}| = 0$. Inserting half the J/ψ mass M/2 for the quark mass M_c we get:

$$\Gamma(1^{--} \to e^+e^-) = \frac{4\,\alpha^2\,Q_c^2}{M^2} \cdot |R(0)|^2 . \qquad (6.2)$$

In analogy with the annihilation into photons in QED, the J/ψ hadronic decay can be visualized as annihilation into vector gluons, and like in QED it has to be an odd number of gluons for $J^{PC} = 1^{--}$. However, single gluon annihilation is excluded since gluons carry colour and the J/ψ state is colour-neutral. Therefore the lowest-order diagram is three-gluon annihilation:

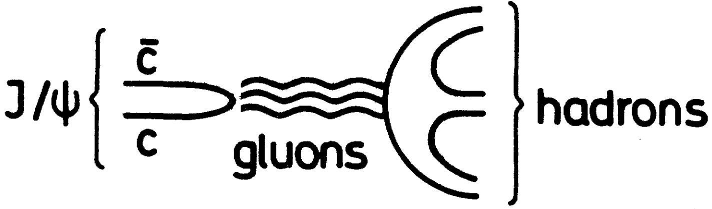

The transition rate is given in accordance with QED; only the coupling constant α^3 is replaced[46)] with $5\,\alpha_s^{\,3}/18$:

$$\Gamma(1^{--} \rightarrow g\ g\ g) = \frac{16}{9\pi}\,(\pi^2 - 9)\,\frac{5}{18}\,\frac{\alpha_s^3}{M^2}\,|R(0)|^2 \tag{6.3}$$

The coupling constant α_s is the same as in the potential (6.1). By taking the ratio of formulas (6.3) and (6.2) and using $Q_c = 2/3$ for the quark charge, we get the ratio of the hadronic to electronic decay witdths of the J/ψ:

$$\frac{\Gamma(J/\psi \rightarrow \text{hadrons})}{\Gamma(J/\psi \rightarrow e^+e^-)} = \frac{5\ (\pi^2 - 9)}{18\ \pi}\,\frac{\alpha_s^3}{\alpha^2}$$

From section 5.8 we know that the experimental value is 10 ± 2 and this fixes the coupling constant at approximately $\alpha_s \simeq 0.2$. This value of α_s is small enough to do perturbation calculation and is the basis for obtaining mass splittings and decay rates. For a more detailed discussion of the formalism the reader is referred to Jackson's report[49)].

By introducing a fourth quark, the symmetry scheme of hadrons is generalized from SU(3) to SU(4). The meson nonets are replaced by hexadecpulets, each consisting out of the original nonet and a singlet meson with hidden charm ($C = 0$) plus two triplets of open charm ($C = \pm 1$). Each level in Fig. 6.1 is a charm singlet member of such a SU(4) multiplet[53)] as we can see from the example of the pseudoscalar multiplet in Fig. 6.2 which includes the 1^1S_0 state η_c of Fig. 6.1. The charm-carrying pseudoscalar mesons D and F are shown above ($C = +1$) and below ($C = -1$) the plane of the SU(3) nonet of conventional pseudoscalar mesons. As one can see from its quark constituents the F meson has in addition to charm also strangeness different from zero. The corresponding vector mesons D^* and F^* can be grouped together with J/ψ , ρ, ω , ϕ and $K^*(89o)$ into a similar SU(4) multiplet. Because the charm quantum number is conserved in strong and electromagnetic interactions, the states of open charm are produced in association with their corresponding anti-states. To prove the existence of charm-carrying particles, one has to find their characteristic weak decays. In the following table some examples of hadronic and semileptonic decays[49,54] are given together with the relative decay rates for each type where c, u, d, s denote the charm and ordinary quarks and θ_c the Cabibbo angle[55].

c decay mode	example	relative rate
hadronic: c → su$\bar{d}$	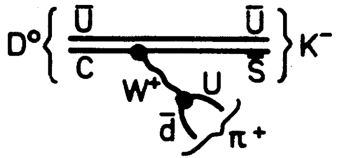	$\cos^2\theta_c \simeq 1$ Cabibbo-angle favoured
c → du$\bar{d}$	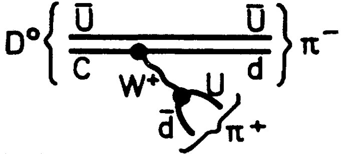	$\sin^2\theta_c \simeq 0.05$ Cabibbo-angle suppressed
semileptonic: c → s$^{e}_{\mu}$ν	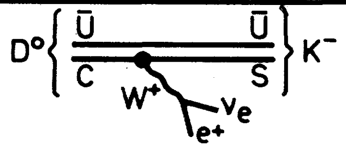	$\cos^2\theta_c \simeq 1$ Cabibbo-angle favoured
c → d$^{e}_{\mu}$ν	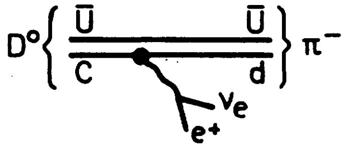	$\sin^2\theta_c \simeq 0.05$ Cabibbo-angle suppressed

The dominant transitions for both hadronic and semileptonic decays are those which change charm and strangeness: $\Delta C = \Delta S = \pm 1$. Therefore we expect for the Cabibbo favoured decays strange particles in the final state. Before we discuss the search for charmed states, we shall look at the results obtained from the spectroscopy of c$\bar{c}$ bound states.

6.2 Evidence for the ψ''

ψ'' is a notation for the 3^3D_1 state in Fig. 6.1. Before its discovery it had been predicted in 1975 by Eichten et al.[56] with a mass of about 3.75 GeV. Last year it was found by the DELCO[57] and MARK I[58] experiments at SLAC. The resonance parameters of the ψ'', reported at the Hamburg Conference 1977, are:

	DELCO	MARK I
mass (MeV)	377 ± 6	3772 ± 6
Γ (MeV)	24 ± 5	28 ± 5
Γ_{ee} (keV)	0.18 ± 0.06	0.37 ± 0.09

As an illustration the data are shown for the DELCO experiment. The experimental arrangement (Fig. 6.3) is characterized by a big Cerenkov counter sensitive only to electrons (π threshold at 3.7 GeV). An axial magnetic field is generated in a small volume around the beam pipe by two discrete coils. How the cross section - normalized to the μ-pair cross section - varies with the centre of mass energy, is shown in Fig. 6.4 a) for the raw data, b) for ψ and ψ' tails subtracted, and c) for the electron pair decays. That the ψ'' was seen so late in the game is certainly due to the fact that the charm spectroscopy is so rich that it was hard to decide what to measure first.

6.3 Investigation of Hidden Charm States between ψ' and J/ψ

From the level scheme in Fig. 6.1 one can see that most of the states between 2^3S_1 and 1^3S_1 have even C-parity and thus can be reached by radiative decays of the ψ'. Three methods have been employed to identify such intermediate states for short denoted as ^3P_J (2^1S_0 and 3^1D_2 could be involved as well).

a) In the cascade decays one detects the J/ψ via its leptonic pair decay and observes one or two photons:

$$\begin{array}{l} \psi' \rightarrow \gamma\ {}^3P_J \\ \qquad\quad \hookrightarrow \gamma\ J/\psi \\ \qquad\qquad\qquad \hookrightarrow \mu^+\mu^- \end{array} \tag{6.4}$$

b) One can look for hadronic decays of the ^3P_J in various final states:

$$\begin{array}{l} \psi' \rightarrow \gamma\ {}^3P_J \\ \qquad\quad \hookrightarrow \text{hadrons} \end{array} \tag{6.5}$$

These two methods have the advantage of completely analysing the final state but the disadvantage of always supplying products of transition rates.

c) Absolute rates for the radiative decays of the ψ' can be obtained from inclusive photon spectra by looking for monochromatic lines:

$$\psi' \rightarrow \gamma\ {}^3P_J \tag{6.6}$$

Let us start by discussing the cascade decays (6.4). A sample of μ-pairs identified in the two spectrometer arms of DASP$^{59)}$ is used to calculate the effective mass $M_{\mu\mu}$; the plot in Fig. 6.5 shows two peaks: one from direct decays and QED processes at a mass of 3.7 GeV and a second one from the cascade decay into J/ψ at 3.1 GeV. Selecting events with $M_{\mu\mu}$ near 3.1 GeV one obtains the spectrum of the recoil mass squared in Fig. 6.6. 88 % of this spectrum can be explained by the final state $\mu^+\mu^-\pi\pi$ (solid curve) since the charged pions have an unique signature in the inner detector and the neutral pions add one half of the charged pions due to isospin considerations (see section 5.2). There is a clear η signal on top of this curve which accounts for 6 % of the spectrum and, therefore, 6 % of the events are left as candidates for cascade decays. However, only those events are taken which have two photons positively identified in the inner detector of DASP. In order to eliminate background from $\psi' \rightarrow J/\psi + \pi^0\pi^0$ it is required, that $J/\psi + \gamma\gamma$ be coplanar, and $J/\psi + \eta$ final states are avoided by selecting events with $M_{\gamma\gamma}$ less than 510 MeV. The kinematic quantities are best determined by fitting the final states with the photon directions, the muon momenta, and the J/ψ mass as input (3 constraints). Since one does not know which photon is emitted first, the invariant masses of the J/ψ with either one of the two photons are plotted in Fig. 6.7 as high and low mass solutions. One sees a clear clustering of events at masses of 3.51 ± 0.01 GeV or 3.28 ± 0.01 GeV respectively. This intermediate state - first seen and called P_c by the DASP collaboration - is narrower than 20 MeV and has the following product of branching ratios:

$$\frac{\Gamma(\psi' \rightarrow P_c + \gamma)}{\Gamma(\psi' \rightarrow \text{all})} \cdot \frac{\Gamma(P_c \rightarrow J/\psi + \gamma)}{\Gamma(P_c \rightarrow \text{all})} = (1.7 \pm 0.4)\ \%$$

The $\pi^0\pi^0$ background - with two decay photons undetected - is smoothly varying and estimated to be less than 0.5 events per 10 MeV interval.

The important question, which photon is emitted first, can be answered by investigating reaction (6.5) which only involves one photon. The detailed discussion in the next paragraph shows that the high solution gives the correct mass assignment for P_c. In order to look for more intermediate states let us add to the 3 constraint events in Fig. 6.7 those with one of the muons only known by its direction (2 constraints) and events[60)] from the MARK I detector with one of photons converting in the beam pipe (also 2 constraints). The data are shown in Fig. 6.8 together with the high mass projection. The dashed line gives the expected $\pi^0\pi^0$ background. We observe two distinct peaks at about 3.51 and 3.55 GeV, and some indication of an enhancement near 3.45 GeV. The same

$\gamma\gamma\,\mu^+\mu^-$ final state was analysed by the DESY-Heidelberg[61)] group with its non-magnetic detector. Since none of the momenta were measured, they used 1 constraint fits (only the J/ψ mass as input) to obtain the invariant mass distribution in Fig. 6.9 which looks remarkably similar to the projection in Fig. 6.8. The $\pi^0\pi^0$ background is again indicated by the dashed line.

In order to investigate the hadronic decay modes of reaction (6.5) one needs a magnetic detector with a large solid angle for measuring particle momenta. SLAC-LBL[62)] has identified the following final states and adjusted the parameters via 1 constraint fits:

$$\begin{aligned}
\psi' &\rightarrow 4\pi^{\pm} && + \gamma \\
&\rightarrow \pi^+\pi^-\,K^+K^- && + \gamma \\
&\rightarrow 6\pi^{\pm} && + \gamma \\
&\rightarrow \pi^+\pi^- && + \gamma \\
&\rightarrow K^+K^- && + \gamma
\end{aligned}$$

The presence of a photon is ascertained by observing a zero missing mass and a non-zero missing momentum. In addition to kinematic fitting, time-of-flight information is used to separate the first two reactions. For the last two reactions the assignment is made solely on the ground of kinematic fitting, since the particle momenta are too high (1.6 - 1.8 GeV) for time-of-flight measurements. The event distributions are shown in Fig. 6.10. We observe three peaks at 3.41, 3.51, and 3.55 GeV in the $4\pi^{\pm}$ channel; the bump at 3.68 GeV is due to ψ' decays without photon emission. These peaks are seen for some of the other final states as well. In particular the $\pi^+\pi^-$ or K^+K^- distribution shows a strong enhancement at 3.41 GeV and an accumulation of a few events around 3.55 GeV. These enhancements have been termed χ-states by the SLAC-LBL group.

In order to obtain information on spin-parity of the observed peaks, one can investigate the angular distribution of the photon with respect to the beam line. Since ψ' has an angular momentum of one, the most general form of the angular distribution is:

$$\frac{d\sigma}{d\cos\Theta} \sim 1 + \alpha\cos^2\Theta$$

For χ spin zero the α value is fixed uniquely and for spins $J \geq 1$ the lowest multipoles have been taken into account:

spin	α	angular distribution
$J = 0$	1	$1 + \cos^2\Theta$
$J = 1$	$-1/3$	$2 + \sin^2\Theta$
$J = 2$	0.08	$13 + \cos^2\Theta$

The angular distributions for the three states $\chi(3.41)$, $\chi(3.51)$, and $\chi(3.55)$ are given in Fig. 6.11. Only the spin zero assignment of the $\chi(3.41)$ is conclusive; the spins of the states at 3.51 and 3.55 are certainly different from zero.

Finally it is possible to look for monochromatic photons of reaction (6.6) in an inclusive way; in other words the recoil system of the intermediate states remains undetected. The MP^2SDS^2 group[63)] has used a highly sequented array of NaI crystals with good energy resolution and good discrimination of charged and neutral particles. The inclusive photon spectra measured by this group are shown in Fig. 6.12: a) data taken at the J/ψ show no structure and agree with the background expected from Monte-Carlo calculations (dotted line); b) at the ψ' one observes several bumps exceeding the Monte-Carlo background. Fig. 6.12.c shows these peaks with Monte-Carl background subtracted. The three lowest photon lines at 121, 169, and 260 MeV correspond to the states at 3.55, 3.51 and 3.41 GeV. The fourth bump around 400 MeV is mainly a reflection of the second photon from the decay via the P_c or $\chi(3.51)$. The absolute branching ratios $BR(\gamma\chi)$ are given in the table on the next page, which summarizes the numerical results of the experiments discussed.

Remembering that we have selected intermediate states with positive C-parity, we may deduce the following quantum number assignment:

a) $\chi(3.41, 3.51, 3.55) \rightarrow$ even number of pions

$\rightsquigarrow$ G-parity is positive and consequently $I = 0$

b) χ (3.41, 3.55) $\rightarrow \pi^+\pi^-, K^+K^-$

$\rightsquigarrow$ $J^{PC} = 0^{++}, 2^{++}, \ldots$

c) $\chi(3.41)$: $J = 0$, $\chi(3.51, 3.55)$: $J \neq 0$

$\rightsquigarrow$ most likely triplet assignment:

$$\left.\begin{array}{ll} \chi(3.41): & J^{PC} = 0^{++} \\ P_c/\chi(3.51): & \quad\;\; = 1^{++} \\ \chi(3.55): & \quad\;\; = 2^{++} \end{array}\right\} \quad 2^3P_J$$

	mass [MEV]	Ref.	$BR(\gamma\chi) \cdot BR(\chi \to \ldots)$			$BR(\gamma\chi)$ [%]	α in $1 + \alpha \cos\theta$
			$J/\psi\ \gamma$	$\pi^+\pi^-$ K^+K^-	$4\pi^\pm$ $\pi^+\pi^-K^+K^-$ $6\pi^\pm$		
$\chi(3.41)$		1	0.3 ± 0.2				
		2	0.2 ± 0.1				
	3413 ± 3	3	0.2 ± 0.2	0.15 ± 0.04	0.8 ± 0.2	7.5 ± 2.6	1.4 ± 0.4
	3413 ± 9	4	3.3 ± 1.7			7.2 ± 2.3	
$\chi\left\{\begin{matrix}3.45\\3.34\end{matrix}\right\}$		1	< 0.4 (90% CL)				
		2	< 0.6 (90% CL)				
	3454 ± 7	3	0.8 ± 0.4				
		4				< 2.5	
$P_c/\chi(3.51)$	3509 ± 11	1	1.7 ± 0.4				
	3505 ± 5	2	2.1 ± 0.5				0.0 ± 0.5
	3503 ± 4	3	2.4 ± 0.8		0.4 ± 0.1		0.1 ± 0.4
	3511 ± 7	4	5.5 ± 1.5			7.1 ± 1.9	
$\chi(3.55)$	3551 ± 11	1	1.4 ± 0.4				
	3547 ± 6	2	1.1 ± 0.4				
	3552 ± 6	3	1.0 ± 0.6	0.019 ± 0.008	0.4 ± 0.1		0.3 ± 0.4
	3561 ± 7	4	2.2 ± 1.0			7.0 ± 2.0	

References: 1 = DASP; 2 = DESY-Heidelberg; 3 = SLAC-LBL; 4 = MP^{2}SDS^2

The evidence for the $\chi(3.45)$ is very weak and consequently nothing is known about its quantum numbers (except C-parity = +1). Even the mass assignment could be 3.34 or 3.45 GeV, since there is no indication which photon is emitted first. Sometimes the $X(3.45)$ is identified in the charm framework with the 2^1S_0 state having $J^{PC} = 0^{-+}$, but it could as well be the 3^1D_2 state with 2^{-+}. Some implications of the level spacing and the branching ratios for the charm picture will be discussed in section 6.7.

6.4 Search for an S-State below the J/ψ

Since the 1^1S_0 state is expected to lie energetically below the 1^3S_1 state and has positive C-parity, a search for the 0^{-+} state has been performed among the radiative decays of the J/ψ. In the following, the results on the three photon final states observed with the DASP detector[64)] shall be reported.

Three photon final states may be caused by direct decays or by quasi-two-body decays:

$$\begin{aligned} J/\psi &\to \pi^0\gamma \to \gamma\gamma\gamma \\ &\to \eta\,\gamma \to \gamma\gamma\gamma \\ &\to \eta'\gamma \to \gamma\gamma\gamma \\ &\to X\,\gamma \to \gamma\gamma\gamma \end{aligned}$$

or by QED contributions:

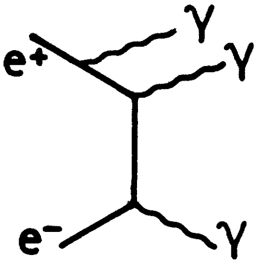

The latter poses a background problem in the search for any two photon intermediate state, because it leads to a smooth contribution to the $\gamma\gamma$ mass distribution which cannot be eliminated by kinematic cuts, but must be subtracted. The following cuts were applied to remove several sources of background:

(i) The smallest of the $\gamma\gamma$ opening angles was required to be larger than 30^0. This avoids overlapping showers from neighbouring photons and eliminates $\pi^0\gamma$ events.

(ii) The coplanarity of the three photons had to be better than 5^0. This removes four and more photon events.

Following these cuts, the three photon energies can be obtained from an 1 constraint fit. That the fitted energies E_{γ}^{c} agree within errors with the energies E_{γ}^{m} measured in shower counters is demonstrated in Fig. 6.13. Among the three $\gamma\gamma$ mass combinations two are independent. Plotting the lowest two photon mass, results in the histogram in Fig. 6.14 which shows a strong η signal and an accumulation of a few events at the η' mass. The calculated QED contribution[65)] (dashed line) accounts for most of the background. The fitted η mass of 547 ± 4 MeV agrees well with the known value of 548.8 MeV, and the width of 24 ± 4 MeV - obtained by a Gaussian fit - corresponds to the expected mass resolution of 20 MeV. Using the η in this way as a bench mark for the experiment we can search for unknown narrow states. The highest two photon mass combination is shown in Fig. 6.15. On top of the expected background - indicated by the QED contribution and the reflections from η and η' - we observe a narrow peak with a significance of 5 standard deviations which is called X(2.83). Its fitted mass is 2.83 ± 0.03 MeV, and its width of 40 ± 14 MeV is compatible with the experimental resolution in this region. The product of the branching ratios is:

$$BR(J/\psi \rightarrow X\gamma) \cdot BR(X \rightarrow \gamma\gamma) = (1.4 \pm 0.4) \times 10^{-4}$$

For the three photon events at the ψ' energy we observe no statistically significant peaks and therefore the measured spectrum of the highest photon pairs in Fig. 6.16 can be directly compared to the QED predictions[66)]. The $\gamma\gamma$ spectrum is similar to the one in Fig. 6.15 and shows that we have correctly estimated the QED background for the J/ψ decays.

Evidence for the X(2.83) was for a long time supported only by the DASP experiment. The DESY-Heidelberg group only quoted an upper limit[61)], and the non-observation in other e^+e^- storage ring experiments created a state of uncertainty as to the existence of the X. Only recently this new state was confirmed by a CERN-Serpukhov experiment[67)] observing the two photon decay of the X(2.83) in the π^-p charge exchange reaction at 40 GeV incident momentum.

In the charm picture one would like to identify the X(2.83) with the 1^1S_0 state or η_c. To do this one has to determine the quantum numbers. But the only thing, which follows from the two photon decay, is that the C-parity is positive and that the spin is different from one.

6.5 Observation of States with Open Charm

In the preceeding three sections we have discussed states with hidden charm. The pursuit of open charm at the e^+e^- storage rings has been mainly a search for the lightest charm particles, the D mesons (see Fig. 6.2), and will be discussed in this section. Let us briefly recall some of the arguments given in section 6.1:

- Charmed particles decay weakly, since $\Delta C = \pm 1$ means changing a quantum number conserved in strong interactions.
- Due to the large mass M_D and the Cabibbo angle Θ_C involved, the rate for semileptonic D decays should be enhanced[49] by several orders of magnitude over semileptonic K decays:
  $\Gamma(D^+ \to \bar{K}^0 e^+\nu) \sim (M_D/M_K)^5 \cot^2 \Theta_C \cdot \Gamma(K^0 \to \pi^- e^+\nu)$.
  These decays are expected to amount to 10 % of all the D decays.
- Due to $\Delta C = \Delta S$, changing charm involves a change in strangeness, and the enhancement factor for K production over purely pionic final states is 20.

In order to establish the existence of charmed mesons, the above characteristics have to be found by experiment. The following reactions have been investigated:

a) Inclusive single electron production aims at finding semileptonic weak decays:

$$\begin{tikzcd} e^+e^- \to & D \arrow[dd] & \bar{D} + \ldots \arrow[d] \\ & & \text{hadrons} \\ & e + \ldots & \end{tikzcd}$$

b) Inclusive K meson production points at the pair production of some kind of hadrons:

$$\begin{tikzcd} e^+e^- \to & D \arrow[dd] & \bar{D} + \ldots \arrow[d] \\ & & \text{hadrons} \\ & K + \ldots & \end{tikzcd}$$

c) e-K correlation is a clear indication that the weak decays involve charm:

$$\begin{tikzcd} e^+e^- \to & D \arrow[dd] & \bar{D} + \ldots \arrow[d] \\ & & K + \text{hadrons} \\ & e + \ldots & \end{tikzcd}$$

d) Whereas in the above reactions one can infer the existence of a heavy meson from a characteristic threshold behaviour, measurements of complete final states would establish the mass, width, and quantum numbers of the D directly:

$$\begin{tikzcd}[row sep=small] e^+e^- \arrow[r] & D \arrow[dd] & \bar{D} + \ldots \arrow[d] \\ & & \text{hadrons} \\ & K + \pi\text{ 's} & \end{tikzcd}$$

In all the reactions one or both of the pseudoscalar D's can be replaced by the vector D^* mesons. The D^*'s will most likely decay via pion or photon emission into D's.

When investigating inclusive electron spectra, one has to keep in mind that low energy electrons can come from radiative QED processes or possibly from the decays of heavy leptons or charmed mesons. Whereas heavy leptons decay mainly leptonically or semileptonically, the decay of charmed mesons is expected to be mostly semileptonic or hadronic. Consequently, the particle multiplicity of heavy lepton decays should be low and the average electron momentum high[68], and the reverse should hold for charmed particles.

In order to improve the electron/pion separation of DASP for low momenta, a Cerenkov counter was needed in addition to the shower counter[69]. This Cerenkov counter was inserted between the second and third wire chamber of the inner detector (Fig. 6.17). in the spring of 1976 and first results were available half a year later.

Data were taken at e^+e^- energies between 3.99 and 5.2 GeV and control measurements performed at 3.6 GeV to obtain a reliable estimate for background events and at 3.68 GeV to see how frequently - with the ψ' as pion source - a pion would fake an electron. Whereas the electron trigger was purely inclusive, it was required in the data analysis that at least one non-showering track was present, and this removed the QED events most of which are produced with $e^+e^-\gamma$ in the final state. In order to discriminate against various types of background, the following cuts were made[70,71]:

(i) The pulse height of the scintillation counters S_0 and S_M in Fig. 6.17 had to be that of a minimum ionizing track. This rejects events with Dalitz decays from π^0 or η or with pair conversion of photons in front of the Cerenkov counter where one of the leptons curls up in the magnetic field.

(ii) The independent identification of particles in the Cerenkov and in the shower counter helps to avoid that pions or kaons fake electrons via knock-on electrons.

(iii) Beam gas events were rejected by an appropiate vertex cut.

After these cuts 256 events with one electron and at least one non-showering track remain for an integrated luminosity of 5540 nb^{-1} between 3.99 and 5.2 GeV centre of mass energy[71)]. In order to distinguish between heavy leptons and charmed particles, the multiplicity of charged tracks including the electron is shown in Fig. 6.18. The shaded histogram gives the event with no additional photons. Remember that photons may occur in the decay of charmed particles (e.g. $D^* \rightarrow D\gamma$) and are unlikely to be found in heavy lepton decays, and in addition heavy lepton events prefer low multiplicities. Observing a particularly high bin of two-prongs with no additional photon in Fig. 6.18, makes one suspect that heavy leptons are in this sample. In fact, attributing all events with multiplicity ≥ 3 to charm one can estimate that only 4.4 events can belong to the (2-prong, no gamma) class, and only 6.7 events can feed through from higher multiplicities due to the limited detection efficiency. This leaves 29 out of 40 events unexmplained. We shall come back to these events in chapter 7 when discussing the evidence for heavy leptons.

For the investigation of charm we shall only consider events with three or more charged tracks including the electron. These events are plotted in Fig. 6.19 as a function of the electron momentum.In spite of the rather strict selection criteria given above, there is still some contamination from multihadron events. But this background is well known from the control measurements at 3.6 GeV and its magnitude and shape is given by the full line. Assuming a 30 % branching ratio of the heavy lepton decays into many hadrons plus neutrino gives a negligible contribution indicated by the dashed line in Fig. 6.19. We observe that most of the electrons are found at low momenta and that only a few have momenta above 1 GeV. The momentum spectrum has been compared to model calculations[72)] in Fig. 6.20. In order to avoid a kinematic broadening of the spectrum, a narrow energy interval from 3.99 to 4.o8 GeV just above the $D\bar{D}^*$ and $D^*\bar{D}^*$ thresholds (see later discussion) has been taken. The full curve in Fig. 6.20 shows an excellent agreement for the $D \rightarrow e \nu K^*(892)$ decay, but with the error bars given the $D \rightarrow e \nu K$ decay (dashed) seems to be acceptable as well.

Finally the energy dependence of the inclusive electron events with at least two additional charged tracks is plotted in Fig. 6.21a. The background of misidentified multihadron events has been subtracted, so that the control point at 3.6 GeV becomes compatible with zero. We observe a steep rise of the cross section near 4 GeV and a slow fall-off above. In order to obtain the fraction of semileptonic decays among all the charm decays we have to estimate what the production cross section is. The simplest way is to subtract from the total cross section σ_{tot} the conbrituion $R \cdot \sigma_{\mu\mu}$ already present below charm threshold and the contribution $\sigma_{\tau\tau}$ from sequential heavy lepton production (see section 7):

$$\sigma_{charm} = \sigma_{tot} - R \cdot \sigma_{\mu\mu} - \sigma_{\tau\tau}$$

Inserting the σ_{tot} measurements of the PLUTO group[73) and the corresponding value R = 2.3, we obtain the data points in Fig. 6.21b. Note, that we have to devide by $2 \cdot \sigma_{charm}$, because the charmed particles are pair produced. From Fig. 6.21b we see that the branching ratio for semileptonic decays is $B_e = 11 \pm 3$ %. If we had taken the somewhat higher cross section values of SLAC-LBL[1o) we would have obtained 8 ± 3. Both numbers agree with the value mentioned in the beginning and show that there is a substantial semileptonic weak decay.

Compared with the electron data just discussed, the experimental procedure for obtaining kaon inclusive data is much simpler, because there is less confusion with background and less competition from other processes like QED or heavy lepton decays. Charged kaons were identified via time-of-flight in the DASP detector[74) (see section 5.7), and neutral kaons were kinematically determined by measuring the momenta of the decay pions in the PLUTO detector[75) and calculating the effective mass. In order to put charged and neutral kaon production on the same basis, one has to account for the fact that long lived neutral kaons escape from the detector and therefore only half of the neutral kaons, the short lived K_S^0's, are seen. For this reason the inclusive K_S^0 cross section is plotted in Fig. 6.22a together with half the inclusive charged kaon cross section, that is to say the measured cross section for pair production is shown. Again we observe a sharp rise between 3.6 and 4 GeV and a levelling off above. In order to obtain the branching ratio for strange decays of the new particles, we can subtract the K pair production below threshold - scaled with s^{-1} and denoted as $\sigma(K_S^0)^{old}$ (dashed line) - and divide this difference by the corresponding difference in the total cross section. The result is shown in Fig. 6.22b. We see that above threshold 40 % of the new events are produced with charged and 40 % with neutral kaon pairs. Therefore, finding a fraction of 80 ± 12 % kaons in the decay products, leaves not much room for purely pionic decays. This certainly agrees well with the charm picture outlined in the beginning. That the kaons are decay products from heavier objects can be seen directly by comparing the charged kaon momentum spectra above and below threshold. Near threshold the pair produced charmed particles are nearly at rest and therefore their decay products can carry at most one quarter of the total energy. This is observed for the invariant kaon spectra in Fig. 6.23, where the excess of kaons at 4.o5 GeV over the kaons at 3.6 GeV ends at about 1 GeV. Therefore the weakly decaying new objects are mostly associated with kaons in their decays.

In going one step further one can try to detect electrons and kaons in coincidence. This was done by the PLUTO group[76)] and the evidence for eK_S^0 correlation is shown in Fig. 6.24. The visible cross section peaks at about 4.05 GeV. After background subtraction and corrections for acceptance, branching ratio, and unobserved K_L^0 mesons one finds a peak cross section for correlated eK_S^0 production of 3 ± 1 nb.

Whereas the experiments at DESY pursued the charm search along the line of inclusive particle spectra, the SLAC-LBL experiment was from the beginning aiming at the detection of exclusive decay channels and followed an independent line of investigation. When plotting all two particle mass combination[77)], SLAC-LBL found small bumps at 1.74, 1.87, and 1.99 GeV in the invariant mass distributions of the $\pi^+\pi^-$,$\pi^\pm K^\mp$, and K^+K^- combinations respectively (see Figs. 6.25 a,b,c). The question then was: which is the correct combination and can the ambiguities be resolved by time-of-flight measurements. The MARK I detector - with 1.5 m flight path and 0.4 nsec time resolution - offers good pion/kaon separation for momenta up to 600 MeV. This is demonstrated by Fig. 6.26 where the particle momentum is plotted versus the time of flight mass squared. However, from our previous discussion we know that the charmed particle two-body decay leads to momenta of about 1 GeV. Instead of attempting a clear-cut event separation, SLAC-LBL plotted the events weighted by the probability for the particular mass assignment. The plots obtained in this way are shown in Figs. 6.25d,e,f. The peak in the $\pi^\pm K^\mp$ combination appears now enhanced whereas the remaining bumps in the $\pi^+\pi^-$ and

and K^+K^- combinations are compatible with misidentifications from the $\pi^\pm K^\mp$ channel. For the neutral four particle combinations the pion/kaon separation is much cleaner because the particle momenta are smaller. The invariant mass plots in Figs. 6.25g,h,i show an enhancement only in the $K\pi\pi\pi$ combination, and its mass value of 1.86 GeV agrees well with 1.87 GeV found in the $K\pi$ distribution. These peaks can be taken as evidence for the lowest lying neutral charmed meson, the D^0.

The corresponding charged mesons, D^+ and D^-, have to be looked for in the invariant mass distribution of three charged tracks. The $K^\mp\pi^\pm\pi^\pm$ distribution78) in Fig. 6.27a reveals a peak at 1.87 GeV whereas no structure is observed for the $K^\pm\pi^+\pi^-$ combination of Fig. 6.27b. How can one explain this difference? In fact, the observation of only one of these decay modes is a confirmation of the selection rule $\Delta C = \Delta S = \pm 1$ for weak decays of charmed particles. Starting with charm $C = 1$ and no strangeness $S = 0$ for the D^+, we end up with $C = 0$ and $S = -1$ for the decay products which means that $K^-\pi^+\pi^+$ is the only correct combination for the D^+ decay. This combination is called exotic because due to the Gell-Mann Nishijima relation (see section 2.3) positively charged mesons are always associated with positive strangeness, or stated differently: positively charged mesons with negative strangeness cannot be constructed within the framework of conventional up, down, and strange quarks. Therefore the charged D meson is observed as a state which cannot be confused with traditional resonances.

Since charm is supposed to be conserved in e^+e^- annihilations, charmed particles have to be produced in association. In order to find the associated partners, SLAC-LBL has looked at the recoil mass spectra of the identified D mesons. The ψ'' resonance at 3.77 GeV (see section 6.2) lies just above charm threshold and is found to decay almost exclusively into $D\bar{D}$53). However, at e^+e^- annihilation energies above 4 GeV the recoil mass spectra reveals no significant peak at the position of the D mesons. Instead, a strong enhancement is seen at higher mass values79), indicating the production of the heavier D^* mesons. In fact, a detailed analysis shows that above a cms energy of 4 GeV charm production mainly proceeds via $D\bar{D}^*$ and $D^*\bar{D}^*$. The most accurate mass assignments obtained by SLAC-LBL58) are:

$$M_{D^o} = 1863.3 \pm 0.9 \quad \mathrm{MeV}$$

$$M_{D^+} = 1868.3 \pm 0.9 \quad \mathrm{MeV}$$

$$M_{D^{*o}} = 2006.0 \pm 1.5 \quad \mathrm{MeV}$$

$$M_{D^{*+}} = 2008.6 \pm 1.0 \quad \mathrm{MeV}$$

From these mass values it follows that three out of four transitions from the D^* to the D mesons are energetically just allowed to proceed via the emission of pions. In the following diagram the numbers give the energy released or Q value when emitting a pion

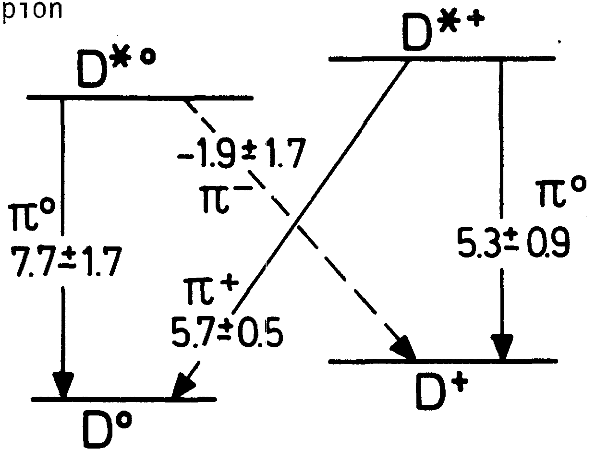

The dashed line indicates the forbidden π^- transition. The widths of the new mesons are compatible with being less than the mass resolution of 40 MeV.

The various $\bar{D}^o$ decay modes and their branching ratios to all mesonic decays expected in the statistical model of Quigg and Rosner[80)] are shon in Fig. 6.28. Three out of the four measured decays only partly fill the provided boxed (hatched areas). There seems to be some diagreement between the model and the data, but many more decay modes still have to be measured.

6.6 The F Meson: a State with Charm and Strangeness

The discovery of the D mesons has been the most evident confirmation of the charm model. Looking at the hexadecuplet of Fig. 6.2 we see that now the F meson is the only missing element. Being a $c\bar{s}$ compound it carries charm and strangeness. In order to find out which decay modes might be accessible by experiment, let us consider the following diagrams for mesonic decays:

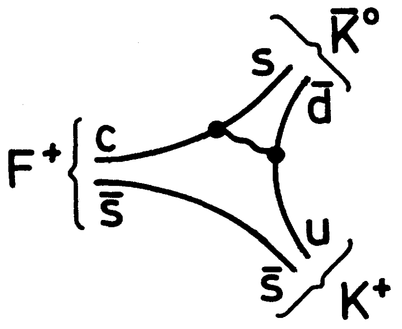

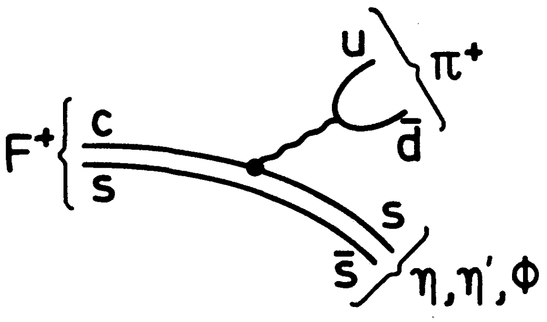

From the left-hand diagram and from the presence of the $s\bar{s}$ state ϕ in the right-hand diagram we may conclude that the F mesons can be a particularly rich source of K mesons. But one has to single out these kaons among many others already present from D meson decays and it may be difficult to detect a small signal. Let us, therefore, look at $\pi\eta$ and $\pi\eta'$ decays more closely. The admixture of $s\bar{s}$ can be found from the quark composition of the singlet and octet states$^{8)}$:

$$\eta_1 = \sqrt{\tfrac{1}{3}}\,(s\bar{s} + u\bar{u} + d\bar{d})$$
$$\eta_8 = \sqrt{\tfrac{2}{3}}\,s\bar{s} - \sqrt{\tfrac{1}{6}}\,(u\bar{u} + d\bar{d})$$

and from the usual mixing ($\theta = 10^0$) in the physical states:

$$\eta = \eta_1 \sin\theta + \eta_8 \cos\theta$$
$$\eta' = \eta_1 \cos\theta - \eta_8 \sin\theta$$

We see that η is mainly an octet state and therefore has the strongest $s\bar{s}$ admixture. In addition the η' decays via the η in 68 % of the cases. Therefore an excessive production of η mesons can be a hint at F meson production.

A search for inclusive η production has been performed with the inner part of the DASP detector$^{81)}$ by looking at the invariant mass spectrum of two photons (38 % of the η decays). To become more selective in the data analysis a soft third photon of less than 140 MeV was required. This additional criterium was chosen because - in analogy with the D meson observations - $F\bar{F}^*$ and $F^*\bar{F}^*$ may be enhanced over $F\bar{F}$ production and the mass difference between F and F^* is expected to be of the order of the pion mass. Since the F mesons are isospin singlets, the F^* may not decay into the F via single pion emission but the emission of a photon is allowed. The result of this restricted inclusive η search is shown in Fig. 6.29 for various energy regions. A clear η signal in the invariant $\gamma\gamma$ mass distribution is observed only at 4.4 GeV.The width of this peak agrees with the expected mass resolution. The background curves were obtained by using uncorrelated photons (i.e. photons from different events) and noramlizing them to the observed number of photon pairs above a $\gamma\gamma$ mass of 0.7 GeV. At the low side of the mass spectrum a π^0 signal is seen. In order to show how significant the η signal is, the visible cross section for η plus low energy photon production is plotted in Fig. 6.30 for the various energies. Having found some encouraging evidence for the possible existence of the F meson, let us try to single out exclusive final states of $F\bar{F}^*$ or $F^*\bar{F}^*$ production. By aiming at detecting the $\pi\eta$ decay mode of the F and the photon transition from F^* to F we may consider the following two reactions:

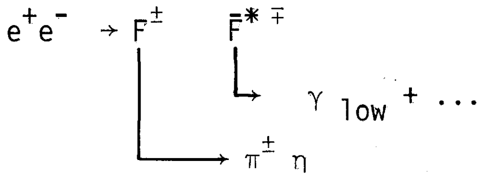

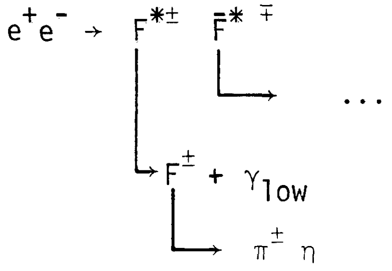

The DASP group employed the following event selection criteria:

a) A pion identified by one of the magnetic spectrometer arms has to have a minimum momentum of 600 MeV.

b) A pair of photons seen by the inner detector has to have an invariant mass between 350 and 650 MeV.

c) A third low energy photon γ_{low} below 200 MeV has to be detected.

This selection leads to 35 events for a total integrated luminosity of 1400 nb^{-1}. In a subsequent fit it is required a) that the mass of the photon pair is compatible with the exact η mass and b) that the recoiling system (indicated by dots in the above reactions) has a mass equal to the $F \rightarrow \pi\eta$ system for the first reaction or equal to the $F^* \rightarrow \pi\eta\ \gamma_{low}$ system for the second reaction. With these two constraints 15 events gave a good fit ($\chi^2 < 8$) for the first reaction. The result is shown in Fig. 6.31 where the fitted $\pi\eta$ mass is plotted vs. the $\bar{F}\gamma_{low}$ mass which includes the recoiling system. We observe that 5 events cluster in a narrow region around $M(\pi\eta) = 2.04$ GeV and $M(\gamma_{low} + \ldots) = 2.17$ GeV; the events below 2 GeV are attributed to background. We may consider the observed clustering as evidence for $F\bar{F}^*$ production. However, the second reaction is kinematically so very similar to $F\bar{F}^*$ production that 14 out of the 15 events for the first reaction fit the second reaction as well, which then can be taken as evidence for $F^*\bar{F}^*$ production. This ambiguity is certainly due to the small F/F^* mass difference. Nevertheless the F and F^* masses can be fairly well determined:

$$M_F = 2.03 \pm 0.06 \text{ GeV} \qquad M_{F*} = 2.14 \pm 0.06 \text{ GeV}$$

where the errors given include systematic uncertainties and the uncertainty about the correct hypothesis.

6.7 Present Status of Charm Investigations

A large amount of experimental information has been collected since the discovery of J/ψ and ψ' in late 1974. This information has in an impressive way confirmed the charm picture, the characteristics of which can be summarized in the following three points:

i) The charm model can be adjusted to account for several of the level splittings and transition rates of $c\bar{c}$ bound states. The observed states and transitions are again shown in Fig. 6.32 and the respective branching ratios in percent are given as numbers next to the emitted particles.

ii) Particles carrying the charm quantum number have been identified in various decay modes as D and F mesons. The pair production of charmed baryons in e^+e^- annihilation is inferred from observed thresholds$^{58)}$ at about 4.6 GeV for inclusive proton and Λ production.

iii) The region above the threshold at 4 GeV is difficult to analyse. Such an analysis will involve model dependent calculations, an example[82)] of which is given in Fig. 6.33. It seems that the various mesonic pair production processes are not sufficient to explain the complex structure of the experimental cross section above 3.9 GeV, a detailed discussion of which is deferred to chapter 8.

After having praised the charm model, let us now turn to some of the problems. It is a remarkable observation that the spin orbit splitting of the P_c or χ states is of the order to 100 MeV and therefore relatively large with respect to the separation of the states J/ψ and ψ' with different main quantum numbers. Furthermore, according to Landé's rule $E(^{2S+1}L_J) - E(^{2S+1}L_{J-1}) \sim J$ for the energy levels E in a Coulombic potential the relative splitting of these P-wave states is expected to be

$$\frac{E\ (^3P_2) - E\ (^3P_1)}{E(^3P_1) - E\ (^3P_0)} = 2,$$

and experimentally we observe

$$\frac{3552 - 3508}{3508 - 3414} = 0.47.$$

However, the second term in the expression (6.1) for the potential reduces this discrepancy[52)] and possibly both terms have to be modified or additional terms included.

Whereas the details of the P-wave splitting may be taken as an indication for an appropriate choice of the potential, the X(2.83) and χ(3.45) states pose a real puzzle. That the hyperfine splitting of these $^1S_0$ states with respect to the corresponding $^3S_1$ states J/ψ and ψ' is of the order of 250 MeV and therefore much larger than the spin orbit splitting is surprising and not easy to explain. However, the real difficulty in associating these states with the charm model arises from the observed transition rates. The hadronic decay of the pseudoscalar states into hadrons should be less suppressed than for the pseudovectors J/ψ and ψ', because the $c\bar{c}$ annihilation may proceed via two gluons instead of three:

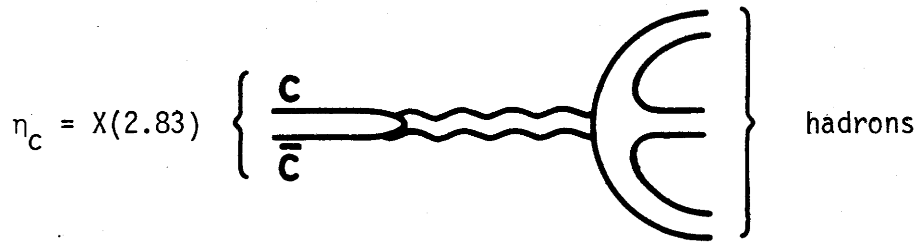

The expected hadronic widths are of the order of a few MeV, but only radiative decays have been observed so far. A quantitative comparison for the radiative transitions reveals a discrepancy of at least a factor of 20 for X(2.83) and of a factor of 10^3 for $\chi(3.45)$:

$$\Gamma_{\text{model}}(J/\psi \to \gamma X) \geq 20 \times \Gamma_{\text{observed}}$$

$$BR_{\text{observed}}\ (\psi' \to \gamma\ \chi(3.45) \to \gamma\gamma\ J/\psi) \sim 10^3 \times BR_{\text{model}}$$

Assigning the quantum numbers $J^{PC} = 2^{-+}$ of the 3^1D_2 state to the $\chi(3.45)$ leads into similar difficulties and seems to be equally unacceptable. These inconsistencies have lead to the suggestion that X(2.83) and $\chi(3.45)$ are not the hyperfine partners of J/ψ and ψ' and that the missing singlet states η_c and η_c' lie just below the triplets where they are as yet undiscovered. The assignment of X(2.83) and $\chi(3.45)$ in the quark model is then again open and various schemes have been devised[83)]. This question will remain unsettled as long as the quantum numbers of these objects are not determined. A certain hope is that a high statistics experiment at the ψ' mass might reveal the decay $\psi' \to \gamma\,\eta_c$.

Only some aspects of the charm model could be treated in this report. For a more detailed discussion of level splittings and transition rates the reader is referred to reports by Jackson[49)] and Schopper[84)].

7. Evidence for Heavy Leptons

The cross section for the pair production of a point-like heavy object τ of spin $\frac{1}{2}$ is given by $\sigma_{\mu\mu}$(see section 2.1) modified with a kinematic factor:

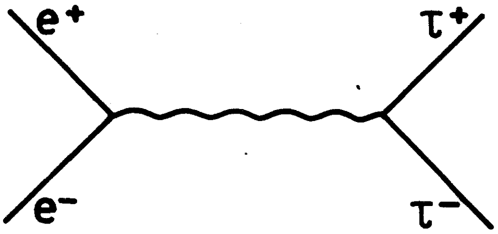

$$\sigma_{\tau\tau} = \sigma_{\mu\mu} \cdot \frac{3\beta - \beta^3}{2}$$

In the following we shall only consider the case of a sequential heavy lepton, which means that the lepton and its associated neutrino carry a separate quantum number and form a third left-handed doublet in the sequence:

$$\begin{pmatrix} \nu_e \\ e \end{pmatrix} \quad \begin{pmatrix} \nu_\mu \\ \mu \end{pmatrix} \quad \begin{pmatrix} \nu_\tau \\ \tau \end{pmatrix} \quad \cdots\cdot$$

The possibility of other types of heavy leptons has been discussed in a parallel series of lectures by Ellis[85)]. Assuming a V-A coupling of the τ and its massless neutrino the following branching ratios have been calculated for the decay of a heavy sequential lepton[86)] with a mass of 1.9 GeV:

τ^- decay mode	branching ratio %	number of charged particles in final state
$\nu_\tau\ e^-\ \bar{\nu}_e$	20	1
$\nu_\tau\ \mu^-\ \bar{\nu}_\mu$	20	1
$\nu_\tau\ \pi^-$	11	1
$\nu_\tau\ K^-$	1	1
$\nu_\tau\ \rho^-$	22	1
$\nu_\tau\ K^{*-}$	1	1,3
$\nu_\tau\ A_1^-$	7	1,3
ν_τ + hadronic continuum	18	1,3,5,...

From all the decays 85 % give only one charged particle in the final state, so that a considerable fraction of heavy lepton pair production and decay should show up in the event class with two observed oppositely charged tracks. The PLUTO detector has a large angular acceptance of 85 % and very general particle trigger which allows to measure the two-prong cross section87). In Fig. 7.1 the ratio R_2 of two-prong to μ-pair cross section is shown. The dashed line indicates what is expected for heavy leptons of the above type and we see that there is sufficient room in the data to accomodate such objects.

7.1 Signatures for Heavy Leptons and Observed Processes

Since the heavy sequential leptons decay with a high percentage purely leptonically into e's or μ's, one would expect the following experimentally observable signatures:

a) $e^\pm \mu^\mp$ events provide a clean signal due to the reaction

$$\begin{tikzcd} e^+e^- \to & \tau^+ \arrow[d, ""] & + & \tau^- \arrow[d] \\ & \bar{\nu}_\tau \; e^+ \; \nu_e & & \nu_\tau \; \mu^- \; \bar{\nu}_\mu \end{tikzcd}$$

The experimental requirements are:

- Find $e^+ \mu^-$ or $e^- \mu^+$. 8 % of the decays are expected to proceed this way (see above table).
- No other charged particles or photons must be present.
- The missing energy has to be large due to the many unobserved neutrinos.
- The lepton momentum spectrum is hard, i.e. it extends to higher values than for charmed particle decays (see section 6.5).

In the following diagram the difference between heavy leptons (full line) and charmed mesons (dash-dotted line) is sketchend and in addition the expected momentum spectrum for 2-body decays (dashed line) is shown:

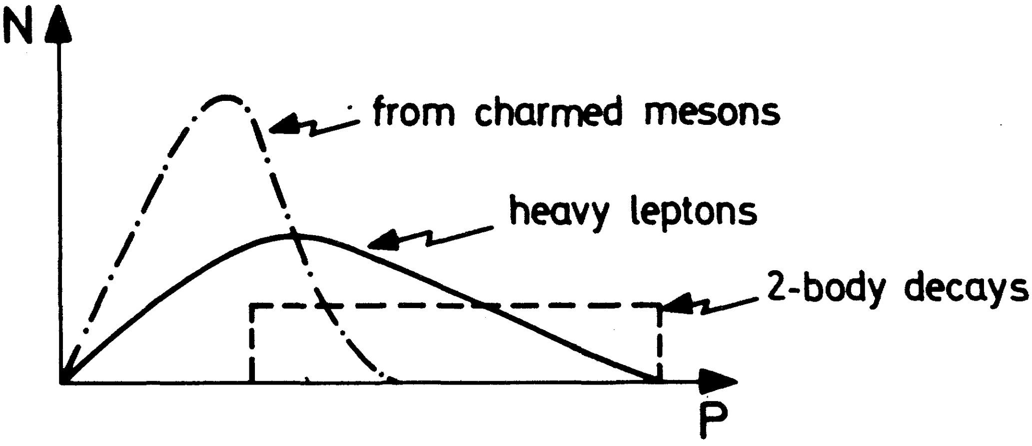

b) $e^{\pm} X^{\mp}$ or $\mu^{\pm} X^{\mp}$ events yield another signature from reactions like:

$$e^+e^- \to \tau^+ + \tau^-$$
$$\hookrightarrow \nu_\tau \; e^+ \; \nu_e \qquad\qquad \hookrightarrow \nu_\tau \quad X^-$$

where X^- can be any charged particle like e^-, μ^-, π^- or K^-. The experimental requirement is to find an $e^{\pm}$ or $\mu^{\pm}$ and one additional particle of opposite charge. With this event selection one can obtain up to 40 % of all decays which is a much larger sample than for the previous signature but the background problems may be more severe.

A background source for the first signature is the QED process $e^+e^- \to e^+e^- \mu^+\mu^-$ with two leptons missing the detector. Because we required two different type leptons for the final state, the much larger background from the QED final states ee, $\mu\mu$, eeγ, $\mu\mu\gamma$, ee$\gamma\gamma$, $\mu\mu\gamma\gamma$ is avoided. Due to the limited acceptance - i.e. hadrons missing the detector - both signatures will contain background from charmed particle decays and from hadronic events with one or two hadrons decaying leptonically and thereby faking leptons. These latter types of background are most severe for the second signature events since only one lepton is identified there.

The first indication for heavy leptons came from $e^{\pm}\mu^{\mp}$ events. Early SLAC-LBL data[88] are shown in Fig. 7.2 and the two curves represent the energy dependence for heavy sequential leptons of two different masses. That one really observes a pair production process, can be seen from the colinearity distribution in Fig. 7.3. Whereas there is little correlation at low energies close to threshold, the two leptons are produced nearly back to back at high energies.

Several measurements[89)] of $\mu^{\pm}X^{\mp}$ events are compiled in Fig. 7.4 and the curve illustrates that the energy dependence is as expected for heavy leptons. In addition, the electron momentum spectrum[81)] from $e^{\pm}X^{\mp}$ events in Fig. 7.5 is that of a 3-body decay and agrees with the model calculation based on V-A coupling, a massless neutrino, and a heavy lepton mass of 1.9 GeV. The experimental distribution is incompatible with a many-body decay like for charmed mesons and with a 2-body decay (see the schematic diagram above).

7.2 Properties of the New Heavy Lepton

When observing a third lepton τ one would like to know whether it has all the properties of the conventional leptons e and μ or if it is different in some properties other than the mass. Let us therefore ask the following questions:

- Has the τ really a 3-body decay?
- Does it couple to its neutrino ν_τ like V-A or V+A?
- What is the upper limit for the mass of ν_τ?
- How do we best determine the τ mass?
- What is the spin of the τ?
- Which semileptonic decay modes do we observe?

The first question had already been answered in the affirmative when presenting the lepton momentum distribution in the previous section. The SLAC-LBL group[88)] has studied this point in detail by combining the $e^{\pm}\,\mu^{\mp}$ events of all enrgies and plotting the scaled momentum $r = \frac{p - 0.65}{p_{max} - 0.65}$ where p_{max} is the maximum possible momentum for a particular energy and p = 0.65 GeV is the cut-off momentum for leptons. The data in Fig. 7.6 agree well with a 3-body decay (full line) but disagree with a 2-body decay (dashed curve for unpolarized bosons and dash-dotted curve for bosons produced in a helicity = 0 state).

The question as to the type of coupling is answered by again comparing the scaled momentum to various model calculations[9o)]. This is done in Fig. 7.7 where the V+A coupling (dashed line) has only a 0.1 % probability to fit the data. Among the curves representing V-A coupling the best agreement is obtained for zero neutrino mass; however, a ν_τ mass of 500 MeV cannot be excluded. In fact, the result from the SLAC-LBL data is that V-A coupling is strongly favoured and that the upper limit for the neutrino mass is 600 MeV. The upper limit quoted by the PLUTO experiment[91)] for the ν_τ mass is 300 MeV.

It was already evident from the two curves in Fig. 7.2 that different mass assignments for the heavy lepton give the strongest variation in the cross section at energies close to threshold. The SLAC-LBL group[92)] has taken a large amount of data at the ψ' and ψ'' resonance and thus obtained accurate cross section values at the threshold for τ pair production. For the $e^{\pm}\mu^{\mp}$ events the quantity

$$R_\tau = \frac{R_{e\mu}}{2\,B_e\,B_\mu}$$

is plotted in Fig. 7.8 where R denotes the ratio with respect to the μ pair production cross section and $B_e = B_\mu = 0.186$ is taken for the leptonic branching ratio of the τ. The three curves show the range of variation. From the $e^{\pm}X^{\mp}$ data of the DASP experiment[93)] a best fit of 1.81 ± 0.02 GeV is obtained for the τ mass.

In order to see whether there is any preferred spin assignment for the τ, we compare the cross section data - e.g. the R values in Fig. 7.8 - with the following cross section formulas[94)] for point-like particles of various spins:

spin 0: $\sigma_{00} = \frac{1}{4}\ \sigma_{\mu\mu}\ \beta^3$

spin $\frac{1}{2}$: $\sigma_{\tau\tau} = \sigma_\mu\,\frac{3\beta - \beta^3}{2}$

spin 1: $\sigma_{11} = \frac{3}{4}\ \sigma_{\mu\mu}\ \beta^3\left(1 - \frac{S}{6M^2}\right)^2$, only $G_E \neq 0$

The observed decay mode $\tau^- \to \nu_\tau\,\mu^-\,\bar{\nu}_\mu$ amounts to roughly 20 % of the spin $\frac{1}{2}$ cross section $\sigma_{\tau\tau}$, but it would by far exceed 100 % of the spin 0 cross section σ_{00} near threshold. There is not only the factor 1/4 but also a strong suppression due to the kinematic factor β^3. Inserting a heavy lepton mass of $M = 1.81$ GeV and a cms energy of $2E = 4$ GeV into the expression $\beta^2 = (E^2 - M^2)/E^2$ we obtain for $(3\beta - \beta^3)/2$ a value of 0.6 as shown in Fig. 7.8. However, $\beta^3 = 0.077$ is almost an order of magnitude smaller. Therefore, due to the large cross sections for the leptonic decays near threshold, spin 0 is excluded and spin 1 is very unlikely. The spin $\frac{1}{2}$ assignment confirms the leptonic nature of this new object.

In addition to the leptonic decays various semileptonic decays have been observed, some branching ratios of which are given in the following table[92)] and compared with the model predictions:

decay mode	BR_{exp}	BR_{model}
$e\nu\nu$ or $\mu\nu\nu$	19 ± 2 %	20 %
$\rho\,\nu$	24 ± 9 %	22 %
$K\,\nu$	< 1.6 %	1 %
$A_1\,\nu$	11 ± 4 %	7 %
$\pi\,\nu$	2 ± 3 % *)	11 %

For $e\nu\nu$ and $\mu\nu\nu$ an average of various experimental numbers has been taken and these numbers imply that the two leptonic decays have the same branching ratios. We see from the table that the semileptonic branching ratios agree reasonably well with the model calculations except for the $\pi\nu$ decay, the measured value of which is much smaller than expected.*) These and many more experimental numbers are reviewed in Perl's talk[92)] at the Hamburg conference.

We can summarize the discussion on heavy leptons by stating, that the τ seems to have all the properties of its light partners e and μ. Because the mass of the τ is so large - 1.81 GeV -, there are many semileptonic decay channels open, the details of which have to be investigated in a model dependent way[86)].

8. Total Cross Section

Measuring the total cross section is one of the first objectives when entering a new range of energies and it keeps the physicist busy until at last he might have succeeded in breaking down the total cross section into its various components. In section 2.3 we have already discussed early measurements and found that 4 quarks and 3 colours are needed to describe the e^+e^- annihilation into hadronic final states. The quark-gluon coupling constant α_s, which we introduced in section 6.1, gives rise to an additional correction. Therefore - outside resonance and threshold regions - the cross section ratio R should behave like[95)]:

$$R = \frac{\sigma(e^+e^- \to \text{hadrons})}{\sigma(e^+e^- \to \mu^+\mu^-)} = 3 \sum_i Q_i^2 \left(1 + \frac{\alpha_s(E)}{\pi}\right)$$

---

*) Note added in proof: Two recent experiments have obtained $\pi\nu$ branching ratios of about 9% (not yet published) in agreement with the model value.

In contrast to the cross section formula in section 2.3, the colour factor of 3 is given explicitly in this expression so that the sum index i extends only over 3 or 4 quarks. The value α_s = 0.2 (see section 6.1) gives a gluon correction of 6 to 7 % and the energy dependence of α_s is such[46,47] that it decreases logarithmically with increasing energy.

Neglecting the correction due to α_s, the PLUTO group[87] has compared the above expression with their measurements. The data points are plotted in Fig. 8.1 and the composition of the total cross section is shown schematically. R = 2 is obtained for the old up, down, and strange quarks. On top of it we find the contribution from heavy lepton pair production, the threshold behaviour of which was discussed in the previous section. The remaining fraction is called the new part of R and most of it can be explained by the charmed quark contribution of 4/3. As indicated in section 6.7, the threshold behaviour of charmed particle production can be very complicated. The top band in Fig. 8.1 is certainly partly due to the thresholds of charmed meson and baryon pair production and the gluon correction might contribute as well.

The DASP collaboration[96] has analysed their data by excluding heavy leptons and obtains the total hadronic cross section in Fig. 8.2. The data points are somewhat lower than in Fig. 8.1 but the overall structure is the same. The full curve is obtained by fitting 3 Breit-Wigner resonances on top of a smooth background (dashed line). This curve represents a convenient parametrization of the cross section and it is understood that part or all of the resonance-like structures might be explained by thresholds for charmed particle production.

One has to point out that the detection technique is quite different for the various experimental arrangements. Whereas SLAC-LBL and PLUTO base their cross section determination on the identification of charged particles (solid angle of 65 % and 85 % respecitvely), the inner non-magnetic part of the DASP detector is sensitive to charged particles and photons. At DASP the trigger- and detection efficiencies for charged particles and photons are nearly the same and the detection acceptance covers 76 % and 62 % of 4π respectively. Because of the different systematic errors involved it is interesting to compare the three experimental results. This is done in Fig. 8.3. The heavy lepton contributions are now included and the curve fitting the DASP data is superimposed on the PLUTO and SLAC-LBL points. The PLUTO and DASP data agree well in shape, but the curve exceeds the PLUTO points by about half a unit in R above 4 GeV. The agreement in magnitude is better between the SLAC-LBL and DASP data, but the separation of the peaks at 4.04 and 4.16 GeV is not so clearly visible in the SLAC-LBL cross section. Remembering that systematic errors of about 15 % are involved, one cannot observe any significant discrepancy between the data. The general energy dependence of all three epxeriments is remarkably similar.

One may now compare the structure in the total cross section with model predictions83) for bound states and thresholds. In Fig. 8.452) the observed vector mesons are given by their symbols and the bumps above charm threshold by their energy values. For the peaks at 4.04 and 4.16 GeV it is an open question whether they can be interpreted as 3^3S_1 and 4^3D_1 states or as threshold enhancements of the pair production processes indicated in the figure. An example for a model predicted threshold behaviour has been given in section 6.7 (Fig. 6.33).

9. e^+e^- Physics at Higher Energies

The unexpected findings at present energies, which brought electron physics into the limelight of physics interest, have caused an ever increasing urge to continue the e^+e^- investigations at energies beyond the presently available range. Some of the points of interest are:

(i) A careful measurement of R, the ratio of hadronic to μ pair cross section, for finding possible new degrees of freedom, i.e. possible evidence for additional quantum numbers.

(ii) Since the electromagnetic cross sections are falling as the inverse square of the cms energy, other types of interaction will become increasingly important, such as weak interactions and two photon processes.

The discovery97) of the Upsilon last year and its recent confirmation98) in e^+e^- collisions at DORIS have already signalled the presence of one or more additional quarks85). However, due to the large Upsilon mass of 9.46 GeV the associated step in R is expected to occur above 10 GeV which is outside the range of present storage rings. Therefore, further implications of these new degrees of freedom have to be investigated at the next generation e^+e^- colliding beams.

As an example of weak interactions, their influence on μ pair production has been studied99). In addition to one photon exchange with its $1 + \cos^2\theta$ angular distribution we have contributions from the weak neutral current:

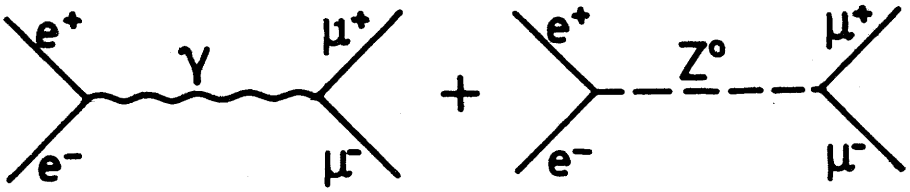

Neglecting effects from electron or positron polarization, the interference of weak and electromagnetic interactions will modify the simple $(1 + \cos^2\theta)$ behaviour in the following way:

$$\frac{d\sigma}{d\Omega} = \frac{\alpha^2}{16E^2} \{(1 + \frac{2E^2 g_V^2}{\pi\alpha(4E^2 - M_Z^2)}) (1 + \cos^2\theta) + \frac{4E^2\, g_A^2}{\pi\alpha(4E^2 - M_Z^2)} \cos\theta\}$$

where E is the cms energy, M_Z the Z^0 mass and g_V, g_A the vector and axial-vector couplings. The difference $\frac{\Delta\sigma}{\sigma}$ in the integrated cross section measures the vector coupling, and the asymmetry $A = \frac{\sigma_- - \sigma_+}{\sigma_- + \sigma_+}$, which can be interpreted as a charge asymmetry, determines the axial vector coupling. From standard V-A theory and from the Weinberg model it is expected that changes in σ and in A will be of the order of 10 % for beam energies of 15 GeV.

Two photon processes, which are of fourth order in QED, become increasingly important at higher energies:

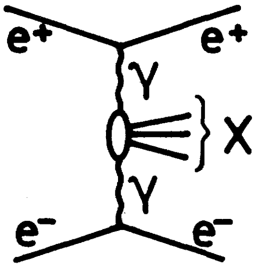

$$\sigma(E) \sim \frac{\alpha^4}{m} (\ln \frac{E}{m_e})^2 \; (\ln \frac{E}{m_e})^n$$

where E, m_e are the electron energy and mass and $n \gtrsim 1$ depends on the specific final state X. Note that this cross section does not drop like 1/s, but the cms energy is replaced by the threshold mass m of the state X. One can also see from the cross section formula that one power of α is approximately cancelled since $(\ln \frac{E}{m_e}) \simeq 100$ for $E = 15$ GeV. However, to positively identify the two photon processes, it would be advantageous to catch at least one of the electrons scattered at small angles with respect to the beam. Therefore, a special forward detector close to the beam line would be a useful tool to obtain information on these processes.

A more detailed discussion of the physics interest in high energy electron positron colliding beams and of possible implications for detector arrangements has been given elsewhere[100].

9.1 Next Generation Storage Rings

As has been the case in the past, the competition in e^+e^- colliding beam physics between SLAC and DESY will also continue in the future. Both electron-positron rings - PEP in Stanford and PETRA in Hamburg - will cover the same energy region, extending up to 36 and 38 GeV respecitvely in their initial phase of operation. Since the PETRA machine is nearly a year ahead of PEP, I shall only discuss the European project and the experimental detectors involved here.

Fig. 9.1 shows the layout of PETRA. The circumference of the ring is 2.3 km and the bending radius 197 m. The ring has octogonal shape with rounded corners. There are eight straight sections, two of which house the radio frequency system. The other six are avialable for experiments, but at the beginning only four interaction regions will be equipped. Fast and relatively inexpensive construction of PETRA is possible by using the 7.5 GeV electron-synchrotron and the storage ring DORIS as injector and intermediate storage ring. The originally forseen scheme of injection is indicated in Fig. 9.2. Electrons and positrons, injected into the synchrotron by two linacs, are accelerated in DESY up to 2 GeV and transferred and accumulated in DORIS. Fast kickers will then eject individual bunches form DORIS for re-injection into DESY. After acceleration up to 7 GeV, these single bunches will be injected into PETRA. This scheme assures short filling times of the ring which are estimated to be of the order of 10 minutes. In order to relieve DORIS of the burden as an intermediate storage ring, a 450 MeV storage ring PIA (Positron Intensity Accumulator) will come into operation in the middle of 1979. Since the electron source is much more intense, no such device is needed for the electron bunches. After an initial phase of restrictions, the physics program at DORIS can proceed without being interrupted during PETRA injection.

The PETRA proposal was submitted to the authorities in the fall of 1974 and approved one year later. Ground breaking took place in January 1976. The construction of the tunnel, the injection channels and the experimental halls were finished in spring 1977. The installation of machine components is expected to be completed in July 1978. First injections into the PETRA tunnel took place in 1977. The installation of the experiments may start in 1978 and data taking commence at the end of the same year. The initial operation of PETRA will be at 15 GeV, and the luminosity is expected to be close to 10^{32} $cm^{-2}sec^{-1}$. The variation of the luminosity with the beam energy is shown in Fig. 9.3, where we see that for the highest energies the number of bunches has to be reduced in order to conform to the maximum available rf power (see section 3.1). It is also indicated in this figure that with the finally envisaged maximum rf power of 9.6 MW the beam energies can extend up to 22.5 GeV.

9.2 Detectors for PETRA

All of the experiments, proposed to be installed in the interaction regions at PETRA, use a magnetic field surrounding the interaction point and try to cover as much as possible of the full solid angle. The various experiments differ in some of the means of particle identification.

Five proposals have been accepted for the first round of experiments. Collaborations from the following universities and institutions are involved, and their projects have been given the short names on the left:

CELLO: DESY-Karlsruhe-Munich-Orsay-Paris-Saclay[101].
TASSO: Aachen-Bonn-DESY-Hamburg-London-Oxford-Rehovot-Rutherford Lab.-Wisconsin[102].
MARK J: Aachen-DESY-MIT-Netherlands[103].
JADE: DESY-Hamburg-Heidelberg-Lancaster-Manchester-Rutherford Lab.-Tokyo[104].
PLUTO: Aachen-DESY-Hamburg-Siegen-Wuppertal[105].

The experiments can be classified according to their physics objectives. Three examples are taken from the list above. Experiment MARK J (Fig. 9.4) has a very narrow core of wire chambers and shower counters surrounded by magnetic iron into which drift chambers are inserted. The main interest of this experiment is to determine weak interaction effects by observing μ pair final states. Experiment JADE (Fig. 9.5) uses a magnetic solenoid of approximately 1 m radius surrounded by lead glass counters and range counters. This set-up intends to carefully identify electrons and photons; the directions of the photons can be obtained by using the coordinates of the interaction point known from the charged tracks. Experiment TASSO (Fig. 9.6) has a magnetic solenoid of close to 1.5 m radius. Electrons and muons are identified by shower and range counters in a large fraction of the solid angle and hadrons are classified by a set of Cerenkov counters with a limited spatial acceptance. Further details on future epxeriments at PETRA should be obtained from the written proposals.

It is a pleasure to acknowledge the help of many colleagues at DESY for supplying me with data and figures on the respective experiments. I want to thank J. Körner for helpful comments.

References and Footnotes

1. N. Schmitz: Lectures at Kupari-Dubrovnik School 1977;
   MPI-PAE/Exp. E1.62 (1977)
2. see for example:
   V. Lüth: Lectures at Baku School 1976; SLAC-PUB-1973 (1977)
   B.H. Wiik and G. Wolf: Lectures courses at several schools;
   DESY 78/23 (1978)
3. Proc. 1977 Intern. Symposium on Lepton and Photon Interactions at High Energies, Hamburg
4. see for example:
   J.M. Jauch and F. Rohrlich: The Theory of Photons and Electrons
   (Addison-Wesley, Reading, Mass. 1955)
   J.D. Bjorken and S.D. Drell: Relativistic Quantum Mechanics
   (McGraw-Hill, N.Y., 1964)
5. R.P. Feynman: Photon-Hadron Interactions
   (W.A. Benjamin, Reading, Mass. 1972)
6. H. Muirhead: Lectures at Kupari-Dubrovnik School 1977,
   Univ. of Liverpool Report (1977)
7. N. Arteago-Romero et al.: Phys. Rev. D3, 1569 (1971)
   S.L. Brodsky et al.: Phys. Rev. D4, 1532 (1971)
   H. Terezawa: Rev. Mod. Phys. 45, 615 (1973)
   G. Bonneau and F. Martin: Nucl. Phys. B27, 381 (1974)
8. B.T. Feld: Models of Elementary Particles (Blaisdell, London, 1969)
9. S.D. Drell and T.M. Yan: Annals Phys. 66, 578 (1971)
10. A.M. Boyarski et al.: Phys. Rev. Lett. 34, 762 (1975)
    J.E. Augustin et al.: Phys. Rev. Lett. 34, 764 (1975)
    R.F. Schwitters: Proc. 1975 Intern. Symposium on Lepton and Photon Interactions at High Energies, Stanford, p.5
11. V. Silvistrini: Proc. XVI Intern. Conf. on High Energy Physics,
    Chicago, 1972, Vol. 4, p. 1
12. Particle Data Group: Rev. Mod. Phys. 48, No. 2, Part II (1976)

13. J.J. Sakurai: Proc. IV International Symposium on Electron and Photon Interactions at High Energies, Liverpool, 1969, p. 91
J.J. Sakurai: Currents and Mesons (Univ. of Chicago Press, Chicago, 1969)
H. Fraas and D. Schildknecht: Nucl. Phys. B14, 543 (1969)
D. Schildknecht: Springer Tracts in Modern Physics (Springer, Berlin, 1972), Vol. 63, p. 57

14. J.-E. Augustin et al.: Phys. Lett. 28B, 508 (1969)

15. C. Bemporad: 1977 Hamburg Symp. (Ref. 3), p. 165
F. Laplanche: 1977 Hamburg Symp. (Ref. 3), p. 189

16. V.L. Auslander et al.: Phys. Lett. 25B, 433 (1967)
J.C. Bizot et al.: Phys. Lett. 32B, 416 (1970)
V.E. Balakin et al.: Phys. Lett. 34B, 328 and 663 (1974)
D. Benaksas et al.: Phys. Lett. 39B, 289 (1972)
A. Litke et al.: Phys. Rev. Lett. 30, 1189 (1973)
G. Tarnopolsky et al.: Phys. Rev. Lett. 32, 432 (1974)

17. H. Wiedemann: Lectures at Herbstschule Maria Laach, 1973, DESY International Report (1974)

18. V.N. Baier: Proc. Intern. School of Physics "Enrico Fermi", Varenna, 1971, Course 46, p. 1 (Academic Press, N.Y., 1972)
J.D. Jackson: Rev. Mod. Phys. 48, 417 (1976)

19. J.J. Aubert et al.: Phys. Rev. Lett. 33, 1404 (1974)

20. J.-E. Augustin et al.: Phys. Rev. Lett. 33, 1406 (1974)

21. A.M. Boyarski et al.: Phys. Rev. Lett. 33, 1453 (1974)

22. C. Bacci et al.: Phys. Rev. Lett. 33, 1408 (1974)
W. Braunschweig et al.: Phys. Lett. 53B, 393 (1974)
L. Criegee et al.: Phys. Lett. 53B, 489 (1974)

23. J.D. Jackson and D.L.Scharre: Nucl. Instr. and Methods 128, 13 (1975)
D.R. Yennie: Phys. Rev. Lett. 34, 239 (1975)

24. A.M. Boyarski et al.: Phys. Rev. Lett. 34, 1357 (1975)
V. Lüth et al.: Phys. Rev. Lett. 35, 1124 (1975)

25. B. Jean-Marie et al.: Phys. Rev. Lett. 36, 291 (1976)

26. W. Braunschweig et al.: Phys. Lett. 63B, 487 (1976)

27. J.G. Körner and M. Kuroda: Phys. Rev. D16, 2165 (1977)

28. B.H. Wiik: Proc. 1975 Intern. Symposium on Lepton and Photon Interactions at High Energies, Stanford, p. 69
G.S. Abrams et al.: Phys. Rev. Lett. 34, 1181 (1975)
W. Tannenbaum et al.: Phys. Rev. Lett. 36, 402 (1976)

29. G.S. Abrams: Proc. 1975 Intern. Symposium on Lepton and Photon Interactions at High Energies, Stanford, p. 25

30. G. Goldhaber: Proc. IV Intern. Symposium on Nucleon-Antinucleon Interactions, Syracuse, N.Y., 1975, addendum; LBL Report LBL-4224 (1975)

31. G.J. Feldman and M.L. Perl: Phys. Reports 190, 233 (1975)

32. M. Bernardini et al.: Phys. Lett. 46B, 261 (1973)

33, R. Gatto: Proc. 1965 Intern. Symposium on Electron and Photon Interactions at High Energies, Hamburg, Vol. I, p. 106

34. M. Conversi et al.: Nuovo Cim. 40A, 690 (1965)
D.L. Hartil et al.: Phys. Rev. 184, 1415 (1969)

35. F.M. Renard: Phys. Lett. 47B, 361 (1973)

36. J.G. Körner and M. Kuroda: Phys. Lett. 67B, 455 (1977)

37. D. Schildknecht and F. Steiner: Phys. Lett. 56B, 36 (1975)
T.F. Walsh: Lett. Nuovo Cim. 14, 290 (1975)
R.N. Cahn and M.S. Chanowitz: Phys. Lett. 59B, 277 (1975)
H. Harari: Phys. Lett. 60B, 172 (1976)
A. Kazi et al.: Lett. Nuovo Cim. 15, 120 (1976)

38. W. Bartel et al.: Phys. Lett. 64B, 483 (1976)

39. W. Bartel et al.: Phys. Lett. 66B, 489 (1977)

40. W. Braunschweig et al.: Phys. Lett. 63B, 115 (1976)

41. J. Engels et al.: Nuovo Cim. 17A, 535 (1973)
F. Elvekjaer: Proc. 1975 High Energy Particle Interactions, Smolenice, Vol. 2, p. 35 (Bratislava, 1976); DESY Report 75/53
F. Elvekjaer and F. Steiner; Phys. Lett. 60B, 456 (1976)

42. B. Alper et al.: Nucl. Phys. B87, 19 (1975)

43. F. Pierre: Lectures at Basko-Polje School, Makarska, 1976; Saclay Report D Ph P E 76-21 (1976)

G.J. Feldmann: Proc. Summer Inst. on Particle Physics, Stanford, SLAC-198 (1976), p. 81; SLAC-PUB-1852 (1976)

44. S. Okubo: Phys. Letters 5, 105 (1963)
G. Zweig: CERN TH 401, 412 (1964)
J. Iizuka et al.: Progr. Theor. Phys. 35, 1061 (1966)

45. Y. Hara: Phys. Rev. B134, 701 (1964)
J.D. Bjorken and S.L. Glashow: Phys. Lett. 11, 255 (1964)
S.L. Glashow et al.: Phys. Rev. D2, 1285 (1970)

46. T. Appelquist and H.D. Politzer: Phys. Rev. Lett. 34, 43 (1975)

47. A. DeRujula and S.L. Glashow: Phys. Rev. Lett. 34, 46 (1975)
C.G. Callan et al.: Phys. Rev. Lett. 34, 52 (1975)
T. Appelquist et al.: Phys. Rev. Lett. 34, 365 (1975)
E. Eichten et al.: Phys. Rev. Lett. 34, 369 (1975)

48. L.B. Okun and M.B. Voloshin: Moscow Inst. of Theoretical and Experimental Physics, ITEP-152, 1976
A. DeRujula: Proc. XVIII International Conf. on High Energy Physics, Tiblisi, 1976

49. J.D. Jackson: Proc. Summer Inst. Particle Physics, Stanford, SLAC-198 (1976), p. 147; LBL Report LBL-5500 (1976)

50. See e.g.: D.H. Perkins: Introduction to High Energy Physics (Addison-Wesley, Reading, Mass., 1972)

51. J. Pumplin et al.: Phys. Rev. Lett. 35, 1538 (1975)
H.J. Schnitzer: Phys. Rev. Lett. 35, 1540 (1975)
H.J. Schnitzer: Phys. Rev. D13, 74 (1976)

52. Throughout this report the number in front of the letter for the angular momentum denotes the principle quantum number, as used in atomic physics; e.g. 2P, 3P,.... In the literature one also finds the nuclear physics notation where the P state numbering starts with 1; e.g. 1p, 2p, ... The latter notation is used in:
J.D. Jackson: Proc. European Conf. on Particle Physics, Budapest, 1977; CERN Report TH. 2351 (1977)

53. M.K. Gaillard et al.: Rev. Mod. Phys. 47, 277 (1975)

54. M.B. Einhorn and C. Quigg: Phys. Rev. D12, 2015 (1975)

55. C. Jarlskog: Proceedings of the 1974 CERN School of Physics, CERN 74/22, 1974, p.1
    J. Leite Lopes: Lectures at Bosko-Polje School, Makarska, 1975
56. E. Eichten et al.: Phys. Rev. Lett. 36, 500 (1976)
57. J. Kirkby: 1977 Hamburg Symp. (Ref. 3), p. 3
58. A. Barbaro-Galtieri: 1977 Hamburg Symp. (Ref. 3), p. 21
59. W. Braunschweig et al.: Phys. Lett. 57B, 407 (1975)
    E. Gadermann: Thesis, Univ. of Hamburg (1978)
60. J.S. Whitaker et al.: Phys. Rev. Lett. 37, 1596 (1976)
61. J. Olson: 1977 Hamburg Symp. (Ref. 3), p. 117
62. G.J. Feldman et al.: Phys. Rev. Lett. 35, 821 (1975)
    G. Goldhaber: Proc. European Conf. on Particle Physics, Budapest, 1977; LBL Report LBL-6732 (1977)
63. C.J. Biddick et al.: Phys. Rev. Lett. 38, 1324 (1977)
64. W. Braunschweig et al.: Phys. Lett. 67B, 243 (1977)
65. F.A. Berends and R. Gastman: Nucl. Phys. B61, 414 (1973)
66. W. Braunschweig et al.: Phys. Lett. 67B, 249 (1977)
67. W.D. Apel et al.: Phys. Lett. 72B, 500 (1978)
68. Y.I. Azimov et al.: Leningrad Nuclear Physics Inst., Report No. 245, 1976
    C.H. Llewellyn-Smith: Heavy Leptons, Oxford Report No. 33/76, and Proc. Royal Society, London, 1976
69. W. Braunschweig et al.: Phys. Lett. 63B, 471 (1976)
70. R. Brandelik et al.: Phys. Lett. 70B, 125 (1977)
71. R. Brandelik et al.: Phys. Lett. 70B, 387 (1977)
72. A. Ali and T.C. Yang: Phys. Lett. 65B, 275 (1977)
73. J. Burmester et al.: Phys. Lett. 66B, 395 (1977)
74. R. Brandelik et al.: Phys. Lett. 67B, 363 (1977)
75. J. Burmester et al.: Phys. Lett. 67B, 367 (1977)
76. J. Burmester et al.: Phys. Lett. 64B, 369 (1976)
77. G. Goldhaber et al.: Phys. Rev. Lett. 37, 255 (1976)
78. I. Peruzzi et al.: Phys. Rev. Lett. 37, 569 (1976)

79. H.F. W. Sadrozinski: 1977 Hamburg Symp. (Ref. 3), p. 47

80. C. Quigg and J.L. Rosner: FERMILAB-PUB-77/60-THY (1977)

81. S. Yamada: 1977 Hamburg Symp. (Ref. 3), p. 69

82. E. Eichten et al.: to be published in Phys. Rev. (see Rev. 83)

83. K. Gottfried: 1977 Hamburg Symp. (Ref. 3), p. 667

84. H. Schopper: Lectures at Erice School 1977; DESY Report 77/79 (1978)

85. J. Ellis: Lectures at Cargèse Summer Inst. and at Kupari-Dubrovnik School 1977; CERN Report TH. 2365 (1977)

86. Y.S. Tsai: Phys. Rev. D4, 2821 (1971)
H.B. Thacker and J.J. Sakurai: Phys. Lett. 36B, 103 (1971)
J.D. Bjorken and C.H. Llewellyn-Smith: Phys. Rev. D7, 887 (1973)
K. Fuyikawa and N. Kawamoto: DESY 76/01
K.J.F. Graemers and R. Raito: SLAC-PUB-1727 (1976)

87. U. Timm: Proc. European Conf. on Particle Physics, Budapest, 1977; DESY Report 77/52 (1977)

88. M.L. Perl et al.: Phys. Rev. Lett. 35, 1489 (1975)
M.L. Perl et al.: Phys. Lett. 63B, 466 (1976)

89. M. Cavalli-Sforza et al.: Phys. Rev. Lett. 36, 558 (1976)
G.J. Feldman et al.: Phys. Rev. Lett. 38, 117 (1976)
J. Burmester et al.: Phys. Lett. 66B, 395 (1977), and 68B, 297 (1977)
G. Flügge: Proc. V Intern. Conf. on Experimental Meson Spectroscopy, Boston, 1977; DESY Report 77/35 (1977)

90. M.L. Perl et al.: Phys. Lett. 70B, 487 (1977)

91. G. Knies: 1977 Hamburg Symp. (Ref. 3), p. 93

92. M.L. Perl: 1977 Hamburg Symp. (Ref. 3), p. 145

93. R. Brandelik et al.: Phys. Lett. 73B, 109 (1978)

94. A. Pais and S.B. Treiman: Phys. Rev. D14, 293 (1976)
S.-Y. Pi and A.I. Sanda: Phys. Rev. D14, 1772 (1976)
and Annals Phys. 106, 134 and 171 (1977)

95. T.W. Appelquist and H. Georgi: Phys. Rev. D8, 4000 (1973)
A. Zee: Phys. Rev. D8, 4038 (1973)

96. R. Brandelik et al.: Phys. 76B, 361 (1978)

97. S.W. Herb et al.: Phys. Rev. Lett. 39, 252 (1977)
W.R. Innes et al.: Phys. Rev. Lett. 39, 1240 (1977)

98. Ch. Berger et al.: to be published in Phys. Lett.;
DESY Report 78/21 (1978)
C.W. Darden et al.: to be published in Phys. Lett.;
DESY Report 78/22 (1978)

99. D. Buchholz et al.: Proc. 1974 PEP Summer Study, SLAC, Stanford, 1974, p. 283

100. Proc. 1974 and 1975 PEP Summer Studies, SLAC, Stanford

101. PETRA Proposal 76/13

102. PETRA Proposal 76/14

103. PETRA Proposals 76/15 and 76/18

104. PETRA Proposal 76/16

105. PETRA Proposal 76/19

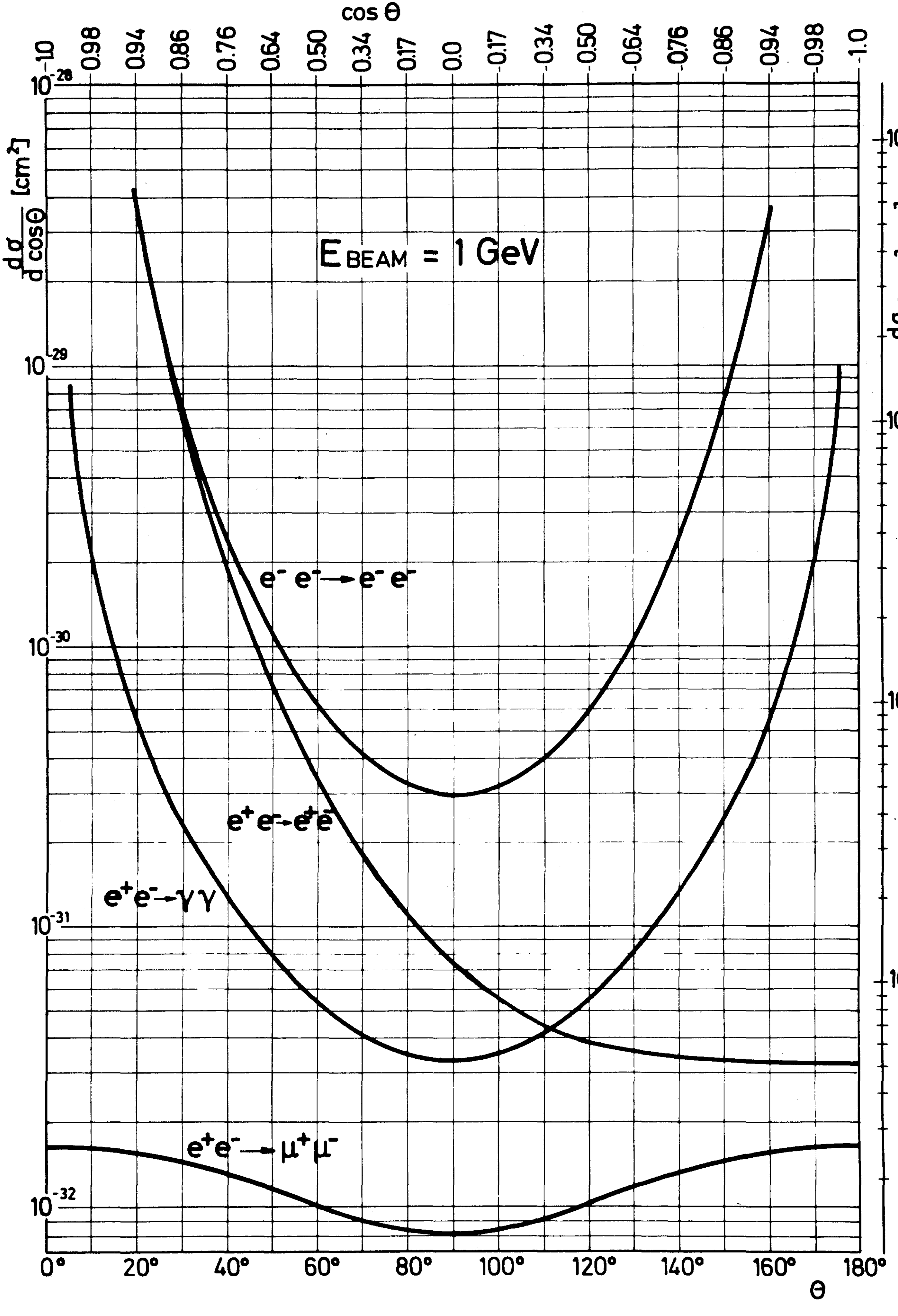

DESY 25658

Fig. 2.1 Differential cross sections of the indicated processes at beam energies of 1 GeV.

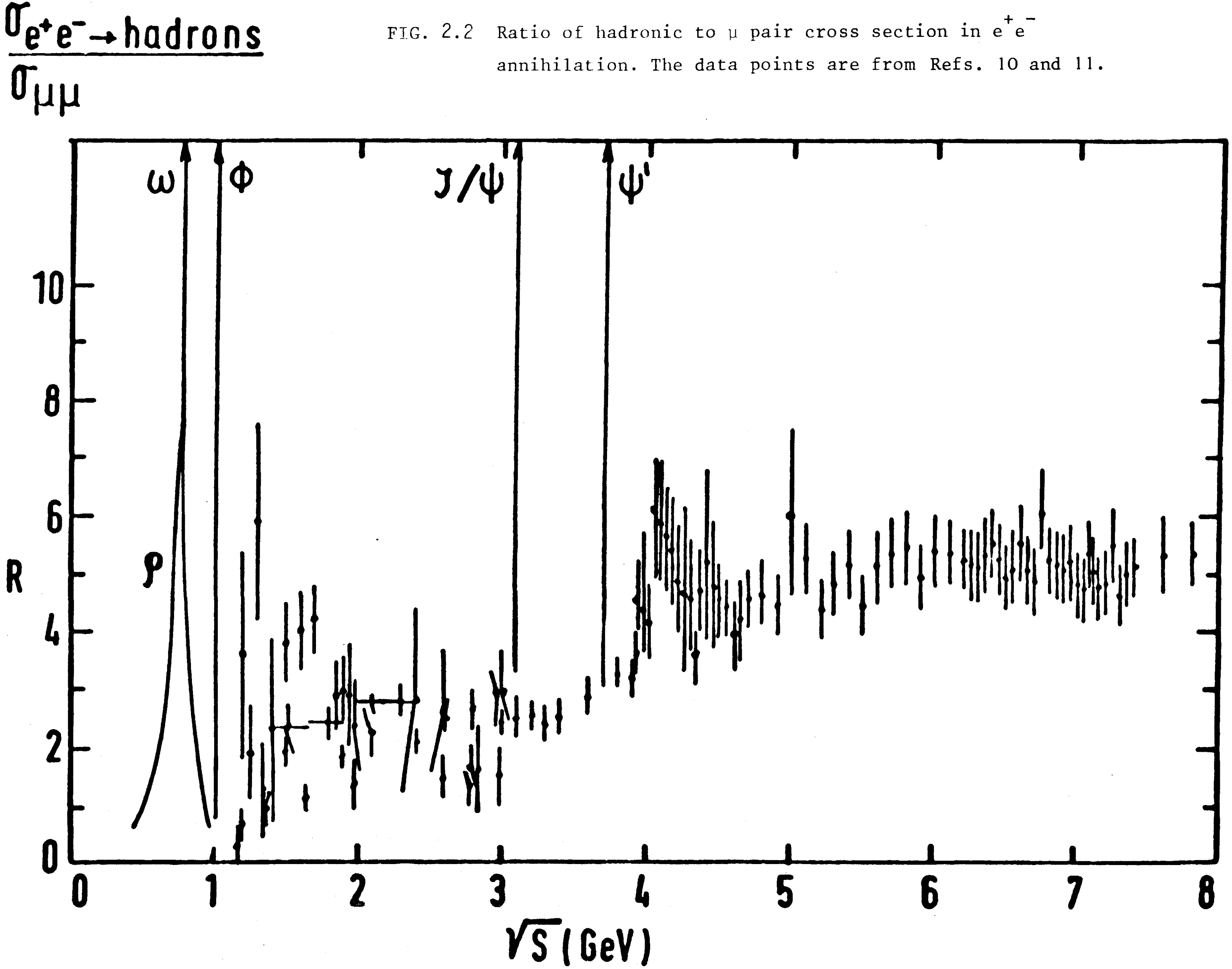

FIG. 2.2 Ratio of hadronic to μ pair cross section in e^+e^- annihilation. The data points are from Refs. 10 and 11.

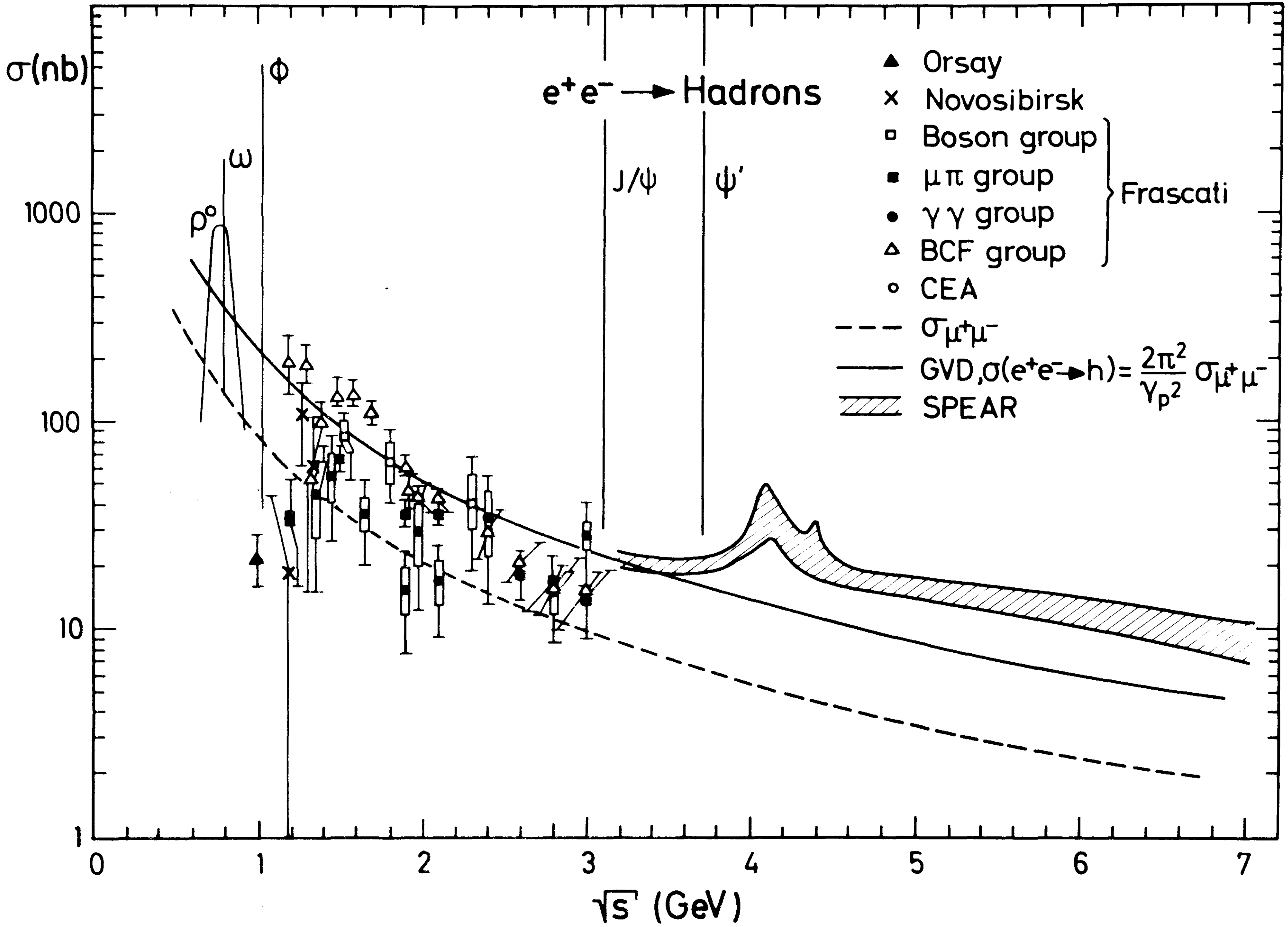

Fig. 2.3 Total cross section for $e^+e^- \rightarrow$ hadrons (Refs. 10, 11, and 16).

DESY

25541

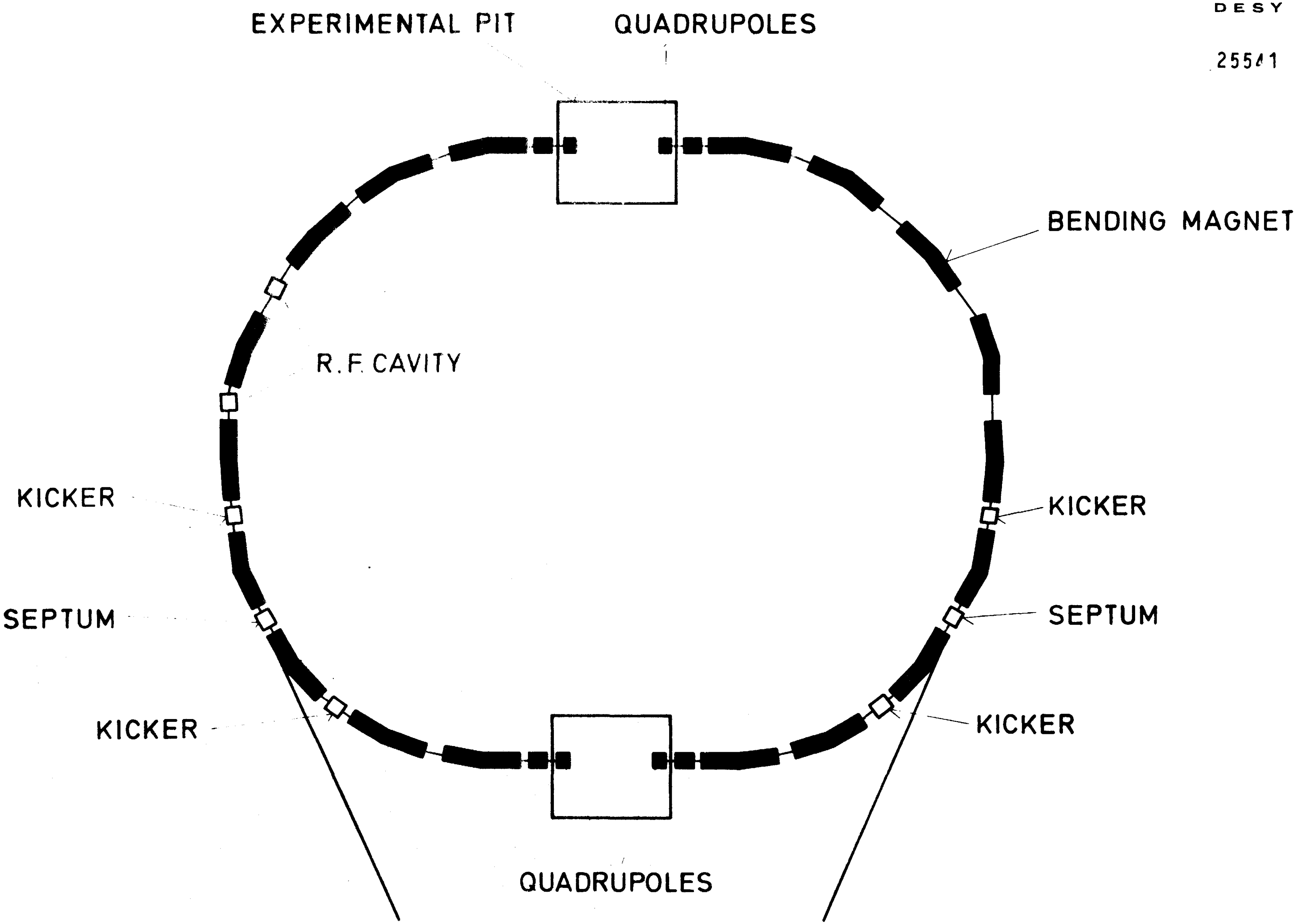

Fig. 3.1 Schematic layout of the storage ring SPEAR.

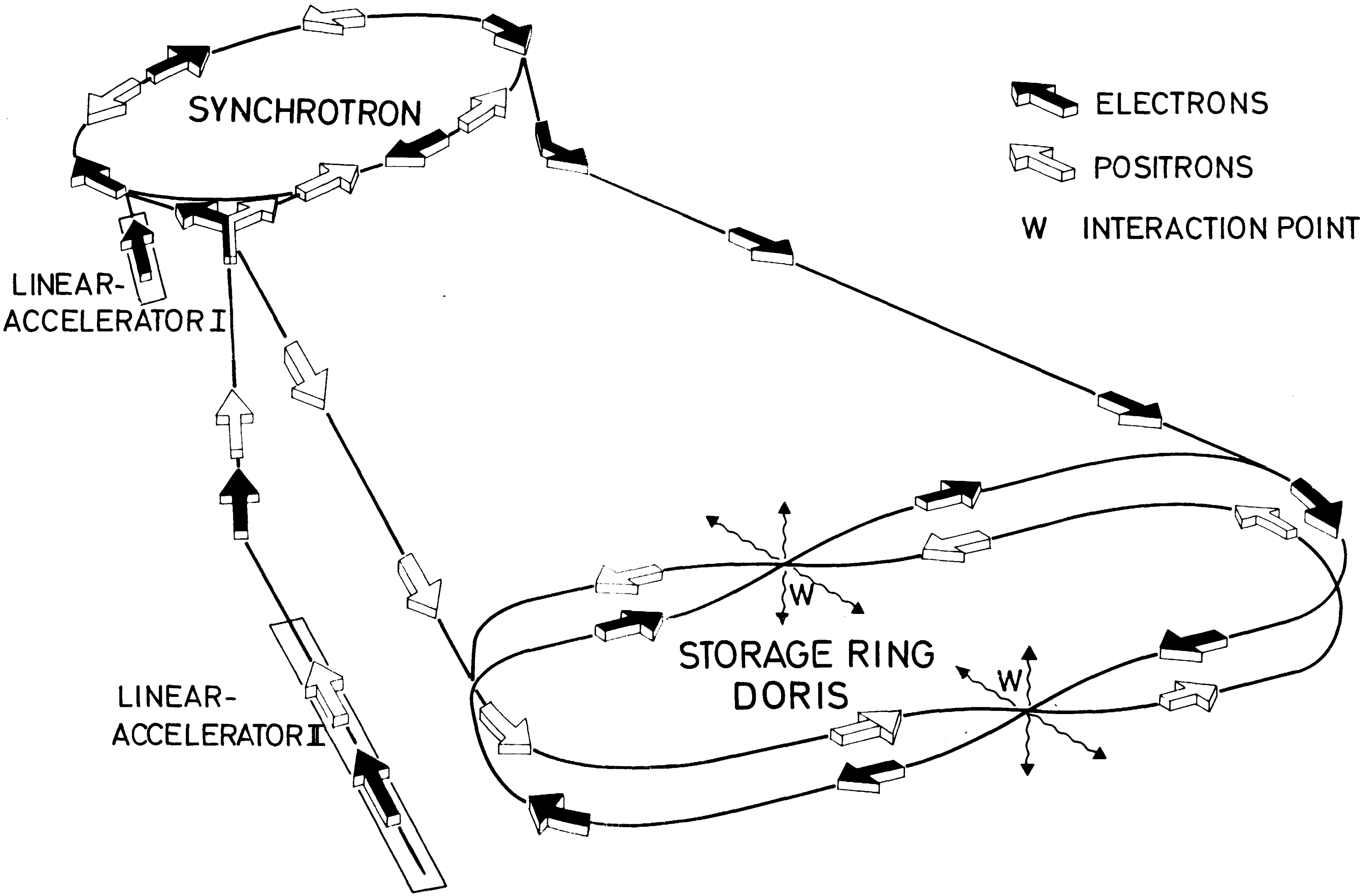

Fig. 3.2 Schematic view of the DORIS storage ring with its injection system.

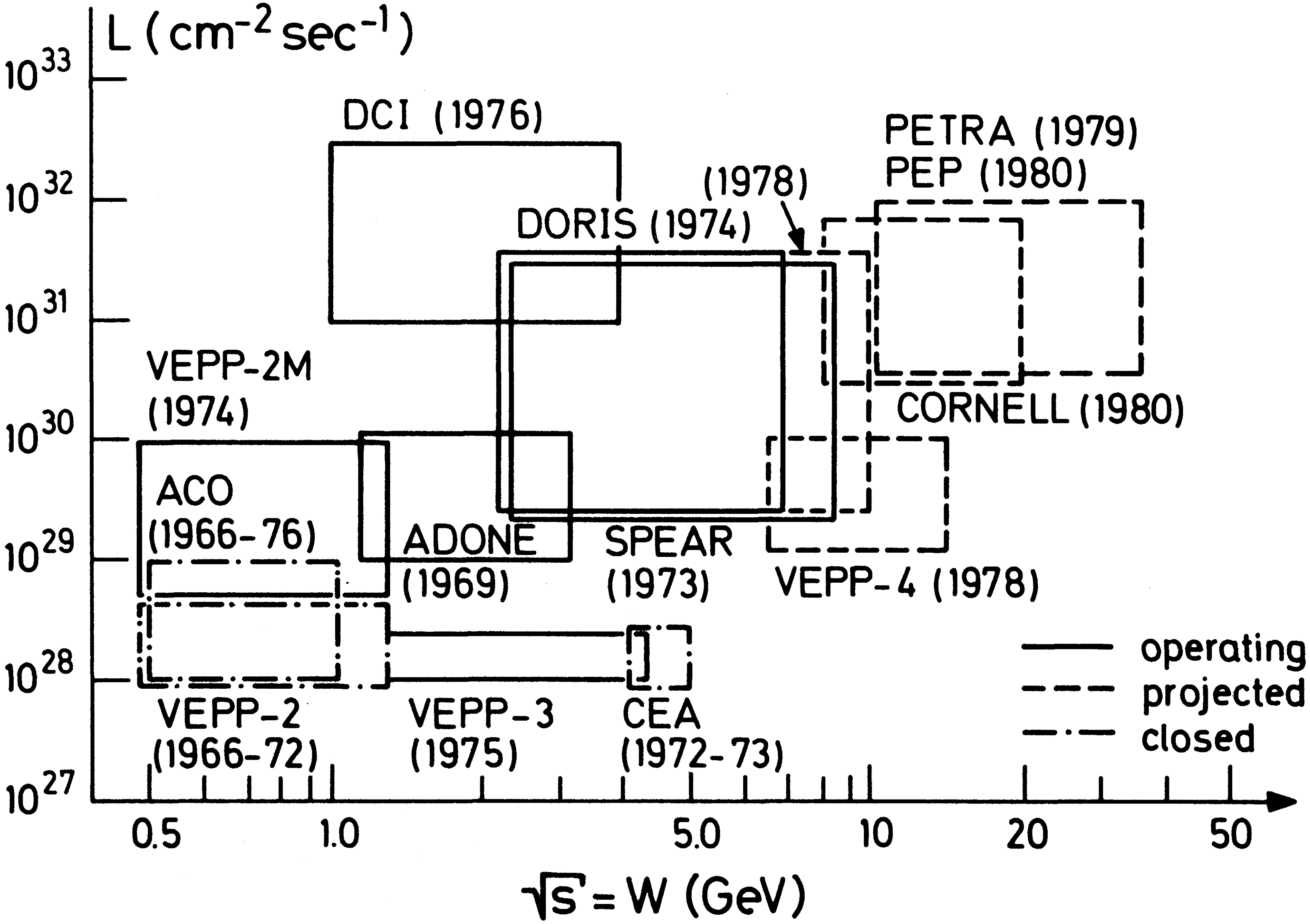

Fig. 3.3 Operating regions of various e^+e^- colliding beam devices. The indicated luminosities are approximate peak luminosities and do not represent the actual energy dependence.

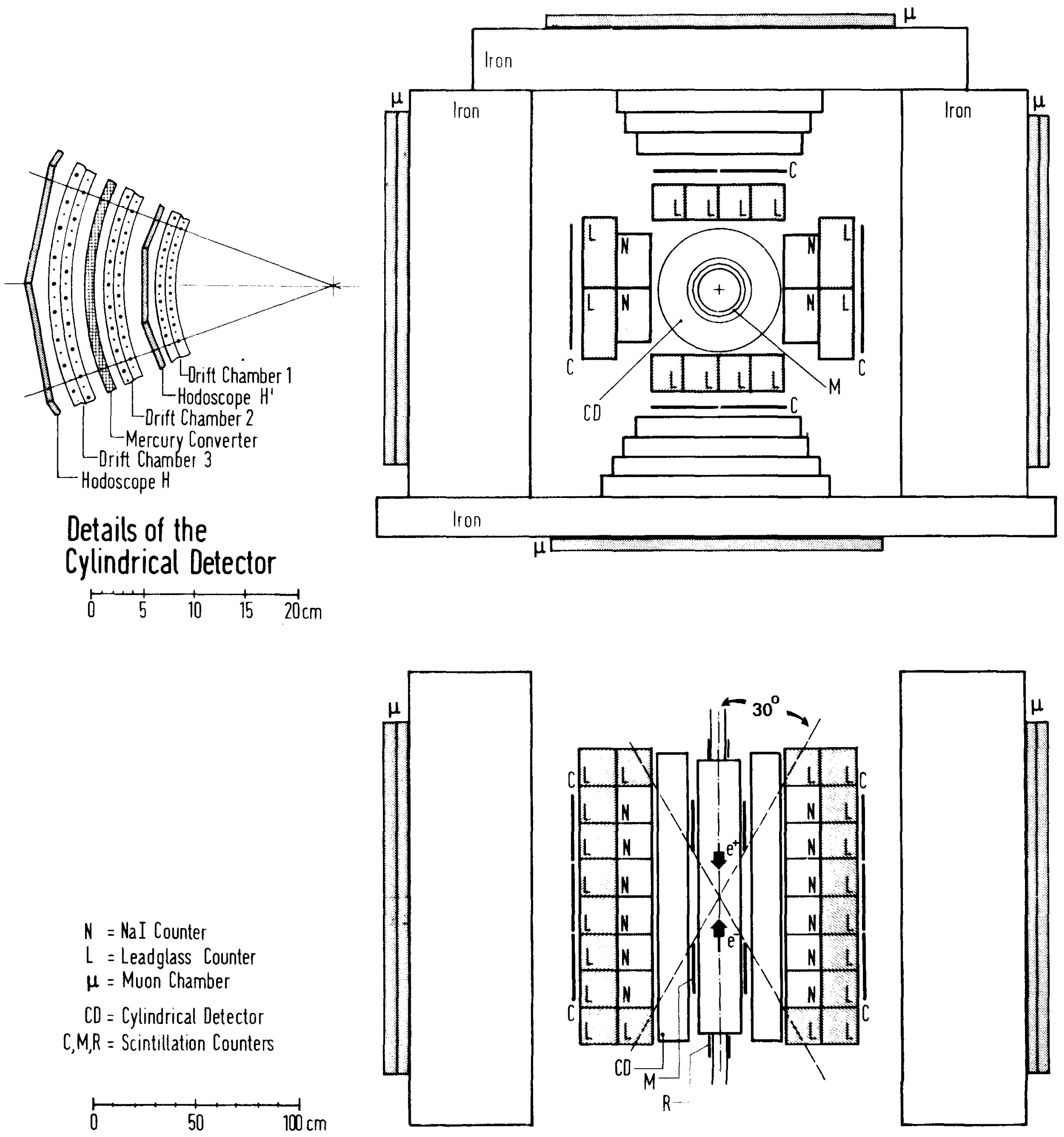

Fig. 4.1 The non-magnetic detector of the DESY-Heidelberg collaboration.

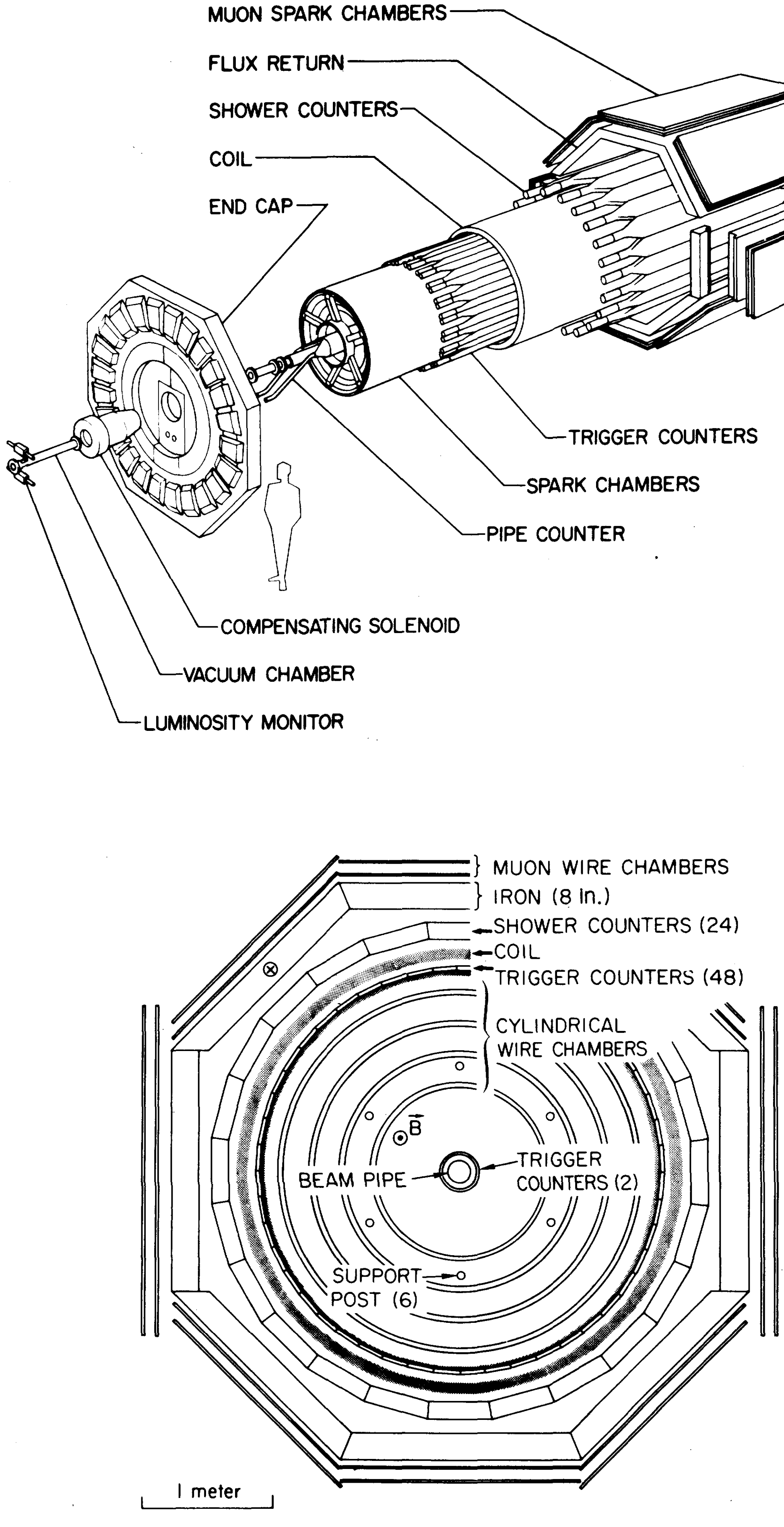

Fig. 4.2 The solenoid detector MARK I of the SLAC-LBL collaboration.

26751

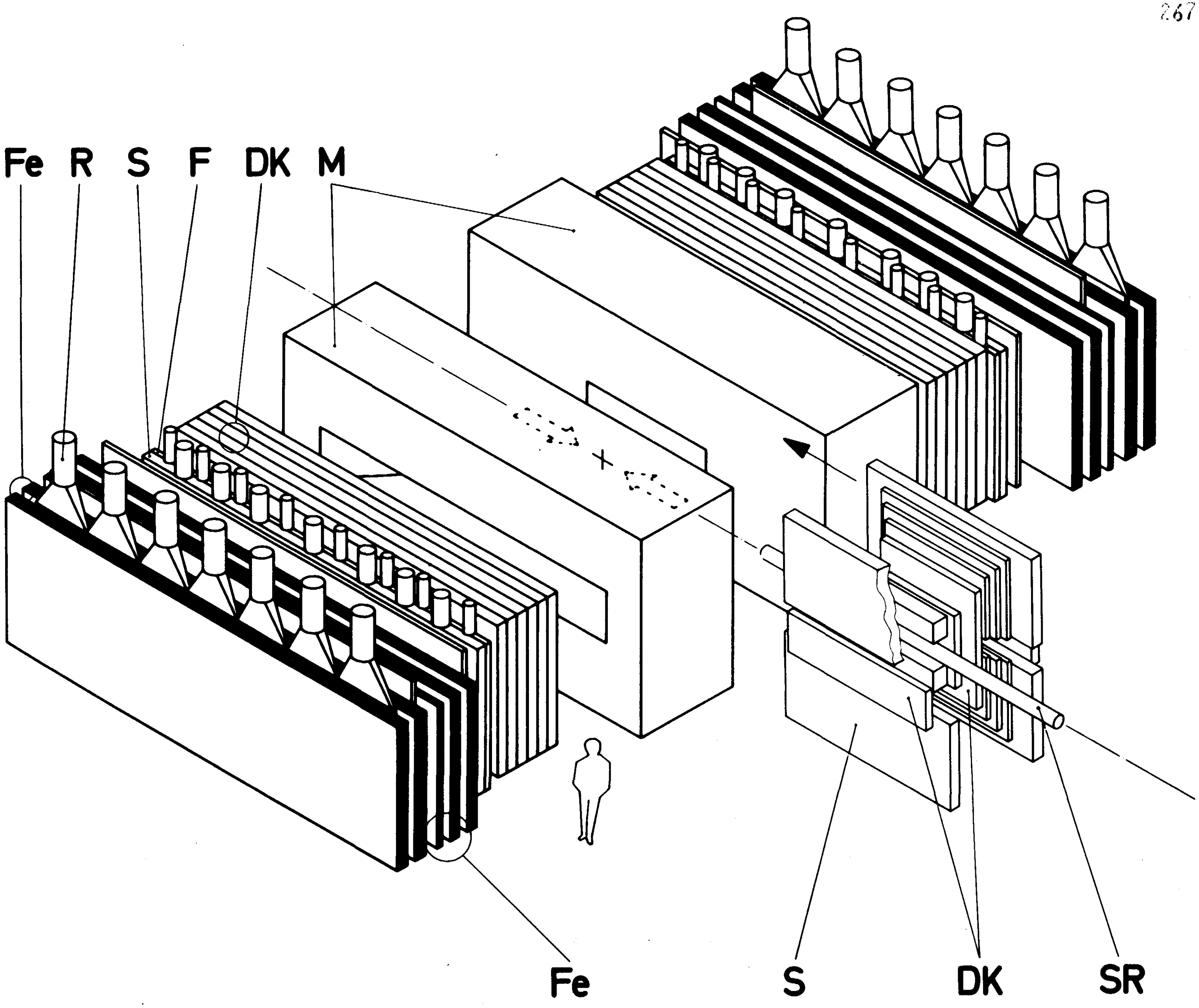

Fig. 4.3 Overall view of the double arm spectrometer DASP.

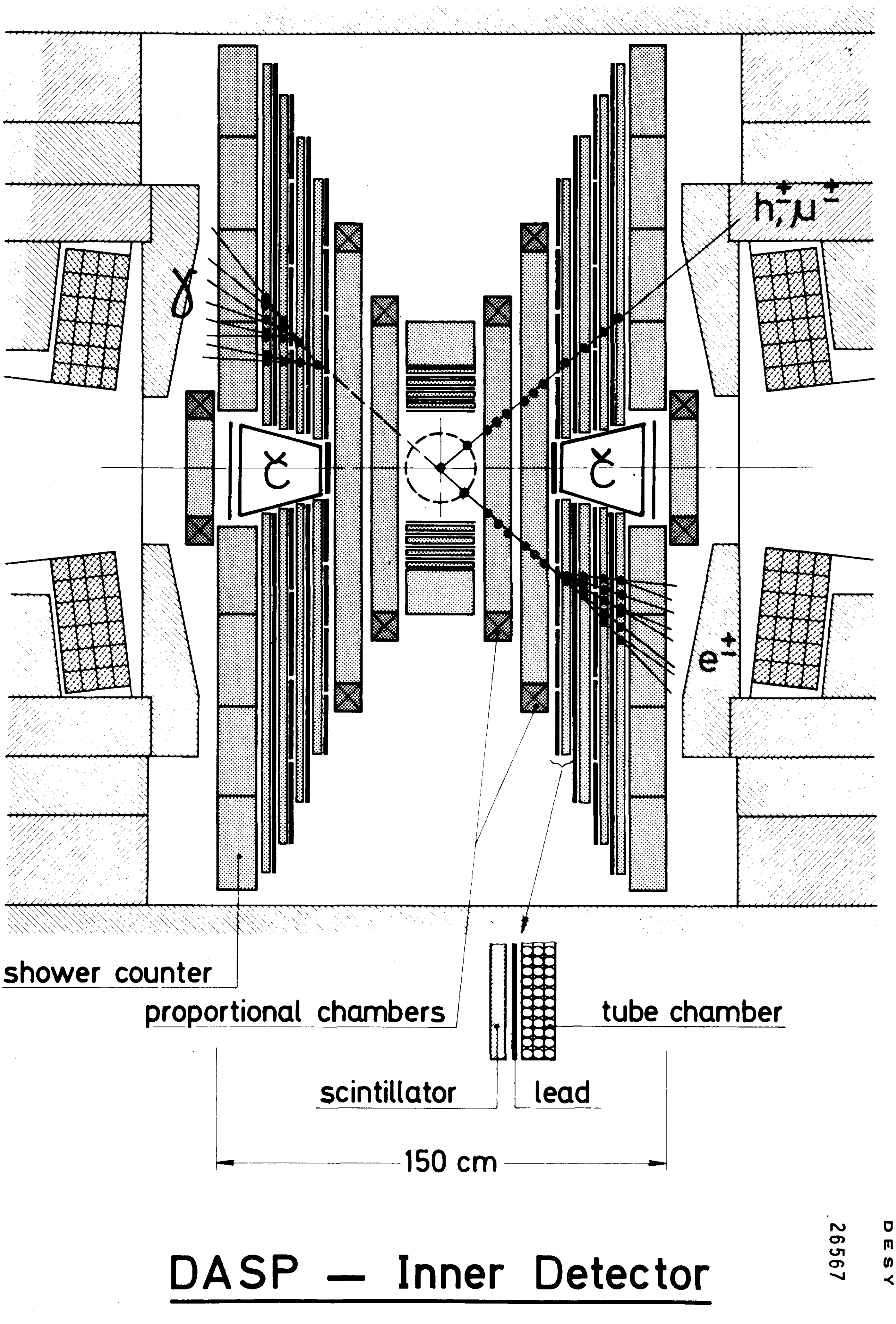

Fig. 4.4 The non-magnetic detector located between the two spectrometer arms of DASP.

BNL: Aubert et al.
28 GeV/c $pBe \rightarrow e^+e^-X$

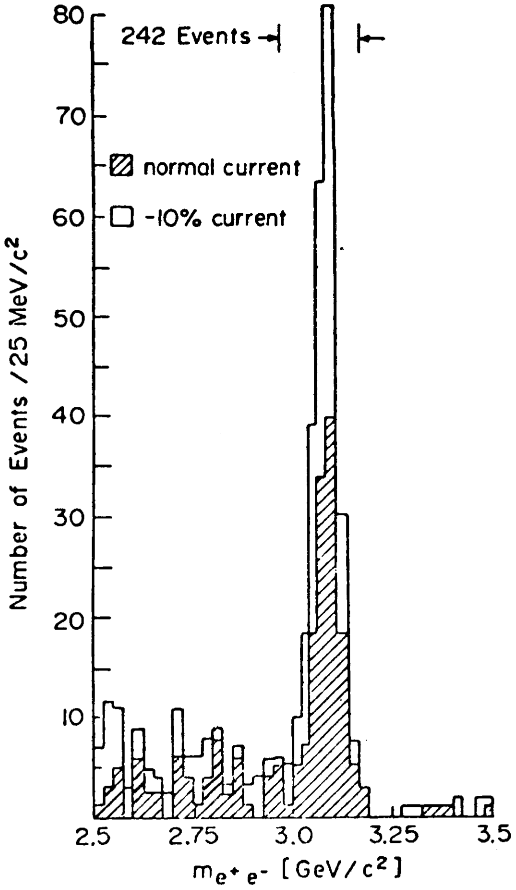

Fig. 5.1 Effective mass spectrum of the observed electron pairs.

SLAC: Boyarski et al.

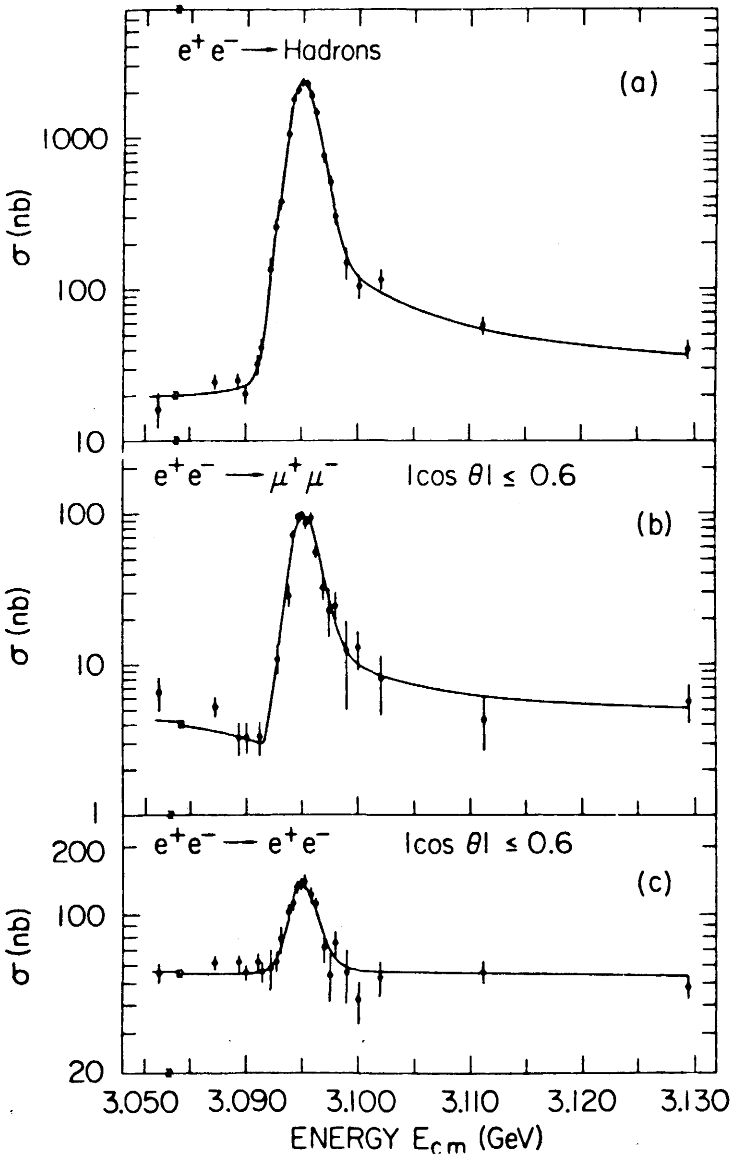

Fig. 5.2 Energy dependence of the cross sections for the indicated processes in the vicinity of the ψ.

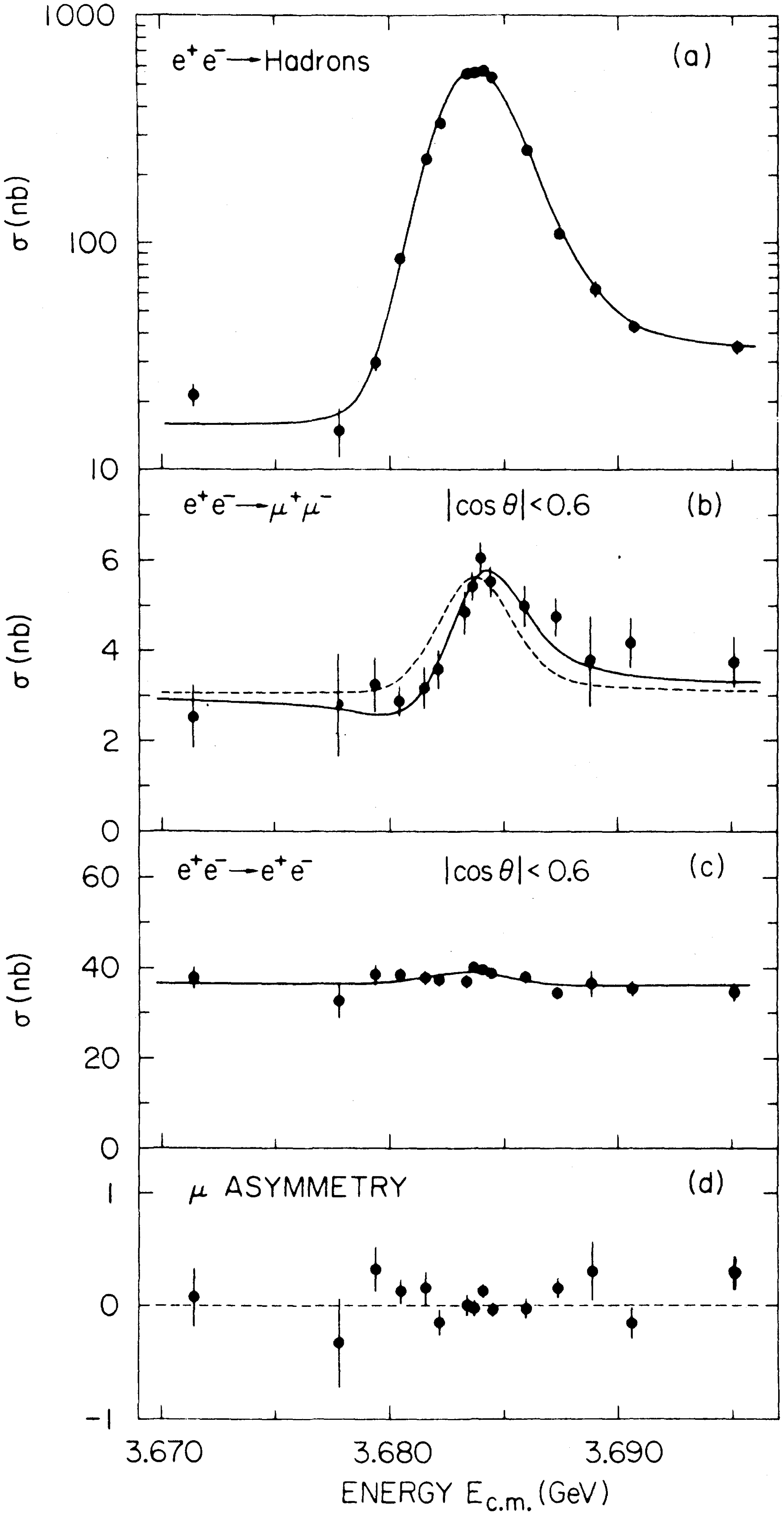

Fig. 5.3 Energy dependence of the cross sections for the indicated processes in the vicinity of the ψ'.

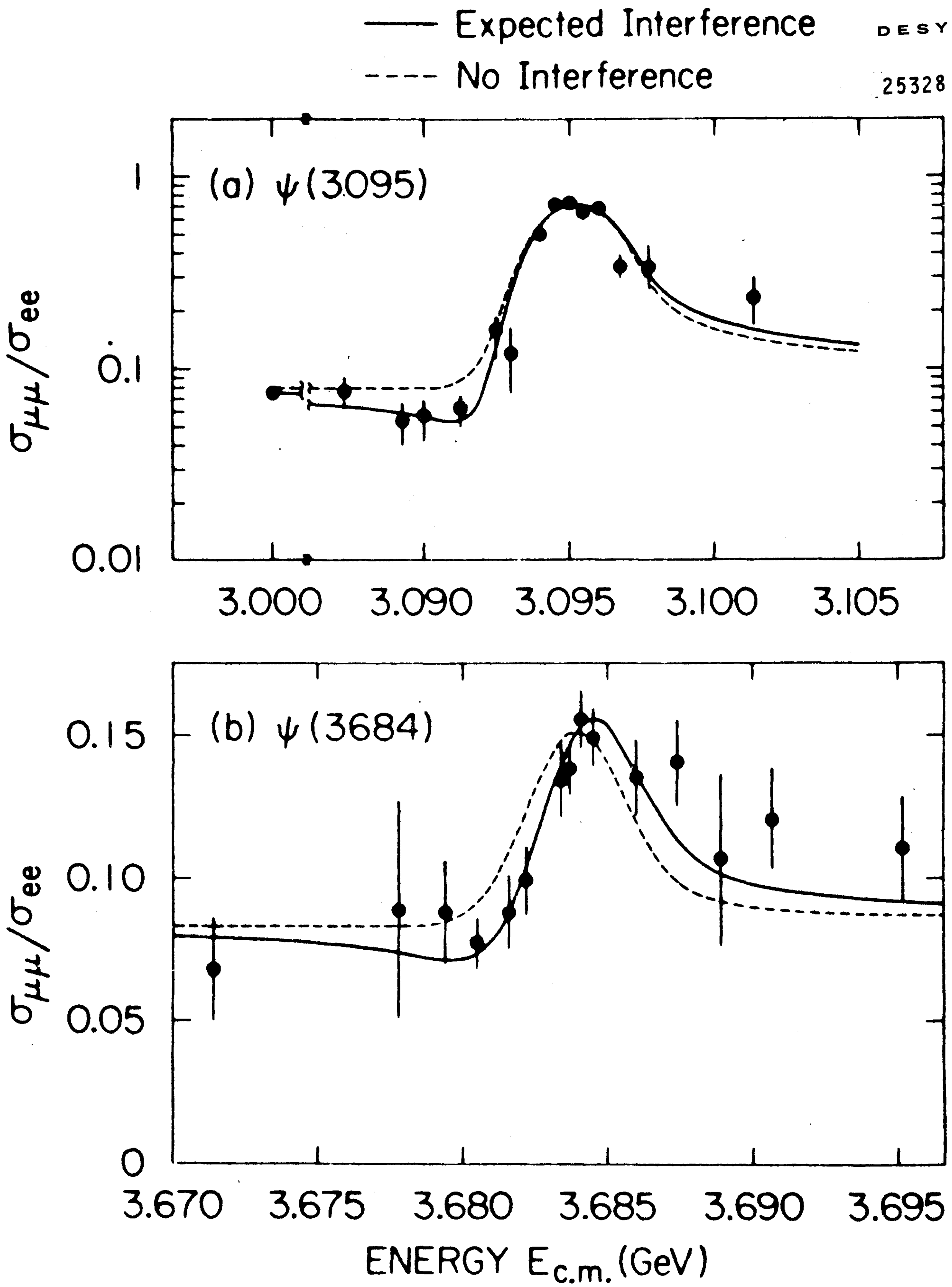

Fig. 5.4 Ratio of lepton pair cross sections for J/ψ and ψ' within the detector acceptance of MARK I.

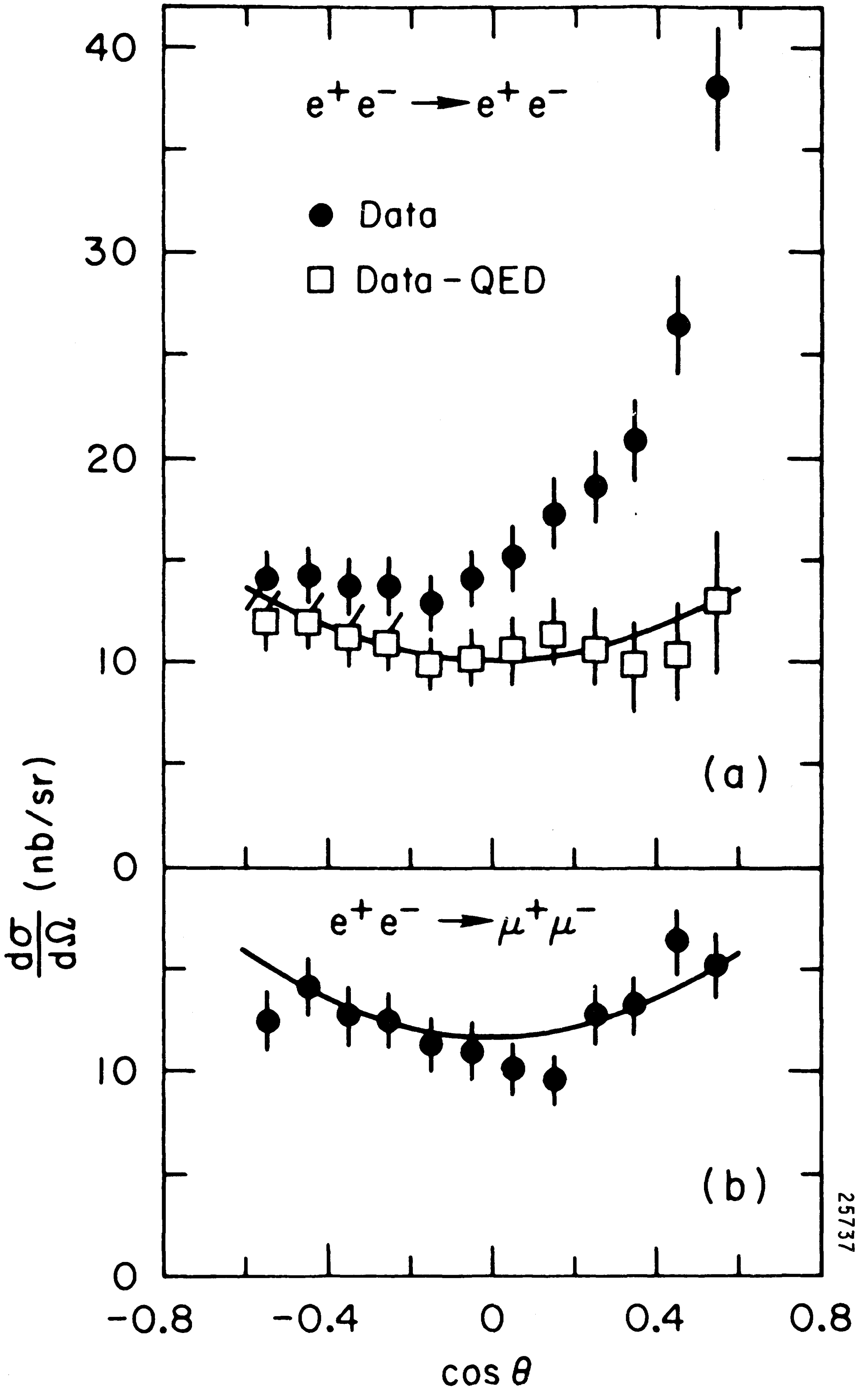

Fig. 5.5 Differential cross section for J/ψ production and decay into lepton pairs.

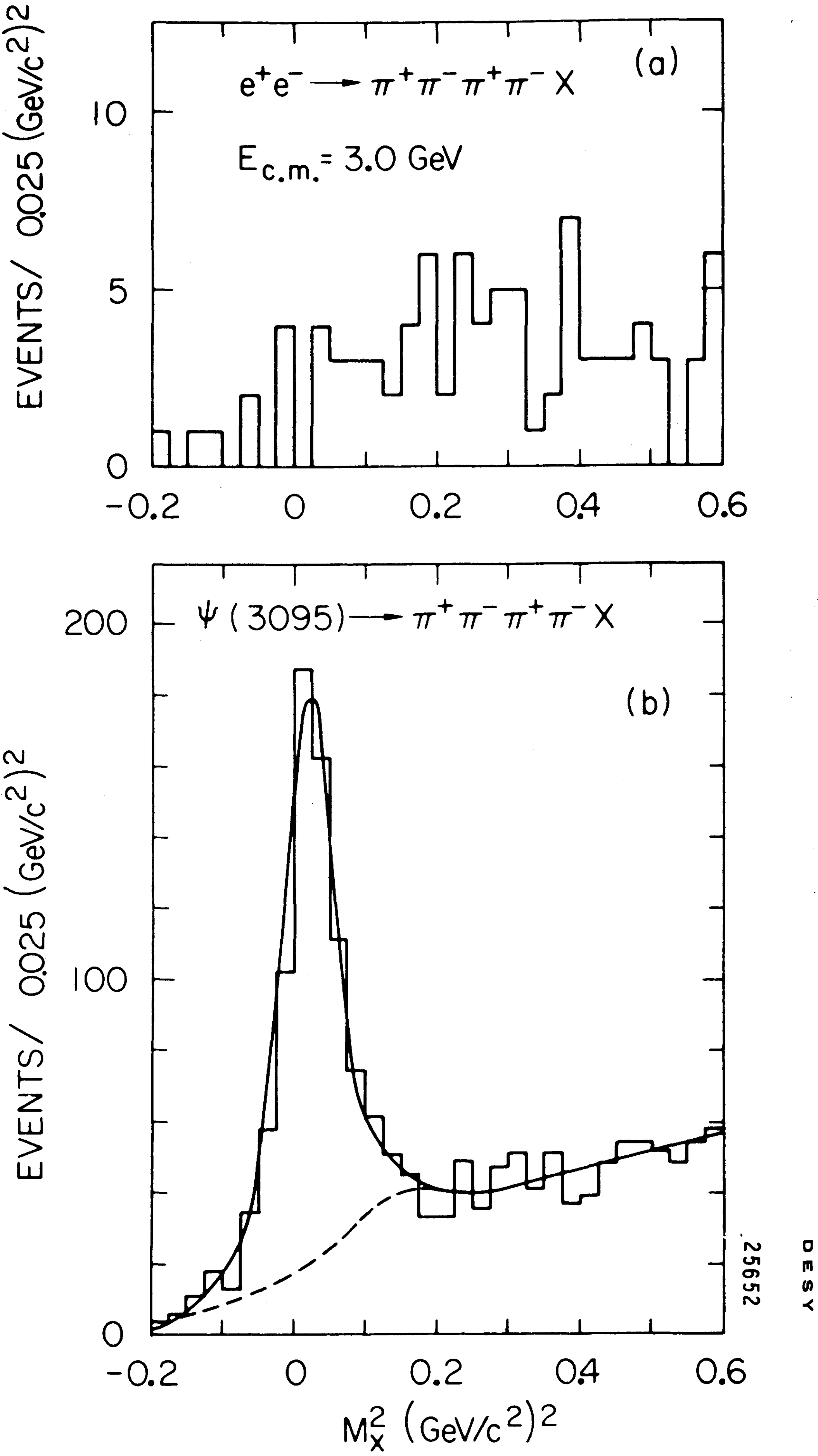

Fig. 5.6 Missing mass squared distribution of events with four charged tracks of total charge 0 and missing momentum < 0.2 GeV: (a) outside the J/ψ resonance, (b) at the J/ψ position.

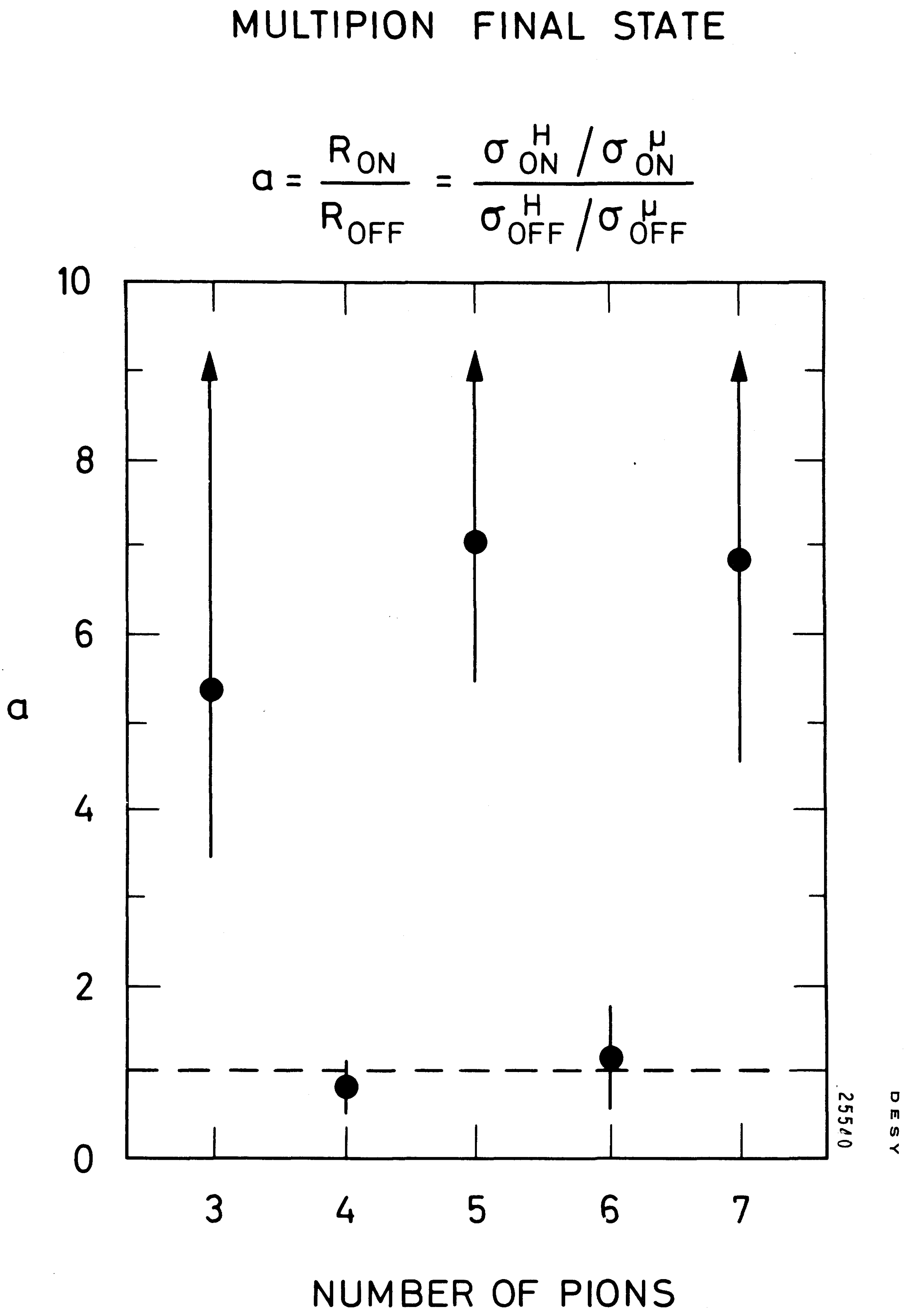

Fig. 5.7 Comparison of the ratio of multi-pion to μ pair cross section at the J/ψ (ON) and at 3 GeV (OFF).

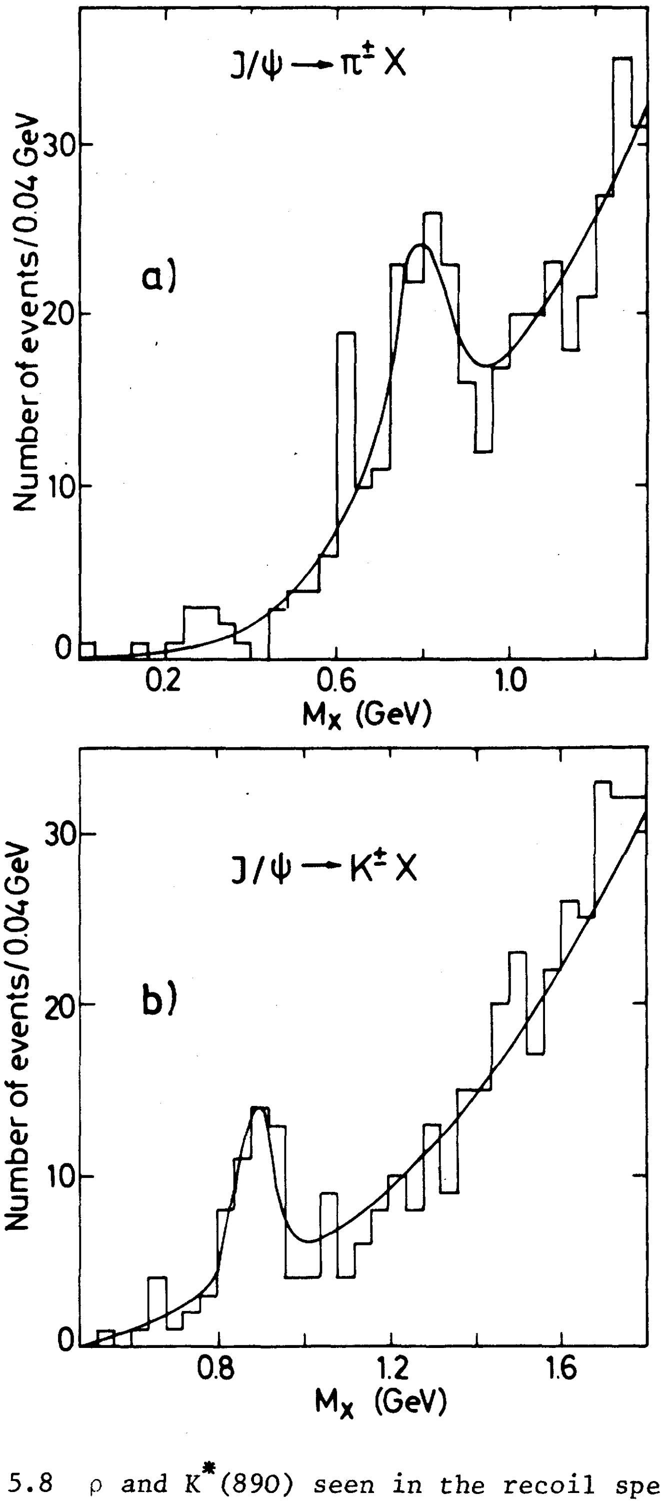

Fig. 5.8 ρ and $K^*(890)$ seen in the recoil spectrum of inclusive π and K measurements at the J/ψ.

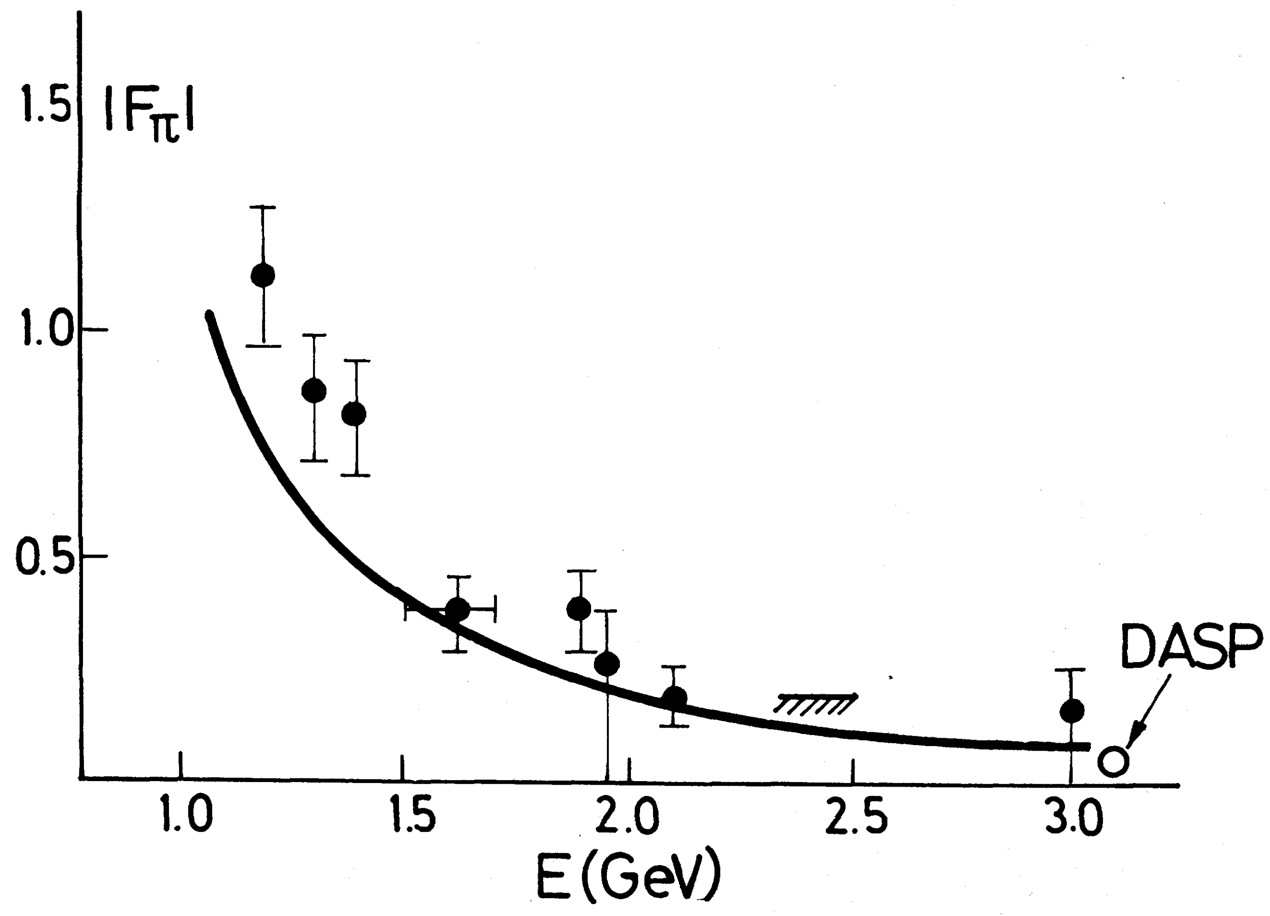

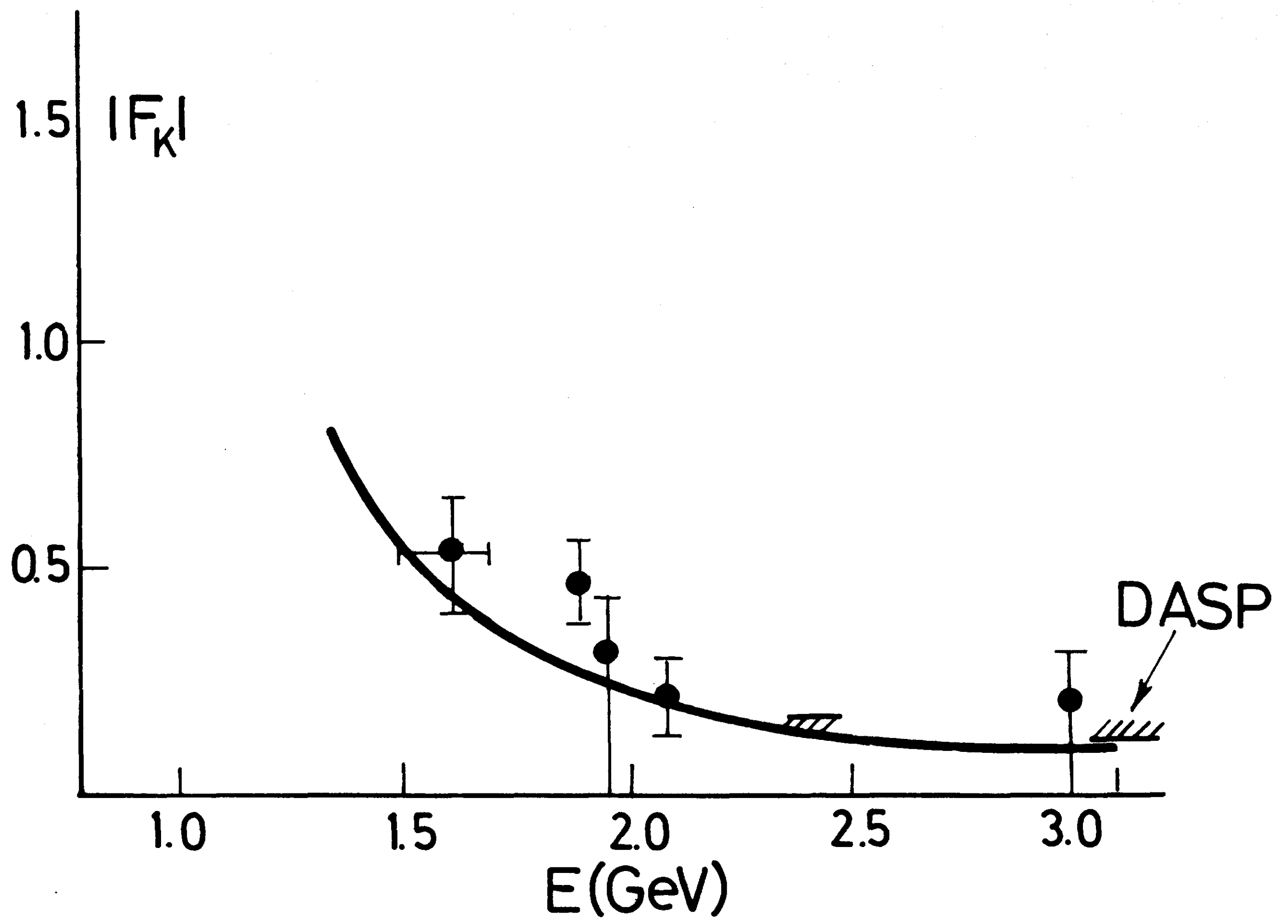

Fig. 5.9 π and K form factors as functions of the c.m. energy W in e^+e^- annihilation. The full circles and the curve are from Ref. 32.

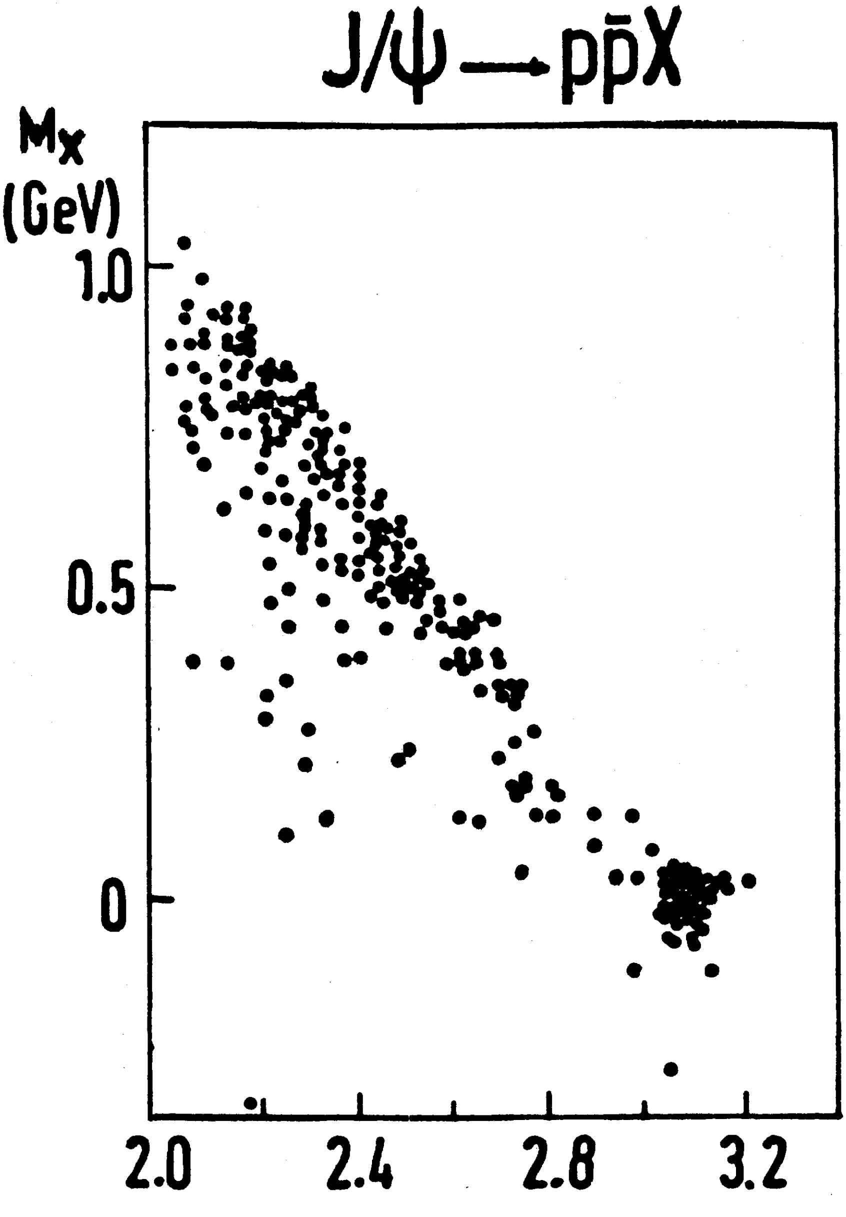

Fig. 5.10 Recoil mass M_x in the decay $J/\psi \rightarrow p\bar{p}X$ plotted versus the invariant mass $M_{p\bar{p}}$ of the $p\bar{p}$ system.

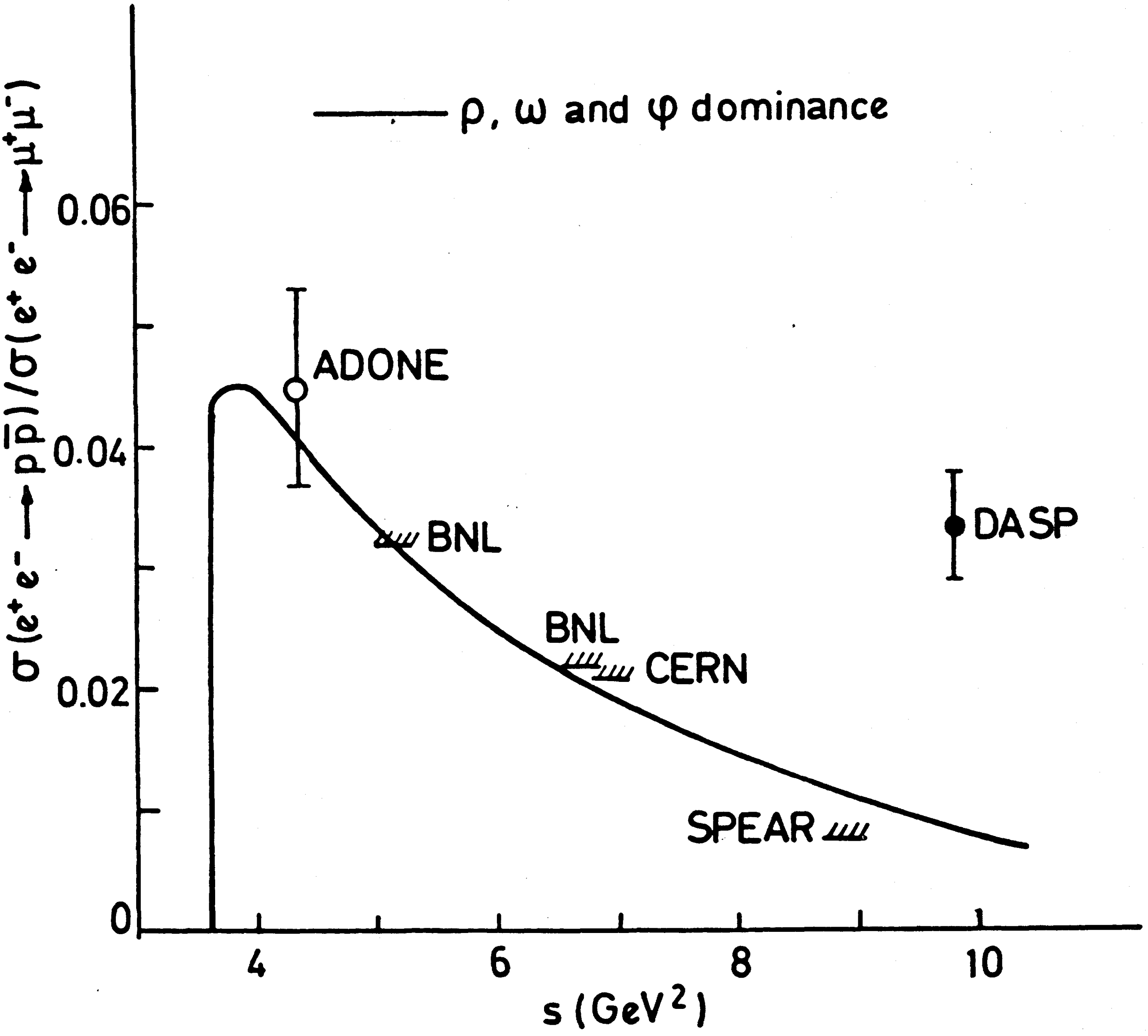

Fig. 5.11 Ratio of $p\bar{p}$ to μ pair cross section. The DASP point at the J/ψ exceeds the value, expected from the upper limits at lower energies (see Refs. 11 and 34) and from the form factor calculation (Ref. 35).

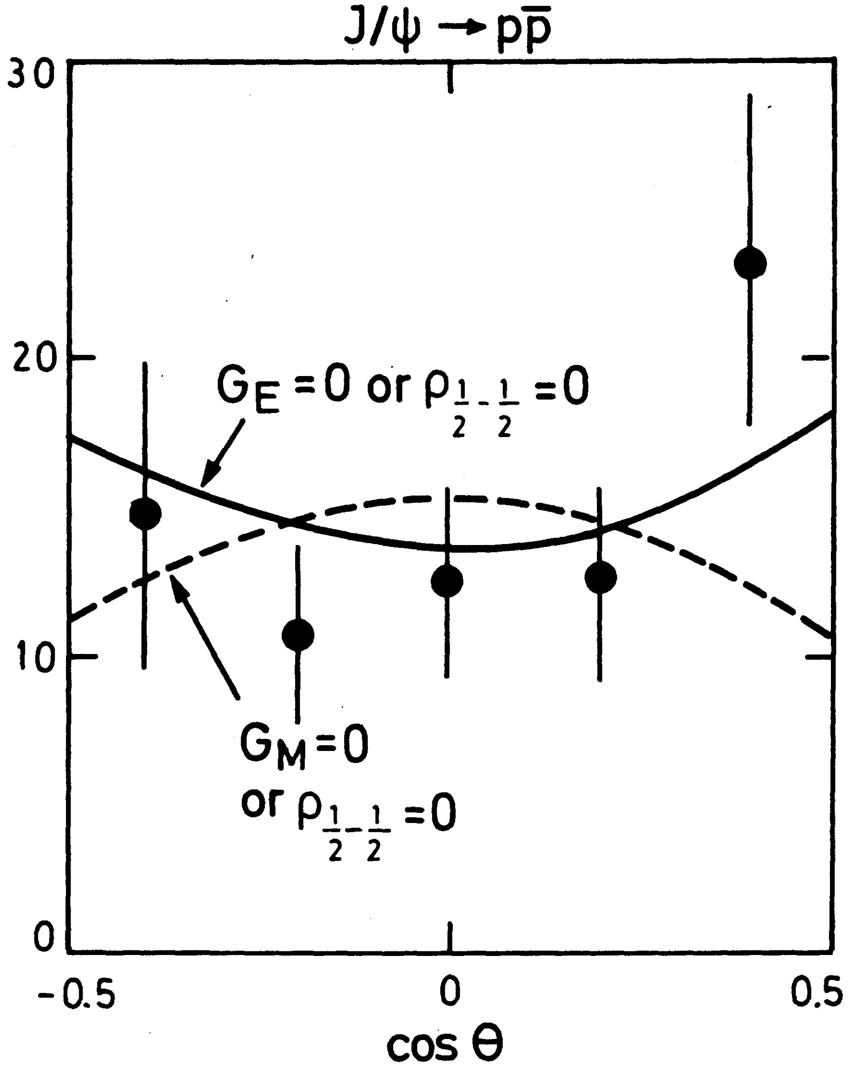

Fig. 5.12 Angular distribution of the decay $J/\psi \to p\bar{p}$. (G's and ρ's are explained in the text).

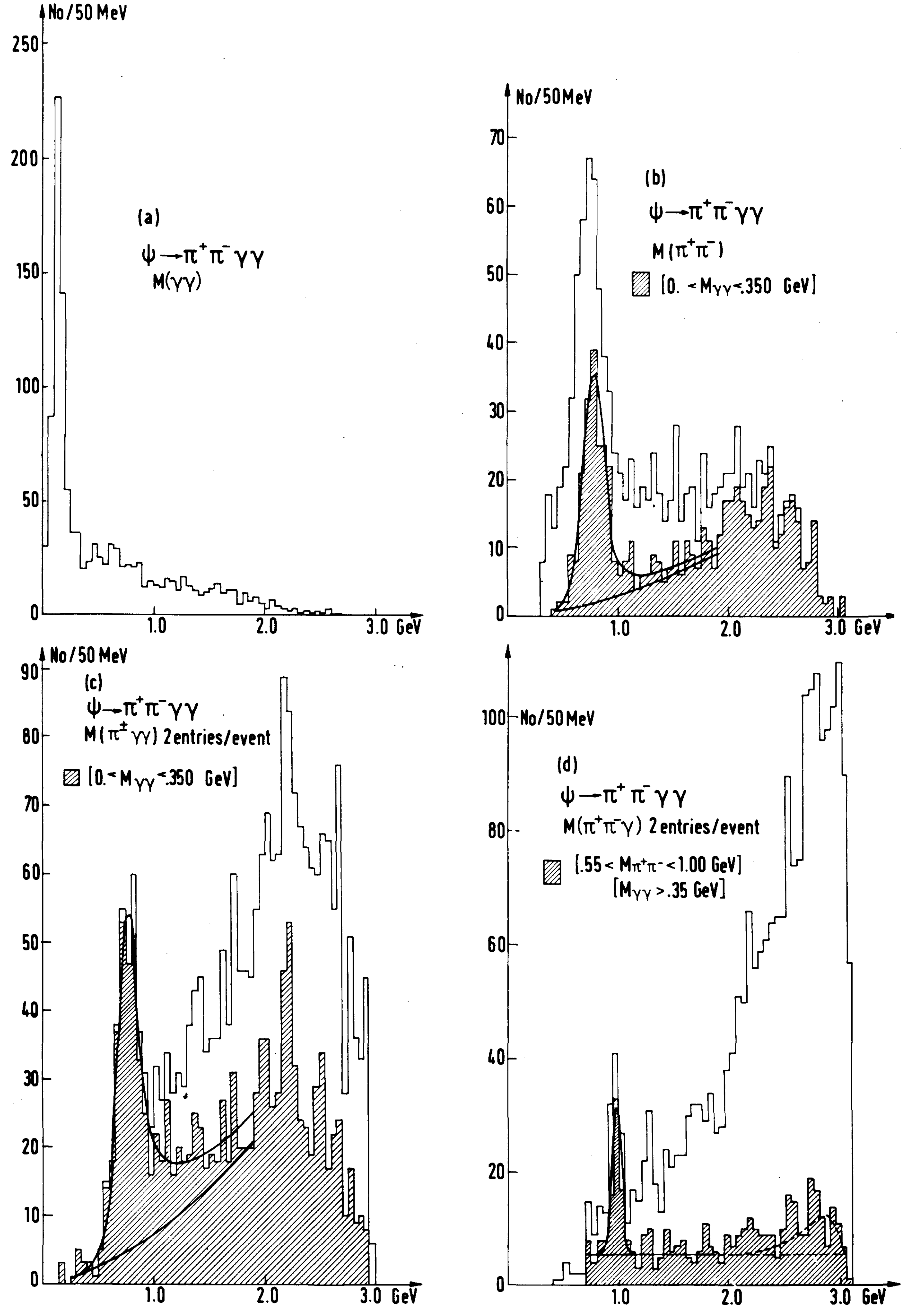

Fig. 5.13 Effective mass distributions of events with two charged tracks and two photons observed in the DESY-Heidelberg detector.

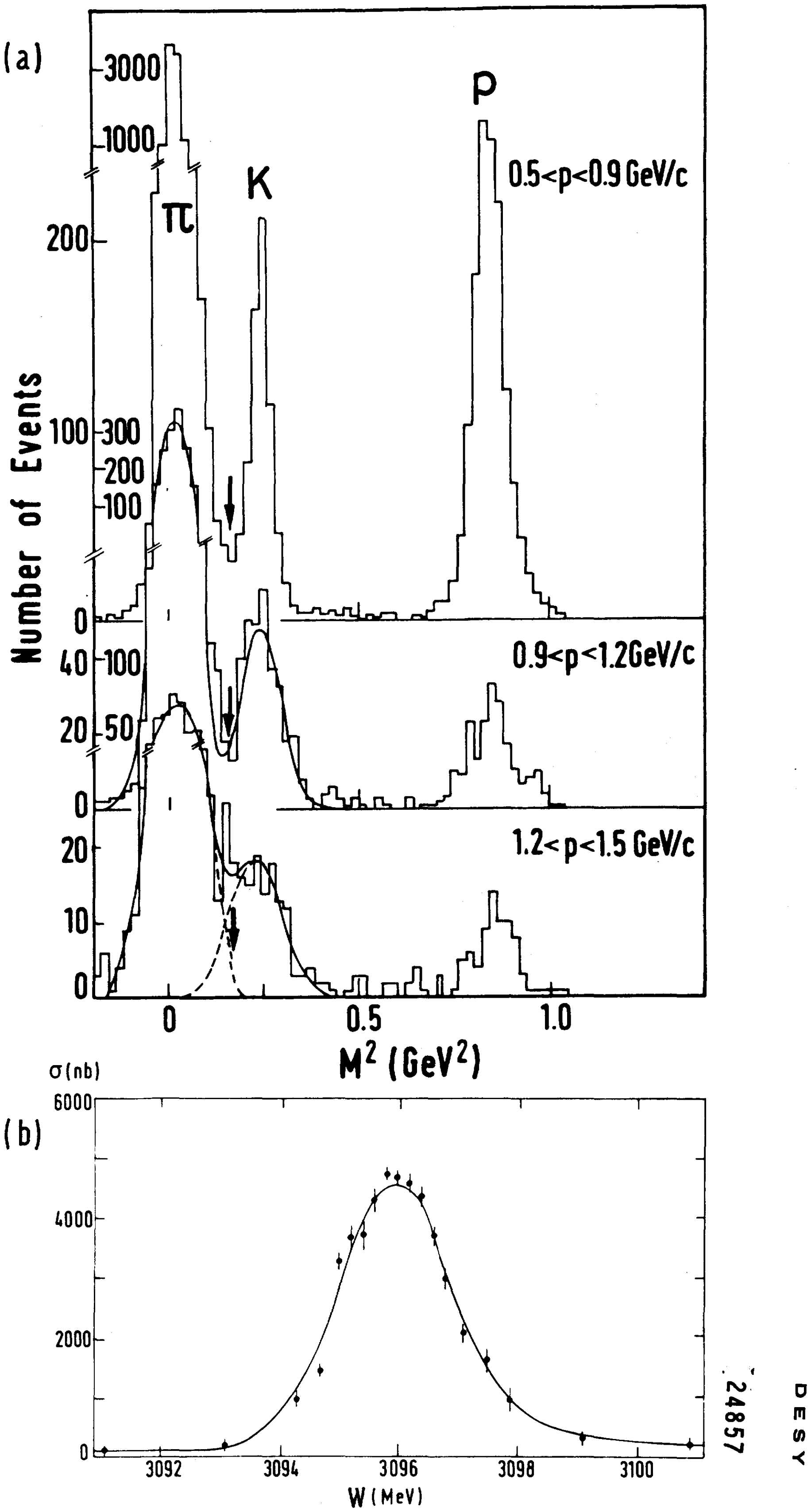

Fig. 5.14 a) π/K/p separation by time-of-flight in the DASP detector

b) Excitation curve of the J/ψ resonance as a function of the c.m. energy, obtained from inclusive measurements with DASP.

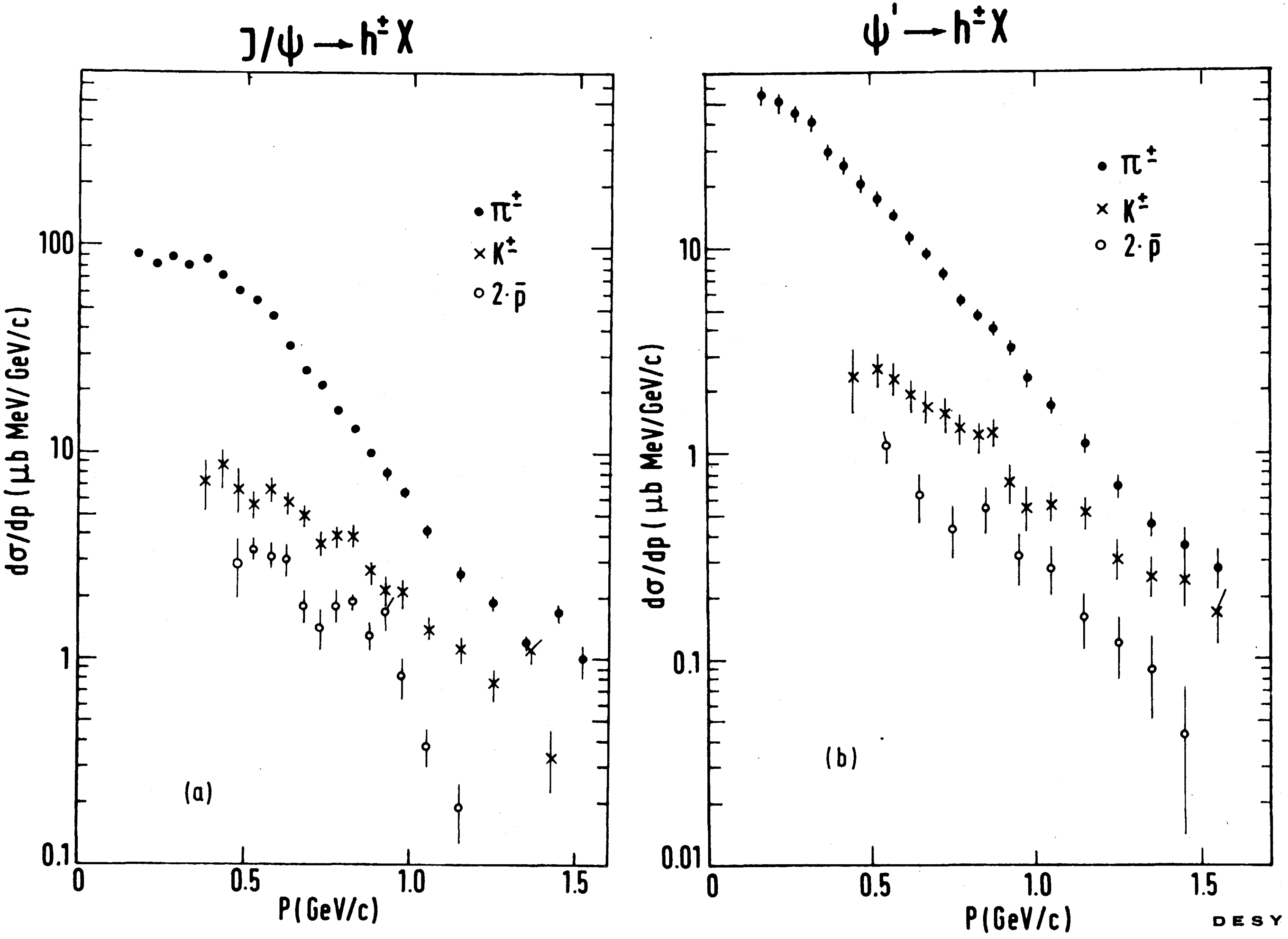

FIG. 5.15 Differential cross section for π, K, and p production as a function of the particle momenta at J/ψ and ψ'.

24856

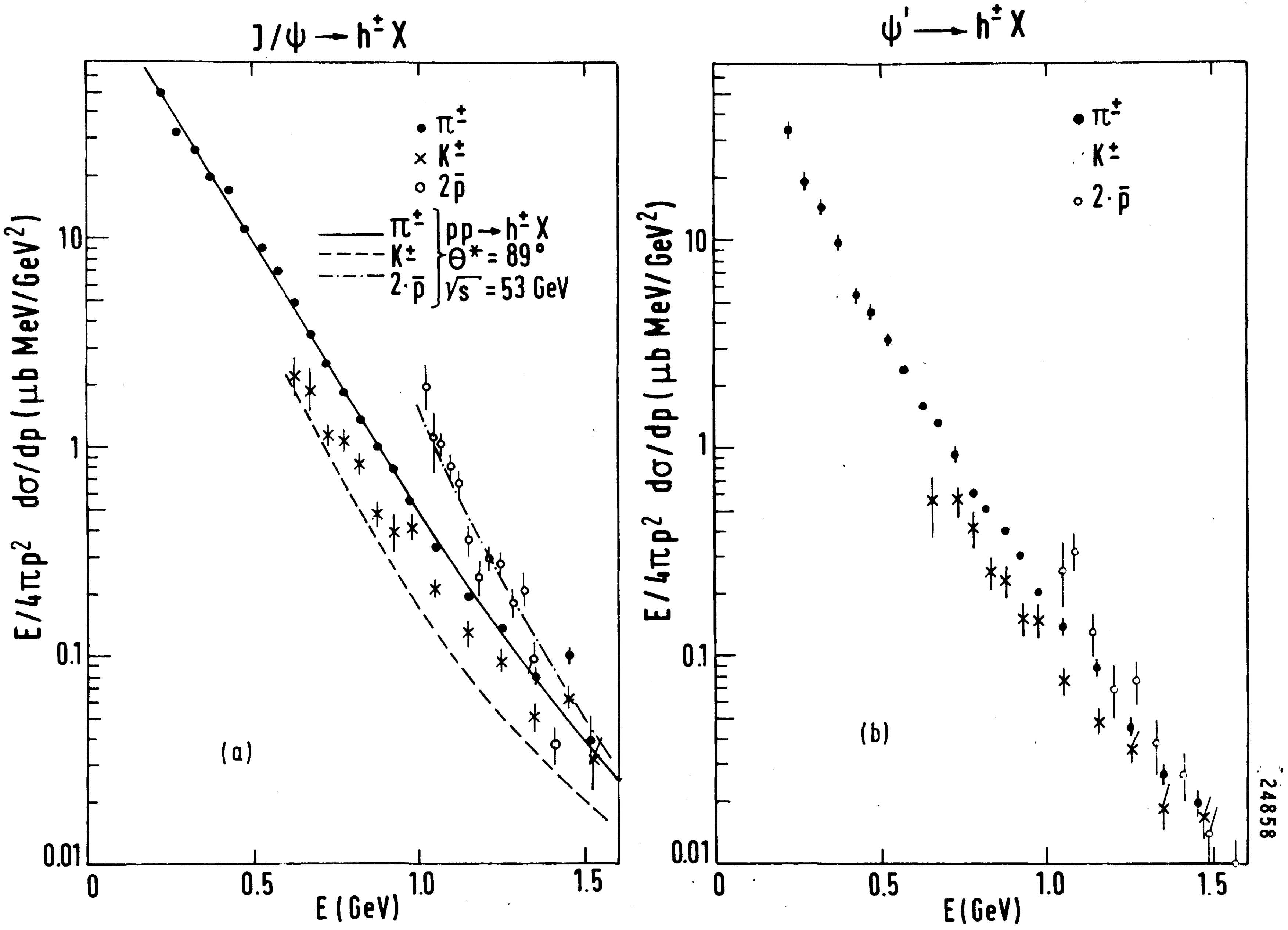

Fig. 5.16 Invariant cross sections as functions of the particle energies. The curves describe the inclusive particle yields from pp → $h^{\pm}$ X (see Ref. 42).

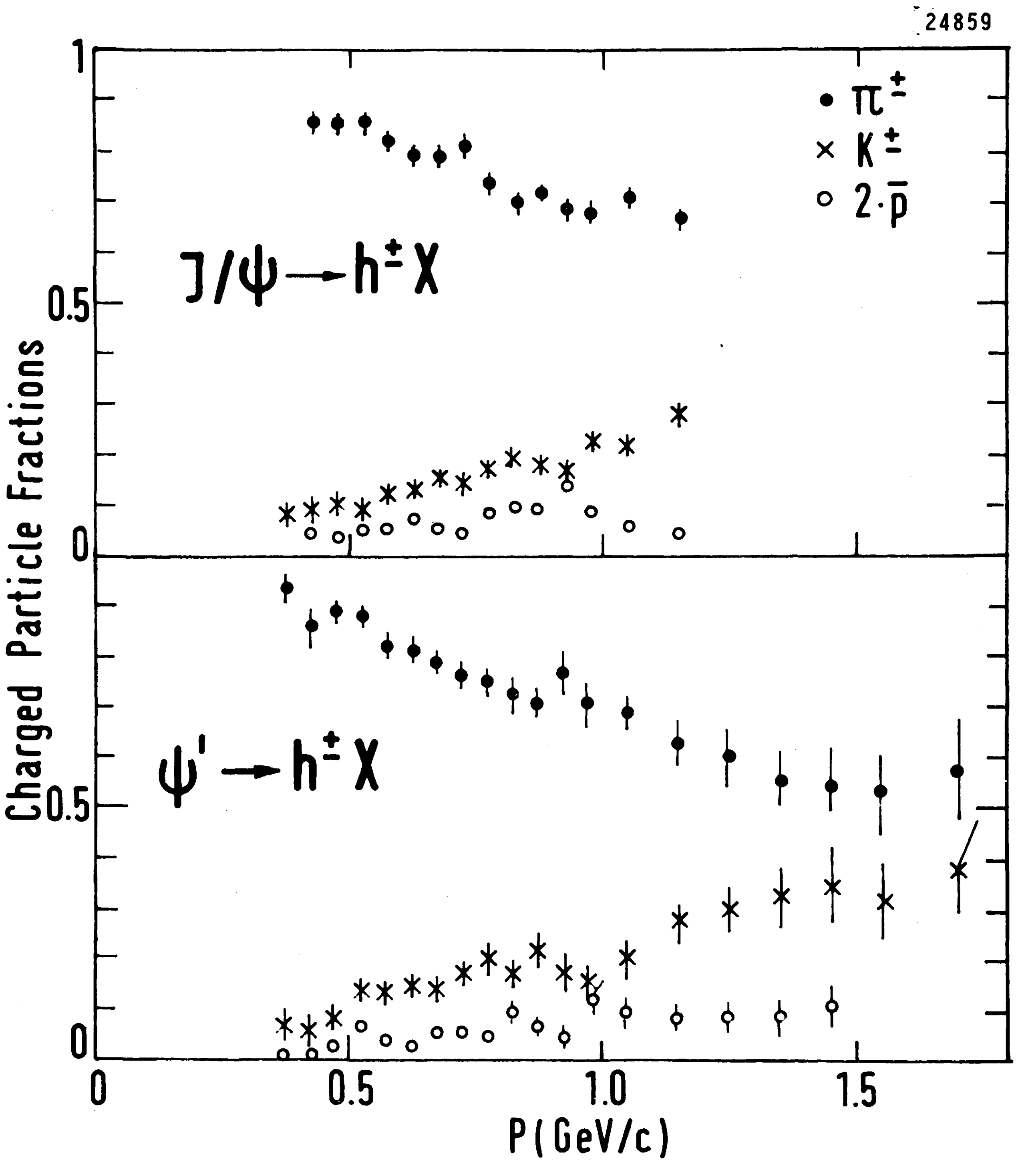

Fig. 5.17 Charged particle fractions at the J/ψ and ψ'.

charmonium level scheme

spectroscopic notation $n^{2S+1}L_J$

J^{PC} : $\vec{J} = \vec{S} + \vec{L}$

$P = -(-1)^L$

$C = (-1)^{L+S}$

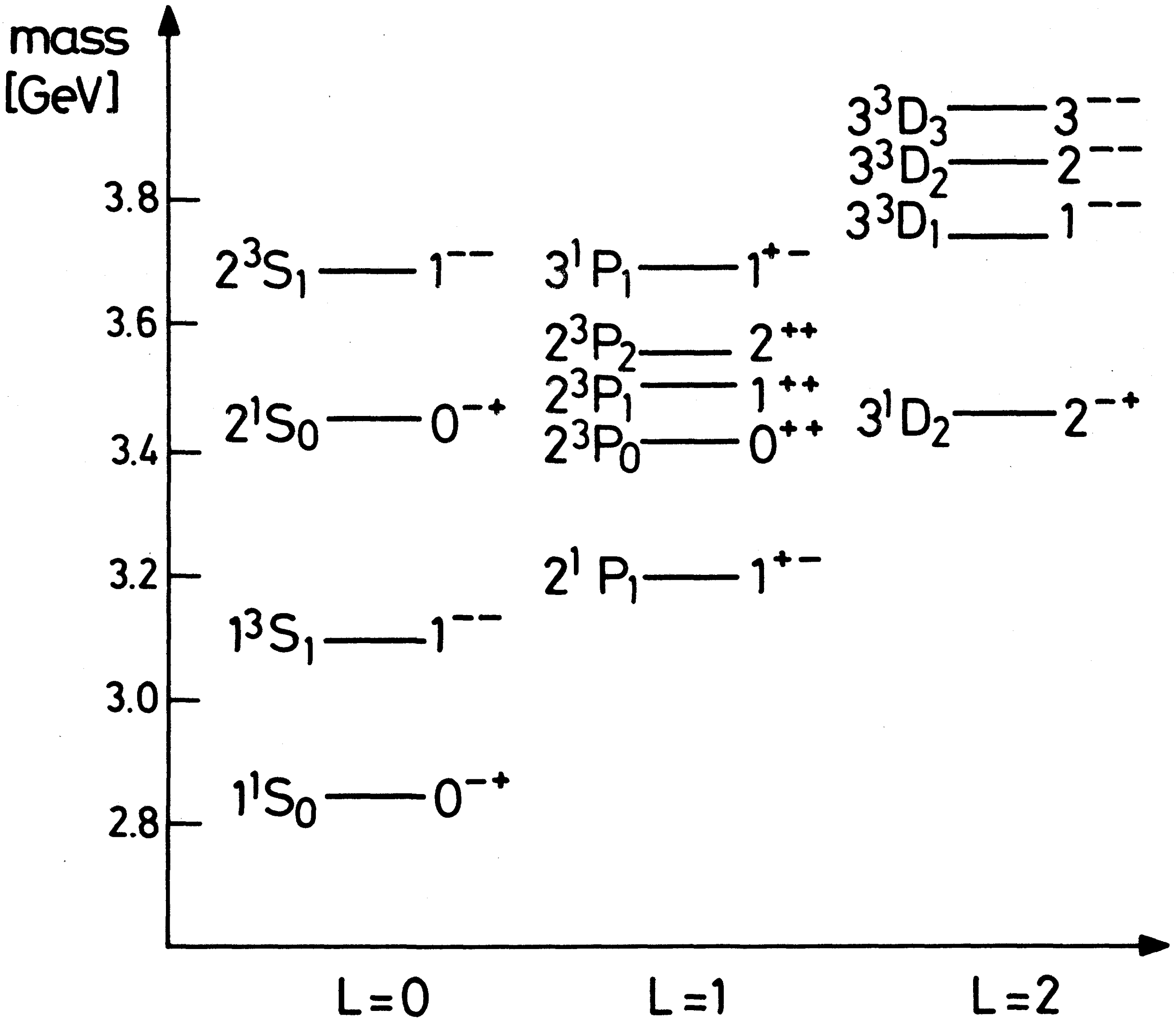

Fig. 6.1

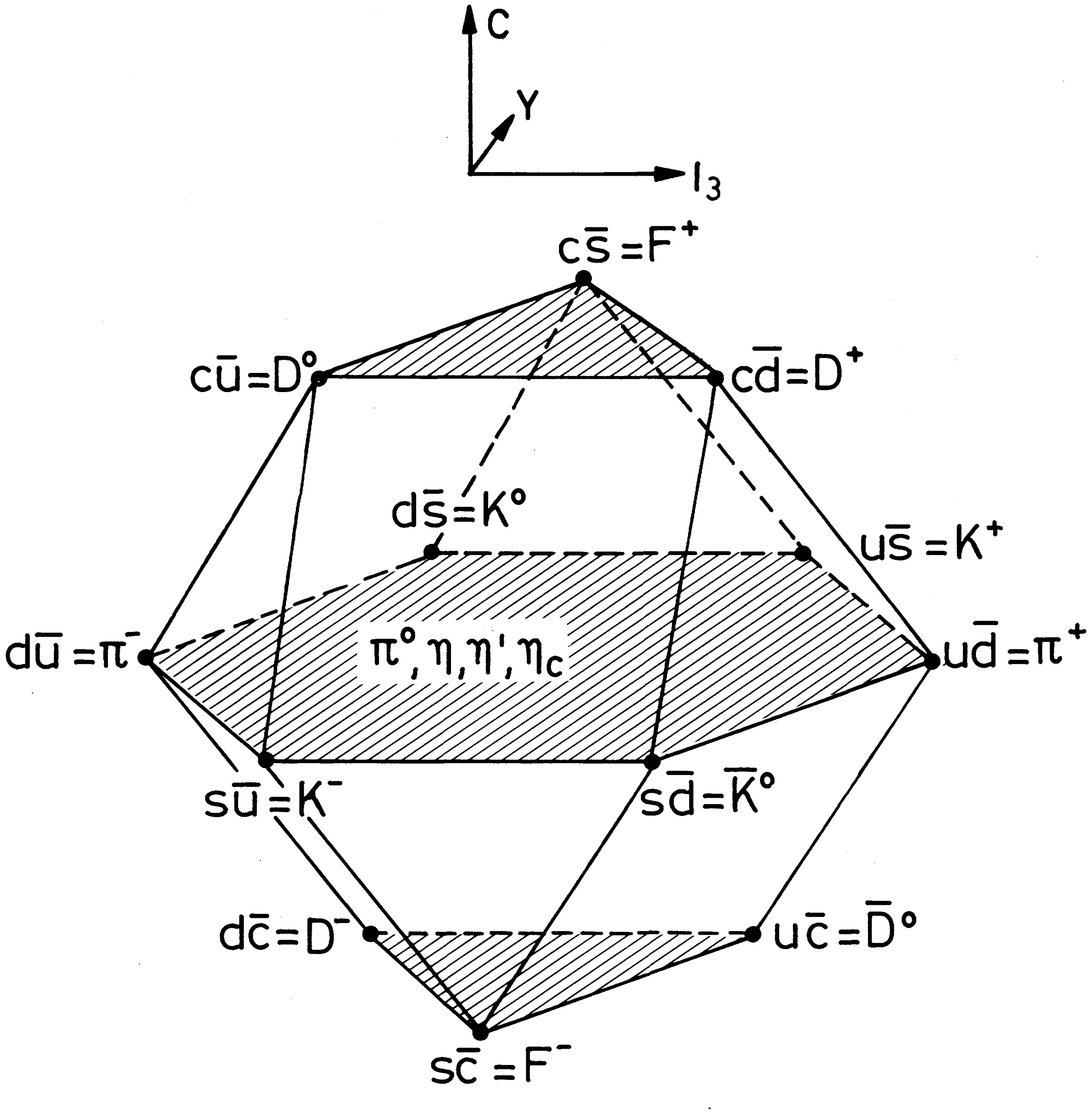

FIG. 6.2 SU(4) multiplet of the pseudoscalar mesons (see Ref.53).

27936

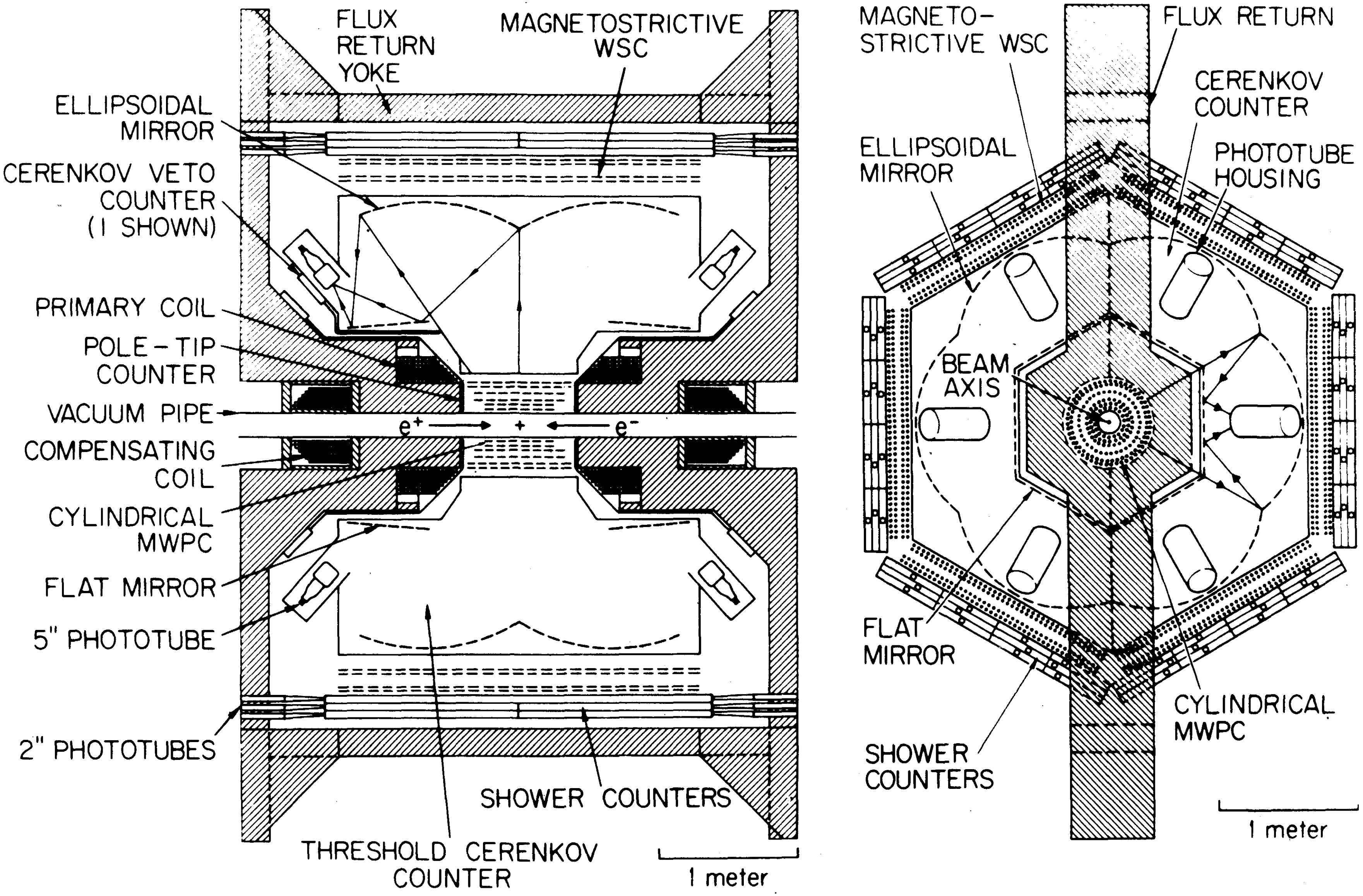

Fig. 6.3 Polar and azimuthal projections of the DELCO detector.

27927

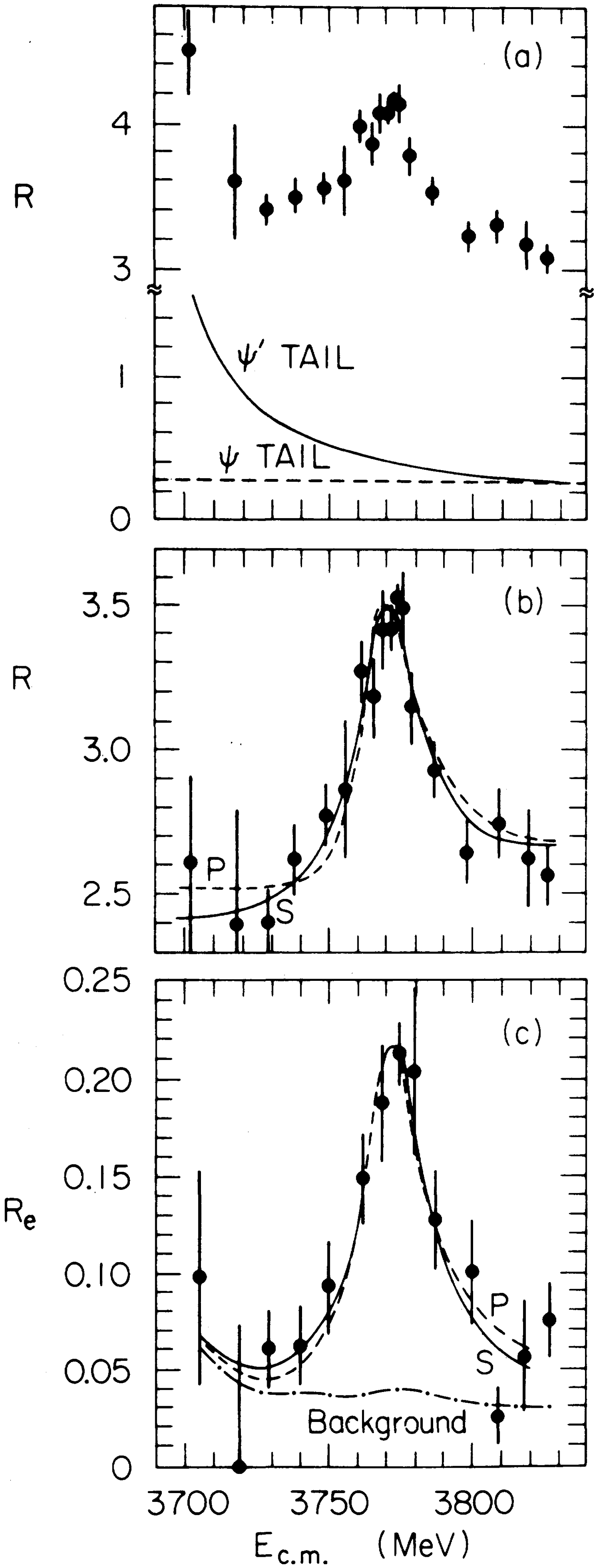

Fig. 6.4 Ratio R with respect to the μ pair cross section: (a) for the decays into hadrons, (b) with the J/ψ and ψ' tails subtracted, (c) for the electron pair decays.

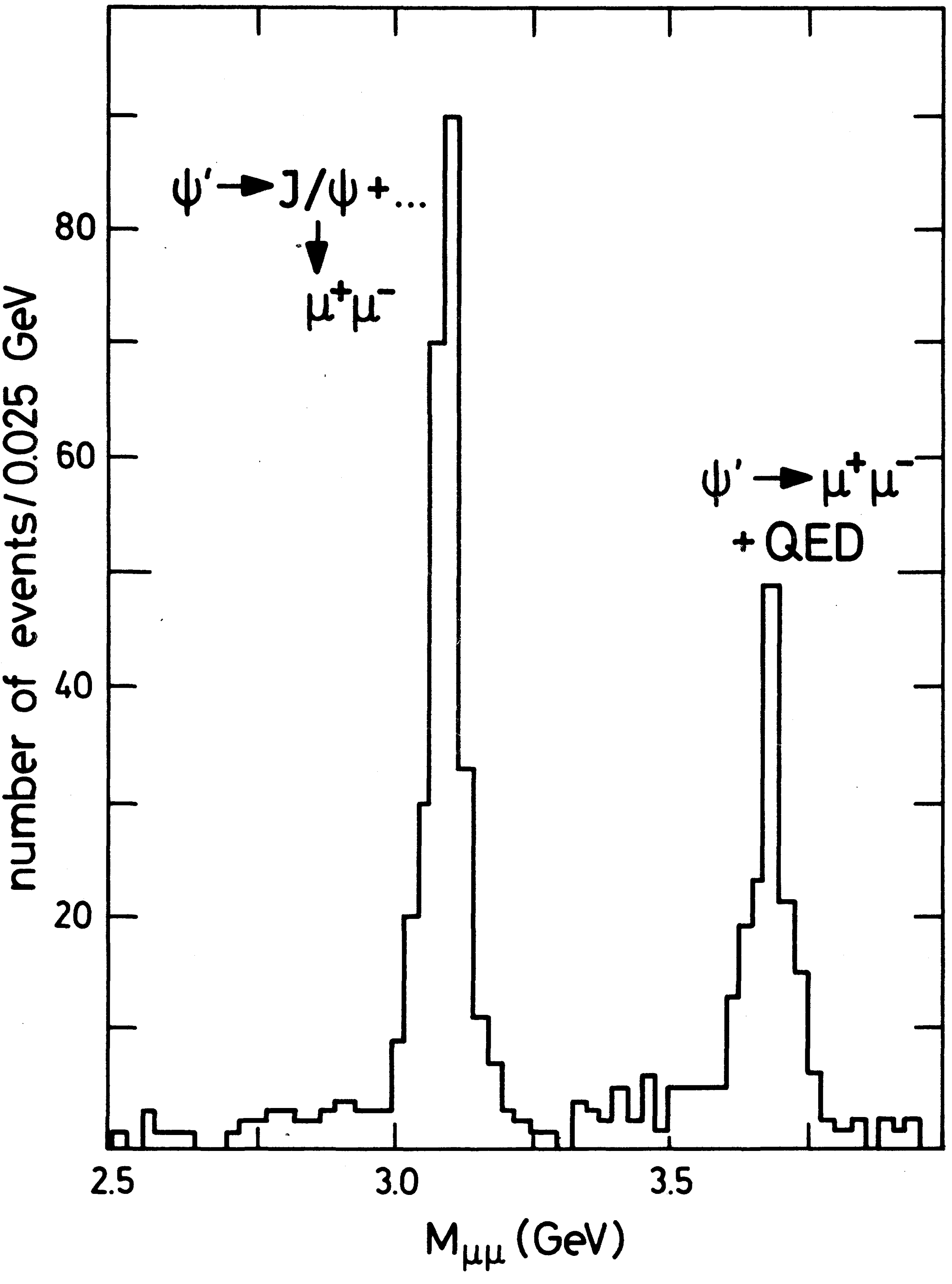

Fig. 6.5 Invariant mass of μ pairs observed in decays of the ψ'.

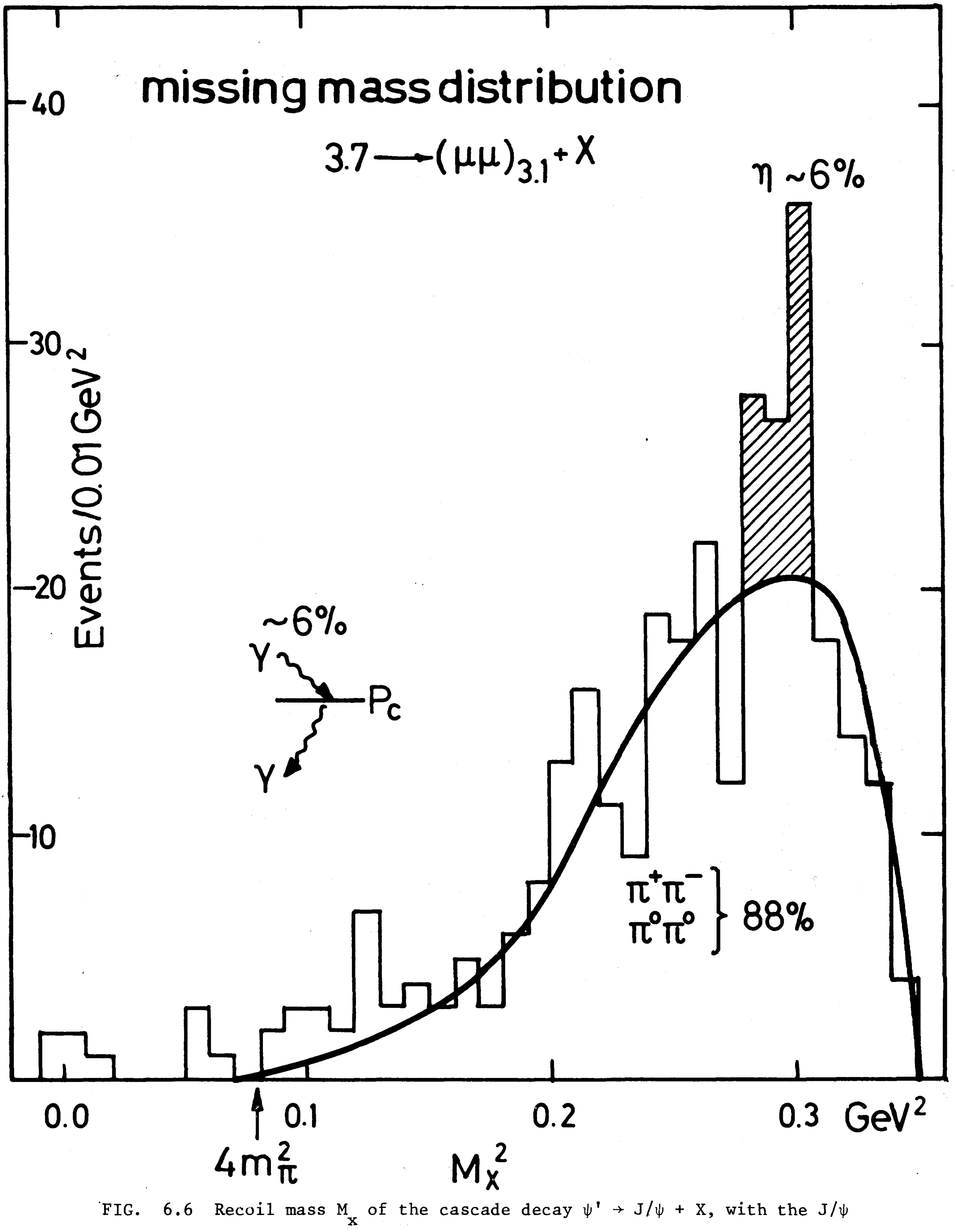

FIG. 6.6 Recoil mass M_x of the cascade decay $\psi' \rightarrow J/\psi + X$, with the J/ψ identified by its μ pair decay. The curve represents the spectrum for the $\mu^+\mu^-\pi\pi$ final state.

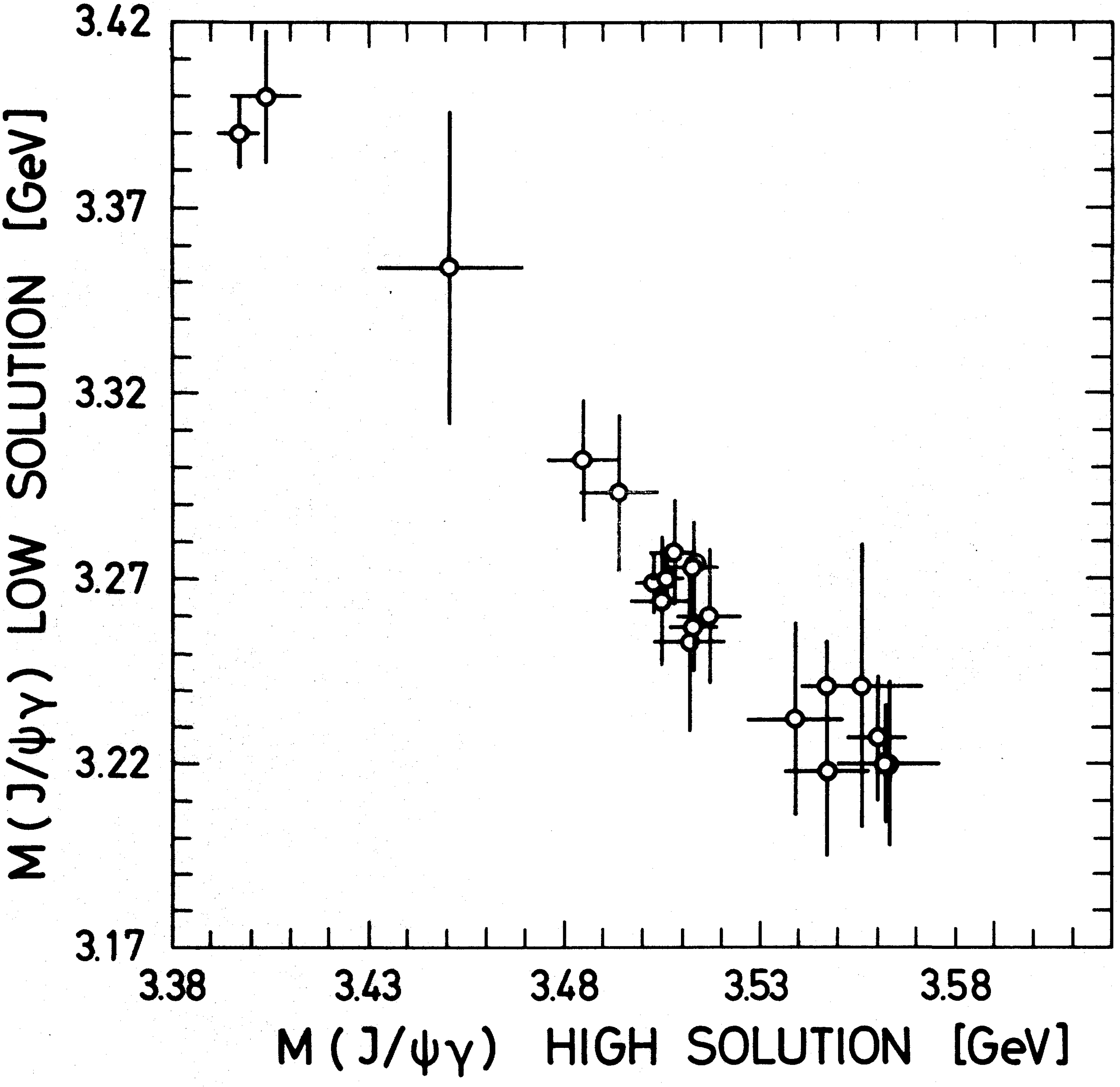

Fig. 6.7 Low versus high invariant mass of the J/ψ with either one of the two photons from the cascade decays $\psi' \to J/\psi\gamma\gamma$ (3C fit data from DASP).

27924

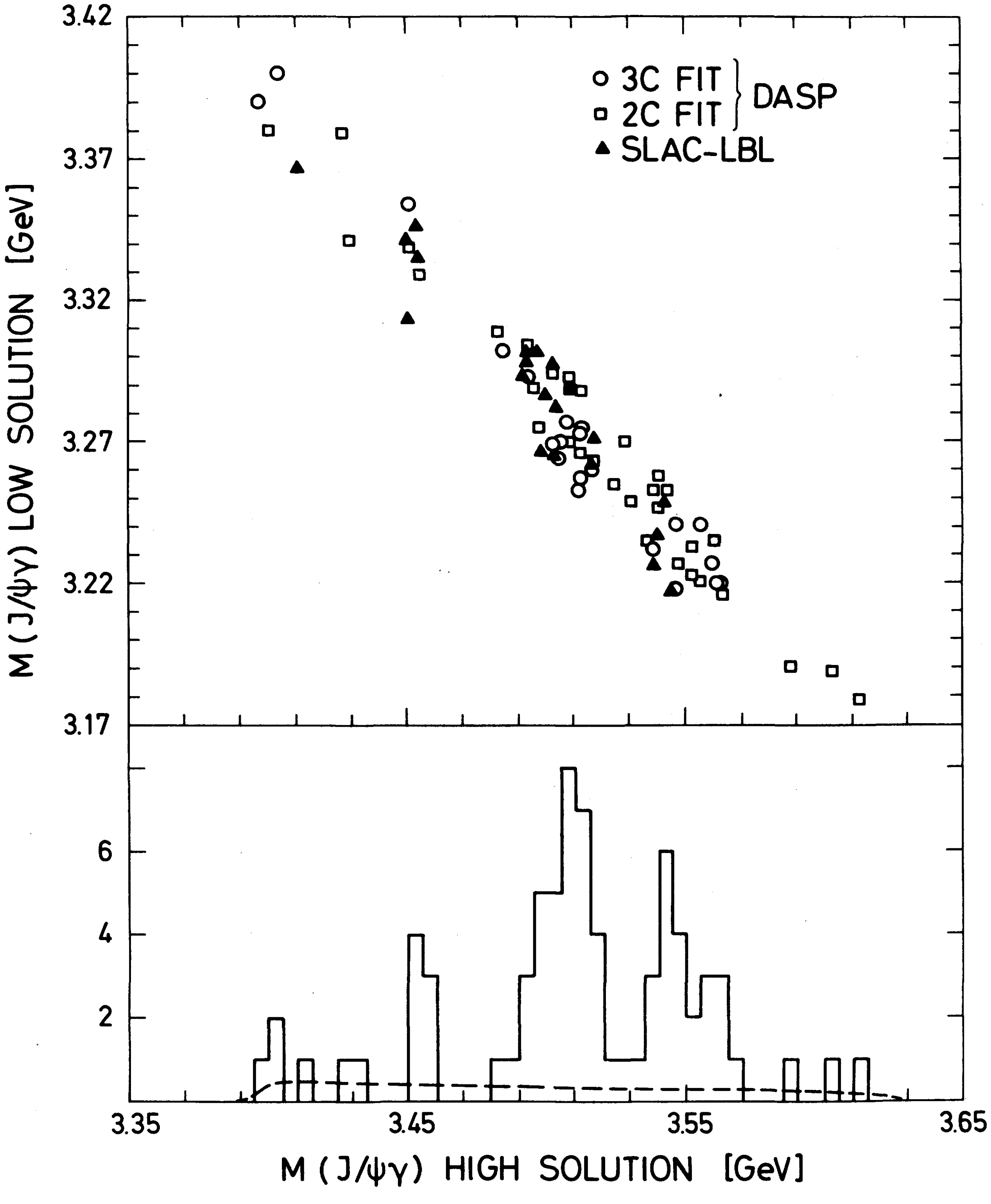

Fig. 6.8 Low versus high invariant mass of the J/ψ with either one of the two photons from the cascade decays ψ' → J/ψγγ and high mass projection (all 2C and 3C fit data from DASP and SLAC-LBL).

27639

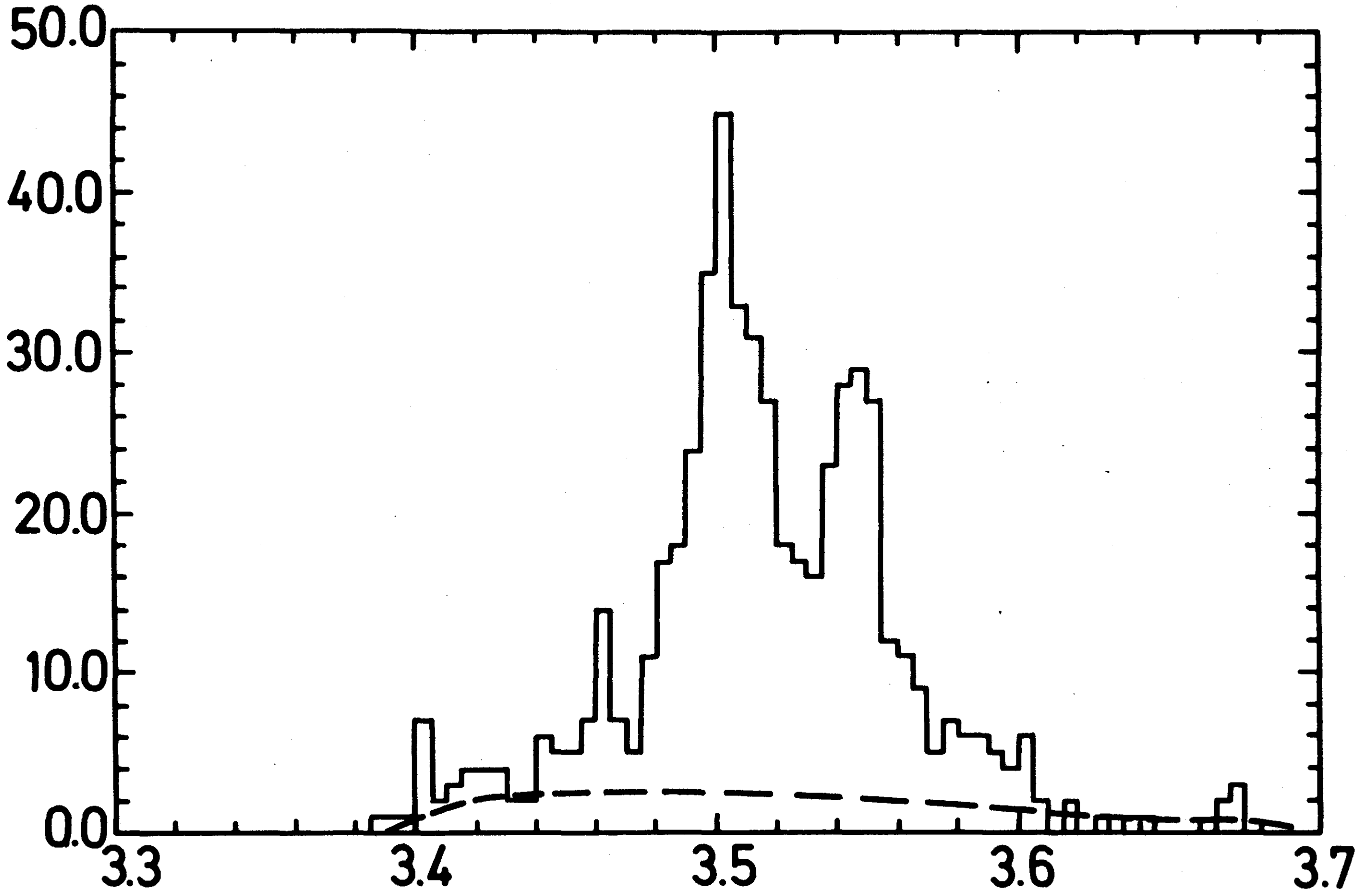

$$BR\left[\psi' \rightarrow \gamma_1 P_C(3.50)\right] \cdot BR\left[P_C \rightarrow \gamma_2 \psi\right] = (2.1 \pm 0.5)\%$$

$$BR\left[\psi' \rightarrow \gamma_1 X(3.55)\right] \cdot BR\left[X_{(3.55)} \rightarrow \gamma_2 \psi\right] = (1.1 \pm 0.4)\%$$

Fig. 6.9 High γ J/ψ mass solution from the cascade decay $\psi' \rightarrow J/\psi\gamma\gamma$ (DESY-Heidelberg data).

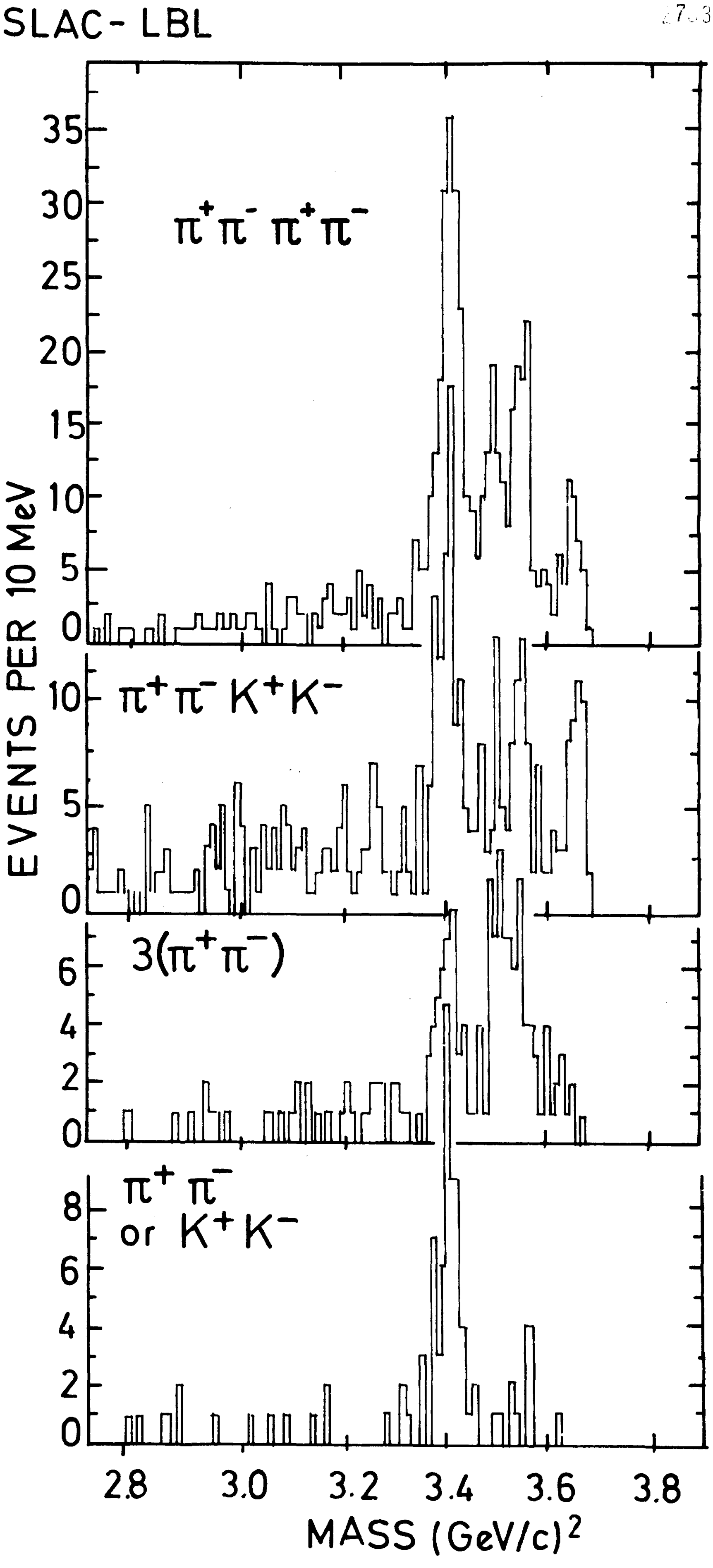

Fig.6.10 Invariant mass distributions of the hadronic systems from the decays $\psi' \rightarrow \gamma$ + charged hadrons.

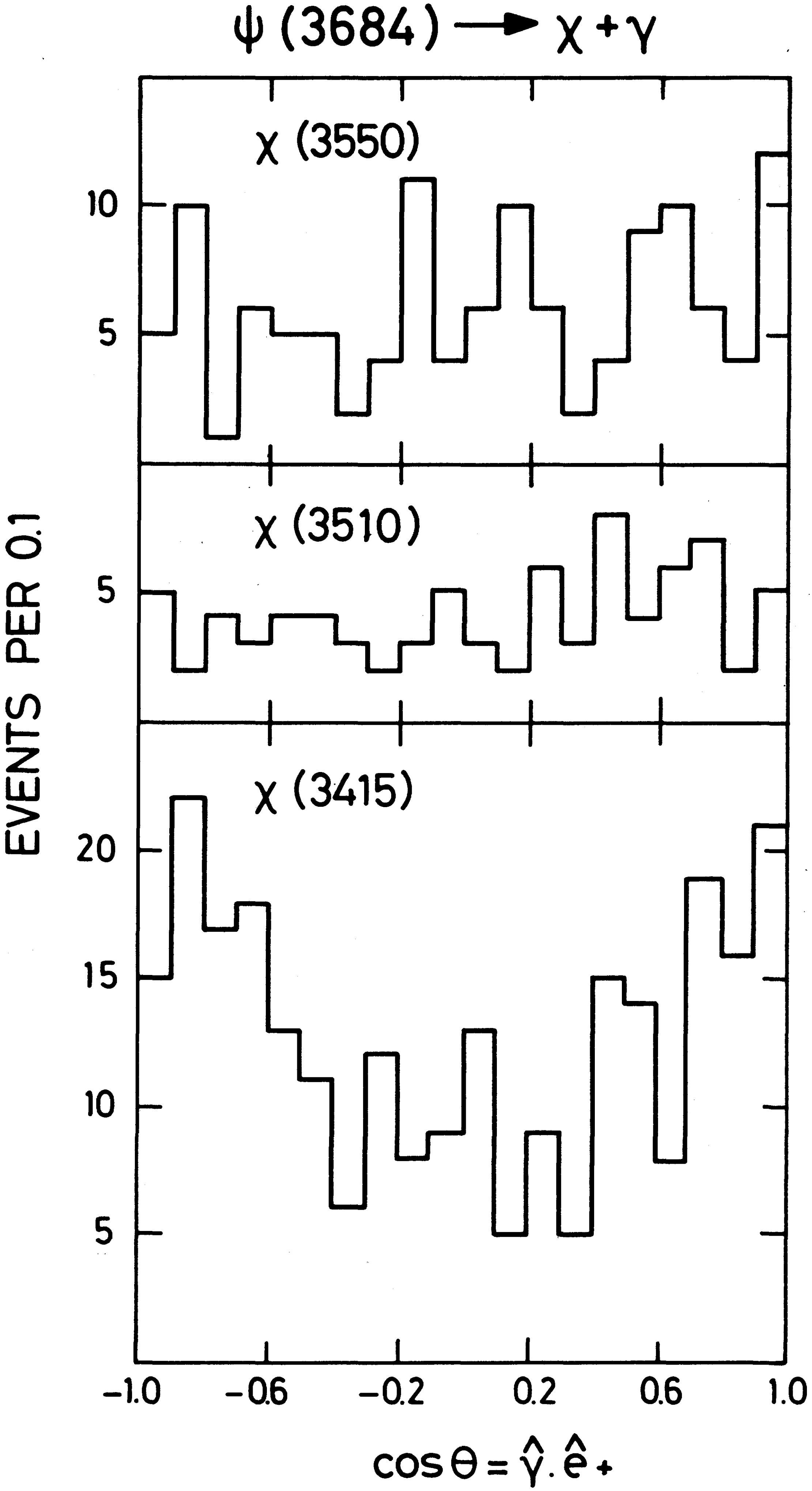

Fig. 6.11 Polar angle distribution of the emitted photon with respect to the positron direction for the three $\chi\gamma$ final states.

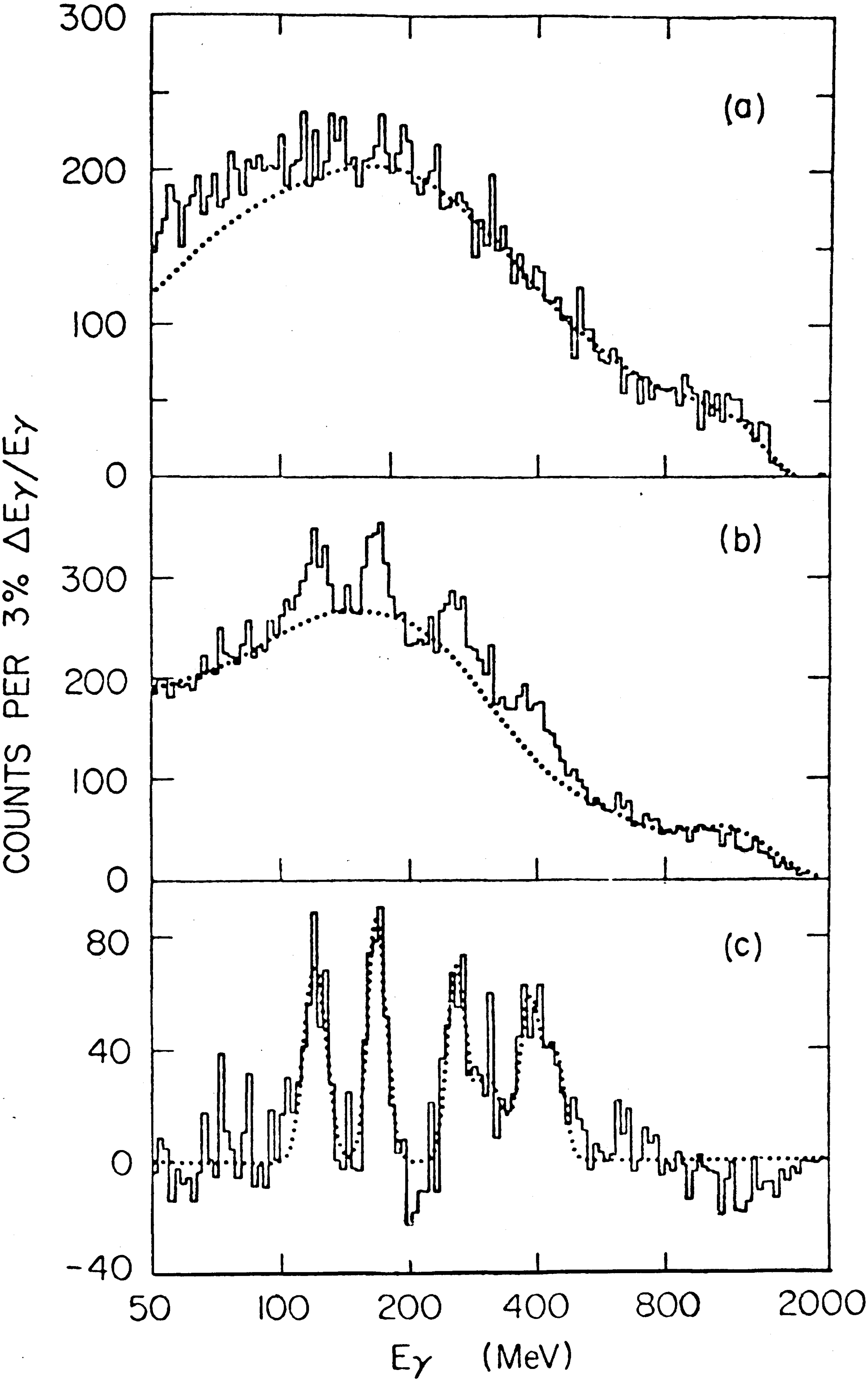

Fig. 6.12 Inclusive photon spectra: (a) J/ψ data with Monte Carlo background (dotted line), (b) ψ' data with M.C. background, (c) ψ' data with M.C. background subtracted and with fit for monochromatic lines.

DESY

25406

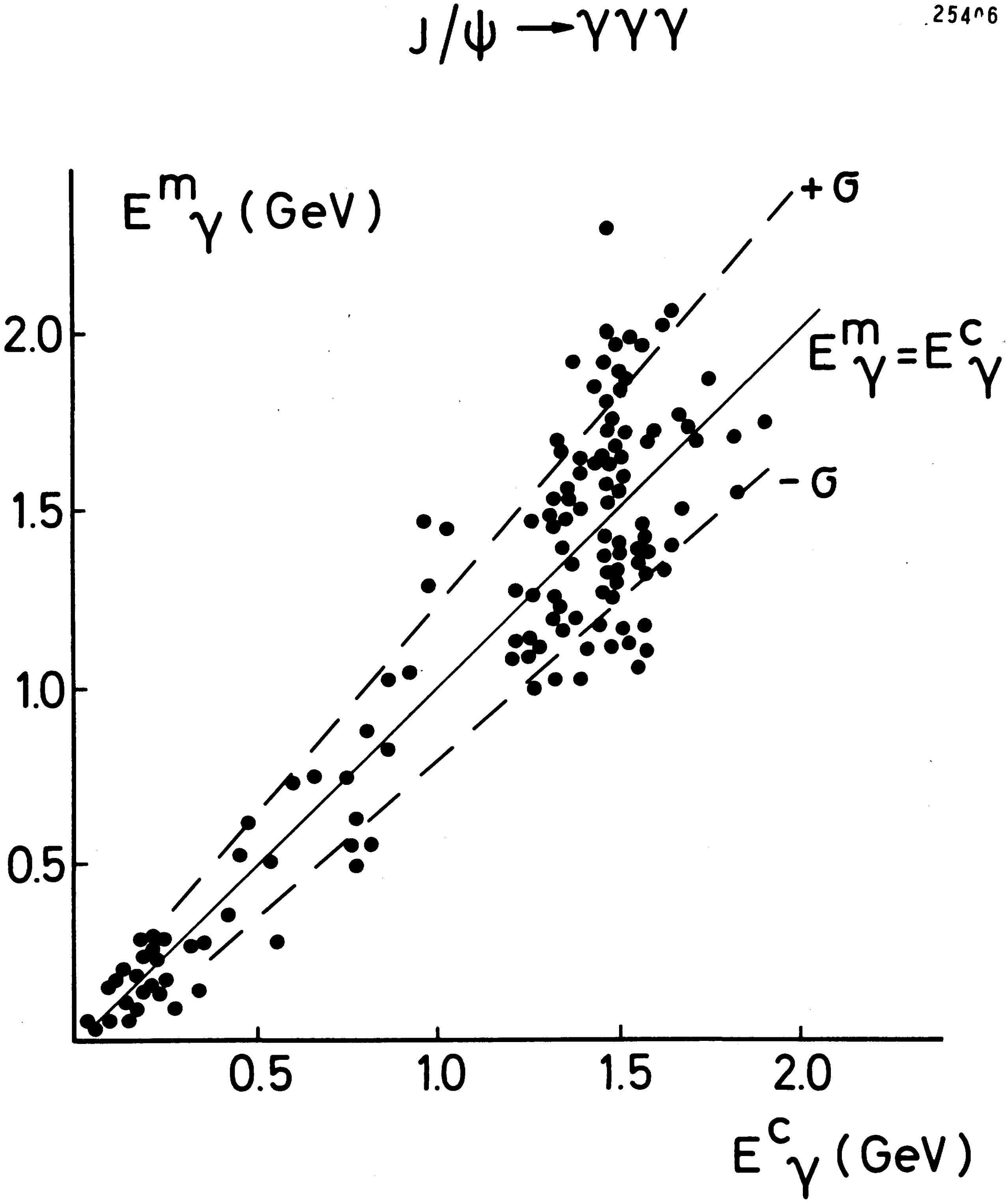

Fig. 6.13 Measured versus computed (1C fit) photon energy for coplanar three photon events.

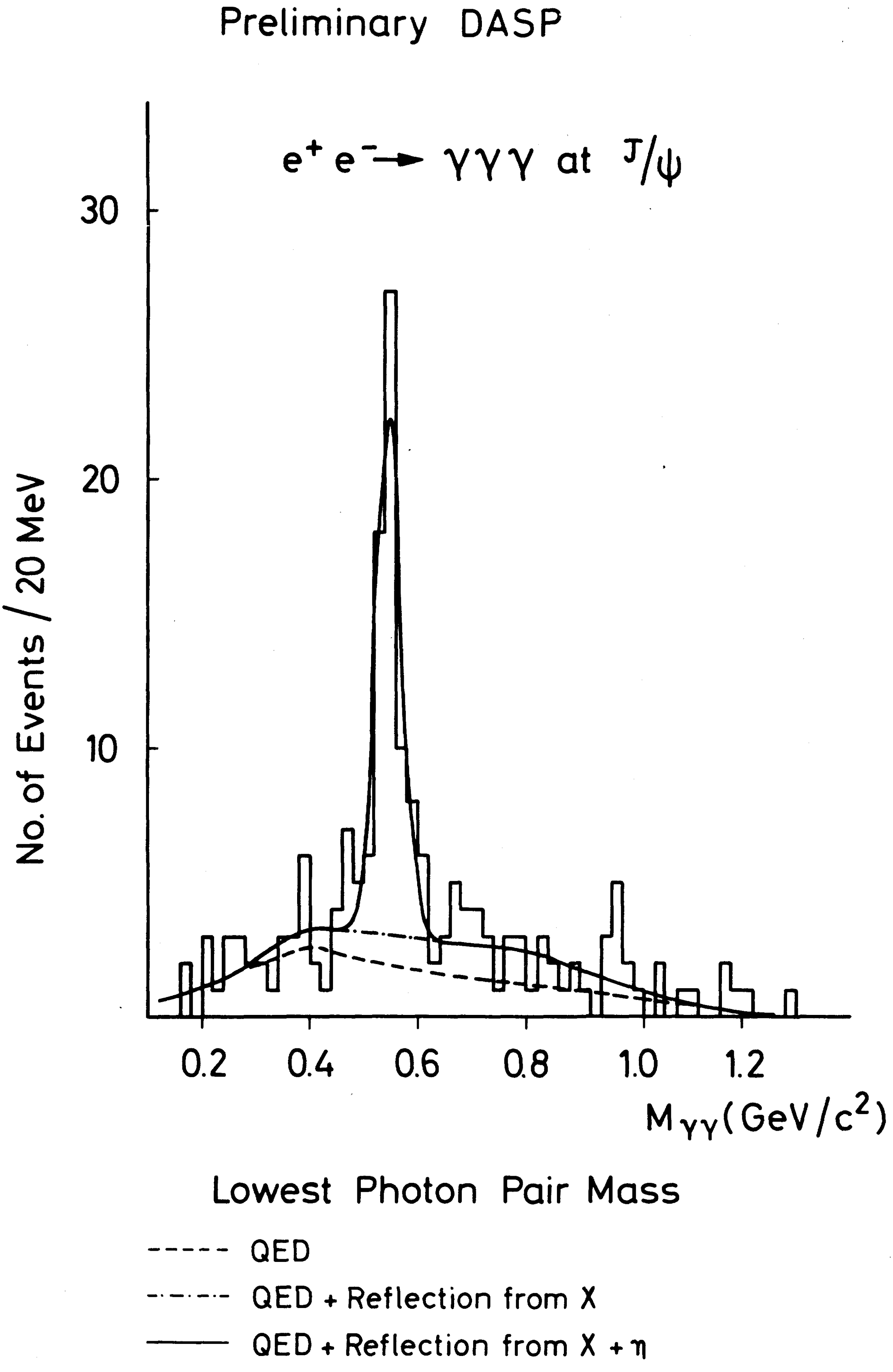

Fig. 6.14 Lowest two photon invariant mass for the three photon events at the J/ψ.

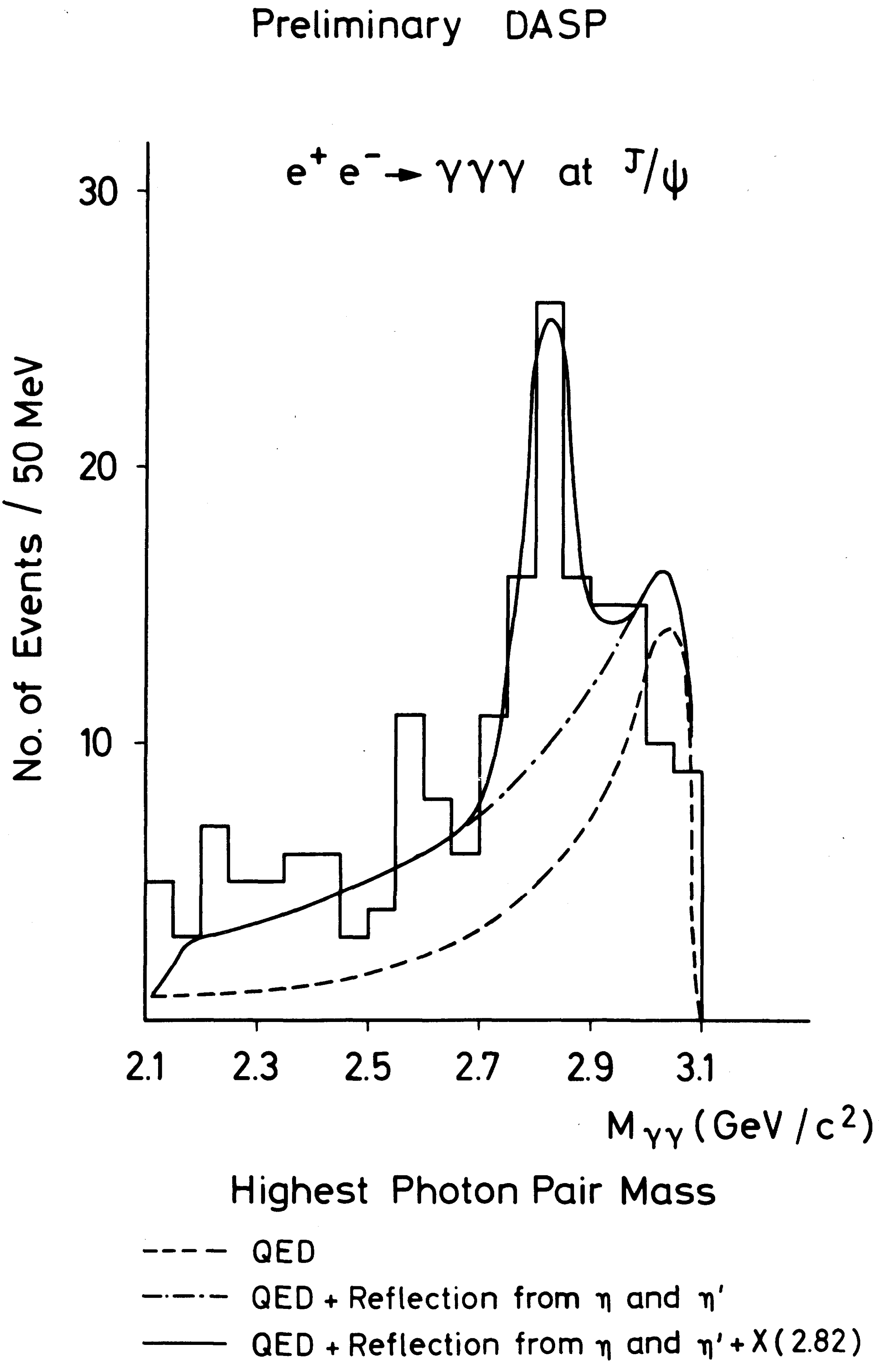

Fig. 6.15 Highest two photon invariant mass for the three photon events at the J/ψ.

26732

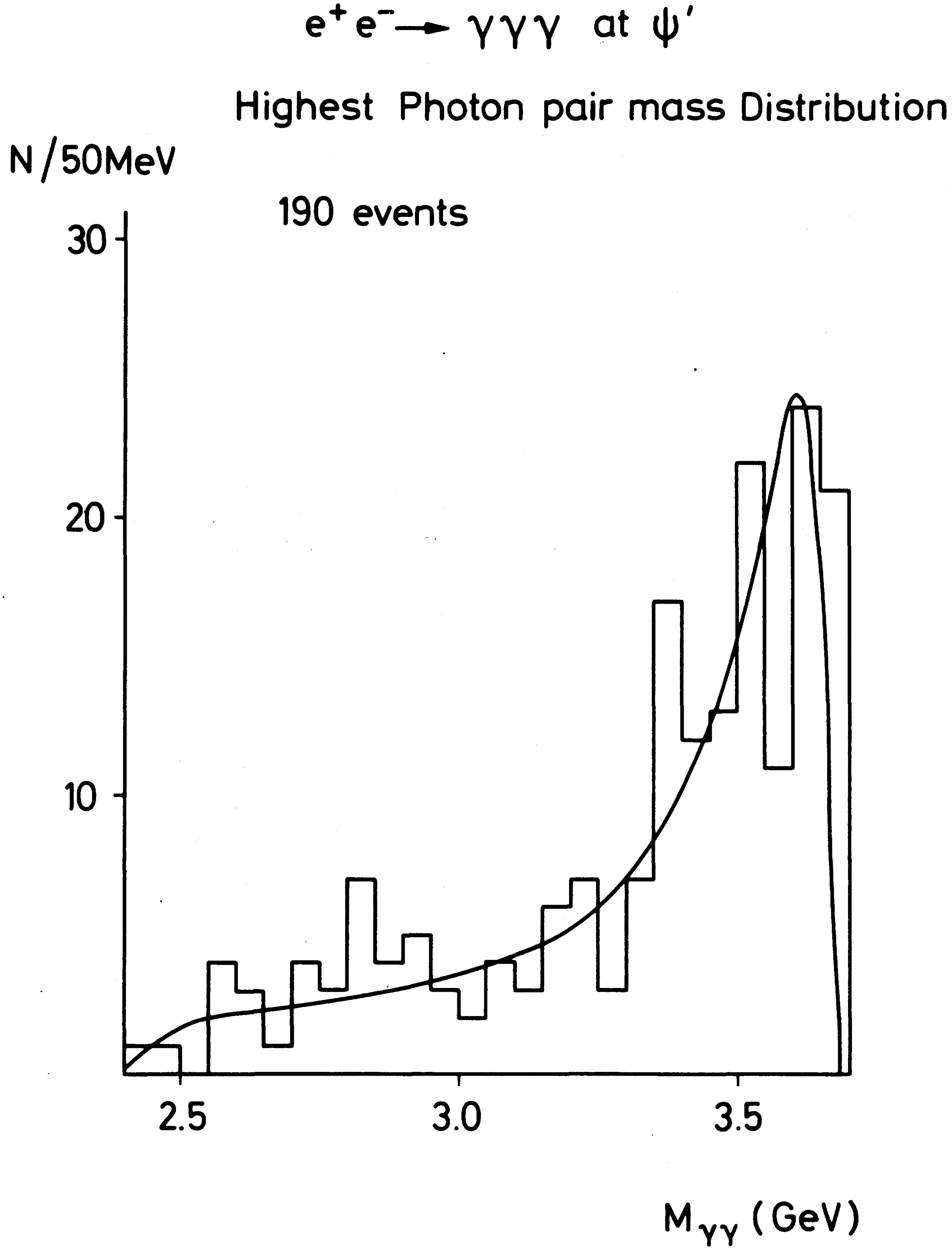

Fig. 6.16 Highest two photon invariant mass for the three photon events at the ψ'.

27931

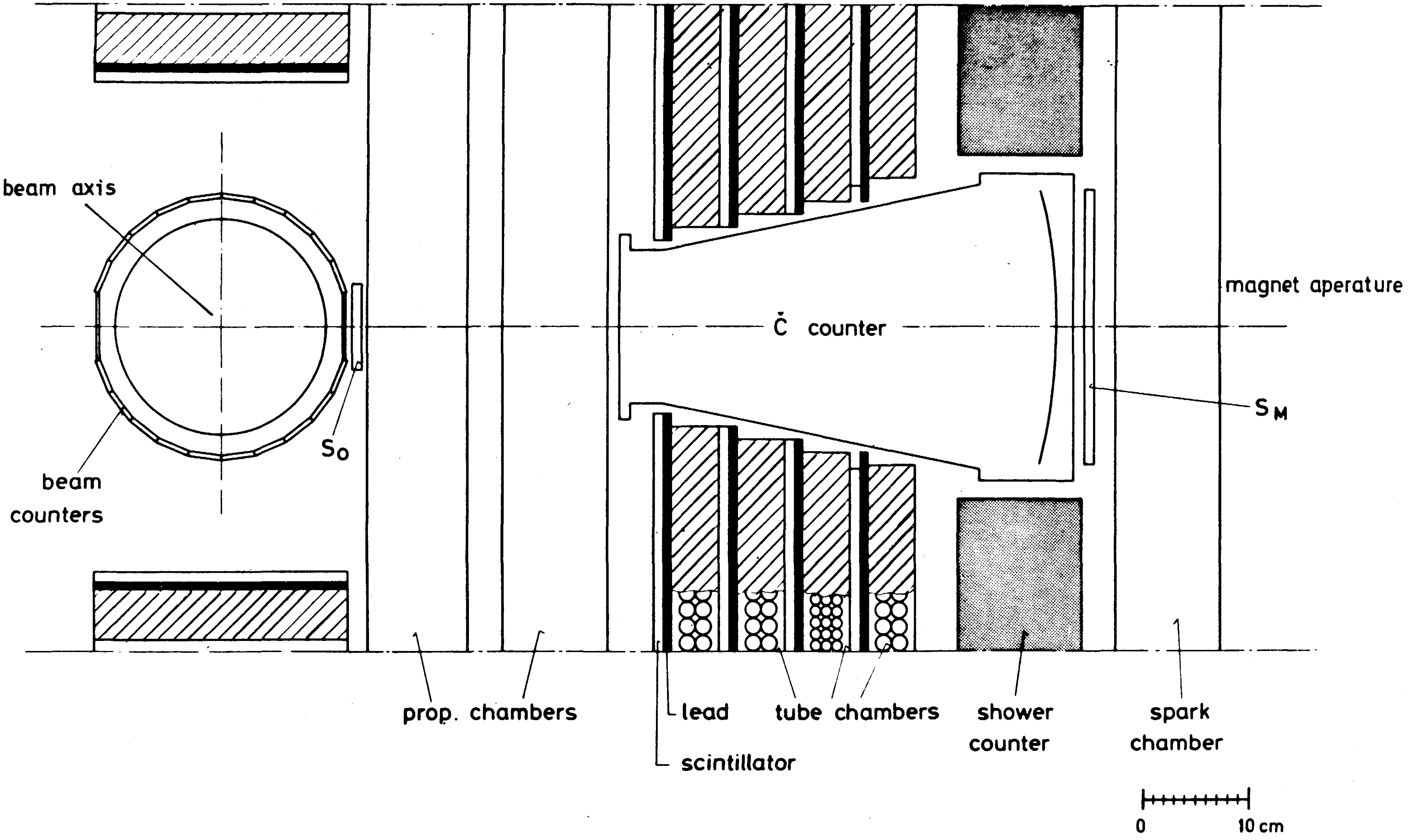

Fig. 6.17 Cerenkov counter installed in front of the magnet gap of DASP.

26737

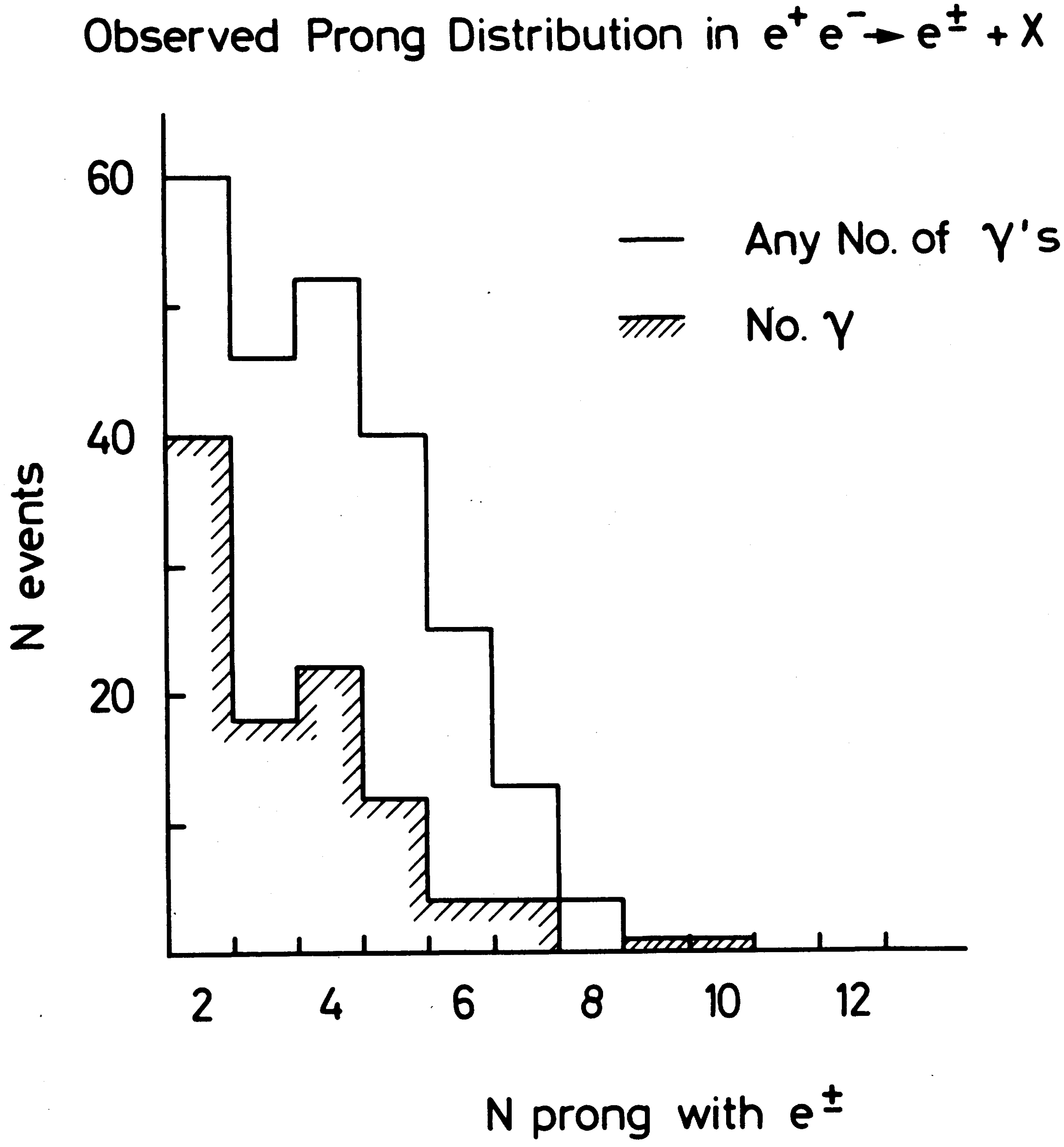

Fig. 6.18 Observed charged track multiplicity (including the electron) for electron inclusive events. The shaded histogram is for events without photons.

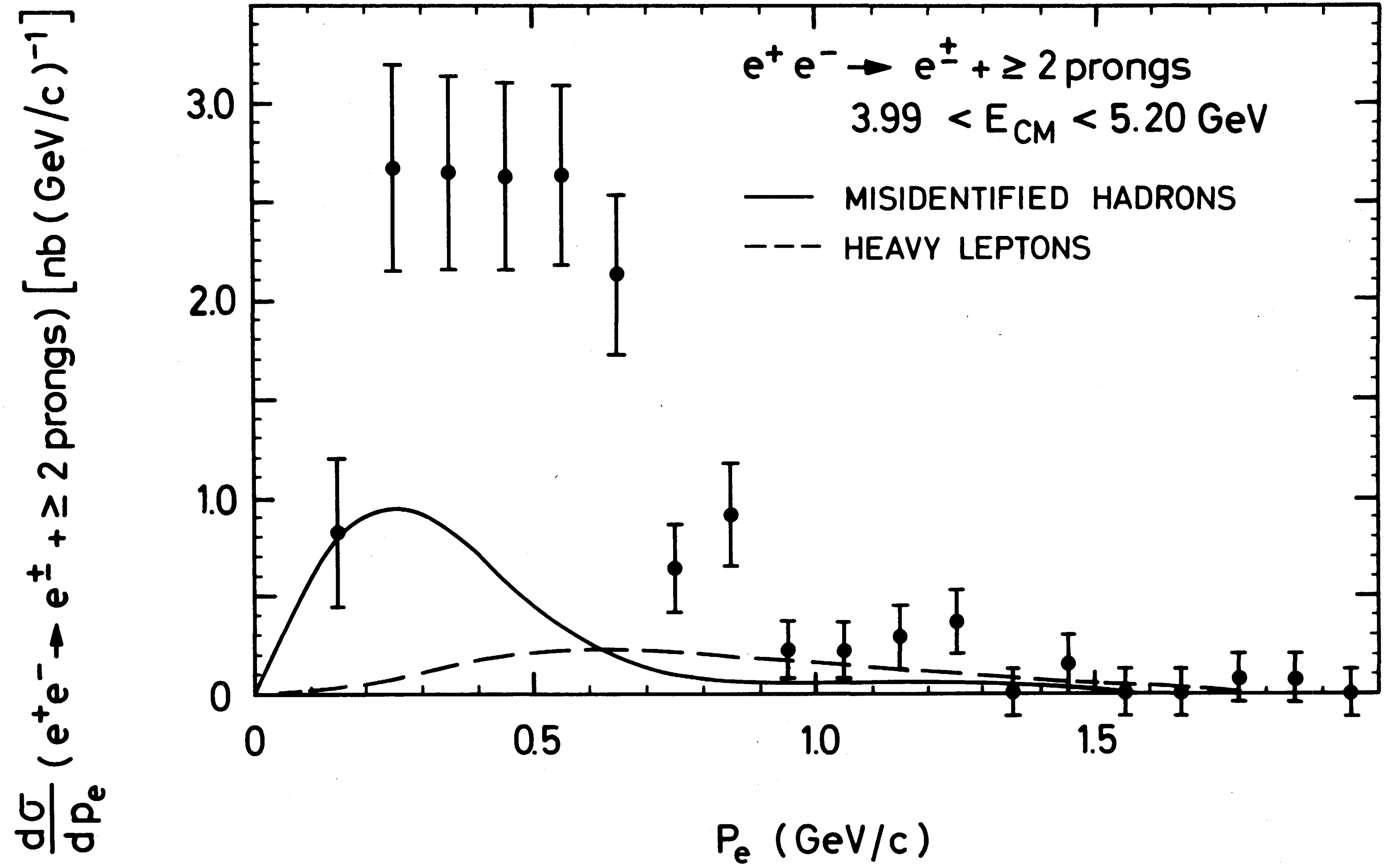

Fig. 6.19 Observed electron momentum spectrum for electron inclusive events with at least two additional charged tracks. The backgrounds expected from hadron misidentification (solid angle) and heavy lepton decays (dashed curve) are indicated.

26723

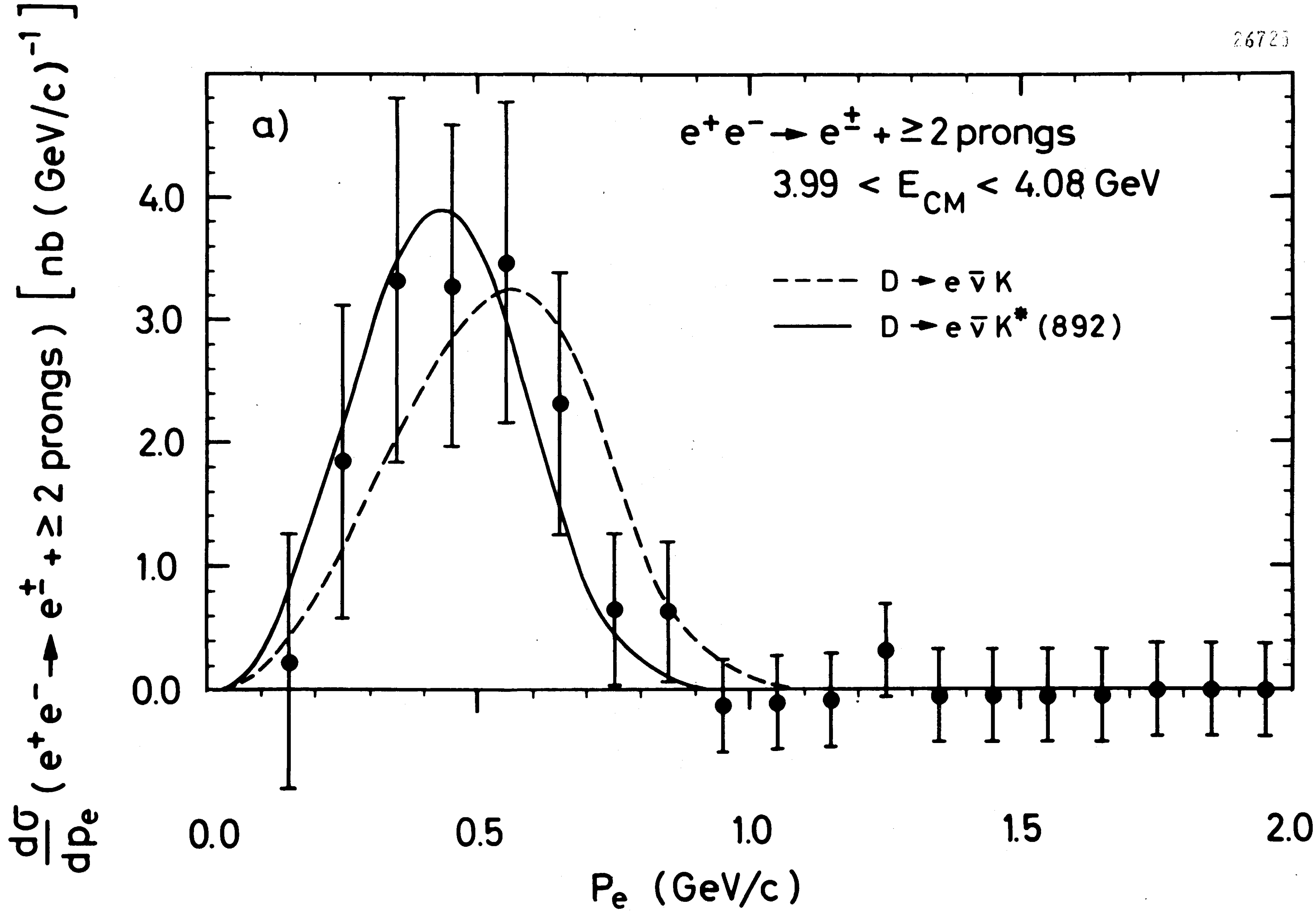

Fig.6.20 Electron momentum spectrum in the restricted energy range from 3.99 to 4.08 GeV. The curves are model calculations[72]) for the two decays indicated.

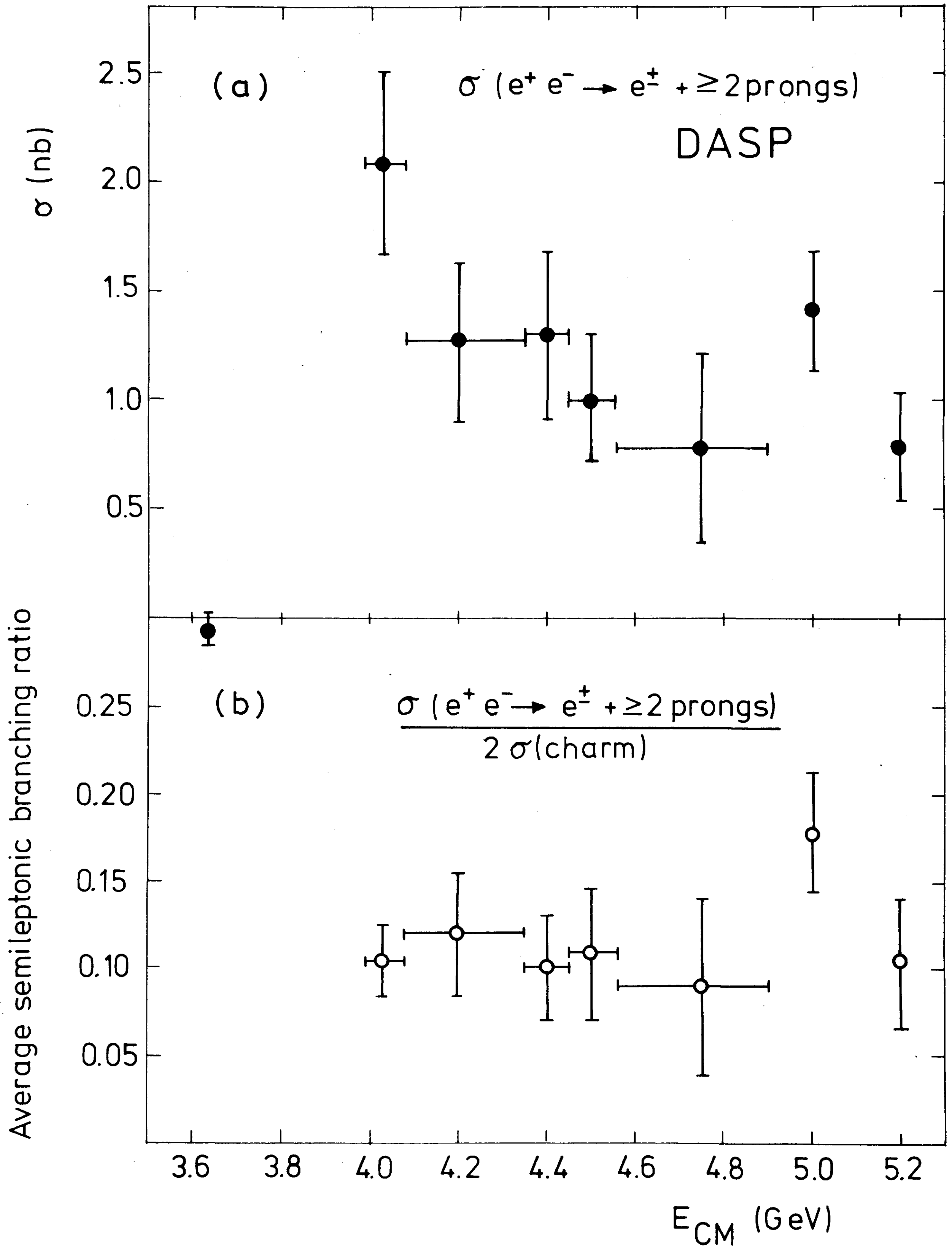

Fig.6.21 (a) Cross section of the electron inclusive events with at least two additional charged tracks.
(b) Semileptonic branching ratio of charmed hadrons; data in (a) normalized with respect to the PLUTO cross section (see text).

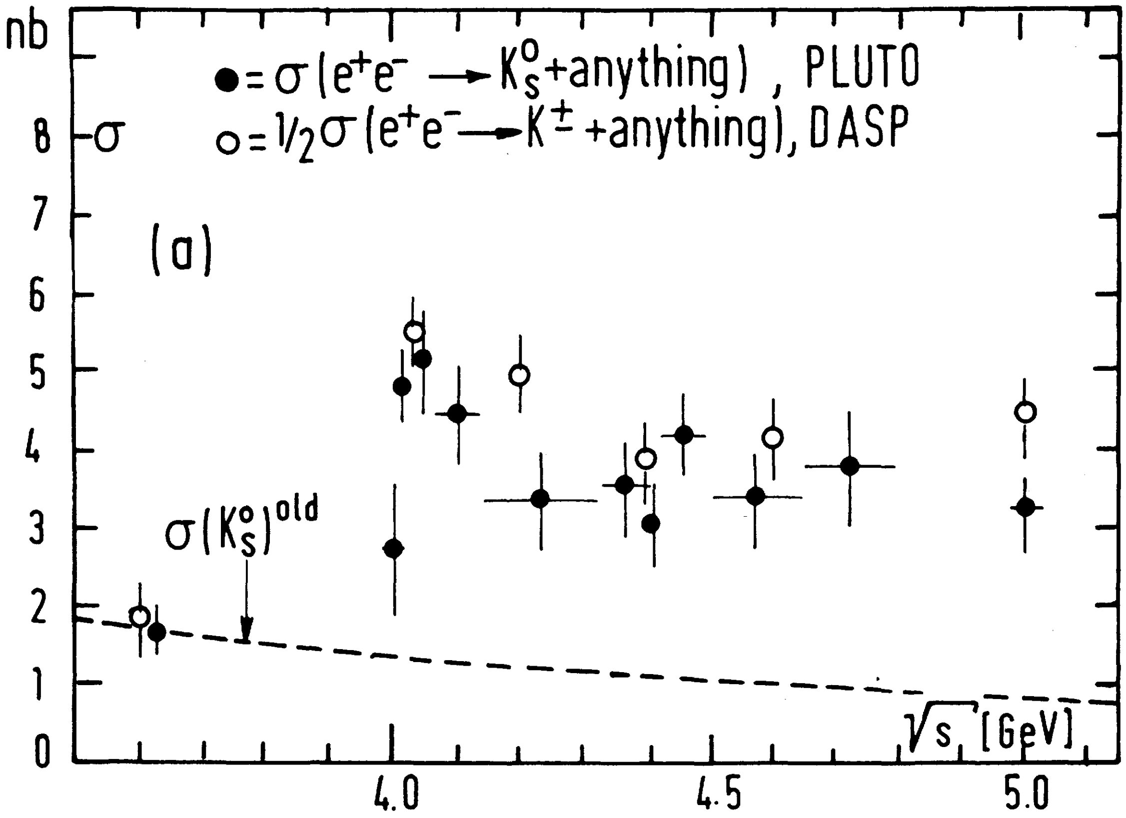

Inclusive Cross Section of Kaons

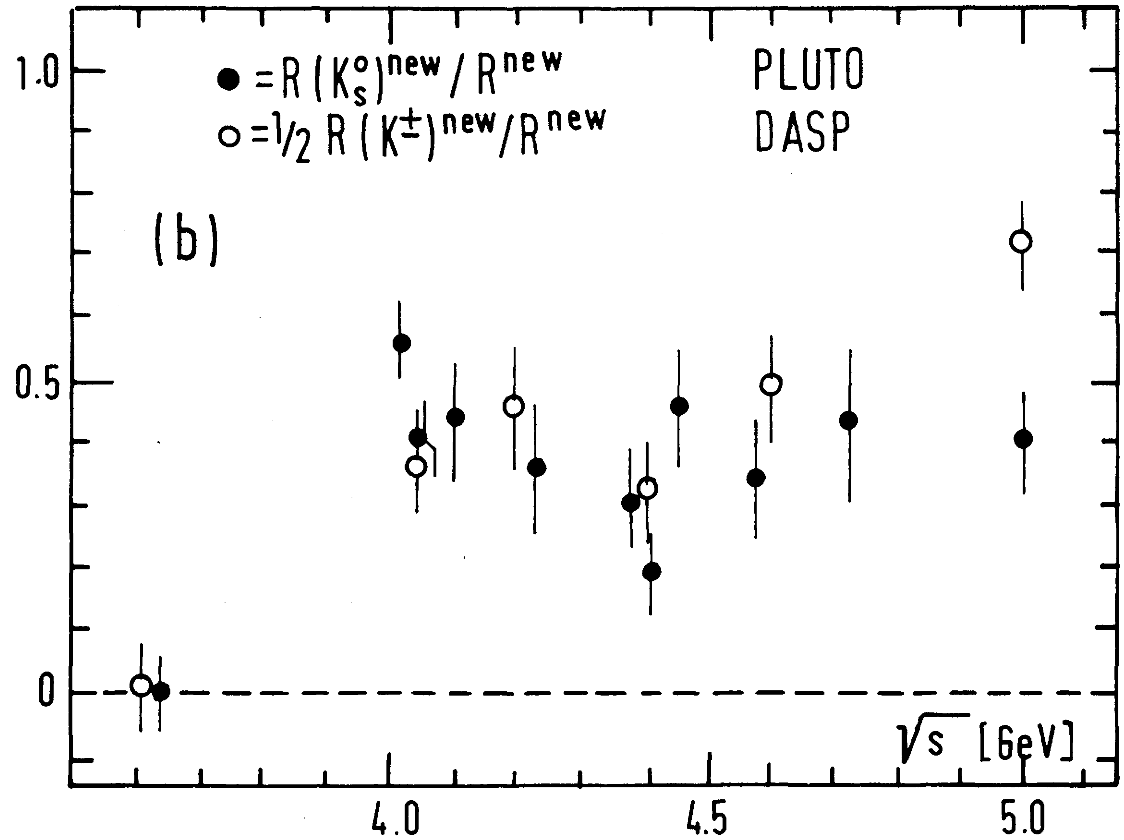

Number of Kaons per new Event

DESY 26431

Fig.6.22 (a) Cross section for kaon pair production. The dashed curve indicates the s^{-1} extrapolation of the data points at 3.6 GeV. (b) Branching ratios of K^0 and $K^{\pm}$ decays of charmed hadrons. The superscript "new" signals that the old physics has been subtracted (dashed line).

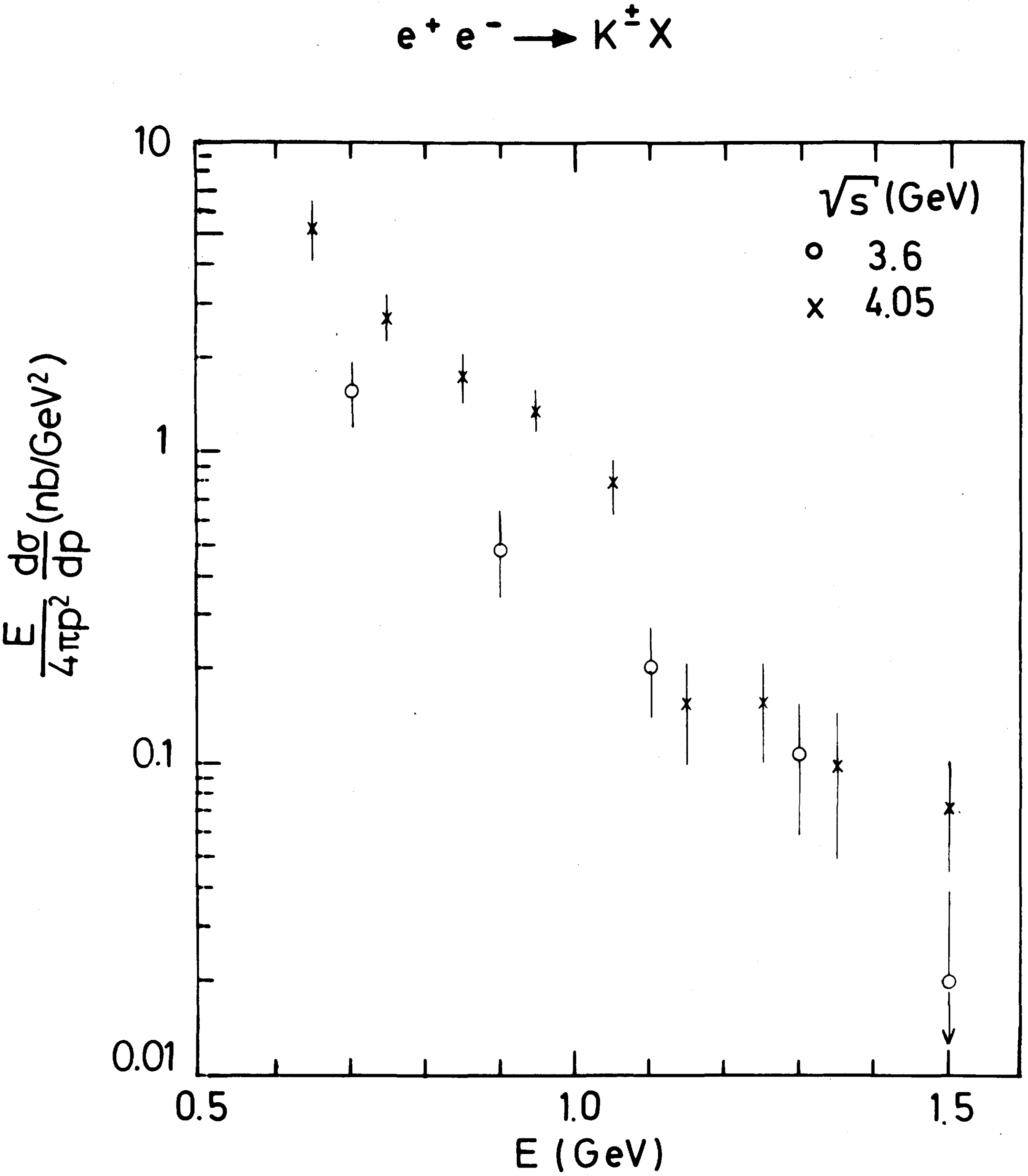

Fig.6.23 Invariant momentum spectrum of charged kaons below and above charm threshold.

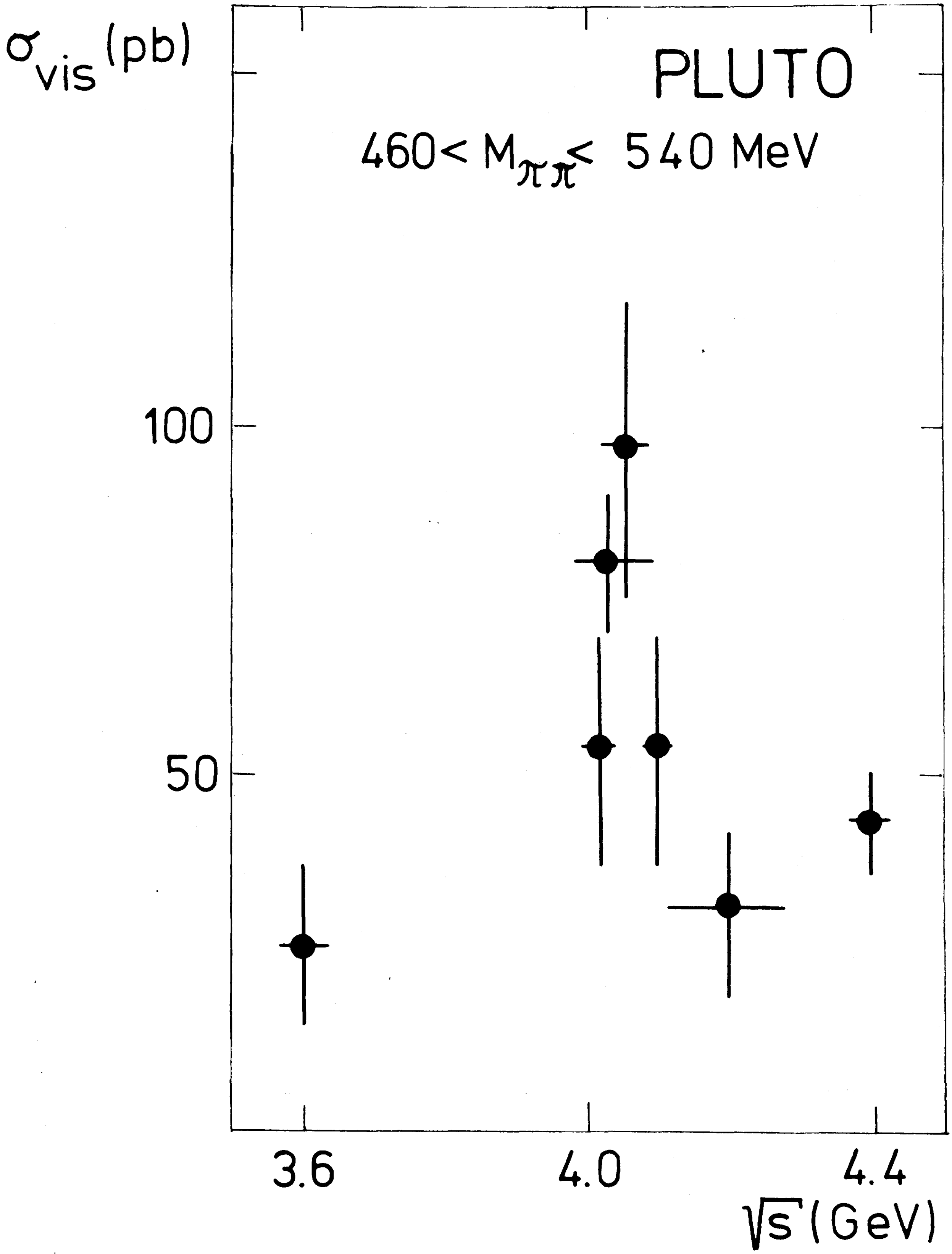

Fig. 6.24 Visible cross section for $e^+e^- \to e^\pm K_S^0$ + anything

DESY

.25617

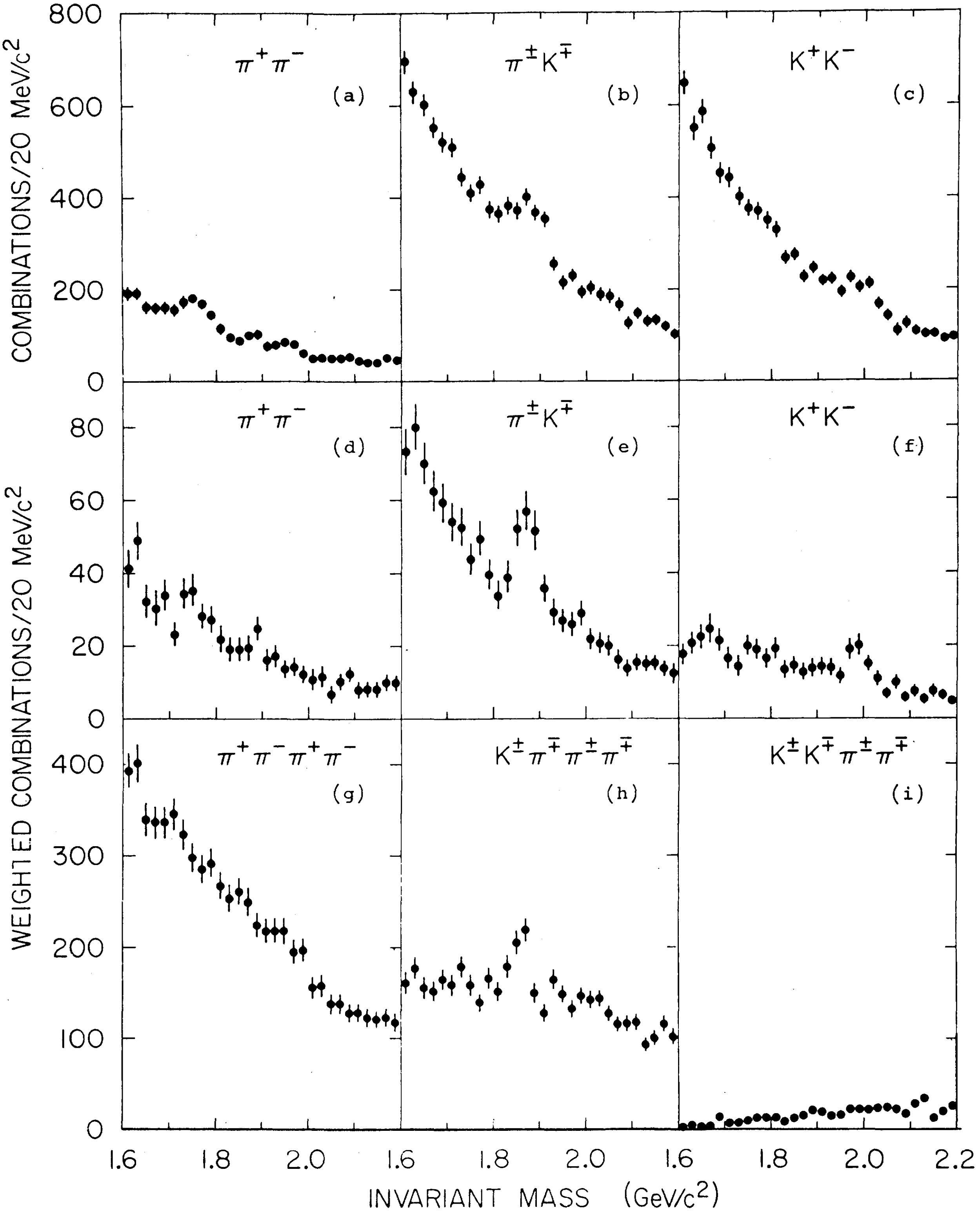

Fig.6.25 Invariant mass distributions for $3.9 < \sqrt{s} < 4.6$ GeV:
(a-c) events with any π/K mass assignment,
(d-i) events with weighted π/K separation due to time of flight measurement.

DESY

25733

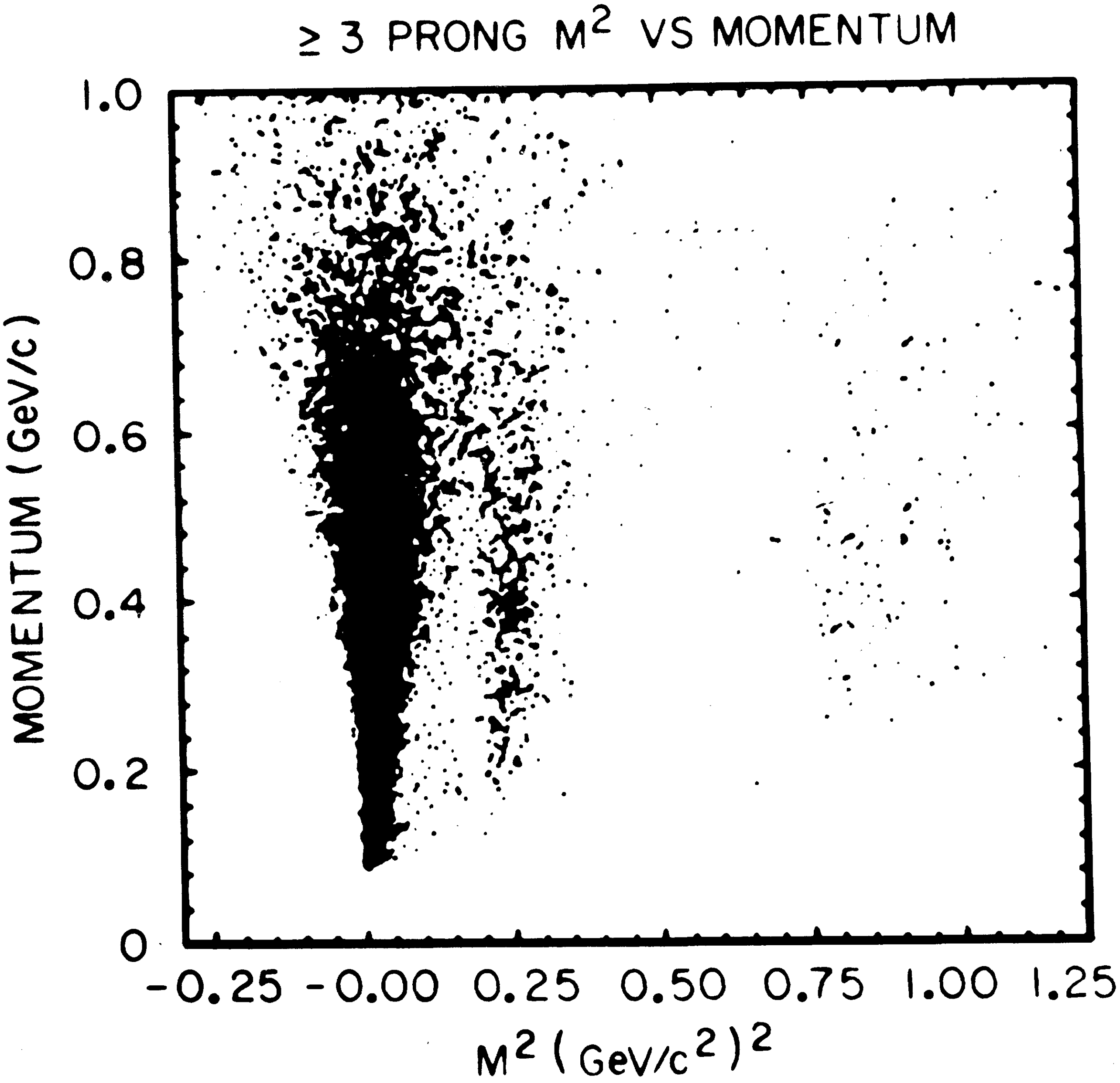

Fig. 6.26 Momentum of negative particles versus the mass squared obtained from time of flight.

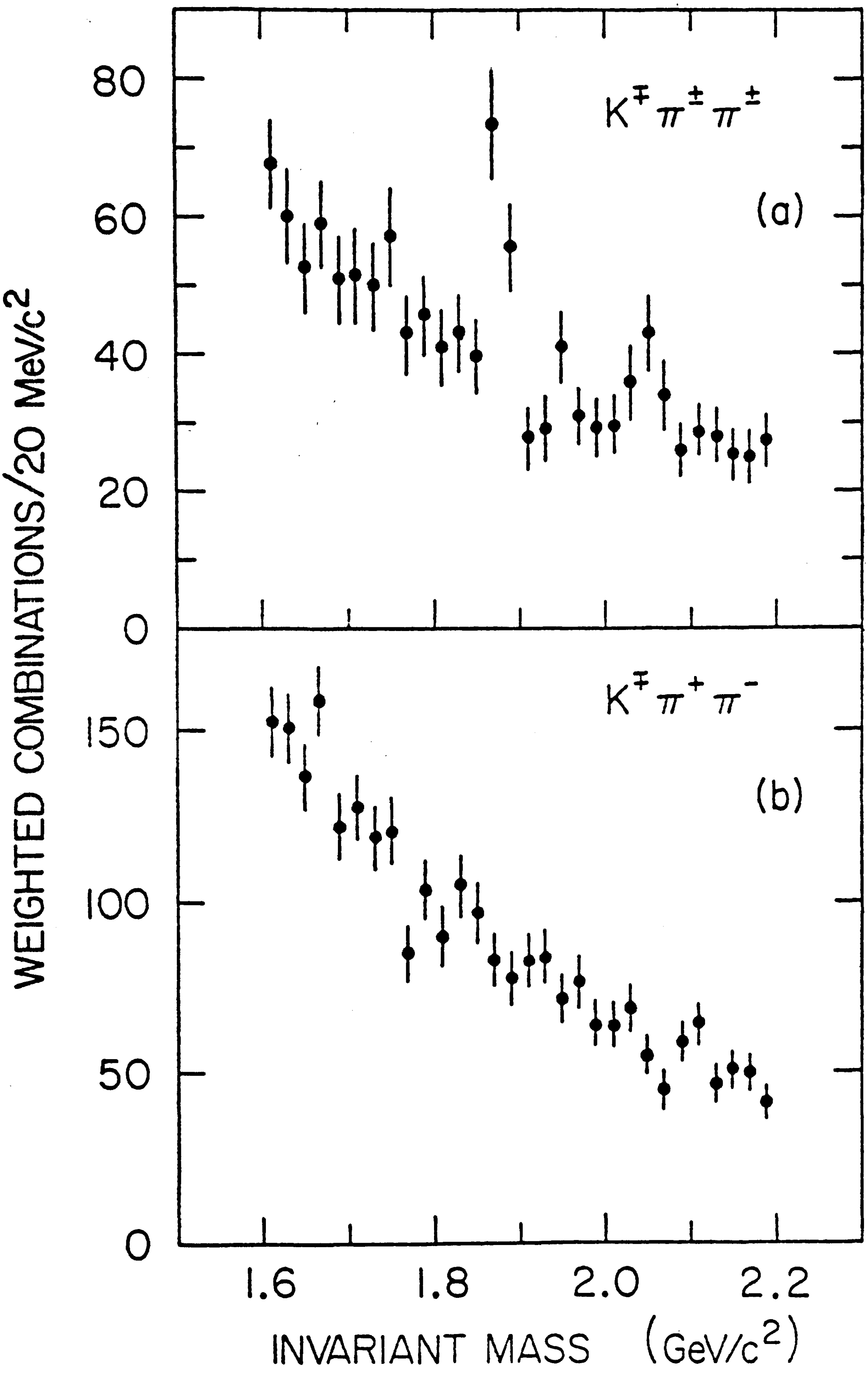

Fig.6.27 Invariant mass of $K\pi\pi$ at $\sqrt{s}$ = 4.03 GeV: The kaon has (a) opposite and (b) same charge as the total $K\pi\pi$ system.

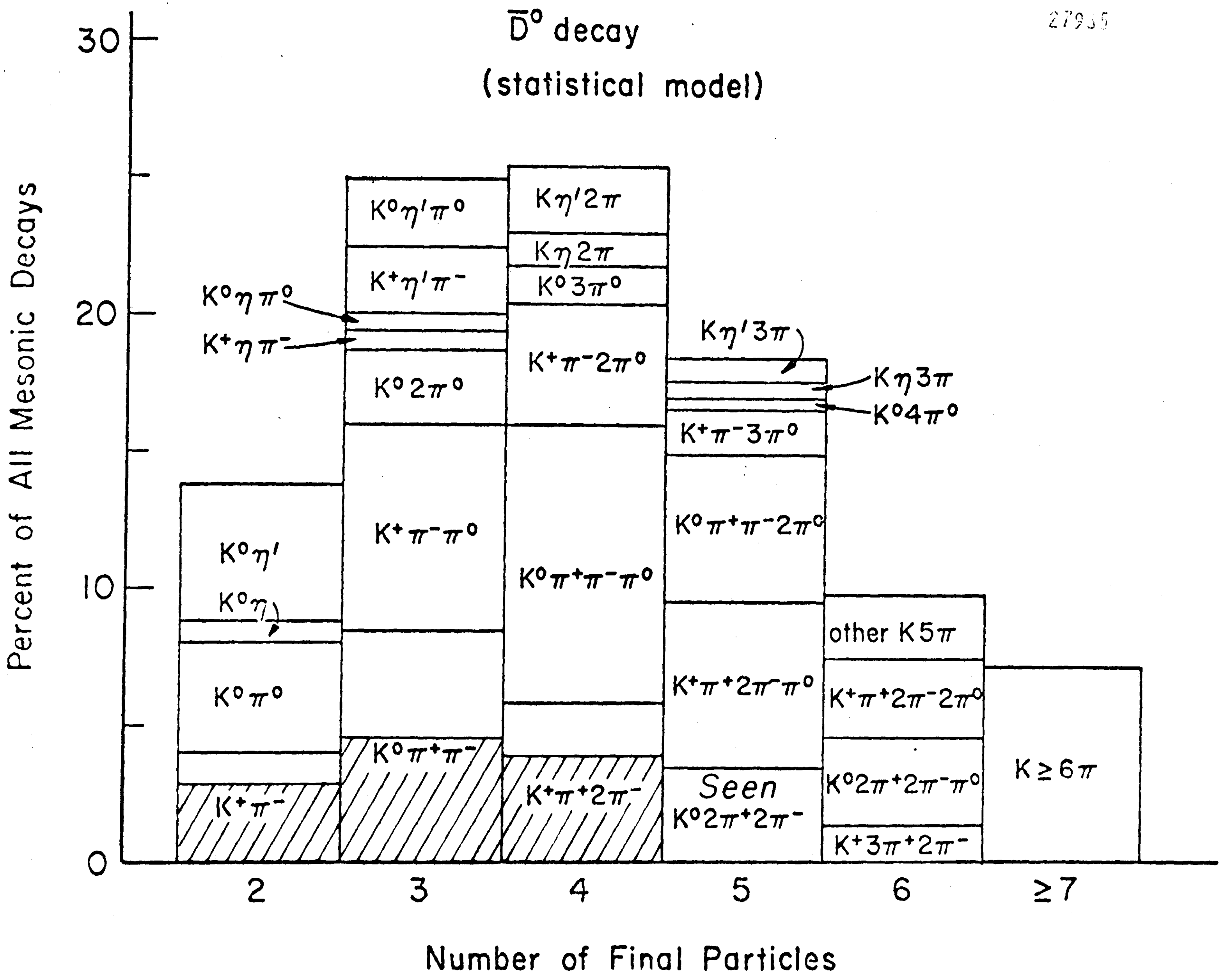

Fig.6.28 Model predictions[80)] for $\bar{D}^0$ decays into all mesonic modes. The hatched areas indicate the seen fractions.

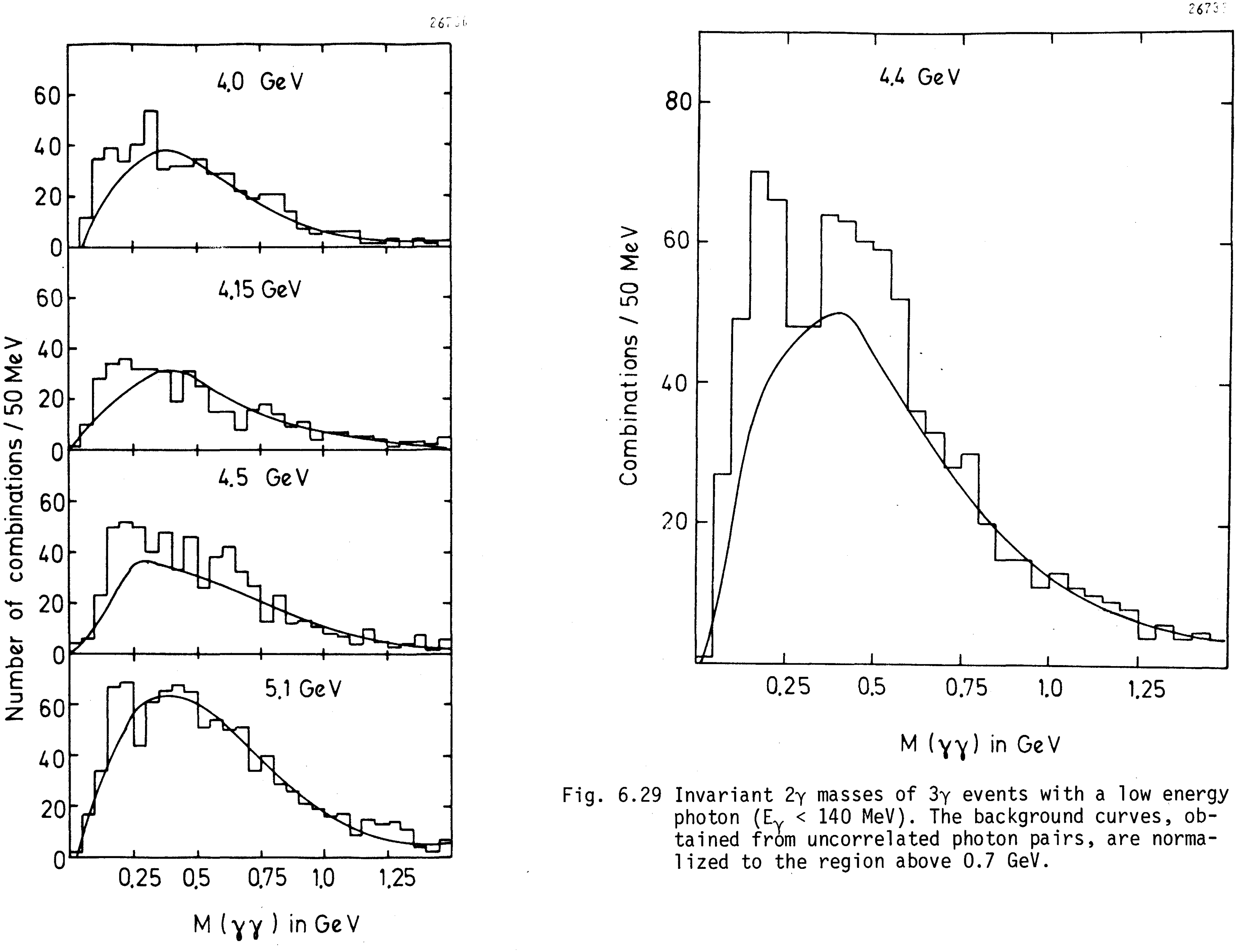

Fig. 6.29 Invariant 2γ masses of 3γ events with a low energy photon ($E_\gamma < 140$ MeV). The background curves, obtained from uncorrelated photon pairs, are normalized to the region above 0.7 GeV.

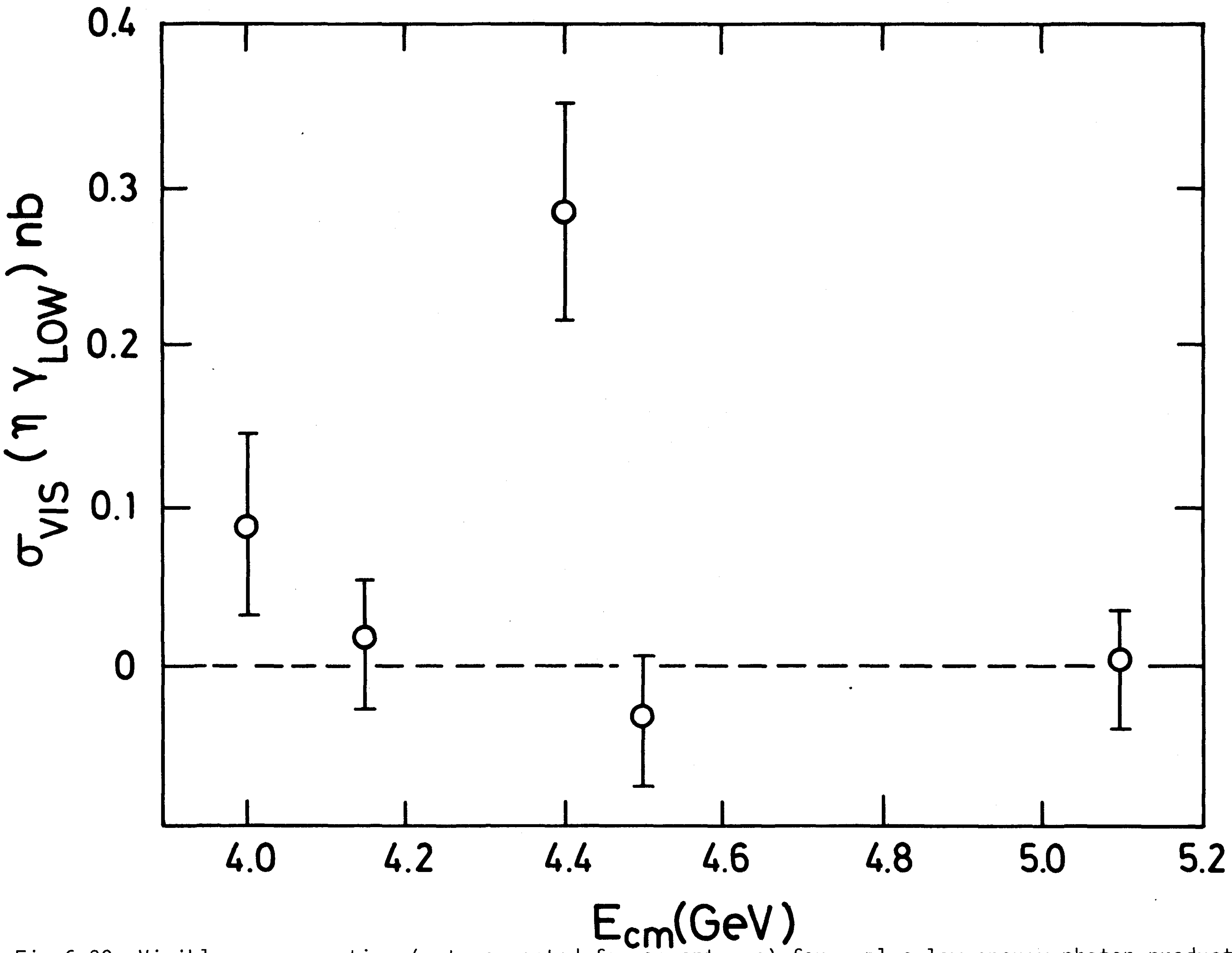

Fig.6.30 Visible cross section (not corrected for acceptance) for η plus low energy photon production.

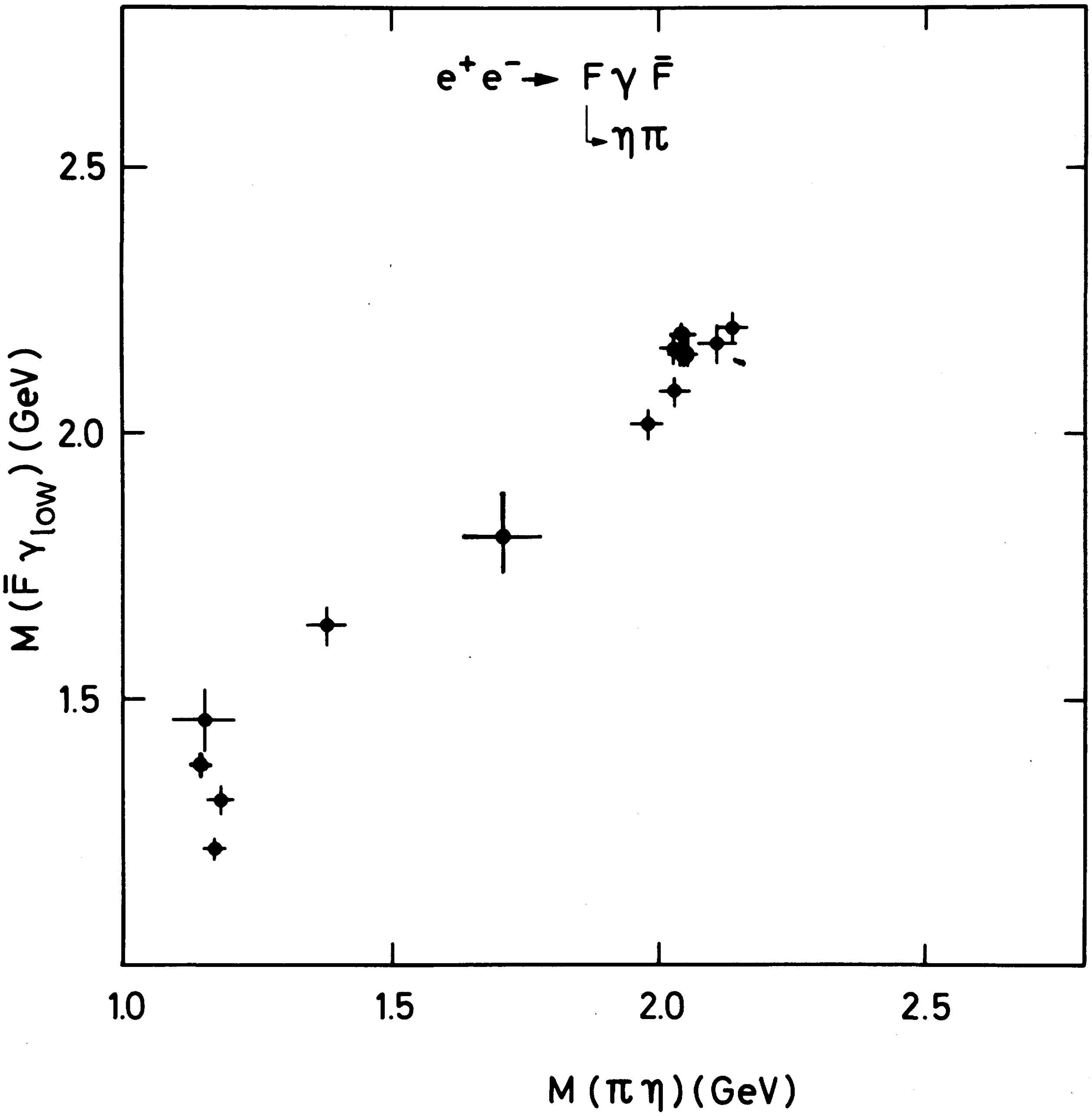

Fig.6.31 Effective $\bar{F}\gamma_{low}$ mass versus $\pi\eta$ mass obtained from the fitted process $e^+e^- \rightarrow F\bar{F}\gamma_{low} \rightarrow \pi\eta\gamma_{low} + \ldots.$ There are 5 events clustering densely at $M_{\pi\eta} = 2.04$ GeV.

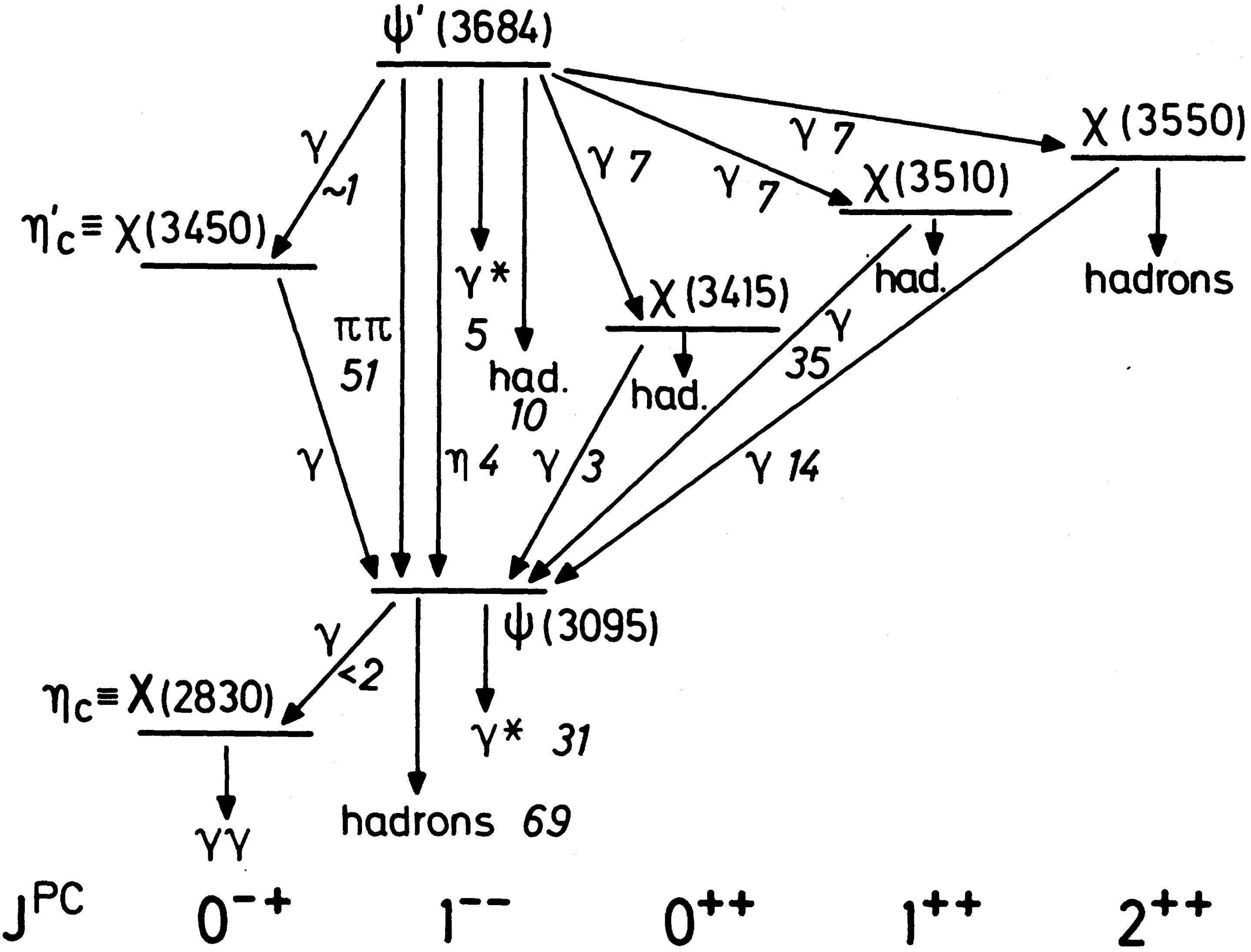

Fig.6.32 Diagram of observed transitions between $c\bar{c}$ bround states with tentative quantum number assignments. The cursive numbers next to the emitted particles show the branching ratios in percent. γ^* denotes all decays via a virtual photon including e^+e^- and $\mu^+\mu^-$ decays.

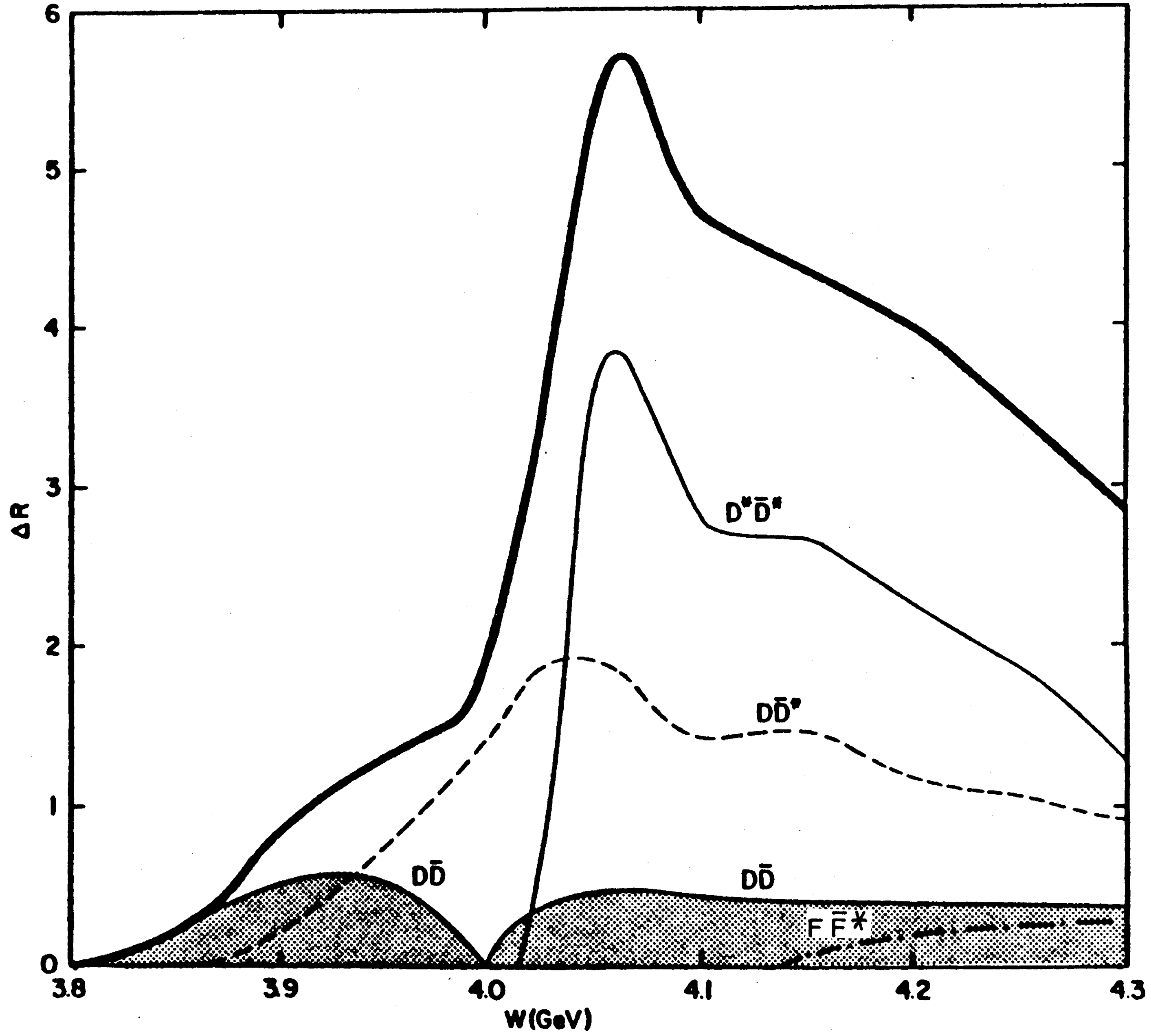

Fig.6.33 Model calculations[82)] for the threshold behaviour of pair produced charmed mesons.

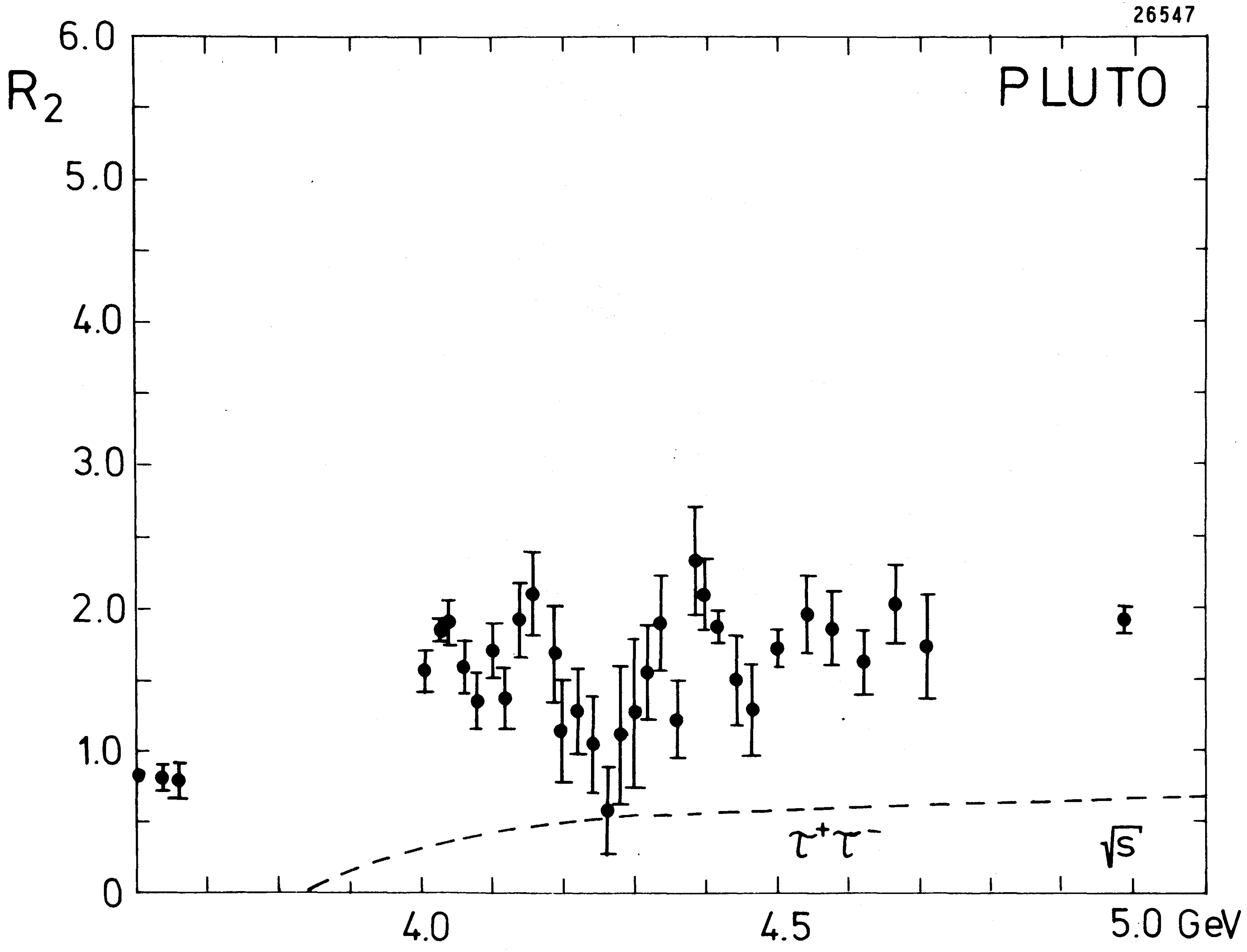

Fig.7.1 Ratio of hadronic two prong to μ pair cross section. The dashed line indicates the expected contribution from heavy leptons.

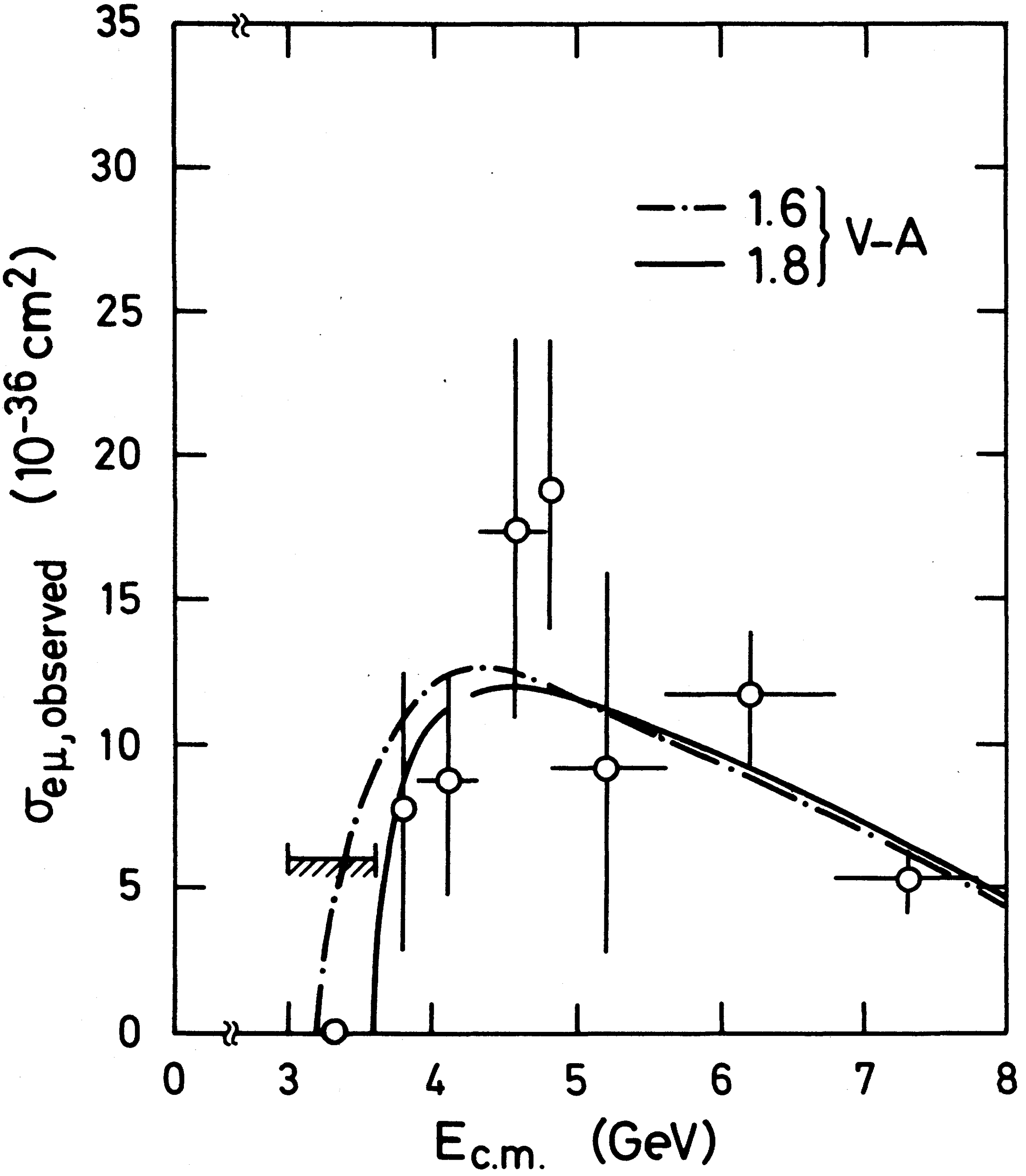

Fig.7.2 Observed eμ cross section. The curves represent model calculations for sequential heavy leptons (1.6 and 1.8 GeV) and associated massless neutrinos.

27926

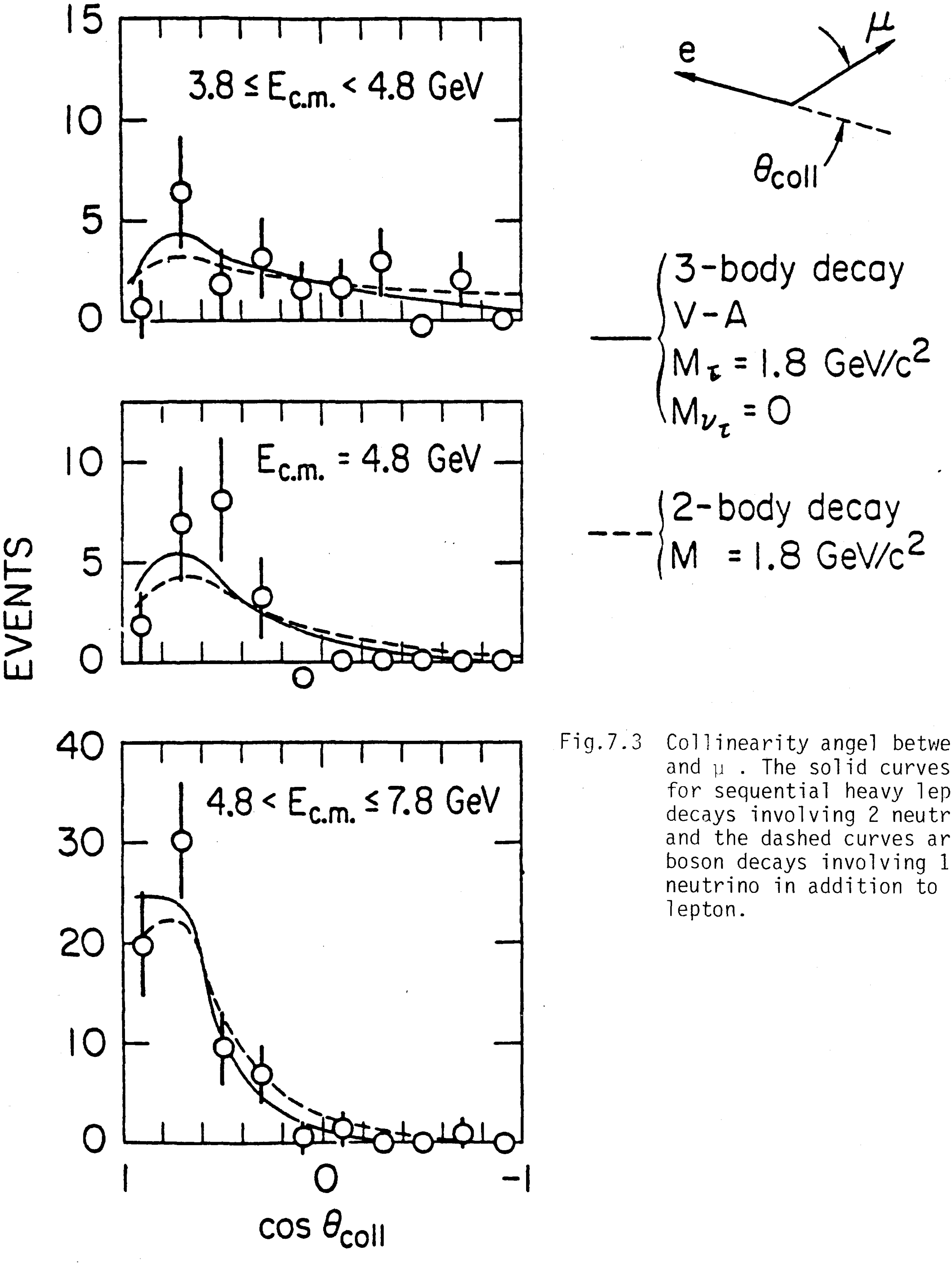

Fig.7.3 Collinearity angel between e and μ . The solid curves are for sequential heavy lepton decays involving 2 neutrinos and the dashed curves are for boson decays involving 1 neutrino in addition to the lepton.

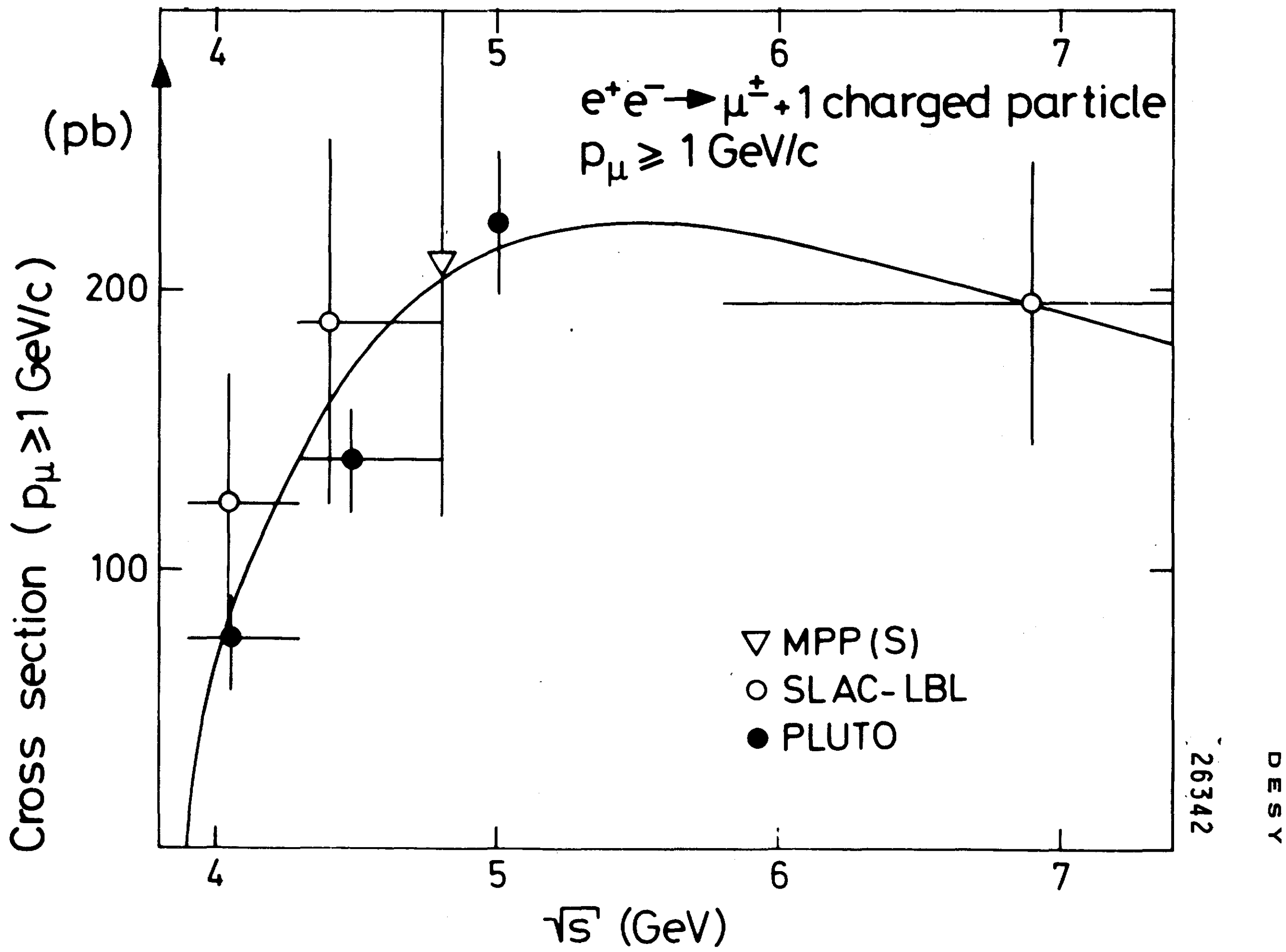

Fig.7.4 Cross section for inclusive μ events with one additional charged track. The curve is for a sequential heavy lepton with a mass of 1.9 GeV.

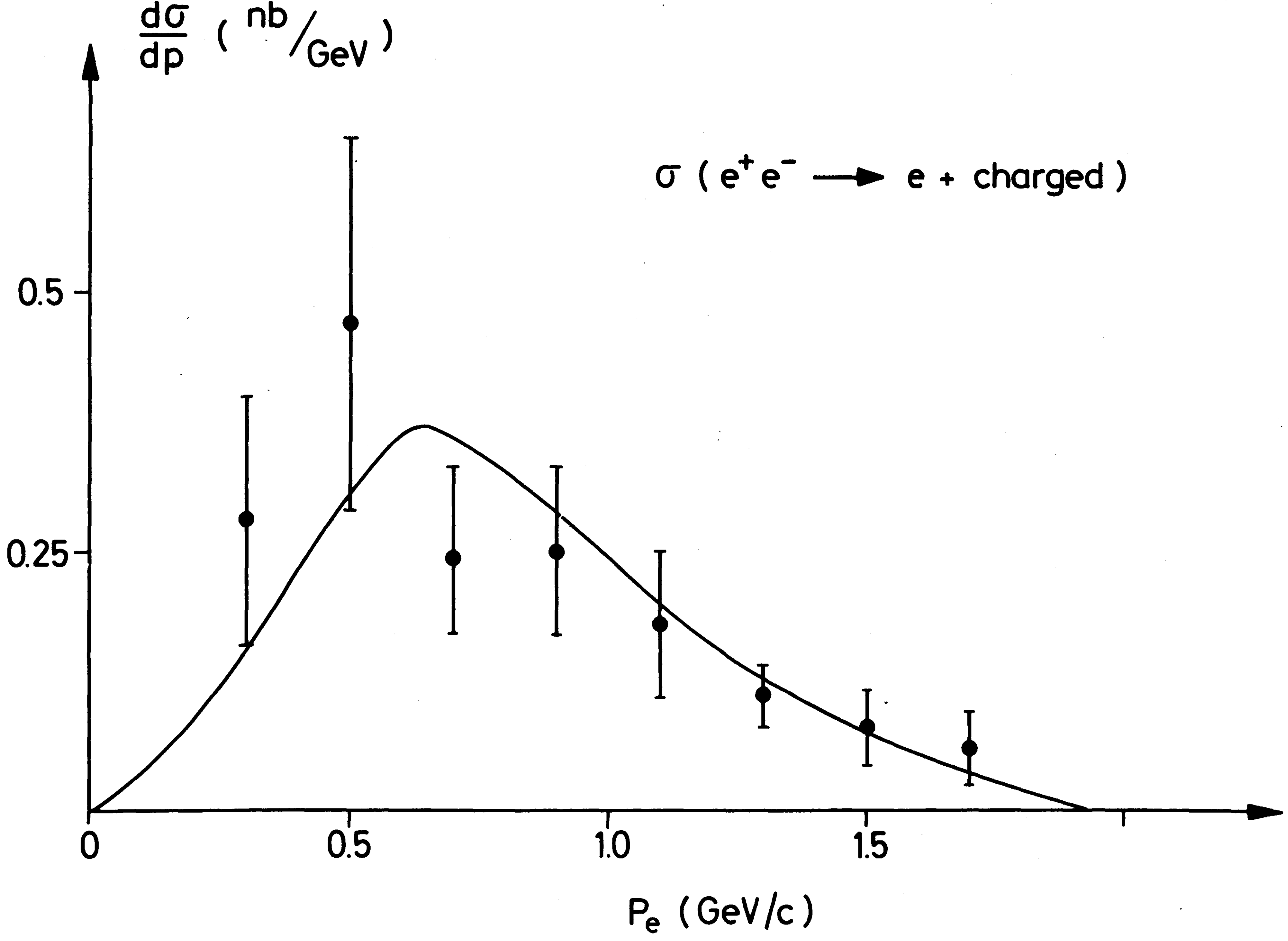

Fig.7.5 Differential cross section for inclusive electron events with an additional minimum ionizing track. The curve is for a sequential heavy lepton with a mass of 1.9 GeV.

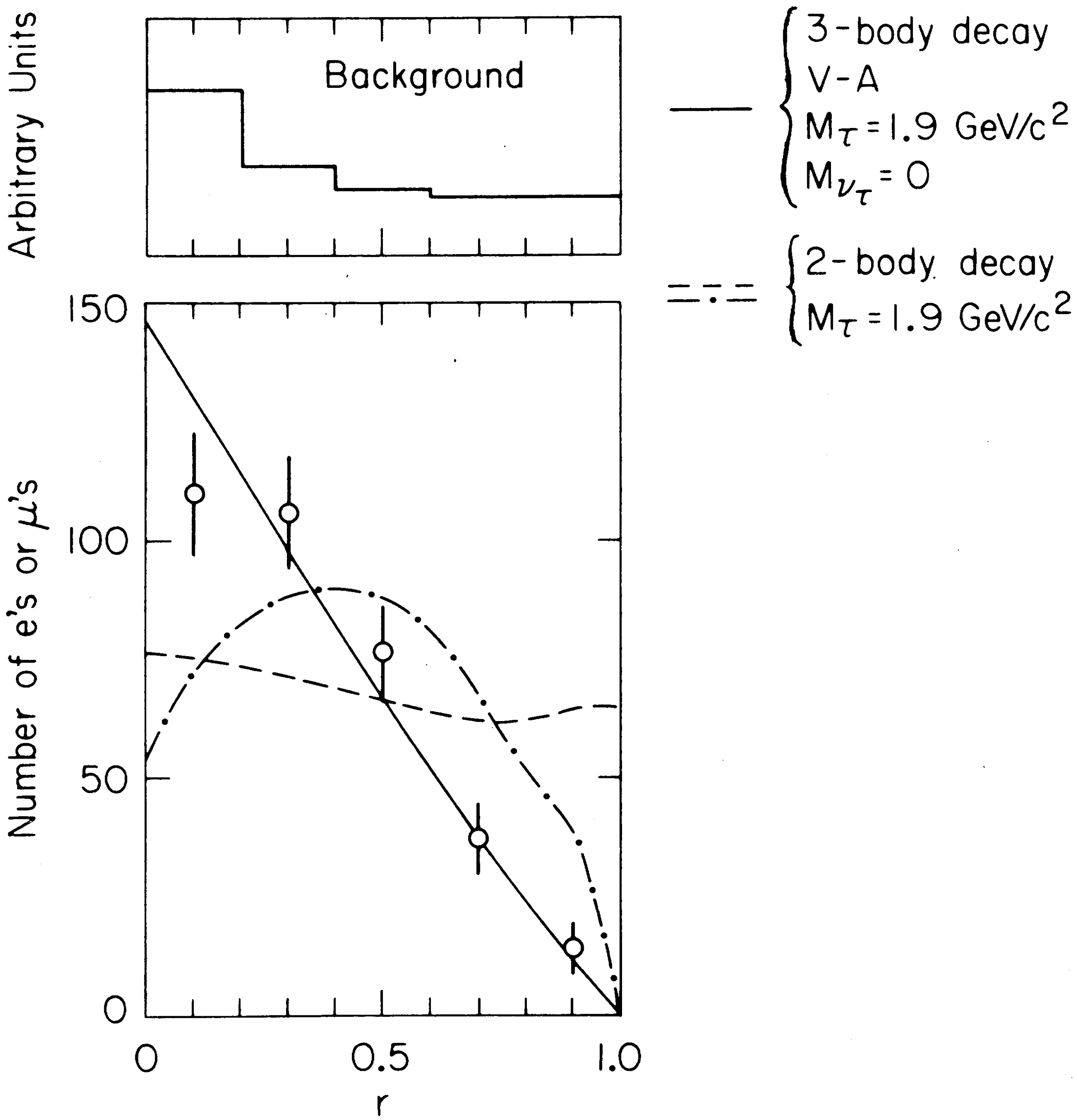

Fig.7.6 Momentum spectrum for eμ events with $3.8 \leq \sqrt{s} \leq 7.8$ GeV. Here $r = (p - 0.65)/(p_{max} - 0.65)$ where p is the e or μ momentum. The solid curve is for a 3-body heavy lepton decay and the dashed and dash-dotted curves are for 2-body decays of an unpolraized boson and a boson produced with helicity = 0 respectively.

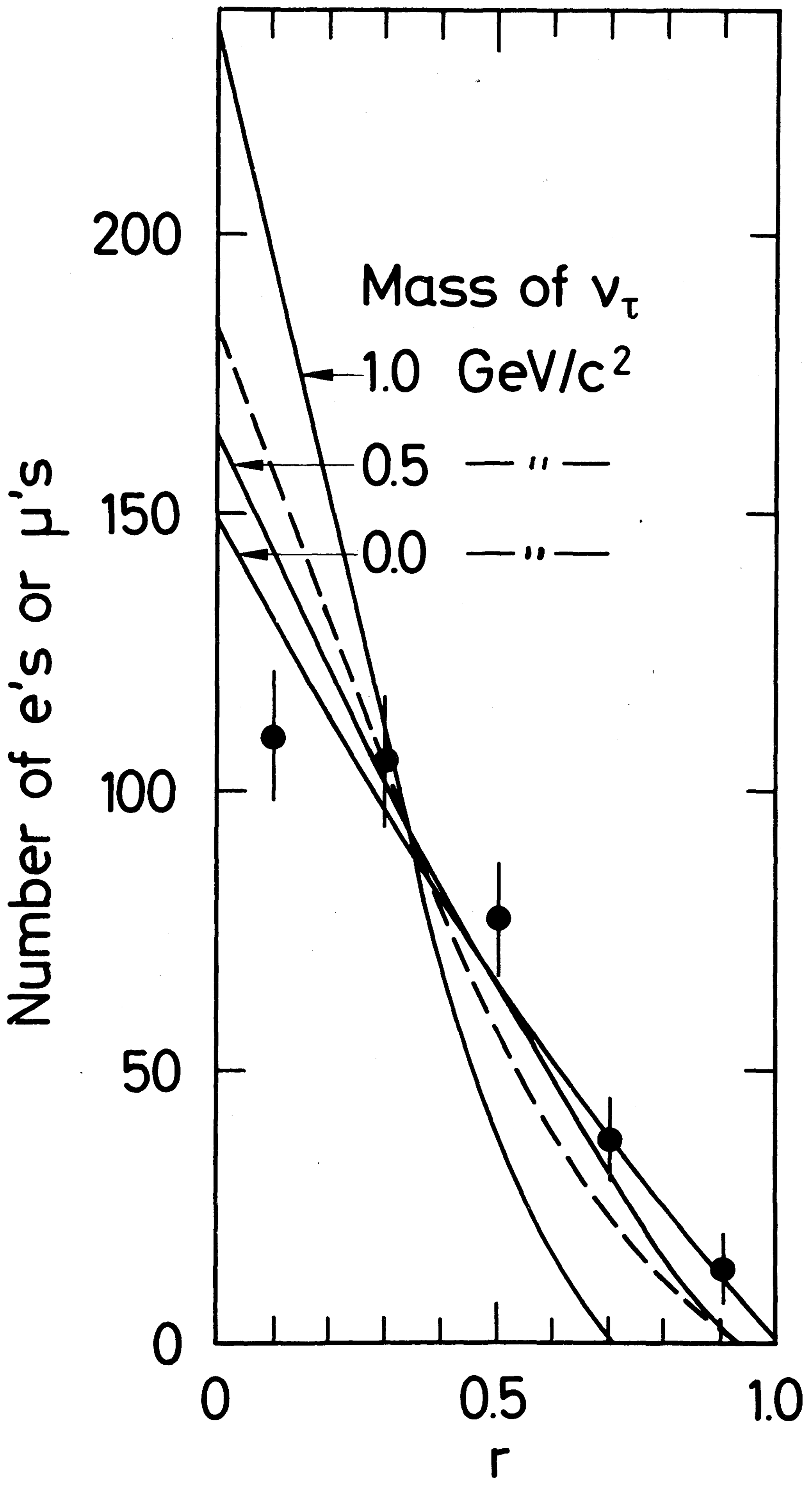

Fig.7.7 Spectrum of the scaled momentum r, as in the previous figure. The solid curves represent V-A couplings with three assumed neutrino masses and the dashed curve is for V+A coupling.

27929

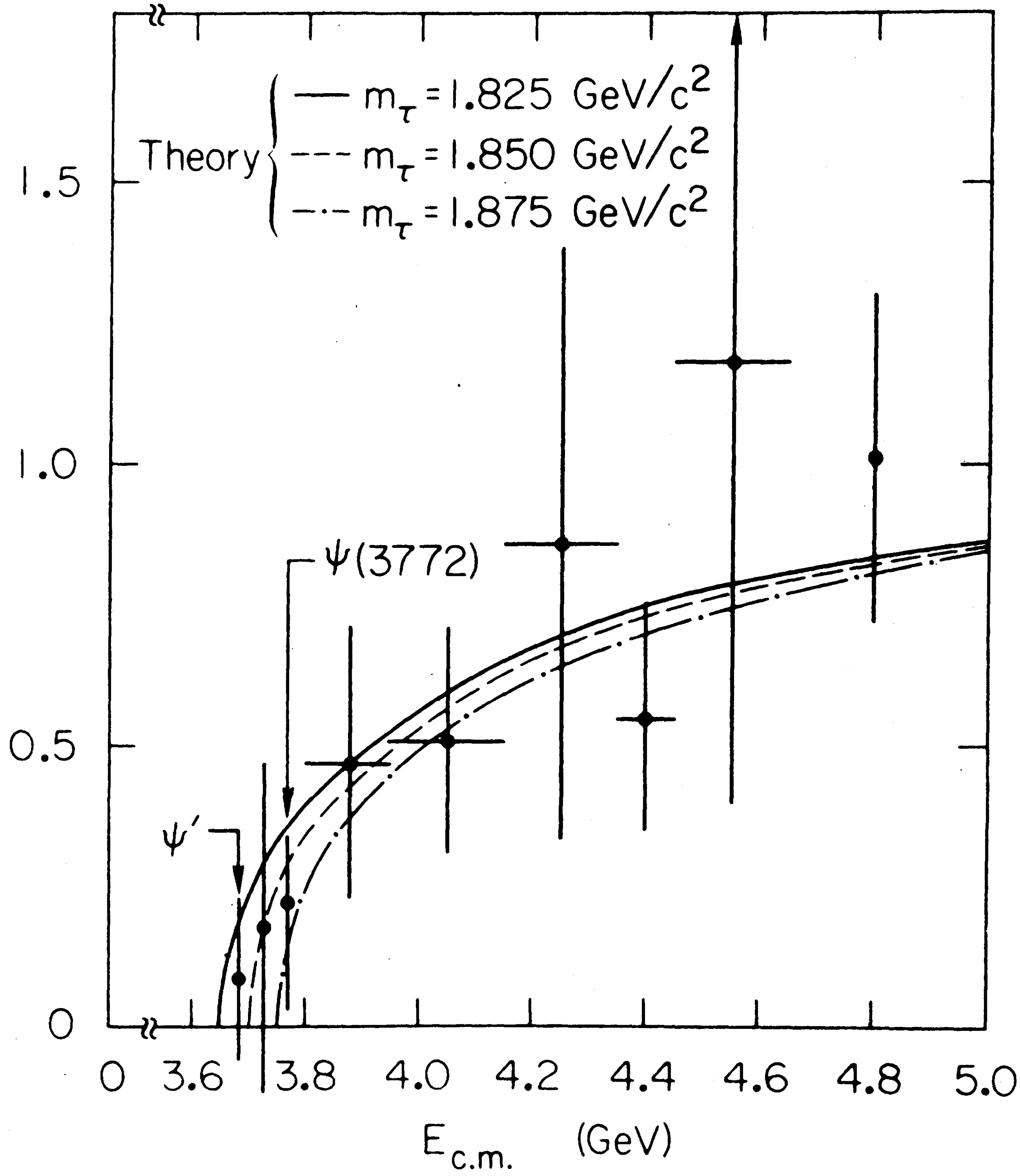

Fig. 7.8 Ratio of heavy lepton to μ pair cross section, compared with three heavy lepton mass assignments.

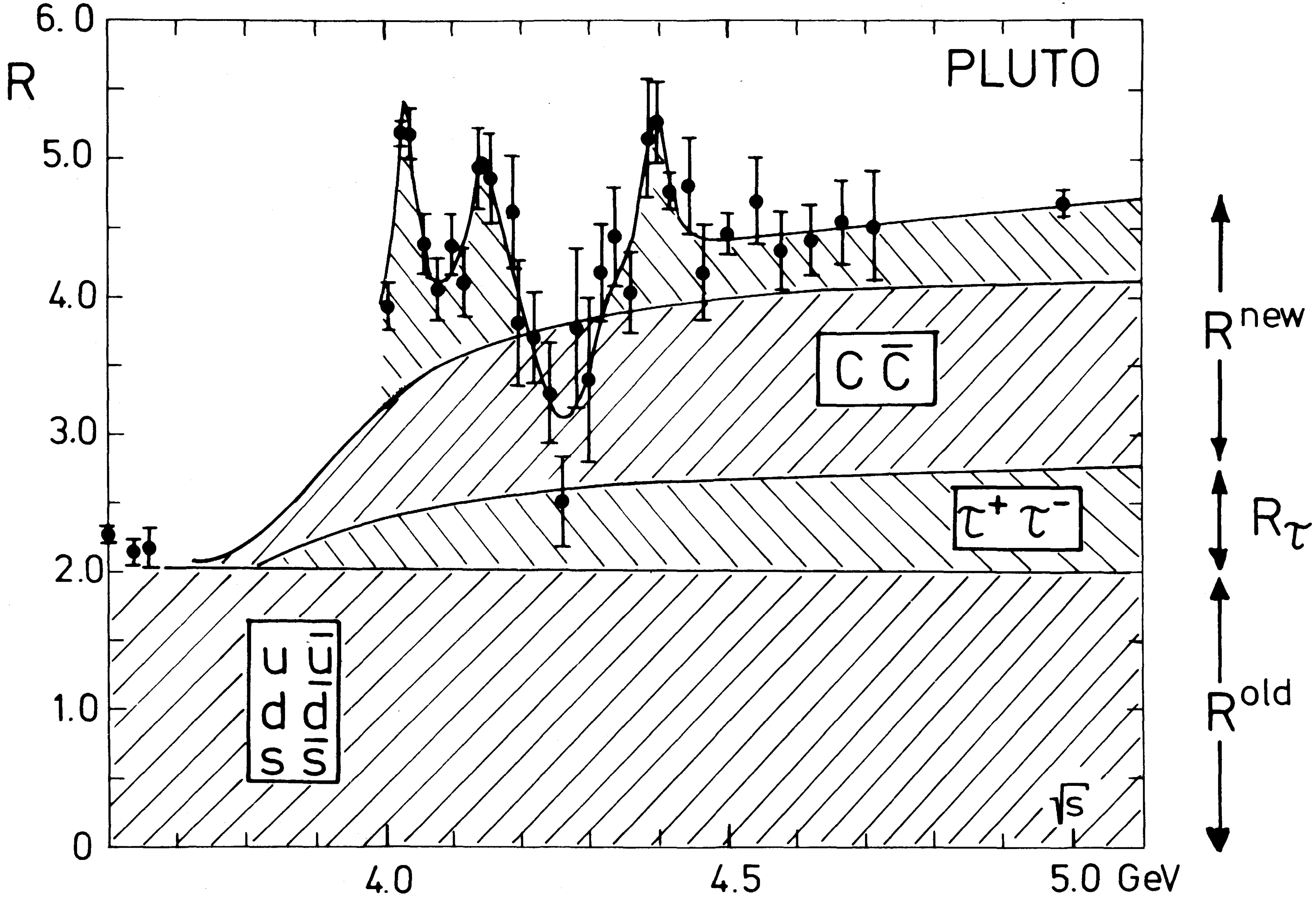

Fig.8.1 Total cross section for e^+e^- annihilation in units of the μ pair cross section (PLUTO data). Schematic representation of expected contributions from the old quarks, heavy leptons, and the new charmed quark.

27937

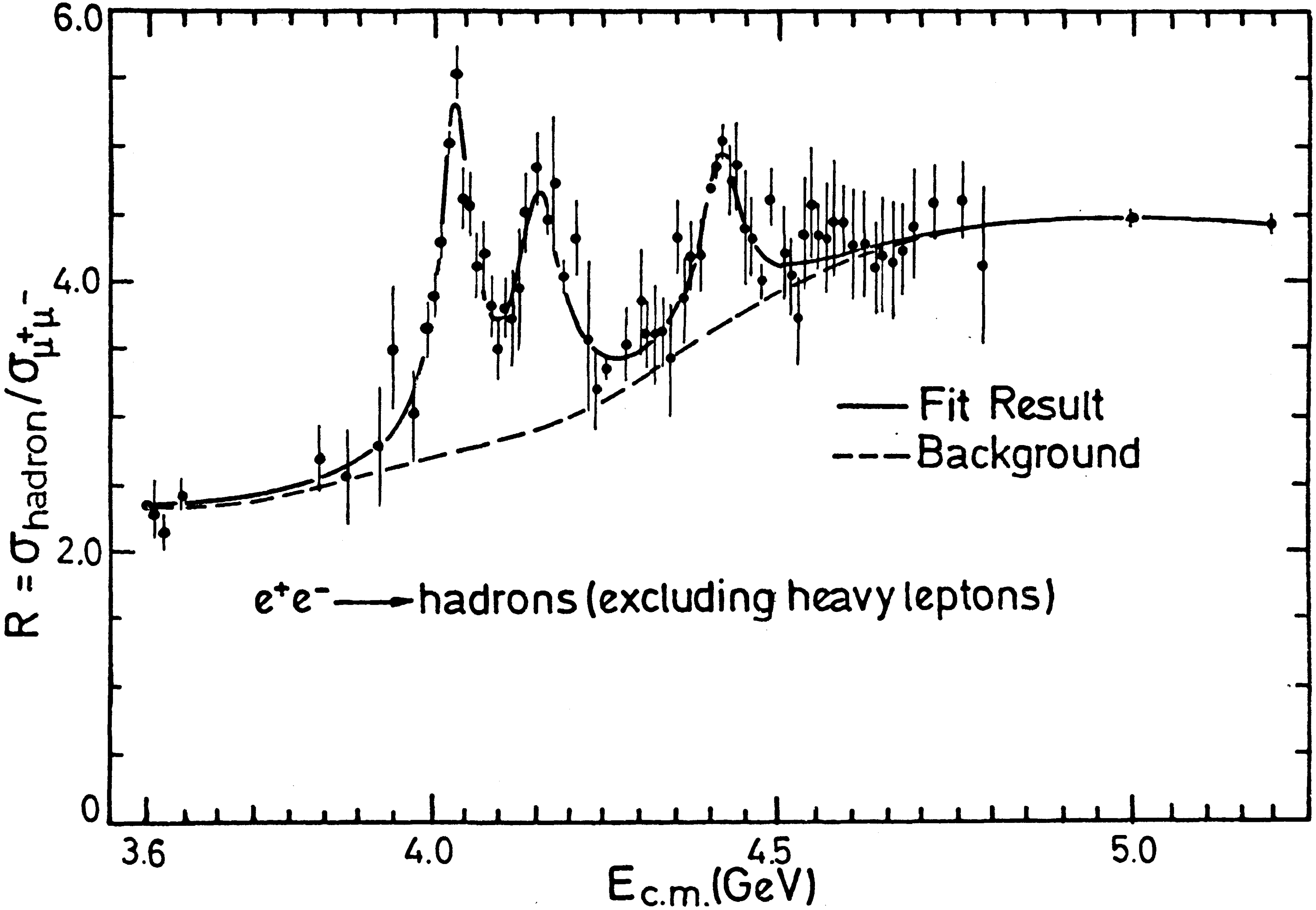

Fig. 8.2 Total hadronic cross section in units of the μ pair cross section (DASP data). The full curve is a fit with 3 Breit-Wigner distribution on top of a smooth background.

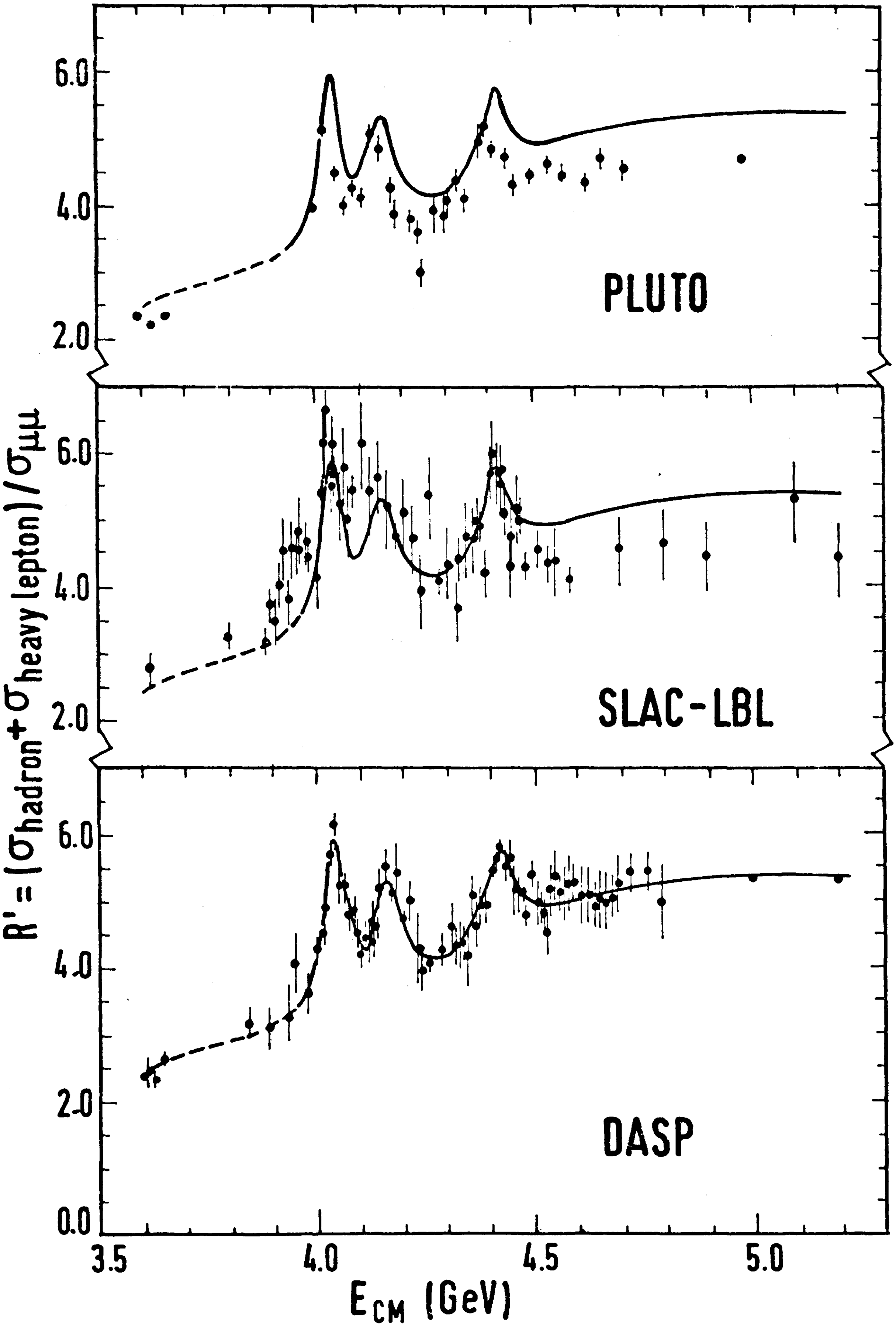

Fig.8.3 Total cross sections (including heavy leptons) from three experiment in units of $\sigma_{\mu\mu}$. The curve is a fit to the DASP data and repeated in the upper histograms for comparison.

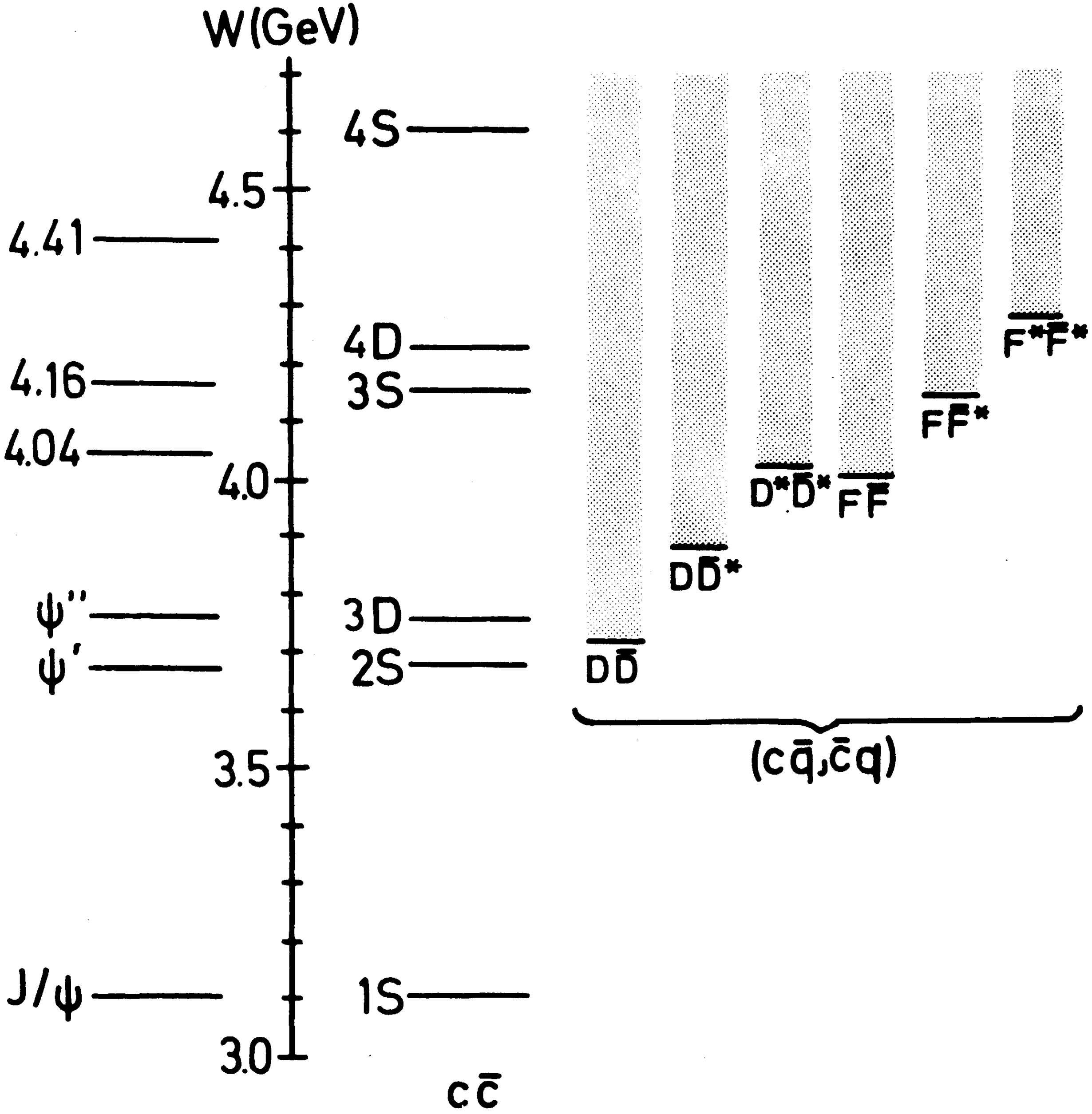

Fig.8.4 $c\bar{c}$ bound states and thresholds for $c\bar{q}$ charmed meson pair production compared to the masses of measured enhancements on the left.

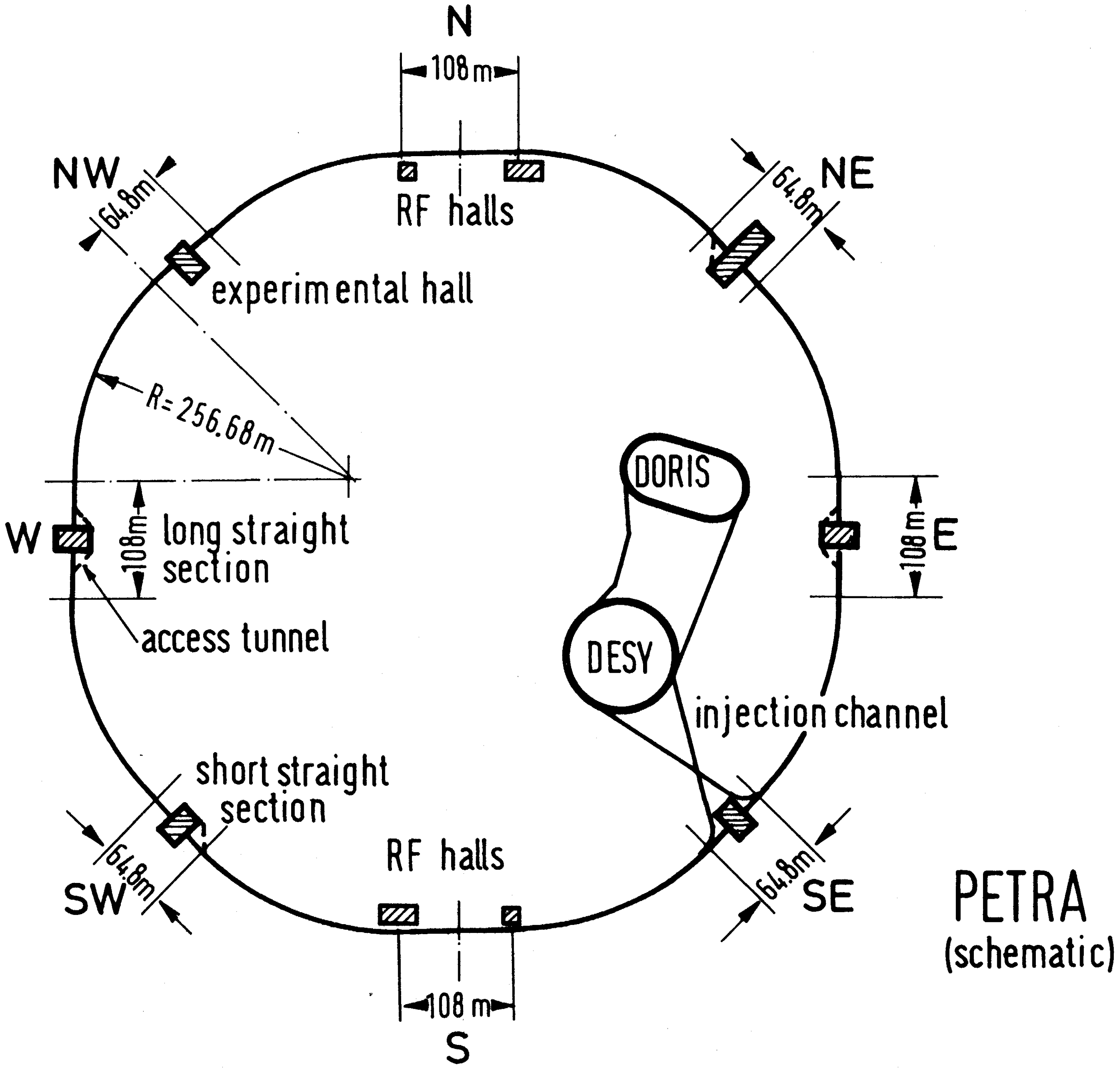

Fig. 9.1 Schematic view of the 2 x 19 GeV storage ring PETRA. On the inside of this new ring, the synchrotron DESY and the 2 x 5 GeV storage ring DORIS.

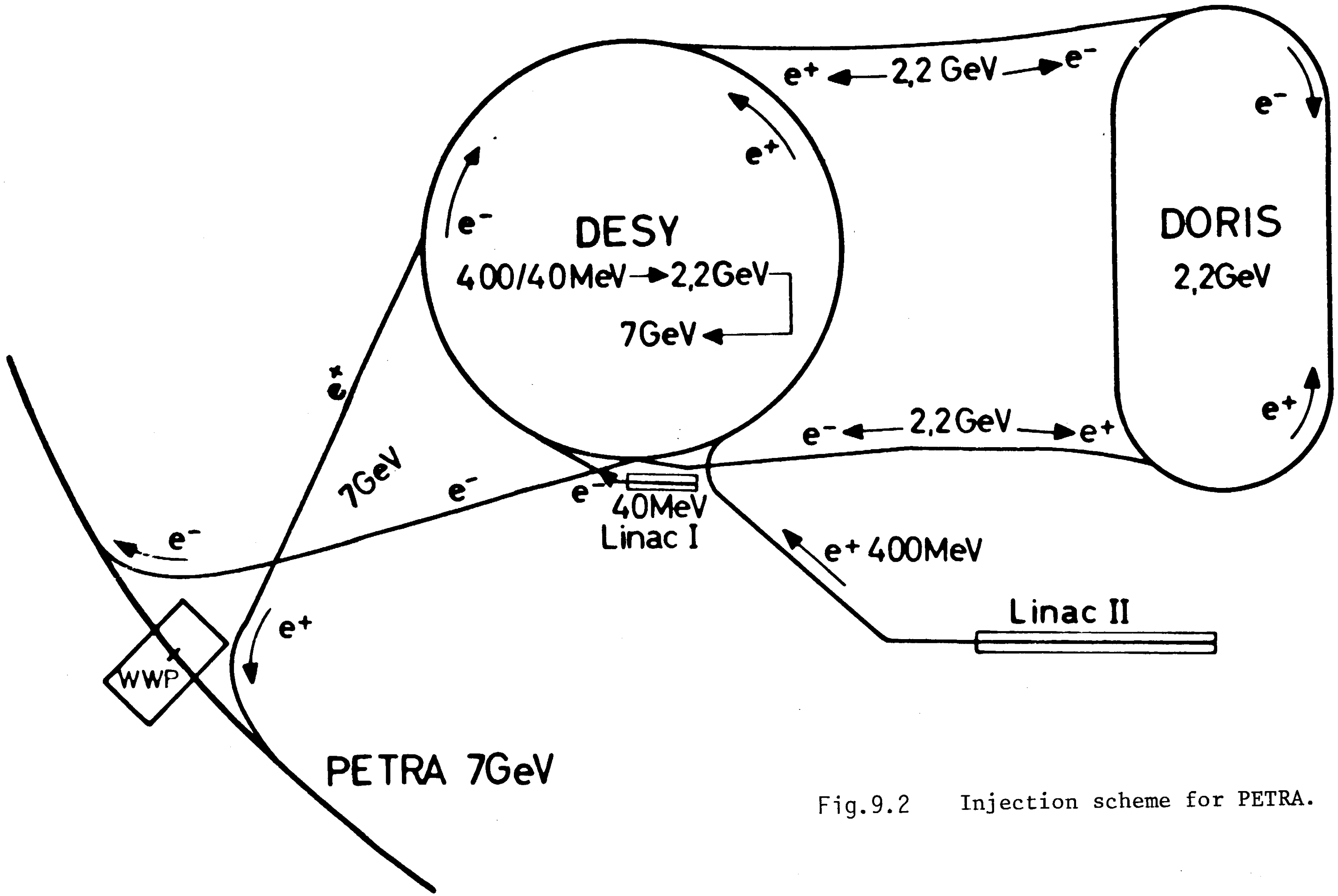

Fig.9.2 Injection scheme for PETRA.

PETRA Luminosity / Interaction region

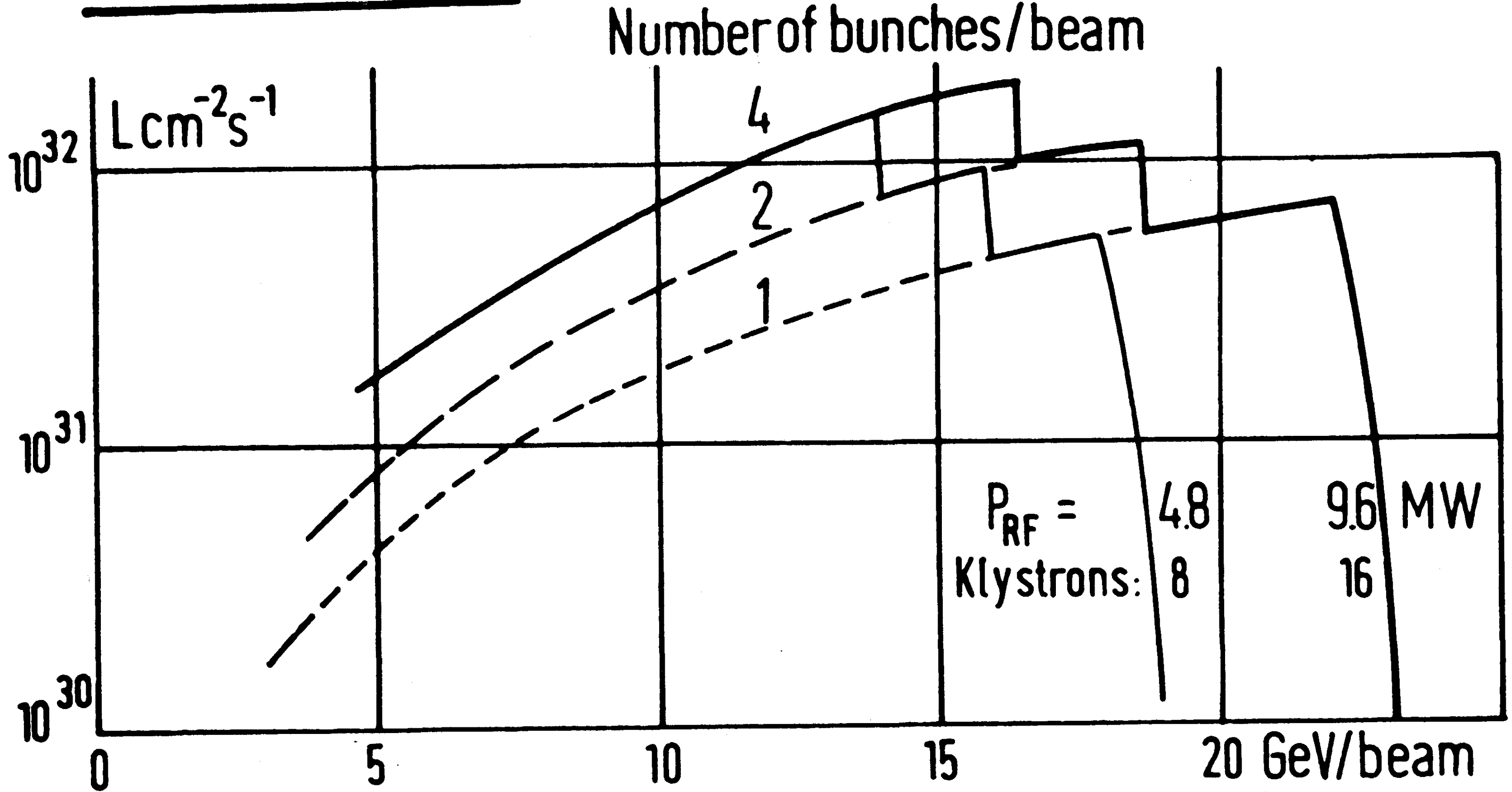

64 cavities, 96m length

Assumptions: $\varepsilon_x = 3.54 \times 10^{-7}\,m$ = const.

$\beta_x = 0.15\,m$

$\Delta Q_x = \Delta Q_z = 0.06$

$\chi = \varepsilon_z / \varepsilon_x = 0.05$

Note: $L \sim \varepsilon_x$, $L \sim \Delta Q^2$, $L \sim 1/\beta_x$

Fig.9.3

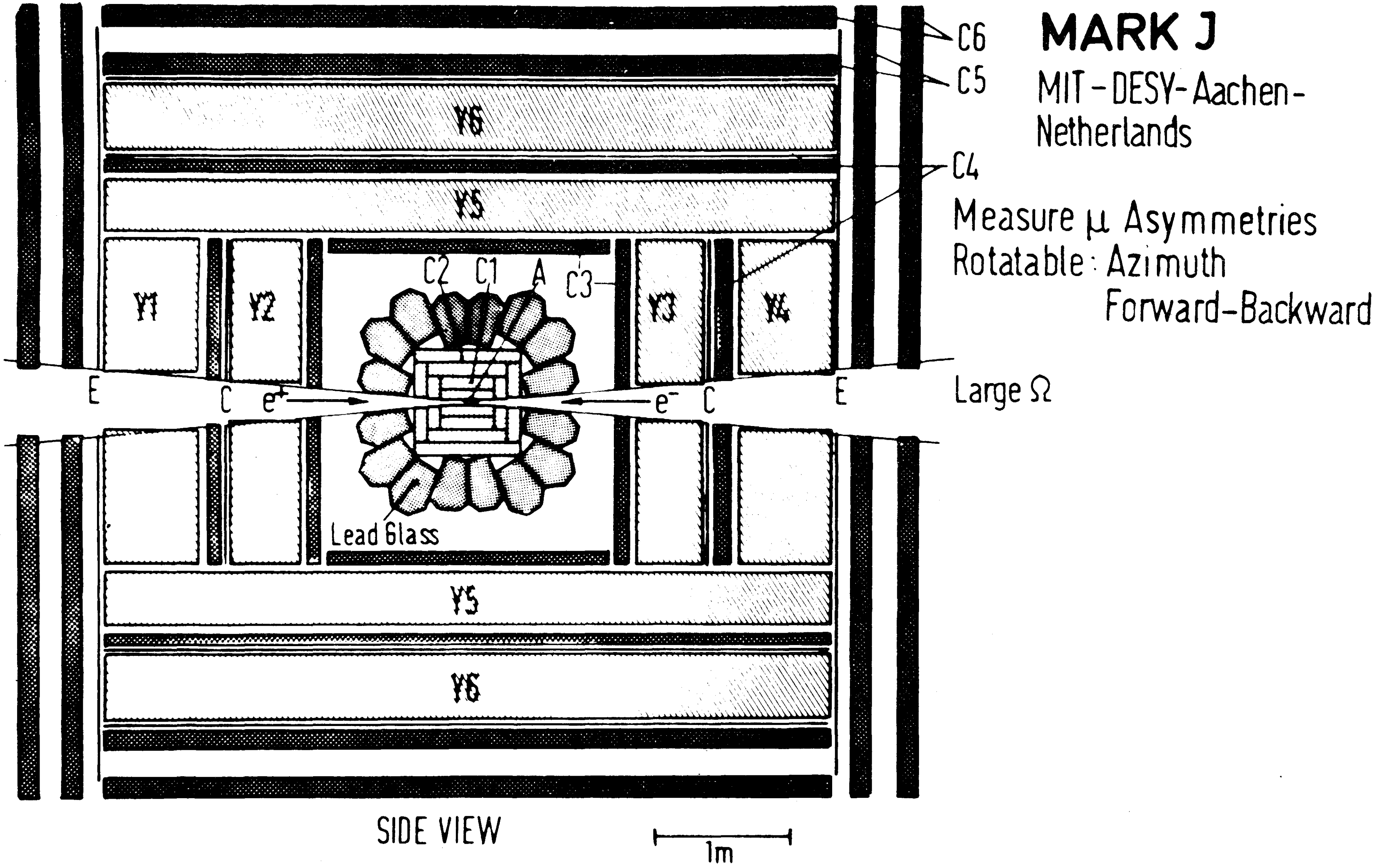
MARK J
MIT-DESY-Aachen-Netherlands
Measure μ Asymmetries
Rotatable: Azimuth
Forward-Backward
Large Ω
C6
C5
C4
C3
C2
C1
A
Y1
Y2
Y3
Y4
Y5
Y6
E
C
e+
e-
Lead Glass
SIDE VIEW
1m

Fig.9.4

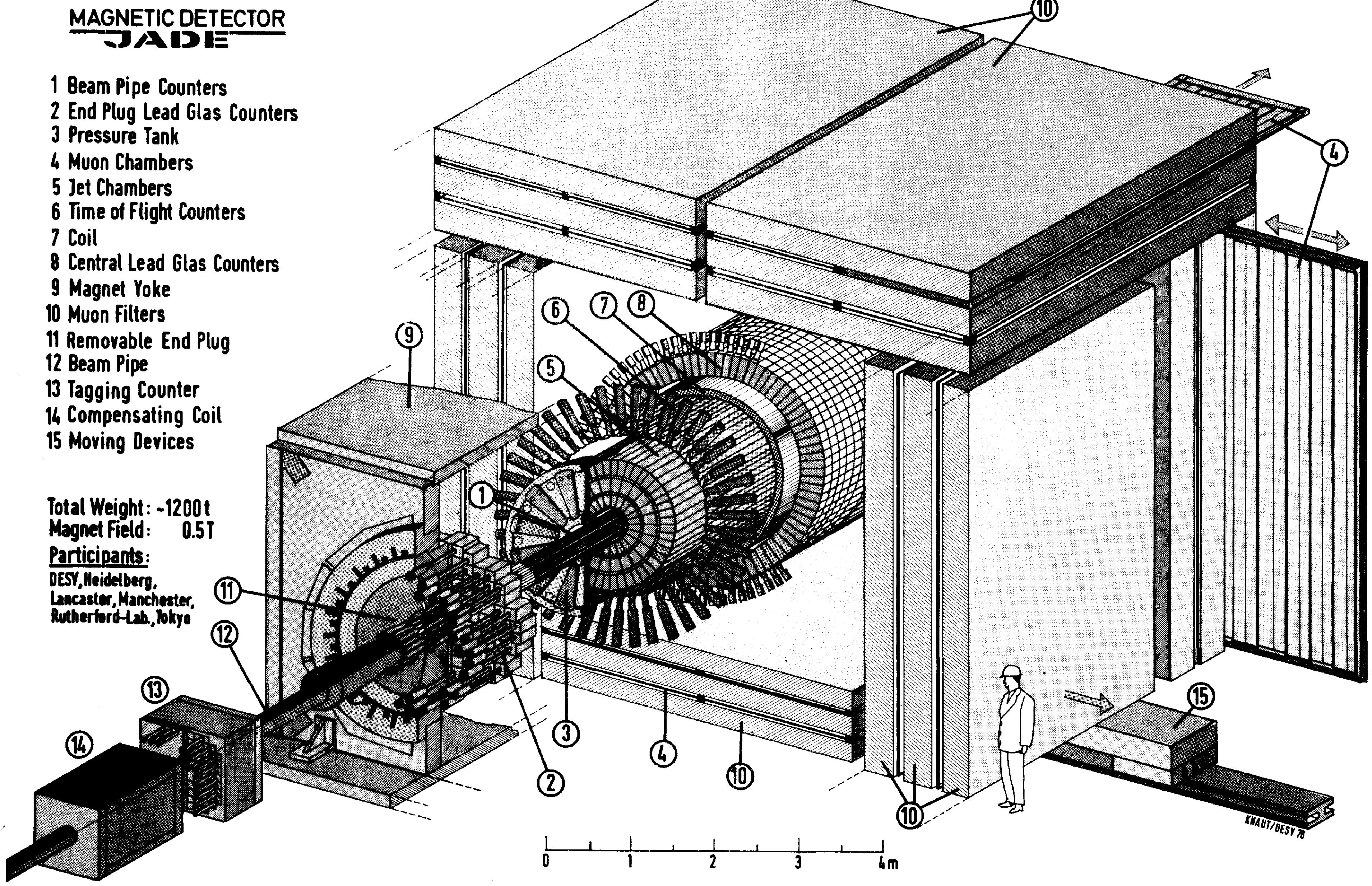
MAGNETIC DETECTOR
JADE
1 Beam Pipe Counters
2 End Plug Lead Glas Counters
3 Pressure Tank
4 Muon Chambers
5 Jet Chambers
6 Time of Flight Counters
7 Coil
8 Central Lead Glas Counters
9 Magnet Yoke
10 Muon Filters
11 Removable End Plug
12 Beam Pipe
13 Tagging Counter
14 Compensating Coil
15 Moving Devices
Total Weight: ~1200 t
Magnet Field: 0.5 T
Participants:
DESY, Heidelberg,
Lancaster, Manchester,
Rutherford-Lab., Tokyo
10
4
9
6
7
8
5
1
11
12
13
14
3
4
10
2
10
15
0
1
2
3
4m
KNAUT/DESY 78

Fig.9.5

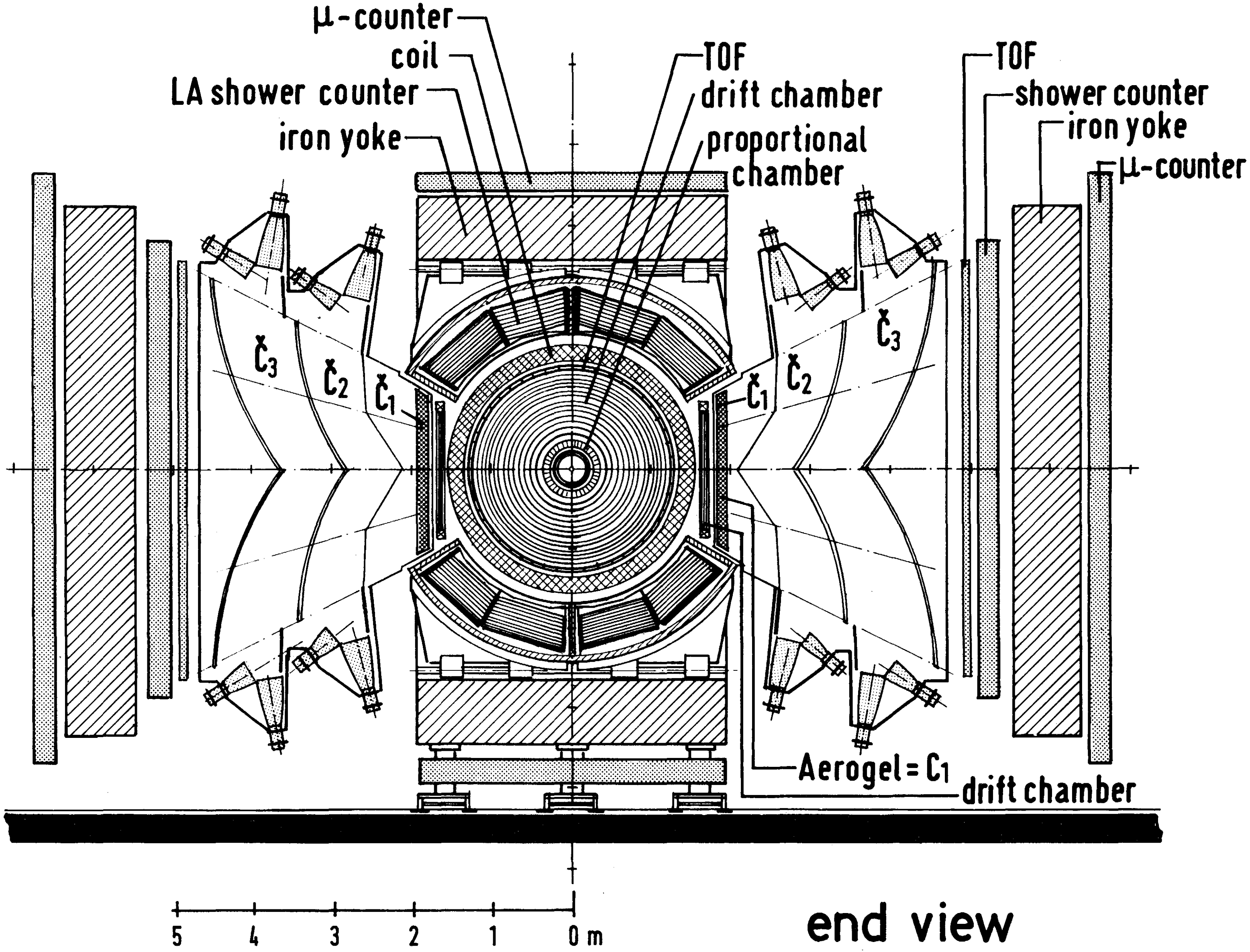

end view
(TASSO)

Fig.9.6